Aus dem Institut für Schlaganfall- und Demenzforschung am
Klinikum der Ludwig-Maximilians-Universität München

Dissertation

zum Erwerb des Doctor of Philosophy (Ph.D.) in Medical Research

an der Medizinischen Fakultät der

Ludwig-Maximilians-Universität zu München

The Role of Neuroinflammatory Mechanisms in Post-Stroke Recovery

vorgelegt von

Steffanie Heindl

aus

Hutthurm, Deutschland

Jahr

2021

Mit Genehmigung der Medizinischen Fakultät der
Ludwig-Maximilians-Universität zu München

First Supervisor: Prof. Dr. med. Arthur Liesz

Second Supervisor*:* Prof. Dr. med. Marco Düring

Dean: Prof. Dr. med. Thomas Gudermann

Date of Defense:

21. October 2021

Affidavit

LUDWIG-
MAXIMILIANS-
UNIVERSITÄT
MÜNCHEN

Dean's Office
Medical Faculty

MMRS

Affidavit

Steffanie Heindl

Surname, first name

Feodor-Lynen-Str. 17

Street

81377 München

Zip code, town

Germany

Country

I hereby declare, that the submitted thesis entitled

The Role of Neuroinflammatory Mechanisms in Post-Stroke Recovery

is my own work. I have only used the sources indicated and have not made unauthorised use of services of a third party. Where the work of others has been quoted or reproduced, the source is always given.

I further declare that the submitted thesis or parts thereof have not been presented as part of an examination degree to any other university.

Munich, 22.10.2021

Place, date

Steffanie Heindl

Signature doctoral candidate

Confirmation of congruency

LMU LUDWIG-MAXIMILIANS-UNIVERSITÄT MÜNCHEN

Dean's Office
Medical Faculty

MMRS

Confirmation of congruency between printed and electronic version of the doctoral thesis

Steffanie Heindl
Surname, first name

Feodor-Lynen-Str. 17
Street

81377 München
Zip code, town

Germany
Country

I hereby declare that the electronic version of the submitted thesis, entitled

The Role of Neuroinflammatory Mechanisms in Post-Stroke Recovery

is congruent with the printed version both in content and format.

Munich, 22.10.2021	Steffanie Heindl
Place, date	Signature doctoral candidate

Table of content

Affidavit 2

Confirmation of congruency 3

Table of content 4

List of abbreviations 5

List of publications 6

1. Introductory summary 7

1.1 The global burden of stroke 7

1.2 The main subtypes of stroke 7

1.3 Available therapies for ischemic stroke 7

1.4 Post-stroke neuroinflammation 8

1.5 Microglial response to stroke 8

1.6 Leukocyte infiltration after stroke 8

1.7 Gut-brain interaction after stroke 9

1.8 Aim of the thesis 9

1.9 Summary of the included publications 10

1.9.1 Chronic T cell proliferation in brains after stroke could interfere with the efficacy of immunotherapies. 10

1.9.2 Microglia monitor and protect neuronal function through specialized somatic purinergic junctions. 12

1.9.3 Short-Chain Fatty Acids Improve Poststroke Recovery via Immunological Mechanisms. 14

1.10 Concluding summary 16

2. Personal contribution to the included publications 17

3. References 18

4. Publication I – Chronic T cell proliferation in brains after stroke could interfere with the efficacy of immunotherapies. 22

5. Publication II - Microglia monitor and protect neuronal function through specialized somatic purinergic junctions. 38

6. Publication III - Short-Chain Fatty Acids Improve Poststroke Recovery via Immunological Mechanisms. 116

7. Acknowledgements 133

8. Scientific publications 134

List of abbreviations

ADP	adenosine diphosphate
ATP	adenosine triphosphate
BDNF	brain derived neurotrophic factor
CD*	cluster of differentiation
DALYs	disability-adjusted live years
DAMPs	damage associated molecular patterns
DREADD	designer receptor exclusively activated by designer drugs
EphA2	ephrin type-A receptor 2
HMGB1	high-mobility group box protein 1
i.c.m.	intra cisterna magna injection
IL-10	interleukin 10
Ki67	nuclear proliferation marker
Kv2.1	voltage-gated potassium channel
NADH	nicotinamide adenine dinucleotide hydride
P2Y12	chemoreceptor for adenosine diphosphate
PSB	PSB0739, selective P2Y12 receptor blocker
PT	photothrombosis
Rag1	recombination activating gene 1
RNA	ribonucleic acid
ROS	reactive oxygen species
SCFAs	short chain fatty acids
tPA	tissue plasminogen activator
TrkB	tropomyosin receptor kinase B
UTP	uridine triphosphate
VGlut1	vesicular glutamate transporter 1

List of publications

Heindl S, Ricci A, Carofiglio O, Zhou Q, Arzberger T, Lenart N, Franzmeier N, Hortobagyi T, Nelson PT, Stowe AM, Denes A, Edbauer D, Liesz A. (2021). Chronic T cell proliferation in brains after stroke could interfere with the efficacy of immunotherapies. ***J Exp Med.*** doi: 10.1084/jem.20202411. doi: 10.1084/jem.20202411

Cserép C, Pósfai B, Lénárt N, Fekete R, László ZI, Lele Z, Orsolits B, Molnár G, **Heindl S**, Schwarcz AD, Ujvári K, Környei Z, Tóth K, Szabadits E, Sperlágh B, Baranyi M, Csiba L, Hortobágyi T, Maglóczky Z, Martinecz B, Szabó G, Erdélyi F, Szipőcs R, Tamkun MM, Gesierich B, Duering M, Katona I, Liesz A, Tamás G, Dénes Á. (2020). Microglia monitor and protect neuronal function through specialized somatic purinergic junctions. ***Science.*** Jan 31;367(6477):528-537. doi: 10.1126/science.aax6752.

Sadler R, Cramer JV, **Heindl S**, Kostidis S, Betz D, Zuurbier KR, Northoff BH, Heijink M, Goldberg MP, Plautz EJ, Roth S, Malik R, Dichgans M, Holdt LM, Benakis C, Giera M, Stowe AM, Liesz A. (2020). Short-Chain Fatty Acids Improve Poststroke Recovery via Immunological Mechanisms. ***J Neurosci.*** Jan 29;40(5):1162-1173. doi: 10.1523/JNEUROSCI.1359-19.2019.

1. Introductory summary

1.1 The global burden of stroke

Despite the growing effort of stroke research for the development of therapeutic strategies, stroke remains an increasing health problem with a vast socioeconomic burden worldwide [1]. According to the World Health Organization's latest report, published in December 2020, stroke caused 11 % of total deaths worldwide, which makes it the second leading cause of death [2]. Moreover, the number of stroke-related long-term disabilities increased tremendously in recent years: In 2000, stroke was the fifth most common global cause for disabilities with 125.9 million and the third in 2019 with 139.4 million DALYs (disability-adjusted live years) [2].

1.2 The main subtypes of stroke

Stroke can be classified in two main subtypes: Ischemic stroke, the subject of this thesis, is the most frequent form causing 88 % of global stroke cases and is triggered by an obstruction of a brain supplying artery by blood clots, or atherosclerotic plaques [3]. The second main subtype, hemorrhagic stroke, is caused by the rupture of a cerebral blood vessel, which provokes bleeding in the subarachnoid space or intracerebral parenchyma and makes up a smaller proportion of 12 % yet results in more deaths and disabilities [4-6].

1.3 Available therapies for ischemic stroke

To date there is only a limited number of clinically approved treatment options for ischemic stroke, including acute recanalization strategies, focusing on rapid reperfusion to reduce cerebral tissue damage ("time is brain") [3, 7]. The first choice of treatment is intravenous thrombolysis using tissue plasminogen activator (tPA), which is only applicable within 4.5 hours after symptom onset [8-10]. Mechanical thrombectomy can be applied for a longer time period after ischemia and is often combined with tPA administration [11-13]. However, both treatment options reach only 5-10 % of stroke patients due to the narrow treatment window, contraindications or the hazard of severe complications [14-16]. Thus, the development of treatment strategies with an extended applicability for the subacute and chronic phase after stroke has highest priority in today's stroke research.

1.4 Post-stroke neuroinflammation

Neuroinflammation is a key pathomechanism of stroke, contributing substantially to secondary tissue damage and exacerbation of the lesion [17-20]. Neuroinflammation is initiated by rapid neuronal cell death within the ischemic territory due to hypoxic stress, intracellular ion disturbances, mitochondrial failure and loss of intracellular structures [21]. In the surrounding, still partially perfused tissue (penumbra) neurons undergo delayed cell death by uncontrolled release of neurotransmitters, resulting in excitotoxicity [21]. Dying and injured cells release danger molecules, including nucleotides (ATP, UTP), reactive oxygen species (ROS) and damage associated molecular patterns (DAMPs), such as high-mobility group box protein 1 (HMGB1) and heat shock proteins, triggering a rapid inflammatory response involving local and peripheral immune cells [20, 22-25].

1.5 Microglial response to stroke

Microglia, the resident cerebral macrophages, are the first cell type reacting to stroke induced tissue injury and DAMPs within minutes to hours [26-28]. Under physiological conditions, microglia are continuously surveilling the brain with fine, ramified processes, allowing them to recognize disturbances in the cerebral microenvironment [29-32]. The recognition of DAMPs initiates rapid activation and morphological transformation of microglia from ramified to amoeboid, enabling them to migrate towards the injured tissue and phagocytose cell debris [33-35]. In addition, microglial activation is characterized by an increased cytokine-release and changed expression of surface molecules [36, 37]. Due to their essential role in synaptic remodeling in the developing and adult brain by synaptic pruning and the release of neurotrophic factors, such as brain derived neurotrophic factor (BDNF), microglia became a major target for stroke research [34, 38, 39]. Moreover, direct contact between microglia and neurons was described to be neuroprotective after stroke [40, 41]. Hence, microglial responses might play an essential role in post-stroke regeneration and have a high potential as therapeutic targets.

1.6 Leukocyte infiltration after stroke

In addition to the acute microglial response, circulating myeloid cells infiltrate into the post-stroke brain and secrete additional chemokines and cytokines [21, 42]. This expanding inflammatory milieu triggers the invasion of circulating lymphocytes within 24 hours after stroke, which peaks after 3-5 days [23, 43]. During the acute phase, T cells can provoke thromboinflammation, resulting in exacerbation of the tissue damage [44-48]. Moreover, cytokine driven effector functions of $CD4^+$ T helper cells and $CD8^+$ cytotoxic T cells can have further detrimental effects, leading to extensive lesion expansion and disease progression [20, 22, 49-51]. In contrast, regulatory T cells exert anti-inflammatory functions after stroke – by secreting the neuroprotective cytokine IL-10 – and play crucial immunosuppressive roles [52-54]. Thus, T cells possess both neuroinflammatory and neuroprotective functions, which play essential roles in regeneration after stroke [42].

1.7 Gut-brain interaction after stroke

Besides neuroinflammation in the brain, ischemic stroke evokes changes in remote organs, including the lung [55], heart [56], and intestine [57]. Previous studies demonstrated an important role for the gut microbiome for stroke outcome, driven by brain-invading lymphocytes originating from the intestine [49, 57-59]. In particular, metabolites from the gut microbiota, such as short-chain fatty acids (SCFAs), can cross the blood-brain barrier and influence brain function during physiological and pathological conditions [60-63]. Previous studies investigating the role of SCFAs in modulating the immune system demonstrated a pivotal role in T cell polarization towards an anti-inflammatory subset and the maturation of microglial cells [64-66]. However, the mechanisms by which SCFAs contribute to these effects and how to utilize them for therapeutic approaches, still requires further investigation.

1.8 Aim of the thesis

In the search of novel therapeutic approaches to promote post-stroke outcome, neuroinflammation became a major focus of current stroke research [18, 54, 67-69]. Therefore, the overarching aim of this doctoral thesis was to investigate the role of neuroinflammatory mechanisms in post-stroke recovery and the evaluation of potential targets for the development of immunomodulatory treatment strategies. This goal was comprehensively addressed from three different perspectives. The first aim was to evaluate the efficacy of an immunomodulatory treatment strategy for stroke, which failed in clinical trials, and investigate the underlying mechanism that led to their failure. The second aim focused more specifically on the direct communication between microglia and neurons and their possible neuroprotective function. The third aim focuses on the role of gut microbiota-derived metabolites in changing the neuroinflammatory response to stroke.

1.9 Summary of the included publications

1.9.1 Chronic T cell proliferation in brains after stroke could interfere with the efficacy of immunotherapies.

T cells have been widely described as key drivers of post-stroke neuroinflammation and secondary disease progression [22, 47]. Consequently, lymphocyte invasion became a major target for several therapeutic strategies, including the use of antibodies against key adhesion molecules or reducing the absolute number of circulating lymphocytes [42, 47, 70]. A prominent example for this translational approach is the treatment with anti-CD49d, which reduced acute lymphocyte invasion and lesion size in preclinical studies [18, 71, 72]. Following these promising results, a first phase 2 clinical trial (ACTION), testing the efficacy of the humanized antibody Natalizumab, showed significantly improved functional outcomes in the subacute phase (30 days), but this effect was no longer apparent in the chronic phase (90 days) [69]. These effects were replicated in a follow-up phase 2b clinical trial (ACTION-II) which also failed to demonstrate improvement following Natalizumab treatment at chronic time-points [68]. Even though the effect of anti-CD49d treatment in preclinical studies was very well characterized, the reasons of this discrepancy were manifold between the outcome of the preclinical and clinical trials. Importantly, different time points were analyzed: In contrast to the clinical trials, which investigated acute infarct progression as a primary endpoint, but were subsequently extended to assess chronic post-stroke outcome, the preclinical studies focused solely on the acute phase. Therefore, we conducted a reverse translational approach and tested whether the treatment with anti-CD49d would have shown chronic efficacy in an experimental animal model [73].

In this study, a photothrombotic stroke (PT) model with consistent lesion size in the acute phase was used to evaluate the efficacy of anti-CD49d in the chronic phase after stroke. Using a panel of sensitive *in vivo* and histological techniques, we assessed cortical plasticity, behavioral deficits, quantification of lesion involution and synaptic plasticity over a period of 3 months after stroke. Anti-CD49d treatment did not improve long-term lesion involution or histologically confirmed lesion volume in the chronic post-stroke phase. Additionally, functional behavioral recovery or neuronal network connectivity, measured by *in vivo* wide-field calcium imaging [74], remained equally unaffected by anti-CD49d treatment over 3 months. Consistent with these results, there was no significant treatment-effect on synaptic spine density, an indicator for synaptic plasticity, measured 3 months after stroke. Taken together, anti-CD49d treatment did not improve post-stroke recovery in the chronic phase in our preclinical approach – comparable to the results of the clinical trials testing the chronic efficacy of Natalizumab [68, 69].

Thus, we aimed to evaluate the biological efficacy of anti-CD49d treatment in reducing lymphocyte invasion in the chronic phase after stroke. As previously demonstrated, anti-CD49d treatment reduced the number of infiltrating T cells in the acute phase in our study [18], but not in the chronic phase after stroke. Instead, we found that T cells accumulated over time within the ischemic lesion in both treatment groups, with a consequent loss of the anti-CD49d associated treatment effect in the chronic phase. Moreover, we observed a close clustering of T cells within the lesion, which led us to the assumption that the accumulation we found in the ischemic brain was the result of local proliferation, rather than delayed chronic infiltration.

To test this hypothesis, we performed an *in vivo* proliferation assay, which allowed us to quantify the proliferation rate of T cells by flow cytometry. We found that T cell-proliferation in the ischemic hemisphere was still significantly elevated in the chronic phase after stroke compared to peripheral organs. This observation was confirmed by immunohistochemical analysis for both the anti-CD49d and control-group. In conclusion, a small number of T cells could have evaded the antibody treatment and infiltrated into the brain in the acute phase after stroke, where local proliferation resulted in the observed chronic intracerebral accumulation of T cells. However, this mechanism is not targeted by the anti-CD49d treatment, and thus, leads to the loss of treatment effect.

To examine the translatability of this mechanism to stroke patients, the number of T cells was quantified in tissue samples from human stroke patients. We detected elevated numbers of T cells in the tissue samples of all patients, specifically located within the lesion area. Comparable to our results in the animal model, we also found dense local clustering and a strong correlation of T cell numbers with time after stroke onset. Using immunofluorescence staining (for $CD3^+$ T cells and the proliferation marker Ki67), we detected proliferating T cells in the lesion of the most chronic patient sample (124 days after stroke), confirming that the mechanism of local, intracerebral T cell proliferation in the chronic post-stroke phase also applies for human stroke patients.

Taken together, the study describes the chronic accumulation of T cells after stroke in brains of mice and stroke patients, most likely due to local and persistent proliferation of T cells invading the brain in the acute phase. As a key limitation, the direct association between T cell proliferation and the lack of anti-CD49d treatment efficacy for improving chronic poststroke outcome has not been covered by this study and remains to be investigated. To achieve this, genetic or pharmaceutical models for complete T cell depletion could be an option for investigating the role of T cells in chronic post-stroke recovery. In addition, this study mainly focused on $CD3^+$ T cells, whereas the underlying composition of T cell subpopulation was only briefly introduced and their chronic functions, which could be both detrimental and neuroprotective, remained uninvestigated. Thus, this study needs to be followed up by additional comprehensive investigations of the roles of T cell proliferation and T cell subpopulations in chronic post-stroke recovery. Nevertheless, chronic T cell proliferation after stroke could be a previously unrecognized confounder for immunotherapies and interfere with many currently conducted clinical trials that target lymphocyte circulation, endothelial adhesion or cerebral invasion. Thus, these findings have a high clinical relevance, urging the strong reconsideration of current similar immunomodulatory approaches for stroke therapy.

1.9.2 Microglia monitor and protect neuronal function through specialized somatic purinergic junctions.

Microglia constantly surveil the brain parenchyma and regularly contact neurons with their motile, finely branched processes [33, 75]. While most studies of microglia-neuron communication focused on synaptic interactions between neurons and microglial processes, alternative mechanisms of microglia-neuron contact remain widely unexplored [76, 77]. However, synaptic structures are highly dynamic and distant from the neuronal soma, which might allow microglia to only insufficient monitor changes in neuronal activity or injury in neuropathological conditions [65, 78]. Thus, mechanisms of microglia-neuron communication need to be further investigated to understand microglial responses to neuronal injury, such as ischemic stroke, and to target these potentially protective mechanisms for therapeutic interventions.

In this study, we described a newly discovered form of microglia-neuron contact via so called somatic microglia-neuron junctions in mice and human brain tissue. Using *in vivo* two-photon imaging of fluorescently labeled microglia and neurons, the contact between microglial processes and neuronal somata in layer 2 to 3 neurons was revealed first in adult mice. In comparison with previously described synaptic connections between microglia and neurons, the newly discovered somatic contacts even surpassed the number of synaptic connections (89-95 % vs 9-11%) in mice and human neocortex and persisted for a longer contact-time (in average 25 minutes vs. 7.5 minutes) [79].

The specialized architecture of these contact sites was characterized using high resolution electron-tomography. The sites of somatic microglia-neuron contacts comprised clusters of Kv2.1 in the neuronal somatic membrane, a voltage-gated potassium channel, which is (in its clustered form) associated with providing exocytotic surfaces and cellular processes for cell-to-cell communication [80, 81]. In addition, mitochondria, reticular membrane structures, intracellular tethers and vesicle like membrane structures are part of the nanoarchitecture of the somatic microglia-neuron junctions. The membrane of microglial processes contacting the neuronal soma showed clusters of P2Y12, a purinergic receptor exclusively expressed by microglia sensing ATP and ADP [82].

In vivo and *in vitro* 2-photon imaging has shown that the recruitment of microglial processes to the somatic junctions is dependent on metabolic activity of neuronal mitochondria and nicotinamide adenine dinucleotide hydride (NADH) release. Further *in vitro* experiments revealed that neurons release ATP-containing vesicles at the somatic junction site in an activity-dependent manner, which are then converted to ADP and sensed by microglia via P2Y12 receptors. Inhibition of P2Y12 receptor signaling by intra cisterna magna (i.c.m.) administration of the selective P2Y12 receptor blocker PSB0739 (PSB), reduced the lifetime of somatic junctions by 45 %, without affecting synapse counts or dendritic contacts between microglia and neurons. Moreover, chemogenetic increase in neuronal signaling, using a designer receptor exclusively activated by designer drugs (DREADD) approach, led to an increase in the number of microglial processes covering the neuronal soma, which was abolished by P2Y12 receptor blockage using PSB. Thus, microglia respond dynamically to changes in neuronal activity at somatic microglia-neuron junctions via P2Y12 receptor signaling.

The role of somatic microglia neuron junctions under neuropathological conditions was tested in an ischemic stroke model (middle cerebral artery occlusion). Ischemic stroke led to the loss of molecular and cellular structures, such as fragmentation of mitochondria and declustering of Kv2.1 in morphologically intact penumbral neurons. As a response, the somatic coverage with microglial processes was 4-fold increased, which was completely abolished, when P2Y12 receptor signaling using PSB or mitochondrial ATP production was blocked. *In vivo* widefield-calcium imaging revealed, that P2Y12 receptor inhibition via PSB increased the area of neuronal disconnection in the ipsilateral hemisphere after middle cerebral artery occlusion. Moreover, seed-based connectivity of the contralateral sensory hindlimb area was significantly increased after PSB administration, accompanied by a substantial and wide-spread increase in connectivity strength over 14 functional cortical areas. Consistent with these results, the calcium load at the single neuron level was significantly increased. Furthermore, P2Y12 receptor inhibition led to increased lesion volumes and neurological impairment after stroke, indicating a protective role of microglia process-coverage at the neuronal soma after acute stroke.

In conclusion, this study describes a novel mechanism of microglia-neuron contact through somatic junctions, which are present on most neurons under physiological conditions. These somatic contacts allow microglia to constantly monitor neuronal status and to rapidly initiate neuroprotective mechanisms under pathological conditions, such as acute ischemic stroke. Therefore, microglia-neuron-communication and its neuroprotective role after stroke could be a promising target for the development of novel therapeutic strategies to promote stroke outcome.

1.9.3 Short-Chain Fatty Acids Improve Poststroke Recovery via Immunological Mechanisms.

In this study, mice were supplemented with SCFAs (mix of acetate, butyrate and propionate) for 4 weeks in the drinking water before a photothrombotic stroke was induced. In the following 4 weeks, still under SCFA supplementation, functional behavioral and neuronal recovery was assessed using an automated lever-pull task and *in vivo* widefield calcium imaging. While the lesion size remained unaltered between treatment groups, mice receiving SCFA-supplement performed significantly better in the lever-pull task (day 56) and had significantly changed cortical network connectivity in the chronic post-stroke phase (day 21 and 42).

Analysis of synaptic plasticity using Golgi-Cox staining of pyramidal neurons revealed a higher density of dendritic spines in naïve animals receiving SCFAs. 14 days after stroke, the density of dendritic spines was still elevated in the contralateral hemisphere of SCFA-treated animals, but not in the ipsilesional hemisphere. Moreover, SCFA treatment induced a shift towards shorter spine length. Synaptic plasticity was further assessed by immunofluorescent co-staining of vesicular glutamate transporter 1 (VGlut1, presynapse) and Homer1 (postsynapse), revealing a significantly reduced number of colocalized VGlut1 and Homer1 puncta in the perilesional cortex of SCFA treated mice. Finally, SCFA treatment significantly increased the expression of key factors associated with synaptic plasticity, such as synaptophysin (presynaptic vesicle molecule) and tropomyosin receptor kinase B (TrkB), the receptor for brain derived neurotrophic factor (BDNF), whereas BDNF and receptor tyrosine kinase ephrin type-A receptor 2 (EphA2) were unaffected.

Ribonucleic acid (RNA) sequencing from infarct tissue 14 days after stroke revealed that the majority of differentially expressed genes were associated with pathways linked to microglial activation and function, which are essential for synaptic pruning, suggesting microglia as the cellular targets of SCFA associated treatment effects [82-86].

Therefore, the effect of SCFA treatment on microglial activation was studied in more detail 14 days after stroke using immunohistochemical assessment of microglial activation markers and morphology using a fully automated algorithm for microglia morphology analysis, which we previously published [35]. In sum, microglia in SCFA treated mice were characterized by a significantly reduced activation profile and inflammatory response after stroke. Besides acute microglial response, we characterized the effect of SCFA on brain-invading lymphocytes as key drivers of neuroinflammation after stroke [53, 73, 87, 88]. Flow cytometry revealed that SCFA supplementation significantly reduced lymphocyte numbers in the brain and spleen of mice 14 days after stroke, suggesting a SCFA associated modification of the systemic inflammatory response. In a genetic model in which mice lack functional lymphocytes (recombination activating gene 1 $(Rag1)^{-/-}$ mice) SCFA had no effect on microglial activation, indicating a messenger role of lymphocytes for the SCFA-triggered anti-inflammatory effect on microglia after stroke.

Taken together, this study describes an immunomodulatory function of SCFAs, which results in reduced microglial inflammatory response and improved post-stroke recovery. However, the SCFA associated immunomodulation is indirectly mediated via brain-invading lymphocytes through altering their maturation, their egress from primary lymphoid organs or polarization of lymphocytic cytokine release after stroke. Thus, the results of this preclinical study indicate an efficacy of SCFA supplementation to improve chronic stroke outcome, which could be translatable as a supplementary therapy to promote stroke rehabilitation in clinical practice.

1.10 Concluding summary

In summary, this Ph.D. thesis contributes fundamentally to addressing central outstanding questions of translational stroke research by investigating neuroinflammatory mechanisms and characterizing immunomodulatory therapeutic approaches to improve stroke outcome. It highlights the importance of a precisely matched study-design between preclinical and clinical studies, especially through the reversed-translational approach of evaluating the long-term efficacy of anti-CD49d treatment to improve post-stroke recovery. It describes in mice and stroke patient samples, that T cells chronically proliferate in brains after stroke, which might interfere with the efficacy of immunotherapies. Therefore, these translational findings are of high clinical relevance for multiple planned or ongoing immunotherapeutic trials, which target lymphocyte migration or circulation. Moreover, this thesis describes the discovery of a previously unrecognized form of communication between microglia and neurons and its potential neuroprotective role during stroke. Previous studies have focused on microglia-neuron contact through connections between microglial branches and neuronal synapses, which seemed to have an insufficient capability to sense neuronal activity and health. Thus, the discovery of somatic contacts between microglia and neurons, which allow microglia to monitor and protect neuronal function, has answered an intriguing question of fundamental neuroscience. Furthermore, the thesis describes how metabolites from the gut microbiome – SCFAs – can influence post-stroke recovery by indirectly modulating immunological mechanisms. The study shows, that SCFA supplementation in mice leads to improved stroke outcome, but in contrast to directly stimulating these effects in the brain, SCFA treatment modulates infiltration and polarization of circulating lymphocytes, which then indirectly modulate inflammatory responses in the brain. Taken together, this thesis sets a framework for numerous future studies in translational stroke research focusing on neuroinflammatory mechanisms and immunomodulatory treatment strategies, to improve chronic stroke outcome in patients and reduce the global burden of stroke.

2. Personal contribution to the included publications

For the first study, where I am first author, I performed the majority of the experimental work (Figure 1 A-G, Figure 2 A, D-E, Figure 3 A-E, Figure S1 A-C, E, Figure S2 A-F and Figure S3 A). The remaining experimental work was contributed by co-authors (Figure 2 B-C, Figure 3 D-F, Figure S1 D-F and Figure S3 B-D). Additionally, I performed the statistical data analysis, whereby I had some assistance or supervision from co-authors (A.R. and N.F., Figure 1 E-F and Figure 2 B-C). Furthermore, I created and designed the figures and wrote the first draft of the manuscript.

For the second study, I was responsible for the *in vivo* widefield calcium imaging of animals receiving the P2Y12 receptor inhibitor PSB0739 by performing the imaging data acquisition, computational data analysis and illustration (Figure 5 F-G). Moreover, I wrote parts of the manuscript and revised the manuscript draft.

For the third study, I performed the statistical data analysis of microglial morphology (Figure 2 B-D), based on a previously published analysis strategy, where I shared the first authorship with a colleague [35]. Additionally, I wrote parts of the manuscript and revised the manuscript draft.

3. References

1. Feigin, V.L., et al., *Prevention of stroke: a strategic global imperative.* Nat Rev Neurol, 2016. **12**(9): p. 501-12.
2. WHO. *The Top 10 Causes of Death*. The Top 10 Causes of Death 2020 09.12.2020 [cited 2021 29.05.2021]; Available from: https://www.who.int/data/stories/leading-causes-of-death-and-disability-2000-2019-a-visual-summary.
3. Campbell, B.C.V., et al., *Ischaemic stroke.* Nat Rev Dis Primers, 2019. **5**(1): p. 70.
4. Katan, M. and A. Luft, *Global Burden of Stroke.* Semin Neurol, 2018. **38**(2): p. 208-211.
5. Lindsay, M.P., et al., *World Stroke Organization (WSO): Global Stroke Fact Sheet 2019.* Int J Stroke, 2019. **14**(8): p. 806-817.
6. Smith, S.D. and C.J. Eskey, *Hemorrhagic stroke.* Radiol Clin North Am, 2011. **49**(1): p. 27-45.
7. Saver, J.L., *Time is brain--quantified.* Stroke, 2006. **37**(1): p. 263-6.
8. Chugh, C., *Acute Ischemic Stroke: Management Approach.* Indian J Crit Care Med, 2019. **23**(Suppl 2): p. S140-s146.
9. Berge, E., et al., *European Stroke Organisation (ESO) guidelines on intravenous thrombolysis for acute ischaemic stroke.* Eur Stroke J, 2021. **6**(1): p. I-lxii.
10. Alper, B.S., et al., *Thrombolysis with alteplase 3-4.5 hours after acute ischaemic stroke: trial reanalysis adjusted for baseline imbalances.* BMJ Evid Based Med, 2020. **25**(5): p. 168-171.
11. Lambrinos, A., et al., *Mechanical Thrombectomy in Acute Ischemic Stroke: A Systematic Review.* Can J Neurol Sci, 2016. **43**(4): p. 455-60.
12. Phipps, M.S. and C.A. Cronin, *Management of acute ischemic stroke.* Bmj, 2020. **368**: p. l6983.
13. Kaesmacher, J., et al., *Safety and efficacy of intra-arterial fibrinolytics as adjunct to mechanical thrombectomy: a systematic review and meta-analysis of observational data.* Journal of NeuroInterventional Surgery, 2021: p. neurintsurg-2020-016680.
14. Modrego, P.J., *The Risk of Symptomatic Intracranial Hemorrhage after Thrombolysis for Acute Stroke: Current Concepts and Perspectives.* Ann Indian Acad Neurol, 2019. **22**(3): p. 336-340.
15. Aguiar de Sousa, D., et al., *Access to and delivery of acute ischaemic stroke treatments: A survey of national scientific societies and stroke experts in 44 European countries.* Eur Stroke J, 2019. **4**(1): p. 13-28.
16. Donnan, G.A., et al., *Stroke.* Lancet, 2008. **371**(9624): p. 1612-23.
17. Moskowitz, M.A., E.H. Lo, and C. Iadecola, *The science of stroke: mechanisms in search of treatments.* Neuron, 2010. **67**(2): p. 181-98.
18. Liesz, A., et al., *Inhibition of lymphocyte trafficking shields the brain against deleterious neuroinflammation after stroke.* Brain, 2011. **134**(Pt 3): p. 704-20.
19. Jayaraj, R.L., et al., *Neuroinflammation: friend and foe for ischemic stroke.* J Neuroinflammation, 2019. **16**(1): p. 142.
20. Iadecola, C. and J. Anrather, *The immunology of stroke: from mechanisms to translation.* Nat Med, 2011. **17**(7): p. 796-808.
21. Anrather, J. and C. Iadecola, *Inflammation and Stroke: An Overview.* Neurotherapeutics, 2016. **13**(4): p. 661-670.
22. Gelderblom, M., P. Arunachalam, and T. Magnus, *γδ T cells as early sensors of tissue damage and mediators of secondary neurodegeneration.* Frontiers in cellular neuroscience, 2014. **8**: p. 368-368.

23. Gelderblom, M., et al., *Temporal and Spatial Dynamics of Cerebral Immune Cell Accumulation in Stroke.* Stroke, 2009. **40**(5): p. 1849-1857.
24. Roth, S., et al., *Brain-released alarmins and stress response synergize in accelerating atherosclerosis progression after stroke.* Sci Transl Med, 2018. **10**(432).
25. Liesz, A., et al., *DAMP signaling is a key pathway inducing immune modulation after brain injury.* The Journal of neuroscience : the official journal of the Society for Neuroscience, 2015. **35**(2): p. 583-598.
26. Fumagalli, S., et al., *The ischemic environment drives microglia and macrophage function.* Front Neurol, 2015. **6**: p. 81.
27. Taylor, R.A. and L.H. Sansing, *Microglial responses after ischemic stroke and intracerebral hemorrhage.* Clin Dev Immunol, 2013. **2013**: p. 746068.
28. Benakis, C., et al., *The role of microglia and myeloid immune cells in acute cerebral ischemia.* Front Cell Neurosci, 2014. **8**: p. 461.
29. Aloisi, F., *Immune function of microglia.* Glia, 2001. **36**(2): p. 165-79.
30. Prinz, M. and J. Priller, *Microglia and brain macrophages in the molecular age: from origin to neuropsychiatric disease.* Nat Rev Neurosci, 2014. **15**(5): p. 300-12.
31. Colonna, M. and O. Butovsky, *Microglia Function in the Central Nervous System During Health and Neurodegeneration.* Annu Rev Immunol, 2017. **35**: p. 441-468.
32. Kettenmann, H., et al., *Physiology of microglia.* Physiol Rev, 2011. **91**(2): p. 461-553.
33. Nimmerjahn, A., F. Kirchhoff, and F. Helmchen, *Resting microglial cells are highly dynamic surveillants of brain parenchyma in vivo.* Science, 2005. **308**(5726): p. 1314-8.
34. Tremblay, M., et al., *The role of microglia in the healthy brain.* J Neurosci, 2011. **31**(45): p. 16064-9.
35. Heindl, S., et al., *Automated Morphological Analysis of Microglia After Stroke.* Front Cell Neurosci, 2018. **12**: p. 106.
36. Kawabori, M. and M.A. Yenari, *The role of the microglia in acute CNS injury.* Metab Brain Dis, 2015. **30**(2): p. 381-92.
37. Wolf, S.A., H.W. Boddeke, and H. Kettenmann, *Microglia in Physiology and Disease.* Annu Rev Physiol, 2017. **79**: p. 619-643.
38. Kettenmann, H., F. Kirchhoff, and A. Verkhratsky, *Microglia: new roles for the synaptic stripper.* Neuron, 2013. **77**(1): p. 10-8.
39. Parkhurst, C.N., et al., *Microglia promote learning-dependent synapse formation through brain-derived neurotrophic factor.* Cell, 2013. **155**(7): p. 1596-609.
40. Cserép, C., et al., *Microglia monitor and protect neuronal function through specialized somatic purinergic junctions.* Science, 2020. **367**(6477): p. 528-537.
41. Szalay, G., et al., *Microglia protect against brain injury and their selective elimination dysregulates neuronal network activity after stroke.* Nat Commun, 2016. **7**: p. 11499.
42. Cramer, J.V., C. Benakis, and A. Liesz, *T cells in the post-ischemic brain: Troopers or paramedics?* Journal of Neuroimmunology, 2019. **326**: p. 33-37.
43. Doyle, K.P., et al., *B-lymphocyte-mediated delayed cognitive impairment following stroke.* The Journal of neuroscience : the official journal of the Society for Neuroscience, 2015. **35**(5): p. 2133-2145.
44. Yilmaz, G., et al., *Role of T Lymphocytes and Interferon-γ in Ischemic Stroke.* Circulation, 2006. **113**(17): p. 2105-2112.
45. De Meyer, S.F., et al., *Thromboinflammation in Stroke Brain Damage.* Stroke, 2016. **47**(4): p. 1165-72.

46. Kleinschnitz, C., et al., *Early detrimental T-cell effects in experimental cerebral ischemia are neither related to adaptive immunity nor thrombus formation.* Blood, 2010. **115**(18): p. 3835-42.
47. Chamorro, Á., et al., *The immunology of acute stroke.* Nat Rev Neurol, 2012. **8**(7): p. 401-10.
48. Macrez, R., et al., *Stroke and the immune system: from pathophysiology to new therapeutic strategies.* Lancet Neurol, 2011. **10**(5): p. 471-80.
49. Benakis, C., et al., *Commensal microbiota affects ischemic stroke outcome by regulating intestinal γδ T cells.* Nature medicine, 2016. **22**(5): p. 516-523.
50. Wan, Y.Y., *Multi-tasking of helper T cells.* Immunology, 2010. **130**(2): p. 166-71.
51. Gill, D. and R. Veltkamp, *Dynamics of T cell responses after stroke.* Curr Opin Pharmacol, 2016. **26**: p. 26-32.
52. Ito, M., et al., *Brain regulatory T cells suppress astrogliosis and potentiate neurological recovery.* Nature, 2019.
53. Liesz, A., et al., *Regulatory T cells are key cerebroprotective immunomodulators in acute experimental stroke.* Nature Medicine, 2009. **15**(2): p. 192-199.
54. Na, S.-Y., et al., *Amplification of Regulatory T Cells Using a CD28 Superagonist Reduces Brain Damage After Ischemic Stroke in Mice.* Stroke, 2015. **46**(1): p. 212-220.
55. Austin, V., et al., *Ischaemic stroke in mice induces lung inflammation but not acute lung injury.* Sci Rep, 2019. **9**(1): p. 3622.
56. Bieber, M., et al., *Stroke-induced chronic systolic dysfunction driven by sympathetic overactivity.* Ann Neurol, 2017. **82**(5): p. 729-743.
57. Singh, V., et al., *Microbiota Dysbiosis Controls the Neuroinflammatory Response after Stroke.* J Neurosci, 2016. **36**(28): p. 7428-40.
58. Xia, G.H., et al., *Stroke Dysbiosis Index (SDI) in Gut Microbiome Are Associated With Brain Injury and Prognosis of Stroke.* Front Neurol, 2019. **10**: p. 397.
59. Singh, V., et al., *The gut microbiome primes a cerebroprotective immune response after stroke.* J Cereb Blood Flow Metab, 2018. **38**(8): p. 1293-1298.
60. Kau, A.L., et al., *Human nutrition, the gut microbiome and the immune system.* Nature, 2011. **474**(7351): p. 327-36.
61. Cryan, J.F. and T.G. Dinan, *Mind-altering microorganisms: the impact of the gut microbiota on brain and behaviour.* Nat Rev Neurosci, 2012. **13**(10): p. 701-12.
62. Frost, G., et al., *The short-chain fatty acid acetate reduces appetite via a central homeostatic mechanism.* Nat Commun, 2014. **5**: p. 3611.
63. Colombo, A.V., et al., *Microbiota-derived short chain fatty acids modulate microglia and promote Aβ plaque deposition.* Elife, 2021. **10**.
64. Smith, P.M., et al., *The microbial metabolites, short-chain fatty acids, regulate colonic Treg cell homeostasis.* Science, 2013. **341**(6145): p. 569-73.
65. Aarum, J., et al., *Migration and differentiation of neural precursor cells can be directed by microglia.* Proc Natl Acad Sci U S A, 2003. **100**(26): p. 15983-8.
66. Erny, D., A.L. Hrabě de Angelis, and M. Prinz, *Communicating systems in the body: how microbiota and microglia cooperate.* Immunology, 2017. **150**(1): p. 7-15.
67. Liesz, A., et al., *FTY720 reduces post-ischemic brain lymphocyte influx but does not improve outcome in permanent murine cerebral ischemia.* PLoS One, 2011. **6**(6): p. e21312.
68. Elkind, M.S.V., et al., *Natalizumab in acute ischemic stroke (ACTION II): A randomized, placebo-controlled trial.* Neurology, 2020. **95**(8): p. e1091-e1104.
69. Elkins, J., et al., *Safety and efficacy of natalizumab in patients with acute ischaemic stroke (ACTION): a randomised, placebo-controlled, double-blind phase 2 trial.* Lancet Neurol, 2017. **16**(3): p. 217-226.

70. Veltkamp, R. and D. Gill, *Clinical Trials of Immunomodulation in Ischemic Stroke.* Neurotherapeutics, 2016. **13**(4): p. 791-800.
71. Becker, K., et al., *Antibody to the alpha4 integrin decreases infarct size in transient focal cerebral ischemia in rats.* Stroke, 2001. **32**(1): p. 206-11.
72. Llovera, G., et al., *Results of a preclinical randomized controlled multicenter trial (pRCT): Anti-CD49d treatment for acute brain ischemia.* Sci Transl Med, 2015. **7**(299): p. 299ra121.
73. Heindl, S., et al., *Chronic T cell proliferation in brains after stroke could interfere with the efficacy of immunotherapies.* J Exp Med, 2021. **218**(8).
74. Cramer, J.V., et al., *In vivo widefield calcium imaging of the mouse cortex for analysis of network connectivity in health and brain disease.* Neuroimage, 2019. **199**: p. 570-584.
75. Davalos, D., et al., *ATP mediates rapid microglial response to local brain injury in vivo.* Nat Neurosci, 2005. **8**(6): p. 752-8.
76. Wu, Y., et al., *Microglia: Dynamic Mediators of Synapse Development and Plasticity.* Trends Immunol, 2015. **36**(10): p. 605-613.
77. Weinhard, L., et al., *Microglia remodel synapses by presynaptic trogocytosis and spine head filopodia induction.* Nat Commun, 2018. **9**(1): p. 1228.
78. Ueno, M., et al., *Layer V cortical neurons require microglial support for survival during postnatal development.* Nat Neurosci, 2013. **16**(5): p. 543-51.
79. Wake, H., et al., *Resting microglia directly monitor the functional state of synapses in vivo and determine the fate of ischemic terminals.* J Neurosci, 2009. **29**(13): p. 3974-80.
80. Kirmiz, M., et al., *Identification of VAPA and VAPB as Kv2 Channel-Interacting Proteins Defining Endoplasmic Reticulum-Plasma Membrane Junctions in Mammalian Brain Neurons.* J Neurosci, 2018. **38**(35): p. 7562-7584.
81. Misonou, H., D.P. Mohapatra, and J.S. Trimmer, *Kv2.1: a voltage-gated k+ channel critical to dynamic control of neuronal excitability.* Neurotoxicology, 2005. **26**(5): p. 743-52.
82. Butovsky, O., et al., *Identification of a unique TGF-β-dependent molecular and functional signature in microglia.* Nat Neurosci, 2014. **17**(1): p. 131-43.
83. Zhong, S., et al., *A single-cell RNA-seq survey of the developmental landscape of the human prefrontal cortex.* Nature, 2018. **555**(7697): p. 524-528.
84. Schafer, D.P., et al., *Microglia sculpt postnatal neural circuits in an activity and complement-dependent manner.* Neuron, 2012. **74**(4): p. 691-705.
85. Stephan, A.H., B.A. Barres, and B. Stevens, *The complement system: an unexpected role in synaptic pruning during development and disease.* Annu Rev Neurosci, 2012. **35**: p. 369-89.
86. Li, Q., et al., *Developmental Heterogeneity of Microglia and Brain Myeloid Cells Revealed by Deep Single-Cell RNA Sequencing.* Neuron, 2019. **101**(2): p. 207-223.e10.
87. Selvaraj, U.M. and A.M. Stowe, *Long-term T cell responses in the brain after an ischemic stroke.* Discovery medicine, 2017. **24**(134): p. 323-333.
88. Meng, H., et al., *Double-negative T cells remarkably promote neuroinflammation after ischemic stroke.* Proc Natl Acad Sci U S A, 2019. **116**(12): p. 5558-5563.

4. Publication I – Chronic T cell proliferation in brains after stroke could interfere with the efficacy of immunotherapies.

Heindl S, Ricci A, Carofiglio O, Zhou Q, Arzberger T, Lenart N, Franzmeier N, Hortobagyi T, Nelson PT, Stowe AM, Denes A, Edbauer D, Liesz A. (2021). Chronic T cell proliferation in brains after stroke could interfere with the efficacy of immunotherapies. ***J Exp Med.*** doi: 10.1084/jem.20202411.

Journal: **Journal of Experimental Medicine**

Impact Factor: 11.743	Ranking: 4/139 in Medicine, Research & Experimental

Source: https://rupress.org/jem/article-abstract/218/8/e20202411/212190/Chronic-T-cell-proliferation-in-brains-after?redirectedFrom=fulltext

Copyright: ROCKEFELLER UNIVERSITY PRESS (2020)

JEM Journal of Experimental Medicine

BRIEF DEFINITIVE REPORT

Chronic T cell proliferation in brains after stroke could interfere with the efficacy of immunotherapies

Steffanie Heindl[1], Alessio Ricci[1], Olga Carofiglio[1], Qihui Zhou[2], Thomas Arzberger[3,4], Nikolett Lenart[5], Nicolai Franzmeier[1], Tibor Hortobagyi[6], Peter T. Nelson[7], Ann M. Stowe[7], Adam Denes[5], Dieter Edbauer[2,8], and Arthur Liesz[1,8]

Downloaded from http://rupress.org/jem/article-pdf/218/8/e20202411/1416415/jem_20202411.pdf by Ludwig-Maximilians-Universitaet Muenchen user on 27 May 2021

Neuroinflammation is an emerging focus of translational stroke research. Preclinical studies have demonstrated a critical role for brain-invading lymphocytes in post-stroke pathophysiology. Reducing cerebral lymphocyte invasion by anti-CD49d antibodies consistently improves outcome in the acute phase after experimental stroke models. However, clinical trials testing this approach failed to show efficacy in stroke patients for the chronic outcome 3 mo after stroke. Here, we identify a potential mechanistic reason for this phenomenon by detecting chronic T cell accumulation—evading the systemic therapy—in the post-ischemic brain. We observed a persistent accumulation of T cells in mice and human autopsy samples for more than 1 mo after stroke. Cerebral T cell accumulation in the post-ischemic brain was driven by increased local T cell proliferation rather than by T cell invasion. This observation urges re-evaluation of current immunotherapeutic approaches, which target circulating lymphocytes for promoting recovery after stroke.

Introduction

Stroke is one of the leading causes of death and permanent disability worldwide (World Health Organization, 2017). Despite the enormous medical need, specific therapies for stroke patients are still limited to vascular recanalization approaches within the acute phase after stroke (Emberson et al., 2014; Fiehler and Gerloff, 2015; Hacke et al., 2008). In the search for alternative therapeutic strategies, post-stroke neuroinflammation has come into focus in current translational stroke research (Iadecola and Anrather, 2011). Neuroinflammation after stroke is a crucial pathomechanism contributing to secondary brain injury, neurodegeneration, and recovery (Iadecola and Anrather, 2011; Moskowitz et al., 2010). While different leukocyte cell populations have been implicated in the neuroinflammatory response to stroke, T cells have been consistently shown to be a key cell population driving secondary brain injury (Chamorro et al., 2012; Macrez et al., 2011). Consequently, several therapeutic strategies targeting the brain invasion of lymphocytes have been tested using antibodies against key adhesion molecules or by reducing the number of circulating lymphocytes (Chamorro et al., 2012; Cramer et al., 2019a).

A prominent and controversial example of this translational approach is the use of anti-CD49d antibodies (Natalizumab), which reduces the invasion of circulating lymphocytes to the brain by blocking a key adhesion molecule. The repurposing of this drug used for patients with multiple sclerosis improved outcome in the acute phase after experimental stroke in the majority of preclinical studies (Becker et al., 2001; Langhauser et al., 2014; Liesz et al., 2011; Neumann et al., 2015; Relton et al., 2001), which was validated in a first-ever multicenter, randomized preclinical trial (Llovera et al., 2015). In a first phase 2 clinical trial (ACTION), Natalizumab treatment significantly improved functional outcome (modified Rankin scale) in the subacute phase (30 d), but this effect was not evident anymore in the chronic phase (90 d; Elkins et al., 2017). Correspondingly, a follow-up phase 2b trial (ACTION-II) also did not report any improvement with Natalizumab treatment in the stroke outcome at 90 d (Elkind et al., 2020).

Failed translations from promising experimental studies to clinical trials are commonly attributed to differences in study design, target engagement, or lack of statistical robustness of the preclinical findings (Endres et al., 2008; Howells et al., 2014; Macleod et al., 2014). However, the efficacy of Natalizumab in preclinical models has been extraordinarily well characterized, and clinical trials have closely mimicked the efficient

---

[1]Institute for Stroke and Dementia Research, University Hospital, Ludwig Maximilians University Munich, Munich, Germany; [2]German Center for Neurodegenerative Diseases, Munich, Germany; [3]Department of Psychiatry and Psychotherapy, University Hospital, Ludwig Maximilians University Munich, Munich, Germany; [4]Center for Neuropathology and Prion Research, Ludwig Maximilians University Munich, Munich, Germany; [5]Momentum Laboratory of Neuroimmunology, Institute of Experimental Medicine, Budapest, Hungary; [6]ELKH-DE Cerebrovascular and Neurodegenerative Research Group, Department of Neurology, University of Debrecen, Debrecen, Hungary; [7]University of Kentucky, Lexington, KY; [8]Munich Cluster for Systems Neurology (SyNergy), Munich, Germany.

Correspondence to Arthur Liesz: arthur.liesz@med.uni-muenchen.de.

© 2021 Heindl et al. This article is distributed under the terms of an Attribution–Noncommercial–Share Alike–No Mirror Sites license for the first six months after the publication date (see http://www.rupress.org/terms/). After six months it is available under a Creative Commons License (Attribution–Noncommercial–Share Alike 4.0 International license, as described at https://creativecommons.org/licenses/by-nc-sa/4.0/).

Rockefeller University Press

Check for updates

https://doi.org/10.1084/jem.20202411

J. Exp. Med. 2021 Vol. 218 No. 8 e20202411

therapeutic approaches in animal models in the design of the treatment regimen and investigated outcome parameters, with the exception of analyzing different time points after stroke: Clinical trials analyzed the chronic phase after stroke as the primary endpoint in contrast to preclinical studies, where only the acute phase was studied. Therefore, we took a reverse translational approach and tested whether the design of the clinical trials—analyzing chronic stroke outcome between patient groups with similar baseline characteristics after stroke—would have been efficacious in the murine experimental stroke model. Confirming a lack of efficacy on chronic post-stroke recovery also in animal models further prompted us to study the potentially underlying mechanisms of the diverging effects in acute versus chronic phases after stroke.

Results and discussion

Natalizumab treatment does not improve post-stroke recovery and neuronal plasticity

To model the clinical study design of Natalizumab treatment for stroke from the two clinical trials in an animal model, we used a photothrombotic stroke (PT) model resulting in equal lesion volumes and behavioral deficits in both treatment groups at the acute phase, corresponding to the equal characteristics of the study populations with Natalizumab or control treatment in the clinical trials. Mice of mixed sex then received anti-CD49d or an isotype control antibody i.p. 2 h after stroke, followed by injections every second week over a period of 3 mo, based on previous reports and the pharmacokinetic analyses of cellular anti-CD49d saturation (Fig. S1, A–D). We used a panel of in vivo imaging techniques for cortical plasticity, behavior tests, the assessment of lesion size and synaptic plasticity, which were proven to sensitively detect therapeutic effects on chronic post-stroke recovery (Cramer et al., 2019b; Cserép et al., 2020; Sadler et al., 2020). Anti-CD49d treatment did not improve long-term lesion involution based on in vivo widefield imaging (Fig. 1, A and B; and Fig. S1 D) and also had no effect on histologically quantified lesion volumes after PT as well as in an independent stroke model of distal middle cerebral artery occlusion (dMCAo) used in the majority of previous reports on the effects in the acute post-stroke phase (Fig. 1 C and Fig. S1 E). Moreover, recovery of behavior deficits using a well-established multiparameter neuroscore (Llovera et al., 2015) and cylinder test (Llovera et al., 2014) also did not differ between treatment groups throughout the observation period of 3 mo after stroke (Fig. 1 D). Additionally, we examined functional neuronal connectivity using in vivo widefield calcium imaging. We observed equal network disturbances in pairwise comparisons of functional cortical areas in both treatment groups after stroke (Fig. 1 E). Moreover, we did not detect anti-CD49d-associated improvement in neuronal network connectivity after stroke neither within the ischemic hemisphere nor across homotopic areas of both brain hemispheres (Fig. 1 F). Correspondingly, quantification of synaptic spine density as a marker of synaptic plasticity at 3 mo after stroke did not reveal a difference between treatment groups, which were both returned to baseline levels (naive). These results clearly indicate a lack of efficacy for anti-CD49d to improve functional recovery in the chronic post-stroke phase in two preclinical stroke models, which is comparable to the outcome of the clinical trials testing the efficacy of Natalizumab in stroke patients (Elkind et al., 2020; Elkins et al., 2017; Liesz et al., 2011; Llovera et al., 2015).

Anti-CD49d only transiently reduces cerebral lymphocyte counts after stroke

Therefore, we next aimed to analyze the biological efficacy of anti-CD49d treatment in reducing long-term lymphocyte invasion to the injured brain, which could not be studied in the clinical trials. To this end, we performed quantitative flow cytometric analyses at acute and chronic time points after stroke. Corresponding to previous studies by us and others, anti-CD49d significantly decreased cerebral lymphocyte invasion at the acute phase in male and female animals (Fig. 2 A and Fig. S3 A). In contrast, no difference in cerebral leukocyte count was detectable between treatment groups at 1 mo after stroke for any of the T cell subtypes, which we quantified in a multidimensional flow cytometric analysis (Fig. 2, B and C). Interestingly, we found T cells among leukocyte populations to specifically accumulate in the chronic phase after stroke (Fig. S2). Next, we performed immunofluorescence labeling of CD3$^+$ T cells to analyze the spatial distribution of T cells after stroke. Consistent with our flow cytometric results and a previous report (Doyle et al., 2015), we found dense T cell accumulation within the chronic lesion but did not detect a difference in intralesional T cell density between control or anti-CD49d–treated groups at 28 d after stroke (Fig. 2 D). We analyzed the spatial clustering of T cells by calculating the Clark–Evans agglomeration index (R index), which indicates cell clustering for an $R < 1$ (Fig. 2 E). Interestingly, the R index ranged between 0.3 and 0.7 for both acute (day 7) as well as for chronic (day 28) time points, regardless of treatment groups. Additionally, chronic T cell accumulation and their local clustering was confirmed in the dMCAo stroke model for both treatment groups (Fig. S3 B). Thus, the chronic accumulation of T cells in the post-ischemic brain associates with local clustering of T cells likely due to local, intracerebral proliferation. This finding could potentially explain the difference in treatment efficacy of anti-CD49d between the acute stroke outcome (with transiently reduced cerebral T cell invasion) and long-term recovery. Taken together, our approach to monitor the treatment efficacy of anti-CD49d for chronic recovery in two independent stroke models could have predicted the inefficacy of Natalizumab in clinical stroke trials. Moreover, this first-ever analysis of long-term effects of anti-CD49d treatment on the cerebral lymphocyte pool provides a mechanistic rationale for the futile treatment effects in the chronic post-stroke phase.

T cells proliferate intracerebrally after stroke

We next aimed to distinguish chronic recruitment versus local proliferation as the potential cause of the chronic lymphocyte accumulation in the post-stroke brain. Therefore, we administered 5-ethynyl-2′-deoxyuridine (EdU), a thymidine analogue labeling proliferating cells, in the drinking water over a 7-d time period, starting either the day of surgery (days 0–7) or 3 wk later

Downloaded from http://rupress.org/jem/article-pdf/218/8/e20202411/1416415/jem_20202411.pdf by Ludwig-Maximilians-Universitaet Muenchen user on 27 May 2021

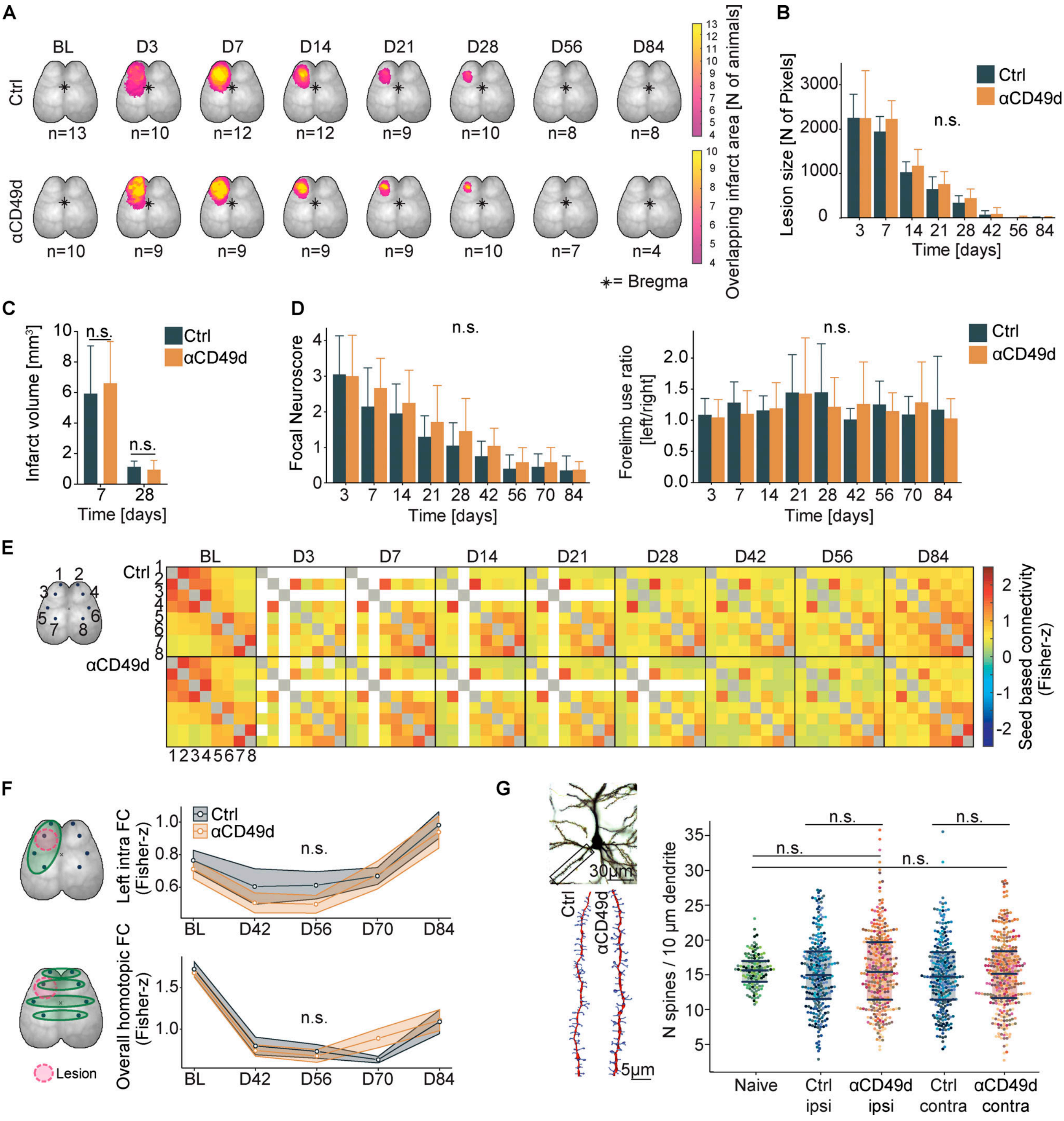

Figure 1. **Longitudinal evaluation of post-stroke recovery in mice receiving anti-CD49d treatment. (A)** The lesion area based on autofluorescence after stroke of individual animals was superimposed to depict the lesion throughout the observation period of 84 d in Thy1-GCaMP6s animals. The color code indicates the sum of overlapping lesion pixels of individual mice per acquisition time point. Data were generated in two independent experiments. BL, baseline; D, day. **(B)** Quantification of the number of autofluorescent pixels seen in calcium imaging of Thy1-GCaMP6s animals. Control (Ctrl): $n = 10$, anti-CD49d: $n = 13$, $P = 0.716$. Data are shown as mean ± SD, linear-mixed-models, group-by-time interaction. Data were generated in two independent experiments. **(C)** The lesion volume was quantified at 7 and 28 d after stroke and shows no difference between treatment groups. Control 7 d: $n = 6$, control 28 d: $n = 11$, anti-CD49d 7 d: $n = 5$, anti-CD49d 28 d: $n = 8$, all WT animals. Data are shown as mean ± SD. Ordinary one-way ANOVA + Tukey's post-hoc test. Data were generated in at least three independent experiments per time point. **(D)** Evaluation of the multi-parameter neuroscore and cylinder test shows no difference between treatment groups. Control: $n = 10$, anti-CD49d: $n = 13$, P (neuroscore) = 0.560, P (cylinder) = 0.691. Data are shown as median ± SE, linear-mixed models, group-by-time interaction. Data were generated in two independent experiments in Thy1-GCaMP6s animals. **(E)** Illustrative pixelmaps show the group-wise averaged seed-based FC between eight seeds representing functional cortical areas over an observation period of 84 d after stroke by longitudinal in vivo calcium imaging: 1, left rostral forelimb; 2, right rostral forelimb; 3, left caudal forelimb; 4, right caudal forelimb; 5, left forelimb sensory area; 6, right forelimb sensory area; 7, left hindlimb sensory area; 8, right hindlimb sensory area.. Gray squares indicate excluded seed autocorrelation, and white squares indicate excluded seeds due to the stroke lesion, when excluded in more than three animals. Data are shown as Fisher z-transformed connectivity scores and were generated in two independent experiments in Thy1-GCaMP6s animals. **(F)** Schematic illustration for longitudinal in vivo widefield calcium imaging acquisition; left intrahemispheric and whole cortex homotopic FC

Downloaded from http://rupress.org/jem/article-pdf/218/8/e20202411/1416415/jem_20202411.pdf by Ludwig-Maximilians-Universitaet Muenchen user on 27 May 2021

of the eight previously defined functional areas. Time course of left intrahemispheric FC (intra FC; P = 0.127) and overall homotopic FC (P = 0.295). Data are shown as median ± SE, linear-mixed models, group-by-time interaction. Data were generated in two independent experiments in Thy1-GCaMP6s animals. **(G)** Representative images of a Golgi-Cox–stained pyramidal neuron layer II/III in a naive animal (scale bar = 30 µm) and 3D reconstruction of pyramidal neuron dendrites (red) with dendritic spines (blue, scale bar = 5 µm). Dendritic spines were quantified in layer II/III in naive (untreated) animals and 84 d after stroke in stroke ipsi- and contralateral hemispheres. Naive: $n = 5$, control: $n = 10$, anti-CD49d: $n = 13$. Data are shown as median ± interquartile range. Wilcoxon rank-sum test with continuity correction and Bonferroni correction for multiple comparisons were used. Data were generated in at least two independent experiments. All data in this figure were obtained in a mixed-sex cohort (anti-CD49d: four male, nine female; control: three male, seven female), except for C (only male mice).

(days 21–28). Then, the rate of proliferating T cells was determined in blood, spleen, and the ischemic brain hemisphere after acute (day 7) or chronic (day 28) EdU labeling in untreated mice (Fig. 3 A). As expected for the acute inflammatory response, we observed an increase in the proliferation rate (percentage of EdU$^+$ cells) for cerebral T cells in comparison to splenic and blood T cells at 7 d after stroke. Surprisingly, the proliferation rate in the chronic phase was still significantly (more than twofold) increased for the cerebral T cell population compared with peripheral organs. In contrast, using systemic antibody labeling of circulating T cells over 3 d (days 25–28), we detected only a small number of T cells still de novo–invading the brain in the chronic phase after stroke (Fig. S3 C). To additionally confirm the local proliferation of cerebral T cells, we analyzed histologically the expression of the direct proliferation marker Ki67 to quantify the percentage of proliferating T cells within the chronic stroke lesion (Fig. 3 B). We found independent of the treatment group a substantial number of >5% Ki67$^+$ T cells, confirming the local intralesional proliferation of T cells 28 d after PT (Fig. 3 C), which was also confirmed in the dMCAo stroke model with comparable findings (Fig. S3 D). These results suggest that—regardless of anti-CD49d treatment—sustained and local proliferation of T cells in the post-stroke brain drives chronic cerebral T cell accumulation after stroke.

Evidence for chronic T cell accumulation in human brain autopsy samples

To verify chronic T cell accumulation after stroke in brains of human stroke patients, we obtained 10 individual samples from two brain banks (Lexington and Debrecen) of six individual stroke patients dying during the acute and chronic phase after confirmed cerebral ischemia and excluding other brain disorders or immunological or inflammatory diseases (Table S1). The area covering the ischemic lesion within the samples was identified based on H&E staining for quantitative analyses. Using immunohistochemical staining, we detected CD3$^+$ T cells in all 10 human brain samples (Fig. 3 D). The number of detected T cells ranged from ~300 to >9,000 cells/cm^2 of tissue section, with an average of 80% located within the lesion area. Additionally, the spatial distribution of T cells within the stroke lesions was determined and showed strong local clustering, with an R index ranging from 0.28 to 0.55 (Fig. 3 E). A Spearman correlation analysis for T cell density and time since stroke revealed a highly significant positive association. These results clearly demonstrate that T cells accumulate chronically and cluster locally in the ischemic lesion of human stroke patients. We additionally performed immunofluorescence staining for CD3$^+$ T cells and Ki67 in the most chronically collected patient sample (124 d after stroke) and detected double-positive cells (Fig. 3 F), confirming that the phenomenon of local, intracerebral proliferation of T cells in the chronic phase after stroke also applies to human stroke patients.

Taken together, we describe here chronic T cell accumulation most likely due to local proliferation after ischemic stroke in mice and human brains, constituting a previously unrecognized potential confounder for immunotherapeutic studies after ischemic stroke. None of the current pharmacological approaches block completely the cerebral invasion of T cells after stroke (in contrast to experimental T cell–depletion approaches; Liesz et al., 2009; Liesz et al., 2011) but rather reduce numbers of invading T cells by various degrees (Liesz et al., 2011; Llovera et al., 2015). Therefore, despite the therapeutic intervention, some T cells invade the ischemic brain. Once in the cerebral microenvironment, T cells might become autonomous from the peripheral immune system and establish a tissue-resident population by local proliferation. Here, we confirm chronic T cell accumulation and local proliferation in two independent experimental stroke models (PT and dMCAo). However, further mechanistic studies will be required to explore the biological function and therapeutic implications of this unexpected phenomenon.

For this study, we mainly used the PT model, which induces a pronounced cellular neuroinflammatory response and allows for sensitive analysis of neuromodulatory effects in the chronic recovery phase after stroke (Cotrina et al., 2017; Sadler et al., 2020). Key findings on lesion volume, T cell accumulation, and proliferation have additionally been confirmed in a widely used dMCAo model with similar findings in male and female animals. However, considering previous reports on model differences concerning the extent and dynamics of the neuroinflammatory response to stroke, future clinical trials need to consider not only potentially unexpected long-term effects, as reported in this study, but also potentially drastic differences in the role of neuroinflammation between stroke subtypes regarding lesion location, size, and etiology (Cotrina et al., 2017; Cramer et al., 2019a; Zhou et al., 2013).

As such, our findings have high clinical relevance for many ongoing or planned immunotherapeutic trials in stroke that target circulating lymphocytes, their endothelial adhesion, or cerebral invasion. According to the ClinicalTrials.gov registry of clinical intervention trials, more than 40 trials are exploring such strategies with pending outcome as of March 2021. The therapeutic approaches in these studies cover a broad range of potential therapies, including (autologous) cell therapies, polarization of T cell responses, or modulating lymphocyte migration. Several of these studies use repurposing of drugs that

Downloaded from http://rupress.org/jem/article-pdf/218/8/e20202411/1416415/jem_20202411.pdf by Ludwig-Maximilians-Universitaet Muenchen user on 27 May 2021

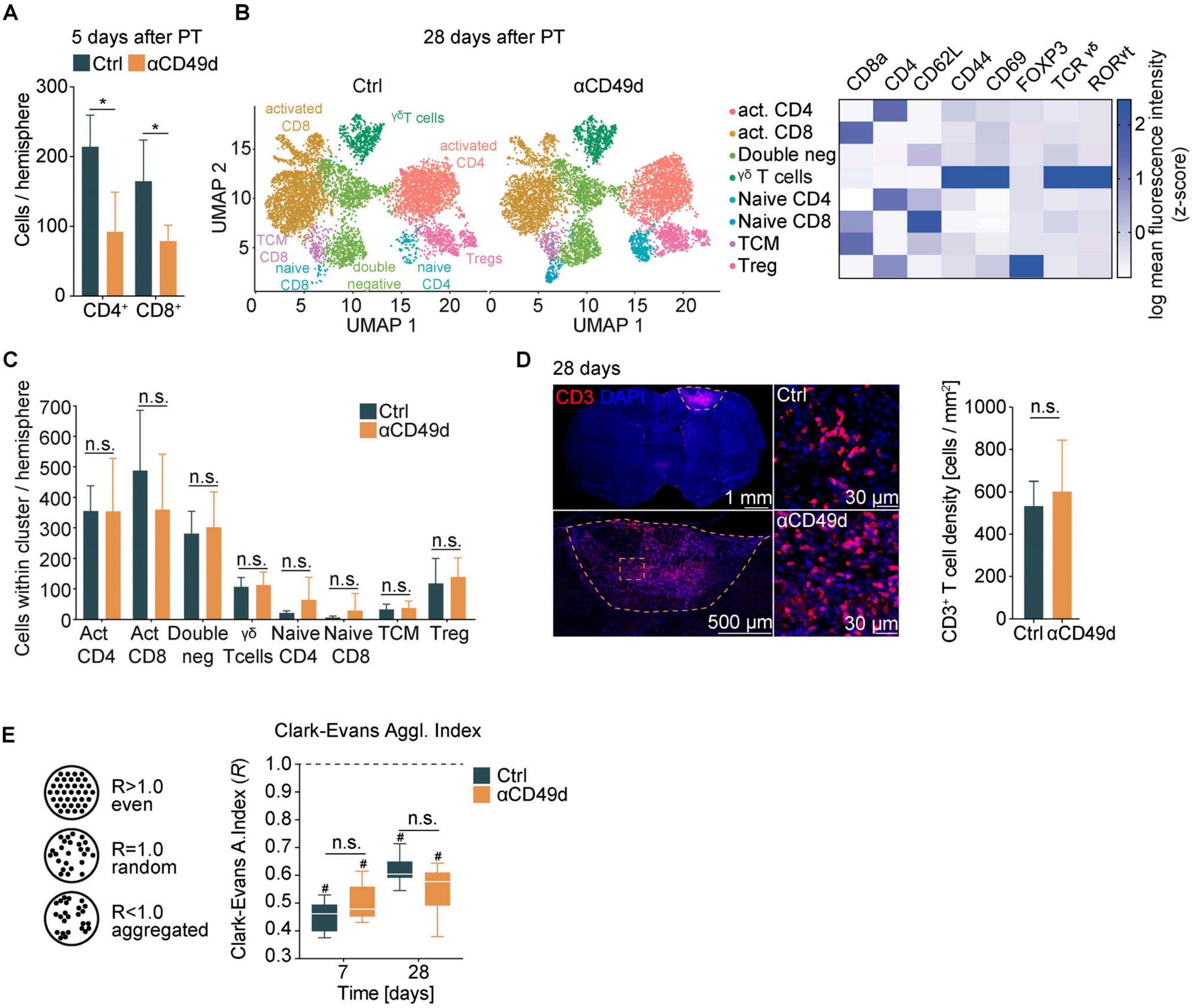

Figure 2. **T cells chronically accumulate in the post-ischemic brain independent of anti-CD49d treatment. (A)** Flow cytometric quantification of CD4$^+$ T helper cells and CD8$^+$ cytotoxic T cells per ipsilateral stroke hemisphere at 5 d after stroke. $n = 5$ per group. Data are shown as mean ± SD, unpaired t test with Holm–Sidak's post-hoc test. Data were generated in two independent experiments in WT animals. **(B)** Quantification of T cell subtypes by multidimensional flow cytometry 28 d after stroke from the ipsilateral stroke hemisphere was achieved by dimensionality reduction using UMAP (Uniform Manifold Approximation and Projection). The individual clusters were identified as CD3$^+$ T cell subtypes by the MFI of CD8a, CD4, CD62L, CD44, CD69, Foxp3, γδ TCR, and RORγt, as shown in the heatmap on the right, including activated (act.) CD4$^+$ T helper cells (CD4$^+$CD69$^+$CD62L$^-$), activated CD8$^+$ cytotoxic T cells (CD8$^+$CD69$^+$CD62L$^-$ RORγt$^+$), double-negative T cells (CD4$^-$CD8$^-$), γδ T cells (TCRγδ$^+$CD44$^+$CD69$^+$), naive CD4$^+$ T helper cells (CD4$^+$CD69$^-$CD62L$^+$), naive CD8$^+$ cytotoxic T cells (CD8$^+$CD69$^-$CD62L$^+$), central memory T cells (TCM; CD8$^+$CD69$^-$CD62L$^+$CD44$^+$), and regulatory T cells (Treg; CD4$^+$FOXP3$^+$). **(C)** Quantification of numbers of T cell subtypes per cluster in the ipsilateral stroke hemisphere shown in B. Control: $n = 5$, anti-CD49d: $n = 7$. Data are shown as mean ± SD; unpaired t test and Holm–Sidak post-hoc test. The data were generated in three independent experiments in WT animals. **(D)** Representative immunofluorescence images of CD3$^+$ T cells in the brain 28 d after stroke of the whole section with demarcation of the lesion (upper left, scale bar = 1 mm), the lesion area (lower left, scale bar = 500 µm), and an area within the lesion from control and anti-CD49d animals (right, scale bars = 30 µm). The T cell density within the lesion (cells per square millimeter) showed no difference between groups. Control: $n = 11$, anti-CD49d: $n = 8$. Data are shown as mean ± SD; unpaired t test. The data were generated in at least three independent experiments in WT animals. **(E)** Schematic representation of the R index for describing cell clustering (left) and the R index for CD3$^+$ T cells within the lesion at 7 and 28 d after stroke for both treatment groups (right). Control 7 d: $n = 6$, control 28 d: $n = 11$, anti-CD49d 7 d: $n = 5$, anti-CD49d 28 d: $n = 8$. Data are shown as median ± interquartile range. *, $P < 0.05$; #, P (clustered [$R < 1$]) <0.0001; ordinary one-way ANOVA + Tukey's post-hoc test. Data were generated in at least three independent experiments per time point in WT animals.

have been established and approved for multiple sclerosis, a disease that not only differs drastically in its pathogenesis but also has distinct neuroimmunological features. However, the differences between acute ischemic lesions and chronic autoimmune brain disorders have not yet been fully characterized and may pose a threat to the success of immunotherapeutic stroke trials.

In light of these findings, current clinical trials targeting lymphocyte migration or brain recruitment (lymphocyte-depleting antibodies, fingolimod, and cell therapy approaches)

Downloaded from http://rupress.org/jem/article-pdf/218/8/e20202411/1416415/jem_20202411.pdf by Ludwig-Maximilians-Universitaet Muenchen user on 27 May 2021

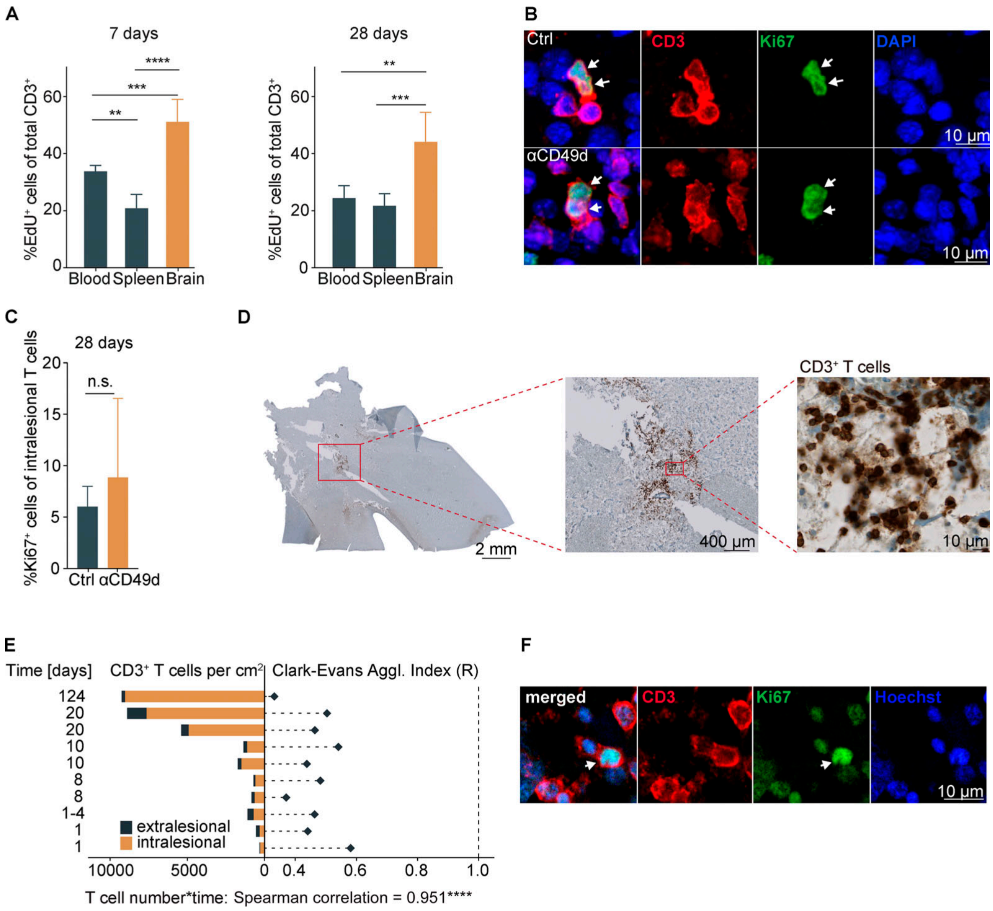

Figure 3. **T cells chronically proliferate in the postischemic brain in mice and stroke patients. (A)** The percentage of EdU⁺ T cells was quantified by flow cytometry in the spleen, blood, and ipsilateral stroke hemisphere at day 7 and day 28 after stroke (n = 5 per group). Data are shown as mean ± SD; ordinary one-way ANOVA and Tukey's post-hoc test. Two independent experiments per time point were performed in WT animals. **(B)** Representative images show immunofluorescence staining for CD3 and Ki67 within the lesion area for the detection of intracerebral T cell proliferation 28 d after stroke in both treatment groups (upper row, control; lower row, anti-CD49d). Arrows point to CD3 and Ki67 double-positive T cells. Scale bars = 10 µm. **(C)** Quantification of the percentage of Ki67⁺ T cells from (B) within the lesion 28 d after stroke showed no difference between the treatment groups. control: n = 11, anti-CD49d: n = 8. Data are shown as mean ± SD. Unpaired t test. The data were generated in at least three independent experiments in WT animals. **(D)** Representative images are shown for CD3⁺ DAB staining on consecutive brain sections from a human sample (124 d since stroke onset). Higher magnification images are shown from respective indicated areas. Scale bars: left, 1 mm; middle, 400 µm; right, 10 µm. **(E)** Cell density (cells/square centimeter) of intra- and extralesional CD3 T cells and cell clustering by R index were quantified. P (clustered [R < 1] <0.0001) for all analyzed samples. Correlation analysis (Spearman) between T cell density and time since stroke onset per sample. **(F)** Representative images of immunofluorescence staining for CD3 and Ki67 within the previously histopathologically identified lesion area are shown for the patient samples with the highest detected T cell count (124 d since stroke onset). Arrows point to CD3 and Ki67 double-positive T cells. Scale bar = 10 µm. **, $P < 0.01$; ***, $P < 0.001$; ****, $P < 0.0001$.

need to be fundamentally reconsidered. Mechanisms of chronic neuroinflammation after stroke and the consequences for post-stroke recovery need to be better understood for the rationale design of efficient immunotherapies in stroke.

Materials and methods

Animals

All experiments in this study were conducted in accordance with the national guidelines for animal experiments and approved by the German governmental committees (Regierungspraesidium Oberbayern, Munich, Germany). For flow cytometric and immunohistochemical analyses, the animals were 8–12-wk-old male or female C57BL/6J mice (Charles River Laboratories). For in vivo widefield calcium imaging and dendritic Golgi spine analysis, the animals were 12–15-wk-old male and female C57BL/6J-Tg(Thy1-GCaMP6s)GP4.12Dkim/J (here termed Thy1-GCaMP6s; Dana et al., 2014) heterozygous mice bred at the Institute for Stroke and Dementia Research, Munich (>12 generations back-crossed on C57Bl6/J WT mice). The animals were housed under controlled temperature (22 ± 2°C) with a 12-h light/dark cycle and access to food and water ad libitum. All animal experiments were performed and reported in accordance with the ARRIVE guidelines (Kilkenny et al., 2010).

Stroke surgery

For PT induction, mice were anaesthetized with isoflurane, delivered in a mixture of 30% O_2 and 70% N_2O. Mice were placed

Downloaded from http://rupress.org/jem/article-pdf/218/8/e20202411/1416415/jem_20202411.pdf by Ludwig-Maximilians-Universitaet Muenchen user on 27 May 2021

into a stereotactic frame, and body temperature was maintained at 37°C with a mouse warming pad. Dexpanthenol eye ointment was applied to both eyes. Animals received 10 µl/g body weight of 1% Rose Bengal (198250-5g; Sigma-Aldrich) in saline i.p. 5 min before the induction of anesthesia (5% isoflurane). A skin incision was used to expose the skull. Bregma was located, and the lesion location was marked in the left hemisphere (1.5 mm lateral and 1.0 mm rostral to bregma). For in vivo widefield calcium imaging experiments, PT was induced as previously described (Cramer et al., 2019b). In brief, an independent vector analysis was performed based on baseline resting-state imaging, which allowed us to define cortical functional regions as independent components. The independent component in the primary motor cortex was then used to individually define the lesion location for every mouse. Shielding was placed on the skull, allowing a 2.0-mm-diameter circular light exposure over the lesion area. 10 min after Rose Bengal injection, the laser (25 mV output) was applied to the lesion area for 17 min (Cobolt Jive 50, 561 nm power at 25 mV; Fiber Collimation Package: 543 nm, f = 7.66 mm, beam diameter [d] ≈ (4)(0.000561 mm)[7.86 mm/(pi × 0.004 mm)] = 1.4 mm). The sham procedure was performed as described previously but without laser illumination.

dMCAo was performed as previously described (Llovera et al., 2014). Briefly, the mouse was positioned on its side and skin was incised between the ear and the eye. After, the temporal muscle was detached from the bone and a craniotomy was performed on top of the middle cerebral artery. The vessel was permanently coagulated, proximal and distal to the MCA bifurcation, with electrocoagulation forceps. Finally, the muscle was placed back and the wound sutured.

Anti-CD49d antibody treatment

Animals were treated with 300 µg anti-CD49d (clone PS/2, catalog no. BE0071; Bio X Cell) or isotype control (LTF-2, catalog no. BE0090; Bio X Cell) in 0.01 M PBS 2 h after PT induction, followed by injection every second week until termination of the experiment. The treatment groups were assigned after randomization, and experimenters were blinded to group assignment.

Neuroscore

The multiparametric neuroscore was assessed as previously described (Orsini et al., 2012). Briefly, the score is composed of the assessment of several subtests of both global and focal deficits. Assessment of global deficits included grooming, status of ears and eyes, posture, spontaneous activity, and epileptic behavior. Focal deficits were evaluated by gait, grip, forelimb asymmetry during tail suspension, circling behavior of the entire body or only a forelimb, body symmetry, and whisker response. Total score ranges from 0 to 54 points (26 points for general and 28 for focal deficits), with a higher score indicating worse deficits. Data were acquired once before stroke and on days 3, 7, 14, 21, 28, 42, 56, 70, and 84 after stroke.

Cylinder test

The cylinder test was assessed as previously described (Llovera et al., 2014). Briefly, the animals were placed in a transparent acrylic glass cylinder (diameter, 8 cm; height, 25 cm) in front of two mirrors, and video was recorded for 10 min. The frequency of forelimb use during a full rear and landing with only one forelimb was counted. At least 20 contacts for one forelimb were counted using slow-motion or frame-by-frame function. The ratio was calculated as the total number of left forelimb contacts divided by the total number of right forelimb contacts with the cylinder wall.

Flow cytometry

Mice were deeply anesthetized and perfused with 20 ml saline. Both brain and spleen were dissected, and blood was collected in EDTA tubes after cardiac puncture. For brain, both hemispheres were carefully removed, and cells were isolated by mechanical dissociation. Cell preparation and staining were performed as previously described (Llovera et al., 2017). Mononuclear cells were enriched using discontinuous Percoll gradients. Cell stainings were performed using the following antibodies: CD45-eF450 (1:250, 48–0451-82, clone: 30-F11; Invitrogen), CD3-FITC (1:250, 11–0032-82, clone: 17A2; Invitrogen), CD8-PE (1:250, 12–0081-82, clone: 53–6.7; Invitrogen), CD4-PerCP-Cy5 (1:250, 45–0042-82, clone: RM4-5; Invitrogen), TCRyd-APC (1:250, 118116, clone: GL3; BioLegend), NK1.1-PE-Cy7 (1:250, 25–5941-82, clone: PK136; Invitrogen), CD19-APC-Cy7 (1:250, 47–0193-82, clone: eBio1D3; Invitrogen), CD11b-PerCP-Cy5 (1:250, 45–0112-82, clone: M1/70; Invitrogen), MHCII-PE (1:250, 12–5322-81, clone: NIMR-4; eBioscience), Ly6C-APC (1:500, 17–5932-82, clone: HK1.4; eBioscience), Ly6G-PE-Cy7 (1:333, 25–5931-82, clone: RB6-8C5; eBioscience), and CD11c-APC-Cy7 (1:250, 117324, clone: N418; BioLegend). Stained cells were analyzed on a BD FACSVerse flow cytometer (BD Biosciences), and analysis was performed using FlowJo software (version 10.0).

For high-dimensional flow cytometry (Fig. 2, B and C), mice were injected i.v. with 3 µg CD45-APC-Cy7 (103116, clone: 30-F11; BioLegend), 3 min before transcardiac perfusion, to exclude blood contamination. Mononuclear cells were then isolated as described above. The samples were stained first with Zombie NIR Fixable Viability Kit (1:200; BioLegend) and surface markers, diluted in Brilliant Stain Buffer (BD Biosciences). The following antibodies were used: CXCR3-BV421 (1:100, 126522, clone: CXCR3-127; BioLegend), CD27-SB436 (1:100, 62–0271-82, clone: LG.7F9; eBioscience), CD69-BV480 (1:50, 746813, clone: H1.2F3; BD Biosciences), CD19-BV570 (1:200, 115535, clone: 6D5; BioLegend), CD11b-BV570 (1:200, 101233, clone: M1/70; BioLegend), PD-1-BV605 (1:100, 563059, clone: J43; BD Biosciences), CD62L-BV650 (1:100, 564108, clone MEL-14; BD Biosciences), TCR-γδ-BV750 (1:100, 746962, clone: GL3; BD Biosciences), CCR7-BV785 (1:100, 120127, clone: 4B12; BioLegend), CD44-AF532 (1:200, 58–0441-82, clone: IM7; eBioscience), CD127-PE-CF594 (1:100, 562419, clone: SB/199; BD Biosciences), NK1.1-AF700 (1:100, 56–5941-82, clone: PK136; eBioscience), CD8a-BV510 (1:200, 563068, clone: 53-6.7; BD Biosciences), CD3-FITC (1:200, 11–0032-82, clone: 17A2; eBioscience), KLRG1-PE (1:200, 138408, clone: 2F1/KLRG1; BioLegend), CD103-PE-Cy7 (1:200, 121426, clone: 2E7; BioLegend), CD4-PerCP-Cy5.5 (1:200, 45–0042-82, clone: RM4-5; eBioscience). For intracellular staining, Foxp3 / Transcription Factor Staining Buffer Set was used following the provider guidelines. The following antibodies

Downloaded from http://rupress.org/jem/article-pdf/218/8/e20202411/1416415/jem_20202411.pdf by Ludwig-Maximilians-Universitaet Muenchen user on 27 May 2021

for intracellular staining were used: FoxP3-AF647 (1:100, 126408, clone: MF-14; BioLegend), T-bet-BV711 (1:100, 644820, clone: 4B10; BioLegend), ROR-γt-APC (1:100, 17-6981-82, clone B2D; eBioscience). Stained cells were analyzed on a Norther Light spectral flow cytometer (Cytek) and analysis performed by FlowJo software (version 10.0).

In vivo proliferation analysis

For analysis of in vivo cell proliferation, mice were treated with EdU (0.5 mg/ml; Invitrogen) in sucrose-enriched drinking water (5 g sucrose in 100 ml) for 7 d before saline perfusion. EdU was detected using a Click-iT EdU Alexa Fluor 647 Flow Cytometry Assay Kit (C10419; Invitrogen) following the manufacturer's instructions. Subsequently, FACS antibody staining was performed as described above using the following cell surface antibodies: CD11b-PE-Cy7 (1:250, 25-0112-82, clone: M1/70; Invitrogen), CD45-BV510 (1:250, 563891, clone: 30-F11; BD Biosciences), CD3-FITC (1:250, 11-0032-82, clone: 17A2; Invitrogen), CD19-eF450 (1:250, 48-0193-82, clone: eBio1D3; eBioscience), CD4-PerCP-Cy5.5 (1:250, 45-0042-82, clone: RM4-5; Invitrogen), and CD8-PE (1:250, Invitrogen, 12-0081-82, clone: 53-6.7). Stained cells were then analyzed on a BD FACSVerse flow cytometer (BD Biosciences), and analysis was performed using FlowJo software (version 10.0).

Pharmacokinetic analysis

To determine cellular anti-CD49d saturation levels, venous blood was collected in EDTA tubes after cardiac puncture, and mononuclear cells were enriched using a Histopaque-1077 gradient (Sigma-Aldrich). Cells were diluted to a concentration of 10^6 cells/ml and stained with a mouse anti-Rat IgG2b PE-conjugated secondary antibody (1:20, clone R2B-7C3; eBioscience) to detect cell-bound anti-CD49d for 30 min at 4°C. For determination of anti-CD49d saturation, cells were incubated with a saturating amount of anti-CD49d (10 μg/ml) for 30 min at room temperature and subsequently stained with the antibody as described above. Stained cells were then analyzed on a BD FACSVerse flow cytometer (BD Biosciences), and analysis was performed using FlowJo software (version 10.0). The anti-CD49d saturation level was then calculated as percentage of the mean fluorescence intensity (MFI) from in vivo bound anti-CD49d from the MFI of in vitro saturated cells by the following equation:

$$\text{anti} - \text{CD49d saturation} = \frac{\text{MFI in vivo}\,\textit{bound anti} - \textit{CD49d}}{\text{MFI in vitro saturated anti} - \text{CD49d}} \times 100.$$

The number of anti-CD49d molecules per cell was determined using a PE fluorescence quantitation kit (BD Quantibrite PE, #340495; BD Biosciences) following the manufacturer's instructions.

Mouse anti-rat IgG ELISA

To analyze neutralizing mouse anti-rat IgG antibodies in mice, we used a customized modification of a commercial ELISA (#88-50400; Thermo Fisher Scientific). Flat-bottom 96-well ELISA plates were coated overnight with the same rat anti-CD49d antibody (100 ng/ml) at 4°C as used for the in vivo treatment (clone PS/2, Cat. BE0071; Bio X Cell). After washing, the antibody-coated plates were incubated for 1 h at room temperature with mouse plasma obtained 28 d after stroke (i.e., two doses of anti-CD49d at 2 h and 14 d) or control plasma from a naive mouse that had been spiked at ~10 ng/ml with the capture antibody of the ELISA kit. Subsequent detection and biochemiluminescent analysis using a microplate reader (Bio-Rad) was performed following the manufacturer's instructions.

Dendritic spine analysis

Following saline perfusion, mice were perfused 84 d after PT with aldehyde fixative solution (003780; Bioenno). Brains were then carefully removed and placed in fixative solution at 4°C overnight. Brains were then sliced at 100 μm using a vibratome and collected in 0.1 M PBS. Slices were placed in impregnation slice Golgi Kit (003760; Bioenno) solution for 5 d in the dark. Staining and post-staining was performed as described by the manufacturer (Bioenno). Images of dendrites were obtained within 500 μm around the lesion area in cortical layer 2/3. In total, 25 dendrites per animal (5 dendrites from 5 neurons) in both hemispheres were recorded using an Axio Imager.M2 and a 100× objective (EC Plan-Neofluar, numerical aperture [NA] = 1.3, oil immersion, acquisition at 18–20°C) using the AxioCam MRc and AxioVision 4.8.2 software. Dendrites from the images were then 3D reconstructed and the spine density evaluated on the reconstructed 3D surface using Imaris x64 (8.4.0; Bitplane).

In vivo widefield neuronal calcium imaging

In vivo widefield calcium imaging was performed as previously published (Cramer et al., 2019b). Briefly, Thy1-GCaMP6s heterozygous mice were scalped and transparent dental cement was placed upon the intact skull at least 3 d before start of the experiment. Resting-state in vivo imaging was performed in mild anesthesia (0.5 mg/kg body weight of medetomidine with 0.75% isoflurane inhalation). Mice were placed in a stereotactic frame below a customized macroscopic imaging setup, and mouse cortex was illuminated with 450-nm blue LED light. Resting-state calcium activity was recorded for 4 min (6 × 1,000 frames) with a high-precision 2/3" Interline charge-coupled device camera (Adimec-1000m/D, pixel size 7.4 × 7.4 μm, acquisition at 20–22°C; Adimec) at a 25-Hz frame rate using longDaq software (Optical Imaging).

In vivo calcium imaging analysis

Functional imaging data were preprocessed as previously described (Cramer et al., 2019b). In particular, the seed-to-seed FCs between eight previously defined seeds were calculated as Pearson's correlation between the time course of each of these seeds and Fisher's z transformation. For left intrahemispheric connectivity, the mean of the Fisher's z-transformed Pearson's correlation coefficient of each connection between the seeds located in the left hemisphere was calculated. The overall homotopic connectivity was calculated as the mean of all Fisher's z-transformed Pearson's correlation coefficients of each homotopic connection between the seeds in both hemispheres. The time course of left intrahemispheric and overall homotopic

Downloaded from http://rupress.org/jem/article-pdf/218/8/e20202411/1416415/jem_20202411.pdf by Ludwig-Maximilians-Universitaet Muenchen user on 27 May 2021

connectivity was displayed from baseline and days 42 to 84 after stroke, ensuring the visibility of all seeds after disappearance of the autofluorescent lesion. Fisher's z-transformed Pearson's correlation was calculated using MATLAB (MathWorks R2016b with Optimization Toolbox, Statistics and Machine Learning Toolbox, Signal Processing Toolbox and Image Processing Toolbox; MathWorks).

Lesion involution quantification

The lesion size was determined by autofluorescence of the ischemic tissue in Thy1-GCaMP6s animals used for in vivo widefield calcium imaging for every time point of imaging acquisition. The area of autofluorescent pixels was previously defined by thresholding and converted into a mask to exclude autofluorescent tissue from the connectivity analysis. The lesion was determined as the size of the exclusion mask by quantification of all pixels within the mask.

Lesion volumetry

Mice were transcardially perfused 28 d after PT or dMCAo stroke induction with saline and 4% paraformaldehyde solution. To protect the cortical lesion from damage, the whole skull was isolated and stored in 4% paraformaldehyde overnight at 4°C and then placed in 0.3 M EDTA for 7 d for decalcification. Subsequently, the brains were dehydrated for 2 d in 30% sucrose in 0.01 M PBS and then snap-frozen in isopentane. Cresyl Violet staining for infarct volumetry was performed as previously described (Llovera et al., 2014), and the lesion size was quantified using FIJI ImageJ.

Immunohistochemical staining of mouse coronal brain sections

Fluorescent immunohistochemical staining for $CD3^+$ and $Ki67^+$ to determine the number of proliferating T cells in control versus anti-CD49d treated animals was performed on 20-µm-thick paraformaldehyde-fixed coronal sections from mice at 7 and/or 28 d after PT or dMCAo. Sections were fixed with cold acetone for 10 min at room temperature and washed with 0.01 M PBS before blocking with goat serum blocking buffer for 1 h at room temperature. Subsequently, sections were stained overnight at 4°C with primary antibody (1:200, CD3e, hamster anti-mouse, clone 500A2; BD PharMingen; and 1:200, Ki-67, rabbit mAb, clone D3B5; Cell Signaling Technology). After washing with 0.1% Triton X-100 in 0.01 M PBS, secondary antibody staining was applied for 2 h at room temperature (1:200, goat anti-hamster, Alexa Fluor 594; Thermo Fisher Scientific; and 1:200, goat anti-rabbit, Alexa Fluor 647; Life Technologies). Nuclei were stained with DAPI (1:5,000; Invitrogen) for 5 min at room temperature.

Per animal, three images for cell quantification were recorded as 6-µm-high tile-scan Z-stacks (slice thickness, 0.4 µm) on a Zeiss confocal microscope (LSM880) with 25× objective (LCI Plan-Neofluar 25×, NA = 0.8, ImmKorr differential interference contrast, water immersion, acquisition at 18°C). The lesion was marked and measured in the tile-scan image and cells were quantified using the Cell Counter Plugin in FIJI. Cell density was calculated as number of cells per square millimeter. The R index for quantification of clustering of cells per area was calculated using the clarkevans.test R function (R package spatstat; Baddeley et al., 2005). For evaluation of clustering, the ratio of the observed average nearest-neighbor distance r (rA) to the expected pattern for a Poisson point process of the same intensity (rE): $R=\frac{rA}{rE}$. An R index of >1.0 indicates ordered spatial distribution, R = 0 indicates even distribution, and R < 1.0 indicates aggregation. Hypothesis testing was performed against the null hypothesis, which is complete spatial randomness/a uniform Poisson process. For every animal, the cell density and R index were calculated and averaged among the three acquired images. Whole-slice images were acquired using a 10× objective (EC Plan-Neofluar 10×, NA = 0.3, air immersion, acquisition at 18°C) and high-resolution images were acquired using a 40× objective (EC Plan-Neofluar 40×, NA = 1.3 oil differential interference contrast, oil immersion, acquisition at 18–20°C).

Patient characteristics for postmortem histological analyses

Ethical approval for the use of human postmortem material was granted according to institutional ethics board protocol and national regulations by the Hungarian Medical Research Council Scientific and Research Ethics Board (19312/2016/EKU) and the University of Kentucky Medical Institutional Review Board (UK IRB #44009), respectively. Clinical information was provided by the respective brain bank (Table S1).

Histological and immunohistochemical staining of human brain tissue samples

Histochemical and immunohistochemical staining was performed on sections cut to 6 µm from paraffin-embedded tissue blocks. Randomly chosen sections of every patient were deparaffinated and rehydrated and subsequently stained with H&E. Immunohistochemistry for CD3 (polyclonal rabbit anti-human CD3, diluted 1:50, A0452; Dako) was performed on sections adjacent to H&E-stained sections with the Ventana Benchmark GX automated staining system using a CC1 (Roche) pretreatment and the iView DAB Detection Kit (Roche). Sections were counterstained with hematoxylin and coverslipped with Entellan (Merck) as mounting medium. Age of infarcts was estimated by two experienced and independent neuropathologists (T. Arzberger and P.T. Nelson) on H&E sections according to published criteria (Mena et al., 2004). CD3 stains were scanned with Zeiss Axio Scan Z1 using a 20× objective. The infarct area was demarcated, and the absolute numbers and coordinates of intra- and extralesional $CD3^+$ T cells were assessed manually using Qupath (version 0.2.2). Cell density was calculated as number of cells per cm^2 of defined lesion area. The R index for quantification of cell clustering per area was calculated as described above in R (version 3.6.0). Intralesional cell density was correlated with time after stroke onset for each sample.

Immunofluorescence staining of human brain tissue samples

Immunofluorescence staining was performed on sections cut to 6 µm from paraffin-embedded tissue blocks. Randomly selected sections were deparaffinated and blocked in 3% H_2O_2. After heat-induced antigen retrieval in Tris-buffered EDTA (pH 9.0) for 30 min at 95°C, sections were blocked with 5% donkey serum for 4 h at room temperature. Then, sections were incubated in

Downloaded from http://rupress.org/jem/article-pdf/218/8/e20202411/1416415/jem_20202411.pdf by Ludwig-Maximilians-Universitaet Muenchen user on 27 May 2021

antibody staining solution (0.3% Triton X-100 and 20 mM sodium azide containing 0.05 M Tris-buffered saline [TBS], pH 7.4) overnight at 4°C (1:50, CD3, polyclonal rabbit anti-human, reference A0452; and 1:100, Ki67, monoclonal mouse anti-human, clone MIB-1, reference M7240; Dako). After washing with 0.05 M TBS, secondary antibody staining was performed with antibody staining solution (0.3% Triton X-100 and 20 mM sodium azide containing 0.05 M TBS, pH 7.4) for 2.5 h at room temperature in the dark (1:500, donkey anti-rabbit, Alexa Fluor 594, reference 711–586-152; and 1:500, donkey anti-mouse, Alexa Fluor 488, reference 715–546-151; Jackson ImmunoResearch). For nuclear staining, Hoechst 33334 (0.02 mg/ml diluted in 0.05 M TBS, pH 7.4, reference 62249; Thermo Fisher Scientific) was applied for 30 min at room temperature. After staining, an autofluorescence eliminator reagent (reference 2160; EMD Millipore) was applied for 5 min before mounting the slides with Fluoromount-G (reference 0100–01; Southern Biotech). The images were acquired at 20× magnification (objective: Plan Apo VC 20×, NA = 0.75, working distance = 1 mm, field of view = 645.12 µm, calibration: 0.62 µm/pixel or with 5× optical zoom, calibration: 0.12 µm/pixel, acquisition at 21°C) using a Nikon Ni C2 confocal microscope.

Statistics

To assess whether the lesion involution (number of autofluorescent pixels), behavioral recovery (neuroscore and cylinder test) or FC (left intra-FC and overall homotopic FC) between anti-CD49d–treated and control-treated animals were significantly different, we performed linear-mixed models for calculating group-by-time interaction in R (version 3.6.0). To test for statistical difference in infarct volume between treatment groups, we used one-way ANOVA and Tukey's post-hoc test. Next, we assessed the difference in dendritic spine numbers between anti-CD49d–treated and control-treated animals using the Wilcoxon rank-sum test with continuity correction and Bonferroni post-hoc correction for multiple testing in R (Version 3.6.0). To test for significantly different numbers of infiltrating T cells between anti-CD49d- and control-treated animals, we used unpaired *t* tests and Holm–Sidak's correction for multiple testing. For determining significant differences in histologically quantified T cells, we used an unpaired *t* test. To assess significant differences in the R index between treatment groups at different time points, we used one-way ANOVA and Tukey's test for correction of multiple comparisons. We next quantified significant differences between the number of EdU$^+$ T cells in different organs using one-way ANOVA and Tukey's test for correction of multiple comparisons. To test for significant differences in the percentage of Ki67$^+$ T cells between treatment groups, we used an unpaired *t* test. We used linear regression analysis to test for a correlation between the intralesional T cell density in stroke patients and time after stroke onset. Unless otherwise mentioned all analyses were performed in GraphPad Prism (version 7.0a). For all analyses, an α level of adjusted $P < 0.05$ was considered statistically significant.

Online supplemental material

Fig. S1 provides pharmacokinetic analysis data for the rationale of the treatment regimen with anti-CD49d and additional results on infarct volumetry supporting the findings in the Fig. 1 in the PT and dMCAo stroke model. Fig. S2 provides information on the temporal dynamics of cerebral invasion on innate and adaptive immune subpopulations over 1 mo after experimental stroke. Fig. S3 shows comparable findings for chronic T cell accumulation in female mice as shown in the main figures for male mice. Additionally, this figure confirms chronic T cell accumulation and proliferation in the dMCAo stroke model. Table S1 lists patient data.

Acknowledgments

We would like to thank Kerstin Thuβ-Silczak and Christina Fürle for technical support as well as Juliet Stowe for the selection and preparation of human tissue samples from the Sanders Brown Center on Aging (supported by National Institutes of Health grant P30 AG028383).

This work was funded by the European Research Council (grant ERC-StGs 802305 to A. Liesz and grant ERC-PoC 875677 to D. Edbauer), the American Heart Association (grant 19EIA34760279 to A.M. Stowe), the Hungarian Brain Research Program (grant 2017-1.2.1-NKP-2017-00002), and the German Research Foundation under Germany's Excellence Strategy (EXC 2145 SyNergy, ID 390857198) through the collaborative research center TRR274 (project ID 408885537) and under grants LI-2534/6-1 and LI-2534/7-1. D. Edbauer received funding from the NOMIS Foundation.

Author contributions: S. Heindl conceptualized experiments, performed most of the experiments, analyzed the data, and wrote the manuscript. A. Ricci performed and analyzed experiments. O. Carofiglio, Q. Zhou, T. Arzberger, and N. Lenart performed experiments. N. Franzmeier analyzed FC data. T. Hortobagyi, P.T. Nelson, A.M. Stowe, and A. Denes selected and provided the human tissue samples. D. Edbauer provided experimental resources. A. Liesz initiated the study, conceptualized and supervised the research, and wrote the manuscript. All authors reviewed the manuscript.

Disclosures: The authors declare no competing interests exist.

Submitted: 11 November 2020
Revised: 31 March 2021
Accepted: 28 April 2021

References

Baddeley, A., E. Rubak, and R. Turner. 2005. Spatial Point Patterns: Methodology and Applications with R. Chapman and Hall/CRC Press, London.

Becker, K., D. Kindrick, J. Relton, J. Harlan, and R. Winn. 2001. Antibody to the alpha4 integrin decreases infarct size in transient focal cerebral ischemia in rats. *Stroke.* 32:206–211. https://doi.org/10.1161/01.STR.32.1.206

Chamorro, Á., A. Meisel, A.M. Planas, X. Urra, D. van de Beek, and R. Veltkamp. 2012. The immunology of acute stroke. *Nat. Rev. Neurol.* 8: 401–410. https://doi.org/10.1038/nrneurol.2012.98

Cotrina, M.L., N. Lou, J. Tome-Garcia, J. Goldman, and M. Nedergaard. 2017. Direct comparison of microglial dynamics and inflammatory profile in photothrombotic and arterial occlusion evoked stroke. *Neuroscience.* 343:483–494. https://doi.org/10.1016/j.neuroscience.2016.12.012

Cramer, J.V., C. Benakis, and A. Liesz. 2019a. T cells in the post-ischemic brain: Troopers or paramedics? *J. Neuroimmunol.* 326:33–37. https://doi.org/10.1016/j.jneuroim.2018.11.006

Downloaded from http://rupress.org/jem/article-pdf/218/8/e20202411/1416415/jem_20202411.pdf by Ludwig-Maximilians-Universitaet Muenchen user on 27 May 2021

Cramer, J.V., B. Gesierich, S. Roth, M. Dichgans, M. Düring, and A. Liesz. 2019b. In vivo widefield calcium imaging of the mouse cortex for analysis of network connectivity in health and brain disease. *Neuroimage.* 199:570–584. https://doi.org/10.1016/j.neuroimage.2019.06.014

Cserép, C., B. Pósfai, N. Lénárt, R. Fekete, Z.I. László, Z. Lele, B. Orsolits, G. Molnár, S. Heindl, A.D. Schwarcz, et al. 2020. Microglia monitor and protect neuronal function through specialized somatic purinergic junctions. *Science.* 367:528–537. https://doi.org/10.1126/science.aax6752

Dana, H., T.W. Chen, A. Hu, B.C. Shields, C. Guo, L.L. Looger, D.S. Kim, and K. Svoboda. 2014. Thy1-GCaMP6 transgenic mice for neuronal population imaging in vivo. *PLoS One.* 9:e108697. https://doi.org/10.1371/journal.pone.0108697

Doyle, K.P., L.N. Quach, M. Solé, R.C. Axtell, T.-V.V. Nguyen, G.J. Soler-Llavina, S. Jurado, J. Han, L. Steinman, F.M. Longo, et al. 2015. B-lymphocyte-mediated delayed cognitive impairment following stroke. *J. Neurosci.* 35: 2133–2145. https://doi.org/10.1523/JNEUROSCI.4098-14.2015

Elkind, M.S.V., R. Veltkamp, J. Montaner, S.C. Johnston, A.B. Singhal, K. Becker, M.G. Lansberg, W. Tang, R. Kasliwal, and J. Elkins. 2020. Natalizumab in acute ischemic stroke (ACTION II): A randomized, placebo-controlled trial. *Neurology.* 95:e1091–e1104. https://doi.org/10.1212/WNL.0000000000010038

Elkins, J., R. Veltkamp, J. Montaner, S.C. Johnston, A.B. Singhal, K. Becker, M.G. Lansberg, W. Tang, I. Chang, K. Muralidharan, et al. 2017. Safety and efficacy of natalizumab in patients with acute ischaemic stroke (ACTION): a randomised, placebo-controlled, double-blind phase 2 trial. *Lancet Neurol.* 16:217–226. https://doi.org/10.1016/S1474-4422(16)30357-X

Emberson, J., K.R. Lees, P. Lyden, L. Blackwell, G. Albers, E. Bluhmki, T. Brott, G. Cohen, S. Davis, G. Donnan, et al. Stroke Thrombolysis Trialists' Collaborative Group. 2014. Effect of treatment delay, age, and stroke severity on the effects of intravenous thrombolysis with alteplase for acute ischaemic stroke: a meta-analysis of individual patient data from randomised trials. *Lancet.* 384:1929–1935. https://doi.org/10.1016/S0140-6736(14)60584-5

Endres, M., B. Engelhardt, J. Koistinaho, O. Lindvall, S. Meairs, J.P. Mohr, A. Planas, N. Rothwell, M. Schwaninger, M.E. Schwab, et al. 2008. Improving outcome after stroke: overcoming the translational roadblock. *Cerebrovasc. Dis.* 25:268–278. https://doi.org/10.1159/000118039

Fiehler, J., and C. Gerloff. 2015. Mechanical Thrombectomy in Stroke. *Dtsch. Arztebl. Int.* 112:830–836.

Hacke, W., M. Kaste, E. Bluhmki, M. Brozman, A. Dávalos, D. Guidetti, V. Larrue, K.R. Lees, Z. Medeghri, T. Machnig, et al. ECASS Investigators. 2008. Thrombolysis with alteplase 3 to 4.5 hours after acute ischemic stroke. *N. Engl. J. Med.* 359:1317–1329. https://doi.org/10.1056/NEJMoa0804656

Howells, D.W., E.S. Sena, and M.R. Macleod. 2014. Bringing rigour to translational medicine. *Nat. Rev. Neurol.* 10:37–43. https://doi.org/10.1038/nrneurol.2013.232

Iadecola, C., and J. Anrather. 2011. The immunology of stroke: from mechanisms to translation. *Nat. Med.* 17:796–808. https://doi.org/10.1038/nm.2399

Kilkenny, C., W.J. Browne, I.C. Cuthill, M. Emerson, and D.G. Altman. 2010. Improving bioscience research reporting: the ARRIVE guidelines for reporting animal research. *PLoS Biol.* 8:e1000412. https://doi.org/10.1371/journal.pbio.1000412

Langhauser, F., P. Kraft, E. Göb, J. Leinweber, M.K. Schuhmann, K. Lorenz, M. Gelderblom, S. Bittner, S.G. Meuth, H. Wiendl, et al. 2014. Blocking of α4 integrin does not protect from acute ischemic stroke in mice. *Stroke.* 45:1799–1806. https://doi.org/10.1161/STROKEAHA.114.005000

Liesz, A., E. Suri-Payer, C. Veltkamp, H. Doerr, C. Sommer, S. Rivest, T. Giese, and R. Veltkamp. 2009. Regulatory T cells are key cerebroprotective immunomodulators in acute experimental stroke. *Nat. Med.* 15:192–199. https://doi.org/10.1038/nm.1927

Liesz, A., W. Zhou, É. Mracskó, S. Karcher, H. Bauer, S. Schwarting, L. Sun, D. Bruder, S. Stegemann, A. Cerwenka, et al. 2011. Inhibition of lymphocyte trafficking shields the brain against deleterious neuroinflammation after stroke. *Brain.* 134:704–720. https://doi.org/10.1093/brain/awr008

Llovera, G., S. Roth, N. Plesnila, R. Veltkamp, and A. Liesz. 2014. Modeling stroke in mice: permanent coagulation of the distal middle cerebral artery. *J. Vis. Exp.* (89):e51729. https://doi.org/10.3791/51729

Llovera, G., K. Hofmann, S. Roth, A. Salas-Pérdomo, M. Ferrer-Ferrer, C. Perego, E.R. Zanier, U. Mamrak, A. Rex, H. Party, et al. 2015. Results of a preclinical randomized controlled multicenter trial (pRCT): Anti-CD49d treatment for acute brain ischemia. *Sci. Transl. Med.* 7:299ra121. https://doi.org/10.1126/scitranslmed.aaa9853

Llovera, G., C. Benakis, G. Enzmann, R. Cai, T. Arzberger, A. Ghasemigharagoz, X. Mao, R. Malik, I. Lazarevic, S. Liebscher, et al. 2017. The choroid plexus is a key cerebral invasion route for T cells after stroke. *Acta Neuropathol.* 134:851–868. https://doi.org/10.1007/s00401-017-1758-y

Macleod, M.R., S. Michie, I. Roberts, U. Dirnagl, I. Chalmers, J.P. Ioannidis, R. Al-Shahi Salman, A.W. Chan, and P. Glasziou. 2014. Biomedical research: increasing value, reducing waste. *Lancet.* 383:101–104. https://doi.org/10.1016/S0140-6736(13)62329-6

Macrez, R., C. Ali, O. Toutirais, B. Le Mauff, G. Defer, U. Dirnagl, and D. Vivien. 2011. Stroke and the immune system: from pathophysiology to new therapeutic strategies. *Lancet Neurol.* 10:471–480. https://doi.org/10.1016/S1474-4422(11)70066-7

Mena, H., D. Cadavid, and E.J. Rushing. 2004. Human cerebral infarct: a proposed histopathologic classification based on 137 cases. *Acta Neuropathol.* 108:524–530. https://doi.org/10.1007/s00401-004-0918-z

Moskowitz, M.A., E.H. Lo, and C. Iadecola. 2010. The science of stroke: mechanisms in search of treatments. *Neuron.* 67:181–198. https://doi.org/10.1016/j.neuron.2010.07.002

Neumann, J., M. Riek-Burchardt, J. Herz, T.R. Doeppner, R. König, H. Hütten, E. Etemire, L. Männ, A. Klingberg, T. Fischer, et al. 2015. Very-late-antigen-4 (VLA-4)-mediated brain invasion by neutrophils leads to interactions with microglia, increased ischemic injury and impaired behavior in experimental stroke. *Acta Neuropathol.* 129:259–277. https://doi.org/10.1007/s00401-014-1355-2

Orsini, F., P. Villa, S. Parrella, R. Zangari, E.R. Zanier, R. Gesuete, M. Stravalaci, S. Fumagalli, R. Ottria, J.J. Reina, et al. 2012. Targeting mannose-binding lectin confers long-lasting protection with a surprisingly wide therapeutic window in cerebral ischemia. *Circulation.* 126:1484–1494. https://doi.org/10.1161/CIRCULATIONAHA.112.103051

Relton, J.K., K.E. Sloan, E.M. Frew, E.T. Whalley, S.P. Adams, and R.R. Lobb. 2001. Inhibition of alpha4 integrin protects against transient focal cerebral ischemia in normotensive and hypertensive rats. *Stroke.* 32: 199–205. https://doi.org/10.1161/01.STR.32.1.199

Sadler, R., J.V. Cramer, S. Heindl, S. Kostidis, D. Betz, K.R. Zuurbier, B.H. Northoff, M. Heijink, M.P. Goldberg, E.J. Plautz, et al. 2020. Short-Chain Fatty Acids Improve Poststroke Recovery via Immunological Mechanisms. *J. Neurosci.* 40:1162–1173. https://doi.org/10.1523/JNEUROSCI.1359-19.2019

World Health Organization. 2017. Top 10 Causes of Death. In World Health Organization. World Health Organization, Geneva.

Zhou, W., A. Liesz, H. Bauer, C. Sommer, B. Lahrmann, N. Valous, N. Grabe, and R. Veltkamp. 2013. Postischemic brain infiltration of leukocyte subpopulations differs among murine permanent and transient focal cerebral ischemia models. *Brain Pathol.* 23:34–44. https://doi.org/10.1111/j.1750-3639.2012.00614.x

Downloaded from http://rupress.org/jem/article-pdf/218/8/e20202411/1416415/jem_20202411.pdf by Ludwig-Maximilians-Universitaet Muenchen user on 27 May 2021

Supplemental material

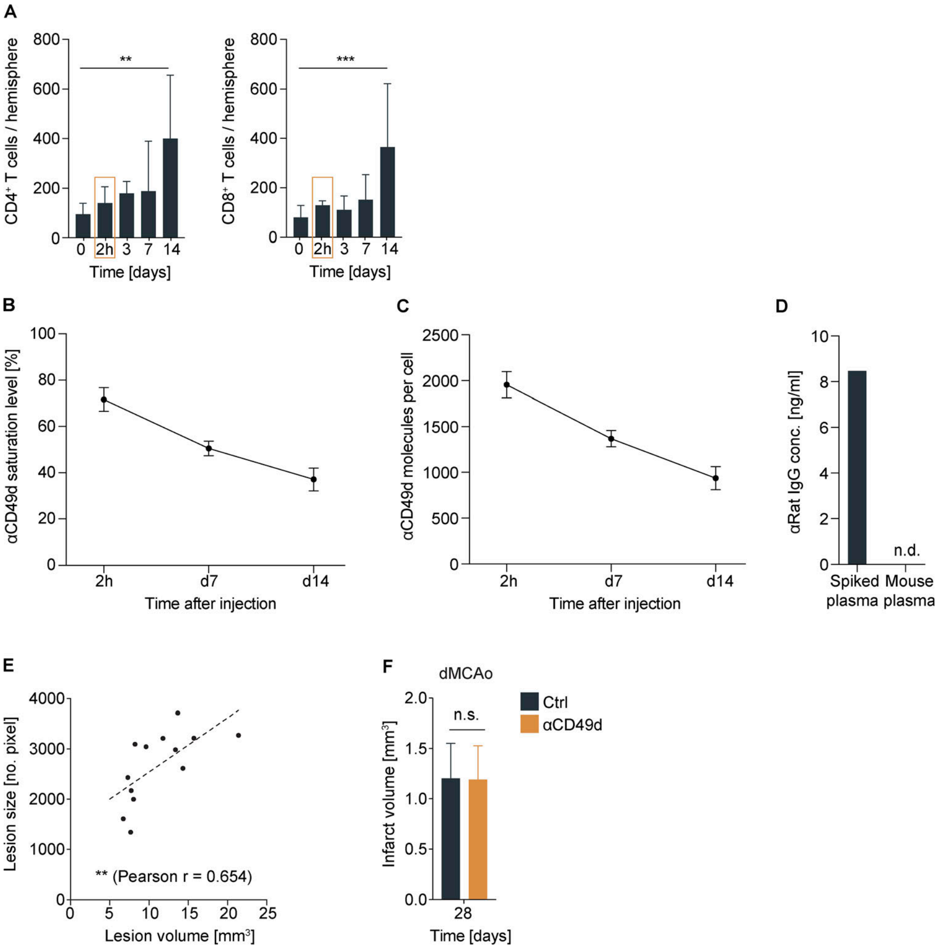

Figure S1. **Rationale for anti-CD49d treatment regimen and infarct volumetric assessment. (A)** Flow cytometric analysis of acute CD4⁺ and CD8⁺ T cell infiltration into the ipsilateral hemisphere after photothrombosis; *n* (0 = sham) = 10, *n* (2 h) = 3, *n* (3 d) = 6, *n* (7 d) = 6, *n* (14 d) = 5. Data are shown as mean + SD; ordinary one-way ANOVA + Dunnett's post-hoc test. At least two independent experiments were performed per time point in WT animals. **(B)** Saturation levels of anti-CD49d measured at 2 h and 7 and 14 d after i.p. injection of 300 µg anti-CD49d per animal; *n* = 3–4 per time point. Data are shown as mean + SD. Data were acquired in at least two independent experiments in WT animals. **(C)** Quantification of anti-CD49d molecules bound per cell at 2 h and 7 and 14 d after anti-CD49d treatment; *n* = 3–4 per time point. Data were acquired in at least two independent experiments in WT animals. **(D)** Mouse plasma concentration of anti-rat IgG is shown at day 28 from mice receiving two injections of 300 µg anti-CD49d at 2 h and 14 d after stroke. Naive mouse plasma was spiked with monoclonal anti-rat IgG as a positive control (spiked plasma); *n* = 3. **(E)** Correlation of lesion volume (histological analysis) and lesion size (autofluorescent pixels). Pearson correlation *n* = 13. Data were acquired in two independent experiments in Thy1GCaMP6s animals. **(F)** Infarct volume 28 d after distal middle cerebral occlusion; *n* (control) = 6, *n* (αCD49d) = 5. Data are shown as mean + SD. Unpaired *t* test. Data were acquired in three independent experiments in WT animals. **, P < 0.01; ***, P < 0.001.

Downloaded from http://rupress.org/jem/article-pdf/218/8/e20202411/1416415/jem_20202411.pdf by Ludwig-Maximilians-Universitaet Muenchen user on 27 May 2021

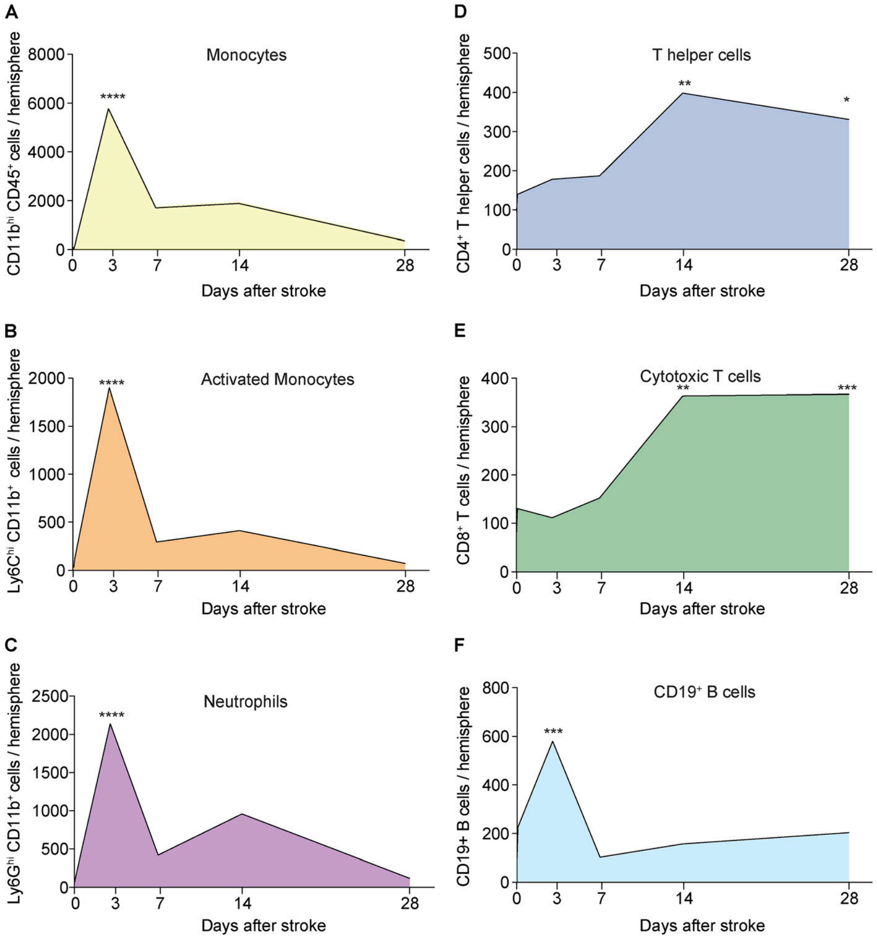

Figure S2. **Temporal dynamics of myeloid and lymphoid immune cell infiltration after stroke. (A–F)** Absolute counts of monocytes (A), activated monocytes (B), neutrophils (C), CD4^{+} T helper cells (D), CD8^{+} cytotoxic T cells (E), and CD19^{+} B cells (F) were assessed using flow cytometry at 2 h and 3–28 d after stroke, as well as after sham surgery (day 0) in the ipsilateral hemisphere; *n* (sham) = 10, *n* (2 h) = 3, *n* (3 d) = 5–6, *n* (7 d) = 5–6, *n* (14 d) = 5, *n* (28 d) = 5. Mean values are shown per time point. Ordinary one-way ANOVA + Dunnett's post-hoc test. At least two independent experiments were performed per time point in WT animals. *, $P < 0.05$; **, $P < 0.01$; ***, $P < 0.001$; ****, $P < 0.0001$.

Downloaded from http://rupress.org/jem/article-pdf/218/8/e20202411/1416415/jem_20202411.pdf by Ludwig-Maximilians-Universitaet Muenchen user on 27 May 2021

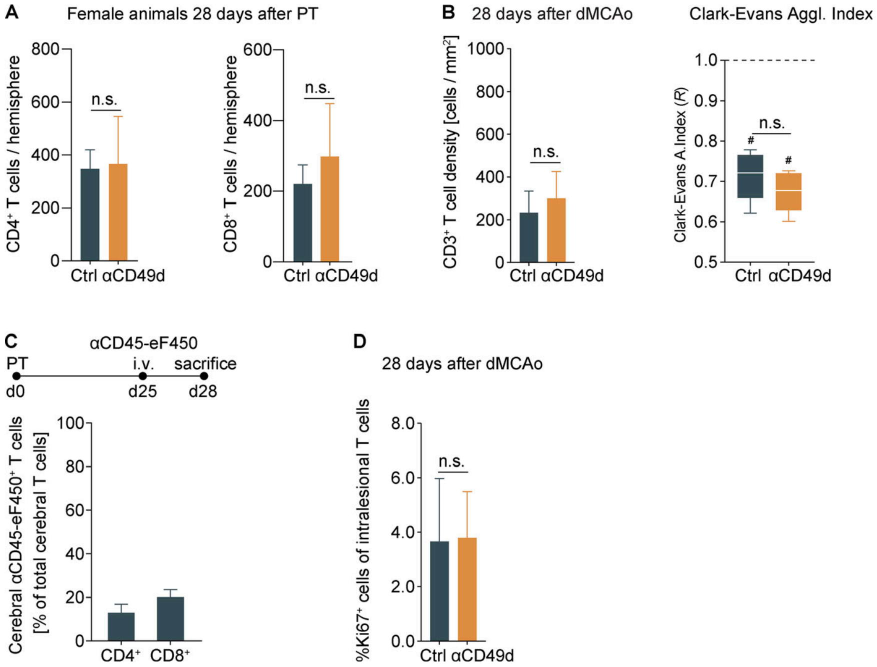

Figure S3. **Chronic T cell accumulation in female mice and after dMCAo. (A)** Flow cytometric analysis of CD4⁺ and CD8⁺ T cells 28 d after stroke in female mice; *n* = 7–8 per group, unpaired *t* test. Data are shown as mean + SD. **(B)** Evaluation of cell density and cell agglomeration of CD3⁺ intralesional T cells 28 d after dMCAo; *n* = 5 per group, unpaired *t* test. Data are shown as mean + SD/median and interquartile range. **(C)** i.v. labeling of circulating CD45⁺ leukocytes over 3 d before flow cytometric brain analysis 28 d after stroke reveals only a small fraction of brain-invading CD4⁺ and CD8⁺ T cells out of total cerebral T cells in the ischemic hemisphere; *n* = 4. Data are shown as mean + SD. **(D)** Percentage of Ki67⁺ T cells 28 d after dMCAo; *n* = 5 per group, unpaired *t* test. Data are shown as mean + SD. All data were generated in three independent experiments in WT animals. #, $P < 0.05$ for $R < 1.0$.

Table S1 is provided online as a Word document and lists patient data.

Downloaded from http://rupress.org/jem/article-pdf/218/8/e20202411/1416415/jem_20202411.pdf by Ludwig-Maximilians-Universitaet Muenchen user on 27 May 2021

Table S1.

Patient number	**Age (yr)**	**Sex (F/M)**	**Days after stroke**	**Cardiovascular risk factors**
1	69	F	124	Hypertension
2	78	F	20	Smoking
3	80	F	10	Hypertension
4	92	F	8	Hypertension
5	85	F	1–4	—
6	98	F	1	Smoking, hypertension, previous TIA

F, female; M, male; TIA, transient ischemic attack.

5. Publication II - Microglia monitor and protect neuronal function through specialized somatic purinergic junctions.

Cserép C, Pósfai B, Lénárt N, Fekete R, László ZI, Lele Z, Orsolits B, Molnár G, **Heindl S**, Schwarcz AD, Ujvári K, Környei Z, Tóth K, Szabadits E, Sperlágh B, Baranyi M, Csiba L, Hortobágyi T, Maglóczky Z, Martinecz B, Szabó G, Erdélyi F, Szipőcs R, Tamkun MM, Gesierich B, Duering M, Katona I, Liesz A, Tamás G, Dénes Á. (2020). Microglia monitor and protect neuronal function through specialized somatic purinergic junctions. ***Science.*** Jan 31;367(6477):528-537. doi: 10.1126/science.aax6752.

Journal: **Science**

Impact Factor: 41.846 Ranking: 2/69 in Multidisciplinary Sciences

Source: https://www-science-org.emedien.ub.uni-muenchen.de/doi/full/10.1126/science.aax6752

Copyright: AAAS (2020)

Microglia monitor and protect neuronal function via specialized somatic purinergic junctions

Short title: Microglia control neurons at somatic junctions

One-sentence summary: Neuronal cell bodies possess specialized, pre-formed sites, through which microglia monitor their status and exert neuroprotection.

Csaba Cserép[1,13], Balázs Pósfai[1,12,13], Nikolett Lénárt[1], Rebeka Fekete[1,12], Zsófia I. László[2,12], Zsolt Lele[2], Barbara Orsolits[1], Gábor Molnár[3], Steffanie Heindl[4], Anett D. Schwarcz[1], Katinka Ujvári[1], Zsuzsanna Környei[1], Krisztina Tóth[1,12], Eszter Szabadits[1], Beáta Sperlágh[5], Mária Baranyi[5], László Csiba[6], Tibor Hortobágyi[7], Zsófia Maglóczky[8], Bernadett Martinecz[1], Gábor Szabó[9], Ferenc Erdélyi[9], Róbert Szipőcs[10], Michael M. Tamkun[11], Benno Gesierich[4], Marco Duering[4], István Katona[2], Arthur Liesz[4], Gábor Tamás[3], Ádám Dénes[1,14,*]

[1] “Momentum” Laboratory of Neuroimmunology, Institute of Experimental Medicine, Hungary;
[2] “Momentum” Laboratory of Molecular Neurobiology, Institute of Experimental Medicine, Hungary;
[3] MTA-SZTE Research Group for Cortical Microcircuits, Department of Physiology, Anatomy and Neuroscience, University of Szeged, Hungary;
[4] Institute for Stroke and Dementia Research, Ludwig-Maximilians-University, Munich, Germany;
[5] Laboratory of Molecular Pharmacology, Institute of Experimental Medicine, Hungary;
[6] MTA-DE Cerebrovascular and Neurodegenerative Research Group, Department of Neurology, University of Debrecen, Debrecen, Hungary;
[7] Institute of Pathology, Faculty of Medicine, University of Szeged, Szeged, Hungary;
[8] Human Brain Research Laboratory, Institute of Experimental Medicine, Hungary;
[9] Medical Gene Technology Unit, Institute of Experimental Medicine, Hungary;
[10] Institute for Solid State Physics and Optics of Wigner RCP, Budapest, Hungary;
[11] Department of Biomedical Sciences, Colorado State University, Fort Collins, Colorado, USA.
[12] Szentágothai János Doctoral School of Neuroscience, Semmelweis University, Budapest
[13] C.C. and B.P. contributed equally to this work
[14] Lead contact

*__Correspondence__: Dr. Ádám Dénes, Institute of Experimental Medicine, Szigony u. 43, 1083 Budapest,

Hungary. Email: denes.adam@koki.mta.hu; Phone: +36 209549149

Abstract

Microglia are the main immune cells in the brain with emerging roles in brain homeostasis and neurological diseases, while mechanisms underlying microglia-neuron communication remain elusive. Here, we identify a novel site of interaction between neuronal cell bodies and microglial processes in mouse and human brain. Somatic microglia-neuron junctions possess specialized nanoarchitecture optimized for purinergic signaling. Activity of neuronal mitochondria is linked with microglial junction formation, which is rapidly induced in response to neuronal activation and blocked by inhibition of P2Y12 receptors (P2Y12R). Brain injury-induced changes at somatic junctions trigger P2Y12R-dependent microglial neuroprotection, regulating neuronal calcium load and functional connectivity. Collectively, our results suggest that microglial processes at these junctions are in ideal position to monitor and protect neuronal functions in both the healthy and injured brain.

Introduction

Microglia are the main immunocompetent cells of the nervous system and their role in brain development and maintenance of proper neuronal function throughout life is widely recognized (*1–3*). Importantly, changes in microglial activity are linked with major human diseases including different forms of neurodegeneration, stroke, epilepsy and psychiatric disorders (*4*, *5*), directing increased attention towards microglial research in recent years.

Microglia perform dynamic surveillance of their microenvironment by motile microglial processes including their constant interactions with neurons (*6*, *7*), yet, the molecular mechanisms of bidirectional microglia-neuron communication have remained elusive. To date, the majority of studies have focused on the interactions between microglial processes and synaptic elements, including axonal boutons and dendritic spines, which have been commonly perceived as the main form of interaction between microglia and neurons (*8*, *9*). However, neurons are extremely polarized cells with a high degree of functional independence concerning metabolism and signal integration in their dendritic and axonal compartments (*10–12*). In line with this, the large-scale structure of neurons (i.e. their cell body and axonal/dendritic branches) in the brain is relatively stable under most conditions, unlike highly dynamic small synaptic structures, such as dendritic spines and axonal boutons (*13*), which are often distant from neuronal cell bodies. Thus, we argued that the interactions between microglia and synapses may not fully explain how microglia are capable of monitoring and influencing the activity of neurons via dynamic surveillance, or detecting early events of cellular injury in the perisomatic compartment. This may be particularly relevant for the migration and differentiation of neural precursors, cell survival and programmed cell death, adult neurogenesis and the phagocytosis of damaged neuronal cell bodies (*14–17*). In line with this, it is not understood how microglia could monitor neuronal status over years or even decades, and discriminate salvageable neurons from irreversibly injured cells mainly based on changes occurring at distant synaptic structures. For example, microglial TAM receptors, which control physiological microglial processes, neurogenesis and phagocytic clearance of apoptotic cells upon binding of their extracellular ligands (*18*), are likely to exert their complex actions via also interacting with different structures on neurons other than synapses.

To understand the possible mechanisms of effective communication between microglia and neuronal cell bodies, we tested the hypothesis that specialized junctions on neuronal somata may be present that support the dynamic monitoring and assistance of neuronal function by microglia. Here, using *in vivo* two-photon (2P) imaging, high-resolution light- and electron microscopy combined with advanced 3D-analysis we identified a novel type of morpho-functional communication site between microglial processes and neuronal cell bodies in mice and human. Surprisingly, these somatic microglial junctions are present on the vast majority of neurons regardless of their cell type, and have specialized molecular composition and a unique nanoarchitecture linked to mitochondrial signaling. Furthermore, we provide direct *in vivo* evidence that these somatic junctions are essential for microglia-neuron communication, and for the neuroprotective effects of microglia after acute brain injury.

Results

Microglial processes contact specialized areas of neuronal cell bodies in the mouse and human brain

To visualize microglia together with cortical neurons and to study microglia-neuron interactions in the intact brain in real-time, CX3CR1$^{+/GFP}$ microglia reporter mice were electroporated *in utero* with *pCAG-IRES-tdTomato* plasmid (Fig. S1a). *In vivo* 2P imaging revealed microglial processes contacting the cell bodies of cortical layer 2-3 neurons in the adult brain (Fig. 1a, b; Movie S1). To our surprise, microglial processes preferentially returned to the same areas on the neuronal soma (observed in the case of 23 neurons out of 28 from 3 mice). Furthermore, trajectory analysis revealed that the average lifetime of somatic microglia-neuron contacts was 25 min (some contacts persisting for more than 1 hour, Fig. S1b), while dendritic contacts had a significantly shorter lifetime of 7.5 min (Fig. 1c, p=0.00035, n=26 contacts from 3 mice), similar to what Wake et al. found for synaptic contacts (*19*). Post-hoc confocal laser scanning microscopy (CLSM) and electron microscopic analysis further validated the direct interaction between microglial processes and the cell bodies of cortical pyramidal neurons (Fig. 1d; Fig. S1c), termed somatic microglial junctions. Similar interactions were present on well-characterized interneuron populations, namely type 3 vesicular glutamate transporter positive (vGluT3+) and parvalbumin-expressing (PV+) cells in the neocortex and the hippocampus (Fig. 1e). Importantly, CLSM revealed the presence of somatic microglia-neuron junctions in the human neocortex as well (Fig. 1f). Quantitative 3D analysis of fully reconstructed neurons uncovered that somatic microglial junctions were present on 91% of cortical pyramidal cells, 96% of vGluT3+, and 87% of PV+ interneurons in mice (n=155 cells from 2 mice). Despite the well-established microglial regulation of neuronal synapses, only 9% of glutamatergic and 14% of GABAergic synapses were associated with microglial processes (Fig. 1g; Fig. S1d, n=800 synapses from 2 mice). Remarkably, 87% of neurons in the human neocortex were found to receive microglial contact onto their cell body (Fig. 1f-g, n=89 cells from 2 patients). We also tested the possible presence of somatic microglial junctions in subcortical areas, and found that 98% of neurons in the caudate putamen, 91% of neurons in the nucleus r*eticularis* gigantocellularis and 96% of neurons in the medial septum were contacted by microglial processes (n=268 cells from 2 mice) confirming that this phenomenon is not only evolutionary conserved, but also broadly present in all main areas of the brain.

Next, we argued that microglia at somatic junctions may sense changes in neuronal state via signals released by exocytosis, which requires a specific molecular machinery supporting membrane trafficking. In neurons, clustered Kv2.1 proteins are well known to provide exocytotic surfaces via anchoring vesicle fusion molecules to the neuronal membrane (*20*, *21*). Furthermore, both Kv2.1 and Kv2.2 proteins are involved in forming endoplasmic reticulum (ER)/plasma membrane (PM)-junctions (membrane trafficking hubs), and anchoring intracellular organelles to the neuronal plasma membrane (*22*). We found that microglia contacted neuronal somatic membranes at sites of Kv2.1/2.2 clustering (Fig. 1h). The integrated density of Kv2.1 signal at these sites was 96% higher, and the density of Kv2.2 signal was 254% higher compared to those without microglial contacts (Fig. 1h, $p<0.0001$ in both cases, $n=114$ and 107 from 3 mice). More importantly, 87% of all microglia-neuron contacts expressed both types of clusters, 6.3% expressed only Kv2.1, 4.5% only Kv2.2 clusters, and only 1.8% of contacts were void of any Kv-clusters (Fig. 1i, $n=111$ contacts from 2 mice). Furthermore, 99% of neocortical and 94% of hippocampal CA1-region neurons coexpressed both Kv2.1 and Kv2.2 channels at the cellular level (Fig. S1i-k). The striking spatial association between Kv2.1 clusters and microglial processes was also observed on human cortical neurons (Fig. S1e, f, $n=21$ cells). Since Kv2.1-clusters are implicated in a large number of cellular processes involved in cell-to-cell communication, we focused on Kv2.1 in our further experiments. We found that these Kv2.1 hot spots are likely to define preformed neuronal microdomains, because Kv2.1 clusters remained unaltered after selective elimination of microglia by PLX5622 (Fig. S1g, h, 4.71 cluster/cross section in control vs. 6.64 cluster/cs in depleted, $n=59$ cells from 4 mice), suggesting their neuron-intrinsic nature. To test the functional involvement of Kv2.1-clusters in the formation of somatic junctions, we developed a dominant-negative Kv2.1 mutant construct (DNKv2.1), which is not able to integrate into the plasma membrane and which blocks the forward trafficking of any endogenous Kv2 proteins that may be expressed. We transfected HEK293-cells, which naturally lack Kv2.1 and Kv2.2 proteins (*23*), with fluorescent protein-coupled Kv2.1 or DNKv2.1 constructs, and cocultured these with microglia. Strikingly, microglial processes contacted Kv2.1-transfected HEK cells preferentially at Kv2.1 clusters, but not the DNKv2.1 transfected ones (Fig. 1j, Movie S2). 84% of Kv2.1-transfected HEK cells received microglial process contacts (97% of these contacts arrived onto Kv2.1-clusters), while only 5.4% of DNKv2.1 transfected HEK cells received process contacts (n=75 cells from 3 experiments).

Because activity-dependent exocytotic ATP or ADP release is known to take place from neuronal cell bodies under physiological conditions (*24*, *25*) and ATP (ADP) is a major chemoattractant for microglial processes via the microglial purinoceptor, P2Y12 receptor (P2Y12R, *6*, *26*), we next tested the hypothesis that signaling via P2Y12R is also essential for microglia-neuron interactions at these somatic junctions.

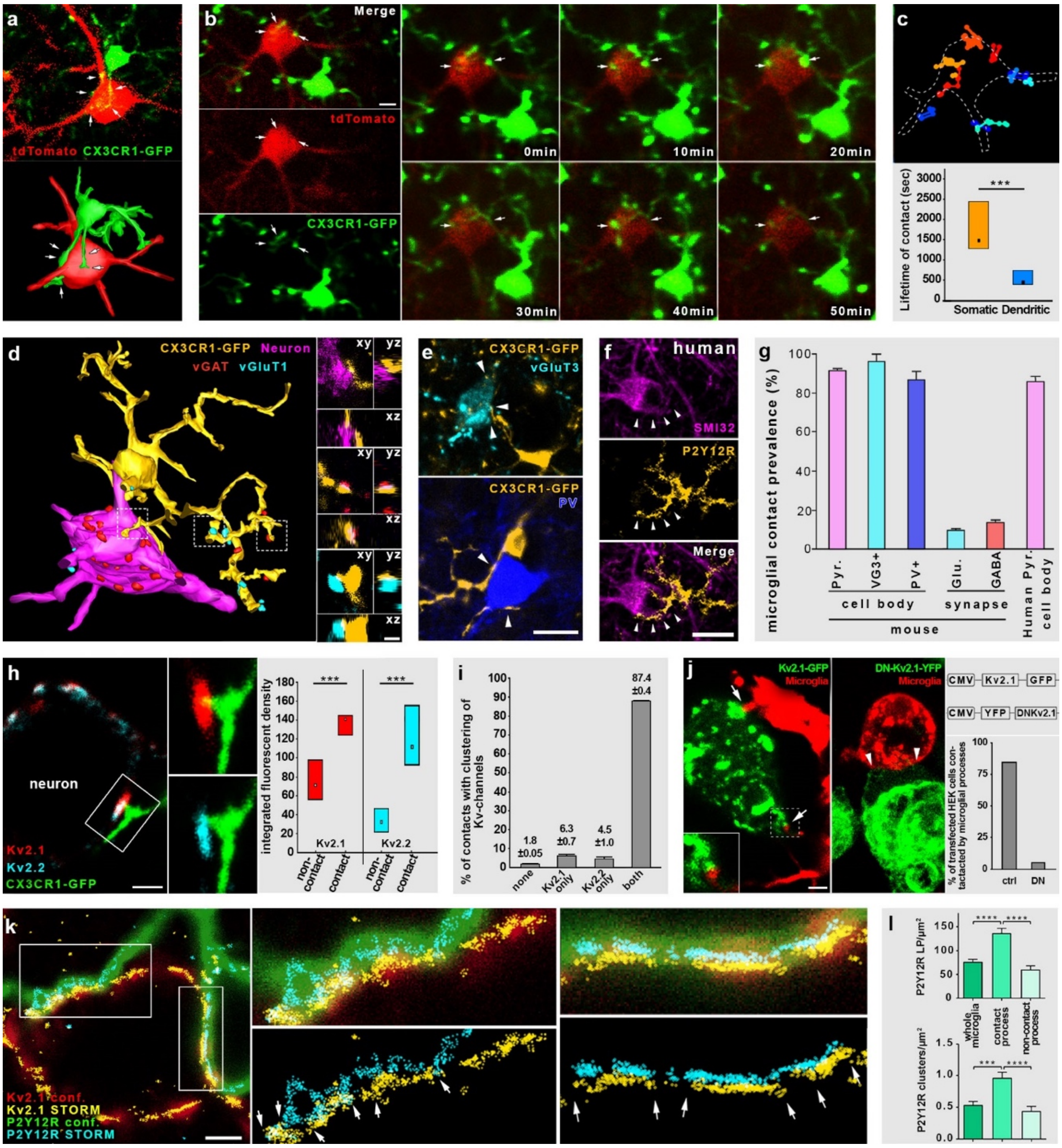
a
tdTomato CX3CR1-GFP
b
Merge
tdTomato
CX3CR1-GFP
0min
10min
20min
30min
40min
50min
c
***
Lifetime of contact (sec)
3000
2500
2000
1500
1000
500
0
Somatic Dendritic
d
CX3CR1-GFP Neuron
vGAT vGluT1
xy yz
xz
e
CX3CR1-GFP
vGluT3
CX3CR1-GFP
PV
f
human
SMI32
P2Y12R
Merge
g
microglial contact prevalence (%)
100
80
60
40
20
0
Pyr.
VG3+
PV+
Glu.
GABA
cell body
synapse
mouse
Human Pyr. cell body
h
neuron
Kv2.1
Kv2.2
CX3CR1-GFP
integrated fluorescent density
180
160
140
120
100
80
60
40
20
0
***
***
Kv2.1
Kv2.2
non-contact
contact
non-contact
contact
i
% of contacts with clustering of Kv-channels
100
90
80
70
60
50
40
30
20
10
0
1.8 ±0.05
6.3 ±0.7
4.5 ±1.0
87.4 ±0.4
none
Kv2.1 only
Kv2.2 only
both
j
Kv2.1-GFP
Microglia
DN-Kv2.1-YFP
Microglia
CMV Kv2.1 GFP
CMV YFP DNKv2.1
% of transfected HEK cells contacted by microglial processes
100
75
50
25
0
ctrl
DN
k
Kv2.1 conf.
Kv2.1 STORM
P2Y12R conf.
P2Y12R STORM
l
P2Y12R LP/µm²
150
100
50
0
****
****
whole microglia
contact process
non-contact process
P2Y12R clusters/µm²
1.5
1.0
0.5
0.0
***
****

Figure 1. Microglia contact specialized areas of neuronal cell bodies in the mouse and the human brain

a) Single image plane (upper panel) and 3D reconstruction (lower panel) from an in vivo 2-photon (2P) Z-stack shows a neocortical neuron (red) being contacted by microglial processes (green). b) In vivo 2P time-lapse imaging shows temporal dynamics of microglia-neuron contacts. c) Analyzed trajectories of microglial processes contacting the neuron on B. The lifetime of somatic contacts was significantly longer than dendritic ones. (p<0.001, n=26 contacts from 3 mice.) d) 3D-reconstruction from high-resolution confocal laser scanning microscopy (CLSM) Z-stack shows that microglial processes (yellow) contact GABAergic (red) and glutamatergic (cyan) boutons as well as the neuronal cell body (Kv2.1 labeling, magenta). Inserts on the right show orthogonal projections of these contacts from the confocal Z-stack. e) CLSM image planes show yellow *microglial processes touching cell bodies of hippocampal vGluT3+ and PV+ interneurons. f) CLSM images show P2Y12R+ microglial processes contacting SMI32+ neuronal cell bodies in human neocortex. g) Quantitative analysis of contact prevalence between microglial processes and different neuronal elements confirms that microglia contact the vast majority of neuronal cell bodies independently from neurochemical identity, while only a small fraction of synapses receive microglial contact. (n=155 neurons and 800 synapses in mice, and 89 neurons in human). h) CLSM image shows a neuronal cell body contacted by a microglial process at a Kv2.1-2.2-cluster. The integrated fluorescent density of both Kv2.1 and Kv2.2 signal is significantly higher within the contact site than elsewhere (p<0.001 in both cases, n=114 and 107 ROIs). i) The vast majority of microglia-neuron junctions expressed both Kv2.1 and 2.2 clusters (n=111 junctions). j) Microglial processes contact Kv2.1-transfected HEK-cells at the clusters, but not those transfected with a dominant-negative mutant (n=50 cells). k) Overlaid images show microglial P2Y12R (green for CLSM and cyan for STORM) and neuronal Kv2.1 (red and yellow) clusters overlapping. Arrows show borders of Kv2.1 clusters. j) P2Y12R clustering depends on the contact with neuronal cell body. Bar graphs show STORM localization point (LP) density (top) and density of identified P2Y12R clusters (bottom) on different parts of microglia (for statistics, see Table S1). Scale bars: 5 µm on b, 1 µm on d and k, 2 µm on h and j, 15 µm on e, 20 µm on f. Median values and interquartile ranges are plotted on c and h, mean and range on g and i, mean+SEM on l.*

In fact, all microglia – but no other cells in the brain, including perivascular macrophages – were found to be P2Y12R-positive (Fig. S3), including their processes recruited to somatic junctions (Fig. S3b). The restriction of P2Y12R expression to microglia within the brain is in perfect agreement with results of earlier single-cell transcriptomics studies (*27*, *28*).

To investigate the nanoscale architecture of P2Y12R at somatic microglia-neuron junctions, we used correlated CLSM and STORM superresolution microscopy, which enables the precise assessment of P2Y12R and Kv2.1 clusters at 20 nm lateral resolution (*29*). We found that P2Y12R forms dense clusters on microglial processes at somatic junctions, directly facing neuronal Kv2.1 clusters (Fig. 1k). Importantly, unbiased cluster analysis revealed that P2Y12R localization point (LP) density and cluster density were both significantly higher on microglial processes inside the junctions than on processes outside the junctions or on the whole microglial cell (Fig. 1l; Fig. S2a; for detailed statistics and numbers see Table S1). Furthermore, somatic contact-dependent clustering of P2Y12R was found to be a general phenomenon occurring on both pyramidal cells and interneurons (Fig. S2b; for detailed statistics and numbers see Table S1). Contact-dependent molecular clustering, however, could not be observed in the case of the microglial calcium-binding protein, Iba1 (Fig. S2c). EM analysis also confirmed, that contact-dependent P2Y12R clustering is specific to somatic junctions, and immunogold density is 62% lower on microglial membranes contacting boutons than on ones contacting somata (p=0.0002, n=26 contacts from 3 mice). All these data suggest the presence of a functionally specialized, yet ubiquitous communication site between P2Y12R-positive microglial processes and neuronal cell bodies.

Somatic microglia-neuron junctions possess a unique nanoarchitecture and molecular fingerprints, suggesting mitochondrion-related purinergic cell-to-cell communication

To further investigate the ultrastructural features of somatic microglia-neuron junctions, we performed transmission electron microscopy and high-resolution electron tomography with 3D reconstruction. P2Y12R immunogold labeling confirmed the formation of direct junctions between microglial processes and neuronal somata both in mice (Fig. 2a) and in postmortem human brain tissue (Fig. S4a). Surprisingly, we found that microglia-neuron junctions possess a unique ultrastructure within the neuronal cell body composed of closely apposed mitochondria, reticular membrane structures, intracellular tethers and associated vesicle-like membrane structures (Fig. 2a). 3D electron tomography confirmed this nano-architecture in neurons (Fig. 2b; Movie S3-4). These morphological features could not be observed in perisomatic boutons contacted by microglia, confirming the specific association of these structures with somatic microglial junctions. Furthermore, automated 3D analysis of tomographic volumes showed that P2Y12R density negatively correlated with the distance between microglial and neuronal membranes within the junctions (Fig. 2c, d; Fig. S4c, $p<0.001$, n=13055 points from 3 contacts), supporting the contact-dependent enrichment of P2Y12Rs on microglial processes. We also compared P2Y12R density between microglial membrane surfaces establishing junctions with neuronal somata and adjacent surfaces (within a few µm-s), that contacted boutons or other neuronal elements. We could detect a significantly higher P2Y12R density at microglial membranes directly contacting neuronal cell bodies (Fig. 2e; Movie S5, $p=0.00115$, n=24 surfaces), suggesting an important role for purinergic signaling in the formation of somatic microglia-neuron junctions.

Taking advantage of the ultra-high isotropic resolution provided by electron tomography, we could also observe discrete intercellular structures in the extracellular space resembling cell adhesion molecules, connecting the membranes of microglia and neuronal cell bodies (average length 23.5±3.1 nm, n=89 from 3 mice, Fig. S4b). This falls in the range of the size of integrins expressed by microglia (*30*, *31*) or the width of immunological synapses between peripheral immune cells (*32*). Mitochondria-associated membranes (MAM, average distance: 19.5 nm; n=104 from 3 mice, Fig. S4b) (*33*), and discrete tethers could also be observed between mitochondria and MAM (Movie S4).

We hypothesized that mitochondrial ATP-production and changes in neuronal activity could trigger microglial process recruitment, therefore we investigated the possible enrichment of neuronal mitochondria at microglial junctions on a large sample size, using an unbiased, semi-automatic analysis of TOM20 expression, which is the main element of the transport protein complex in the outer mitochondrial membrane (*34*). TOM20 immunofluorescent intensity was 420% higher at somatic junctions compared to adjacent areas (Fig. 2f, g, $p<0.001$, n=14 contacts from 2 mice), confirming the strong accumulation of neuronal mitochondria at the somatic junctions.

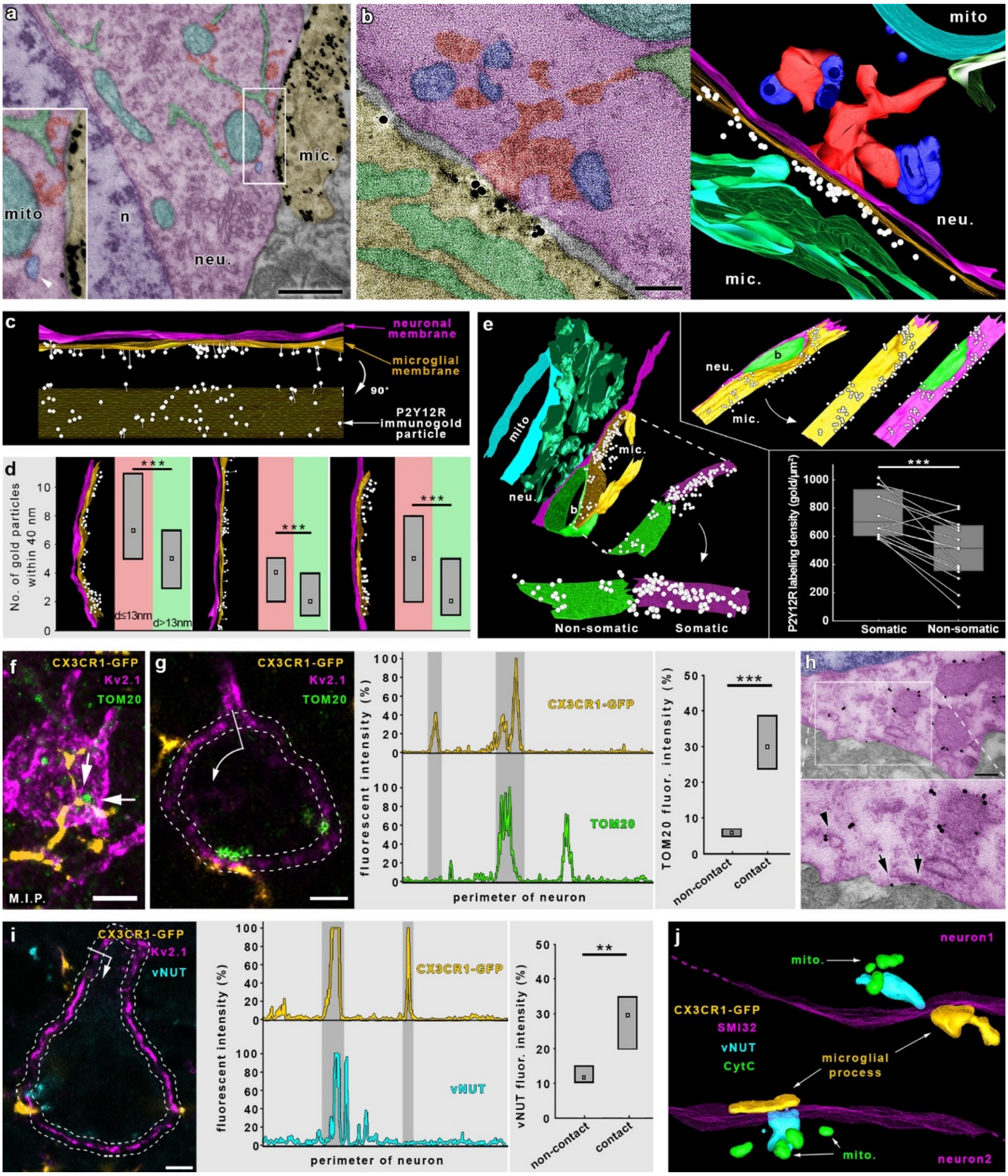
a
mic.
mito
n
neu.
b
mito
neu.
mic.
c
neuronal membrane
microglial membrane
90°
P2Y12R immunogold particle
d
No. of gold particles within 40 nm
10
8
6
4
2
0
***
d≤13nm
d>13nm
***
***
e
mito
neu.
mic.
b
neu.
mic.
Non-somatic
Somatic
***
P2Y12R labeling density (gold/µm²)
1000
800
600
400
200
0
Somatic
Non-somatic
f
CX3CR1-GFP
Kv2.1
TOM20
M.I.P.
g
CX3CR1-GFP
Kv2.1
TOM20
fluorescent intensity (%)
100
80
60
40
20
0
CX3CR1-GFP
TOM20
perimeter of neuron
TOM20 fluor. intensity (%)
50
40
30
20
10
0
***
non-contact
contact
h
i
CX3CR1-GFP
Kv2.1
vNUT
fluorescent intensity (%)
100
80
60
40
20
0
CX3CR1-GFP
vNUT
perimeter of neuron
vNUT fluor. intensity (%)
50
40
30
20
10
0
**
non-contact
contact
j
neuron1
mito.
CX3CR1-GFP
SMI32
vNUT
CytC
microglial process
mito.
neuron2

Figure 2. Microglia-neuron junctions possess a specialized nano-architecture and molecular machinery optimized for purinergic cell-to-cell communication

a) Transmission electron micrograph shows the area of the neuronal cell body (neu.) contacted by a P2Y12R-immunogold (black grains) labeled microglial process (mic.). The junction possesses a unique ultrastructure with closely apposed mitochondria (mito., cyan), reticular membrane structures (green), intracellular tethers (red). A mitochondria-associated vesicle (blue, marked by white arrowhead) is also visible. The nucleus (n) of *the neuron is purple. b) 0.5 nm thick virtual section of an electron tomographic volume (left) and 3D model (right) shows the special nano-architecture of a somatic microglia-neuron junction (colors represent the same structures, as in panel a). Note the specific enrichment of P2Y12R labeling at the core of the junction. c-d) P2Y12R density negatively correlates with the distance between microglial and neuronal membranes within the junctions. c) Side- and face (90 degrees rotated) view of the 3D model of a contact site. Immunogold density is the highest where the intercellular distance is the smallest. d) Density versus distance analysis performed on 3D models of contact sites confirms that the density of P2Y12R-immunogold particles within the junction is significantly higher where the distance between neuronal and microglial membrane is smaller than 13 nm ($p<0.001$, n=13055 points from 3 neocortical contacts, 3 mice). e) P2Y12R density is highest at those surfaces of microglial processes that are in direct contact with the neuronal cell bodies. Different views of the 3D models of two junctions illustrate that P2Y12R-immunogold density shows an uneven distribution along microglial membranes, being strongly and selectively enriched where the processes are in direct contact with neuronal somata (mitochondria – mito., neuron – neu., microglia – mic., bouton – b., microglial membrane contacting neuronal cell body – „Somatic", microglial membrane contacting profiles other than neuronal somata – „Non-somatic"). ($p<0.001$, n=24 surfaces, neocortex, 3 mice). f) CLSM maximal intensity projection (M.I.P.) shows microglial processes (yellow) contacting neuronal somata (magenta) with adjacent mitochondria (green). g) Neuronal mitochondria are enriched at microglial junction sites, as TOM20 immunofluorescent intensity is significantly higher along neuronal membrane parts where microglial processes contact the somata. ($p<0.001$, n=14, 2 mice). h) Transmission electron micrographs show TOM20-immunogold labeling in neocortical neurons. Immunogold labeling (black grains) is specifically associated with outer mitochondrial membranes, while TOM20-positive vesicles can also be observed (arrowheads). Some immunogold particles can be found on the plasma membrane of the neurons (arrows), suggesting the exocytosis of mitochondria-derived vesicles. i) vNUT immunofluorescent intensity is significantly higher in neurons where microglial processes contact the somata. ($p=0.002$, n=15, 2 mice). j) 3D reconstruction of high-resolution confocal Z-stack shows parts of two neuronal cell bodies (magenta), both contacted by microglial processes (yellow). The vNUT signal (cyan) was concentrated between the junctions and closely positioned mitochondria (green). Scale bars: 500 nm on a, 100 nm on b, 5 µm on f, 2 µm on g, 300 nm on h and 3 µm on i. Median values and interquartile ranges are plotted on d, e, f and i.*

Immunoelectron microscopy demonstrated the presence of TOM20-containing vesicles between mitochondria and the neuronal membrane in addition to TOM20-negative vesicles, suggesting the trafficking and possible exocytosis of mitochondria-derived vesicles (*35*) at somatic microglial junctions (Fig. 2h; Fig. S4e, f). Mitochondria-derived vesicles (MDVs) often integrate into the endo-lysosomal pathway (*35*), and these vesicles are positive for the lysosomal marker LAMP1 (*36*). Therefore, we investigated the presence of this marker, and found that LAMP1-positive puncta were closely associated to 83.3% of all Kv2.1 clusters at somatic junctions (Fig. S4g, n=72 contacts from 2 mice), suggesting the release of MDVs and lysosomal content at these junctions.

We also found that Kv2.1-immunogold clusters were tightly associated with the observed neuronal structures (i.e. closely apposed mitochondria, MAMs, ER, vesicle-like structures, cytoplasmatic densities) within these junctions (Fig. S4d). Similarly to our CLSM results (Fig. S1g), Kv2.1 nanoclustering was not affected by the absence of microglia (Fig. S4d), confirming the neuron-intrinsic nature of these morpho-functional units, and suggesting that they may function as mitochondria-related signaling hubs in neurons that microglia can specifically recognize. Vesicular release of mitochondria-derived ATP from neurons may occur in a vesicular nucleotide transporter (vNUT) dependent manner (*37*, *38*). Indeed, we found that vNUT signal intensity was 2.5 times higher in the vicinity of the neuronal membranes at somatic microglia-neuron junctions than at areas outside the junctions (Fig. 2i, p=0.002, n=15 contacts from 2 mice). Neuronal vNUT labeling was concentrated between mitochondria and the microglia-contacted neuronal membranes (Fig. 2j).

Importantly, Kv2.1 or vNUT signal was not present in perisomatic axon terminals (GABAergic synaptic boutons) including those contacted by microglial processes (Fig. S4h, i, n=220 boutons for Kv2.1, n=194 boutons for vNUT, from 2 mice), confirming again that these molecular fingerprints are associated specifically with somatic microglia-neuron junctions.

Physiological microglia-neuron communication at somatic junctions is P2Y12R-dependent and is linked with neuronal mitochondrial activity

Next, we aimed to test whether microglial process recruitment to somatic junctions is functionally linked with the activity of mitochondria in neurons. To this end, CX3CR1$^{+/GFP}$ mice were electroporated *in utero* with the mitochondria-targeted *CAG-Mito-R-Geco1* reporter construct (Fig. S5a), which further confirmed the involvement of somatic mitochondria in microglial junctions (Fig. 3a). *In vivo* 2P imaging was performed to monitor microglial process recruitment to neuronal mitochondria in the cerebral cortex (Fig. 3b). In line with our histological data, our *in vivo* results show that recruited microglial processes came to close apposition with neuronal mitochondria. These processes stayed in the vicinity of neuronal mitochondria for around 29 minutes *in vivo* (Fig. 3b, Movie S6, n=25 contacts on 19 neurons from 3 mice, median value), which number closely matches the value measured in case of tdTomato electroporated mice (Fig. 1c). Next, to study the functional relationship between microglial junction formation and activity of neuronal mitochondria, we assessed intracellular changes of the metabolic electron carrier nicotinamide adenine dinucleotide (NADH) (*39*, *40*) in coronal slices of visual and somatosensory cortices from CX3CR1$^{+/GFP}$ mice. Intracellular NADH fluorescence showed a granular pattern indicating mitochondrial NADH source. Indeed, the NADH signal perfectly co-localized with *Mito-R-Geco1* signal, confirming its mitochondrial origin (Fig. 3c). To search for somatic junction formation, we performed 2P imaging, which allowed us to track the movement of microglial processes and monitor cytosolic NADH in viable layer 2/3 neurons simultaneously (Fig. S5c). We could detect apparent increases in NADH intrinsic fluorescence (Fig. 3d, f, p=0.024, n=10 cells) parallel with the formation of somatic microglial junctions. In contrast, we found no changes in the mean intrinsic NADH fluorescence detected at neuronal somata contacted by microglial processes in P2Y12R$^{-/-}$ tissue (Fig. 3e, f, p=0.3, n=11 cells). These data suggest that microglial process recruitment to somatic junctions is linked to the metabolic activity of neuronal mitochondria via a P2Y12R-dependent mechanism.

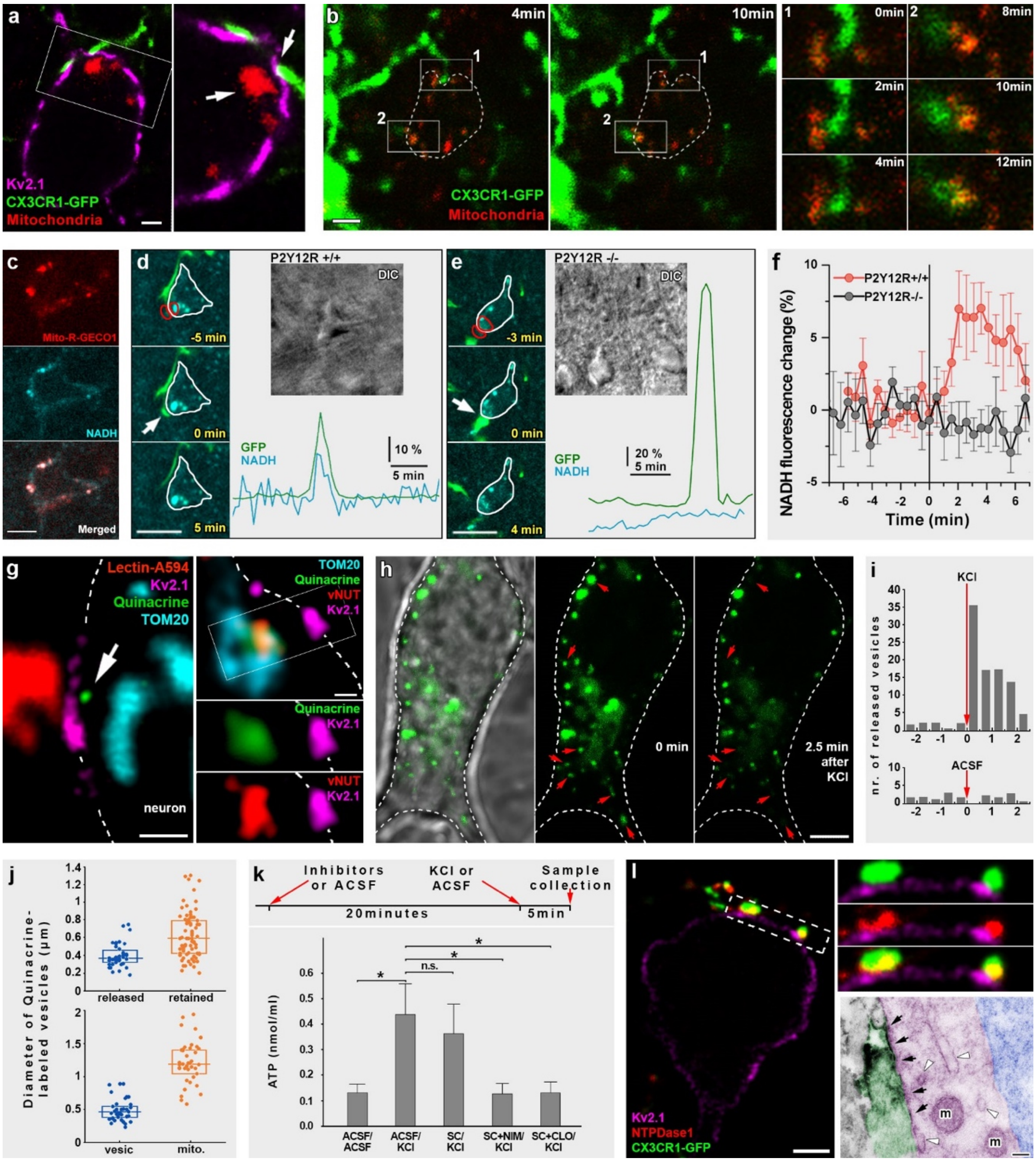
a
Kv2.1
CX3CR1-GFP
Mitochondria
b
4min
10min
1
2
0min
8min
2min
10min
4min
12min
CX3CR1-GFP
Mitochondria
c
Mito-R-GECO1
NADH
Merged
d
-5 min
0 min
5 min
P2Y12R +/+
DIC
GFP
NADH
10 %
5 min
e
-3 min
0 min
4 min
P2Y12R -/-
DIC
GFP
NADH
20 %
5 min
f
P2Y12R+/+
P2Y12R-/-
NADH fluorescence change (%)
10
5
0
-5
-6
-4
-2
0
2
4
6
Time (min)
g
Lectin-A594
Kv2.1
Quinacrine
TOM20
neuron
TOM20
Quinacrine
vNUT
Kv2.1
Quinacrine
Kv2.1
vNUT
Kv2.1
h
0 min
2.5 min after KCl
i
KCl
ACSF
nr. of released vesicles
40
35
30
25
20
15
10
5
0
-2
-1
0
1
2
10
5
0
-2
-1
0
1
2
j
Diameter of Quinacrine-labeled vesicles (μm)
1.4
1.2
1
0.8
0.6
0.4
0.2
0
released
retained
2
1.5
1
0.5
0
vesic
mito.
k
Inhibitors or ACSF
KCl or ACSF
Sample collection
20minutes
5min
ATP (nmol/ml)
0.6
0.5
0.4
0.3
0.2
0.1
0.0
*
*
*
*
n.s.
ACSF/ ACSF
ACSF/ KCl
SC/ KCl
SC+NIM/ KCl
SC+CLO/ KCl
l
Kv2.1
NTPDase1
CX3CR1-GFP
m
m

Figure 3. Neuronal mitochondrial activity and purinergic signaling is involved in microglia-neuron communication

a) CLSM image shows a microglial process (green) contacting Kv2.1 clusters (magenta) on a neuronal soma in the vicinity of a mitochondrion (Mito-R-Geco1, red) in perfusion-fixed brain. b) In vivo 2P imaging of CX3CR1$^{+/GFP}$ *mice in utero electroporated with CAG-Mito-R-Geco1 construct. Dashed line shows the outline of the neuron, green microglial processes touch neuronal cell body where somatic mitochondria are present. Contact lifetime was 29 min (median, 10-41 interquartile, n=25 contacts on 19 neurons from 3 mice). ROIs 1 and 2 are enlarged to show the development of somatic junctions. c) Mito-R-Geco1 expression colocalizes with NADH intrinsic fluorescence. d-e) Representative samples from time-lapse imaging of microglia show processes extending and contacting neuronal soma in CX3CR1*$^{+/GFP}$*/P2Y12R*$^{+/+}$ *(d) and CX3CR1*$^{+/GFP}$*/P2Y12R*$^{-/-}$ *(e) mice. White arrow indicates the contact site of microglia. DIC images of the imaged neurons and the fluorescence signal of GFP (green) and NADH (dark cyan) of red outlined areas are shown. f) Average of NADH intrinsic fluorescence of all neurons in P2Y12R*$^{+/+}$ *(red, n=10) and P2Y12R*$^{-/-}$ *mice (black, n=11). g) CLSM image shows microglial process contacting a neuronal Kv2.1 cluster with closely apposed quinacrine-labeled ATP-containing vesicle and closely localized neuronal mitochondria. Quinacrine-labeling colocalizes with vNUT-signal. h) Images from CLSM in vitro time-lapse imaging show that quinacrine-labeled ATP-containing vesicles (green) are released (red arrows) from neuronal cell body (white dashed outline) after KCl-stimulation (M.I.P. of z-stack of 2.5 µm). i) Number of released quinacrine+ vesicles plotted as a function of time after KCl or vehicle treatment. j) Size distribution of quinacrine-labeled puncta. The measured diameter of the released puncta can correspond to sub-diffraction sized emitters because of the point-spread function size (~0.3-0.4 µm at 488 nm), meaning that the size of the released vesicles can be as small as 40 nm. The smaller ones (vesicles) tend to be released, and the larger ones (mitochondria) are retained. k) KCl induces a robust ATP release in cultured neurons (p=0.0218, n=11), which could not be inhibited by a mixture of the synaptic calcium-channel blockers ω-Agatoxin and ω-Conotoxin (SC, p=0.6532, n=11), but is almost completely inhibited by the L-type calcium channel blocker Nimodipine (NIM, p=0.0271, n=10), or the vNUT-inhibitor clodronate (CLO, p=0.0284, n=10). l) CLSM image shows robust NTPDase1 expression on microglial processes within the somatic junctions. Electron microscopic insert shows NTPDase1-labeled (dark precipitate) microglial process contacting neuronal cell body. Neuronal mitochondria (m), vesicles and membrane structures (white arrowheads) are closely apposed to the contact site (black arrows), where NTPDase1 is expressed on microglial membrane. Scale bars: 2 µm on a and l, 4 µm on b, 5 µm on c, 10 µm on d and e, 500 nm on g, 3 µm on h, and 200 on the EM insert on l. Median values and interquartile ranges are plotted on j, mean+SD on f, mean+SEM on k.*

The molecular machinery and intercellular interactions identified above strongly suggested the involvement of purinergic signaling in these somatic junctions. To test whether neuronal somata could release ATP at these sites, we conducted a series of *in vitro* experiments. We found quinacrine labeled ATP-containing vesicles localized between neuronal mitochondria and neuronal membranes present at sites where microglial processes contacted neuronal Kv2.1 clusters in neuron-microglia cocultures (Fig. 3g). Quinacrine labeling also colocalized with vNUT signal (Fig. 3g), as previously demonstrated for neurons (*37*).

Next, we tested whether neuronal activity could release ATP-containing vesicles from neuronal cell bodies. 40 mM KCl-stimulation induced a rapid membrane depolarization and calcium influx in cultured neurons (Fig. S5d, n=23 cells for FluoVolt measurements, n=20 cells for Rhod3 measurements). CLSM in vitro time-lapse imaging confirmed that quinacrine-labeled (ATP-containing) vesicles are released from neuronal cell bodies after KCl-stimulation (Fig. 3h, i, 880% increase in release events after KCl vs. 27% decrease after vehicle, n=13 cells). Size analysis confirmed that the smaller profiles were released (Fig. 3j, median diameter of released: 0.37 µm and retained: 0.59 µm, n=118 puncta, similarly to previous reports (*37*, *41*)). The larger ones were identified as mitochondria by their uniform TOM20-labeling (Fig. 3j, median diameter of vesicle-labeling: 0.45 µm and mitochondrial-labeling: 1.2 µm, n=83 puncta).

Next, we applied high sensitivity HPLC to detect the levels of released ATP in the medium (Fig 3k). KCl induced a robust ATP release in cultured neurons (p=0.0218, n=11), which could not be significantly inhibited by a mixture of the synaptic calcium-channel blockers ω-Agatoxin and ω-Conotoxin (SC, p=0.6532, n=11), but was almost completely inhibited by the L-type calcium channel blocker Nimodipine (known to be important for somatic vesicular release (*42*, *43*); NIM, p=0.0271, n=10), or the vNUT-inhibitor clodronate (CLO, p=0.0284, n=10). These data confirmed the presence of an activity-dependent somatic ATP release from neurons. Since the main ligand for microglial P2Y12Rs is ADP, we tested the possible presence of nucleosidase expression at microglia-neuron contacts. Using CLSM and electron microscopy we found robust NTPDase1 expression on 99.6% of all microglial processes within the somatic junctions (Fig. 3l, n=275 contacts from 2 mice). Thus, neuron-derived ATP can readily be converted into ADP, and sensed by microglia right within the somatic junctions.

Because our data strongly suggest that microglial processes are in the perfect position at the somatic junctions to sense neuronal activity, we aimed to further explore the signaling mechanisms at these sites *in vivo,* by 2P imaging in CX3CR1$^{+/GFP}$ microglia reporter mice that were electroporated *in utero* with the neuronal reporter *pCAG-IRES-tdTomato* (Fig. 4a, b). Administration of the potent and selective P2Y12R-inhibitor PSB0739 (PSB) into the cisterna magna (i.c.m.) significantly reduced somatic junction lifetime by 45%, but did not affect the lifetime of dendritic microglia-neuron contacts (Fig. 4c, ctrl som. vs. PSB som. p=0.0331, n=40). We also tested synapse density after acute i.c.m. administration of vehicle (control) or PSB. PSB treatment did not alter neocortical synapse numbers (Fig. S6g, 0.353 synapse/µm^2 in control, and 0.352 synapse/µm^2 in PSB-injected, n=423 appositions from 4 animals). Since these data showed that the maintenance of somatic microglia-neuron junctions depends on physiological P2Y12R function, we aimed to test whether microglia would react directly to changes in neuronal activity. To this end, we induced neuronal activation by using the chemogenetic DREADD (Designer Receptor Exclusively Activated by Designer Drug) approach. pAAV carrying the hSyn-hM3D(Gq)-mCherry construct was injected into the cerebral cortex of P2Y12R$^{+/+}$ and P2Y12R$^{-/-}$ mice that had been crossed with CX3CR1$^{+/GFP}$ mice to visualize microglial responses in the presence or absence of P2Y12R signaling (Fig. 4d, e). After intraperitoneal injection of clozapine-N-oxide (CNO) to induce hM3D(Gq)-DREADD activation, we observed a 234% increase in neuronal cFos signal compared to vehicle treatment (Fig. 4f, $p<0.001$, $n=100$), confirming a specific and robust neuronal activation.

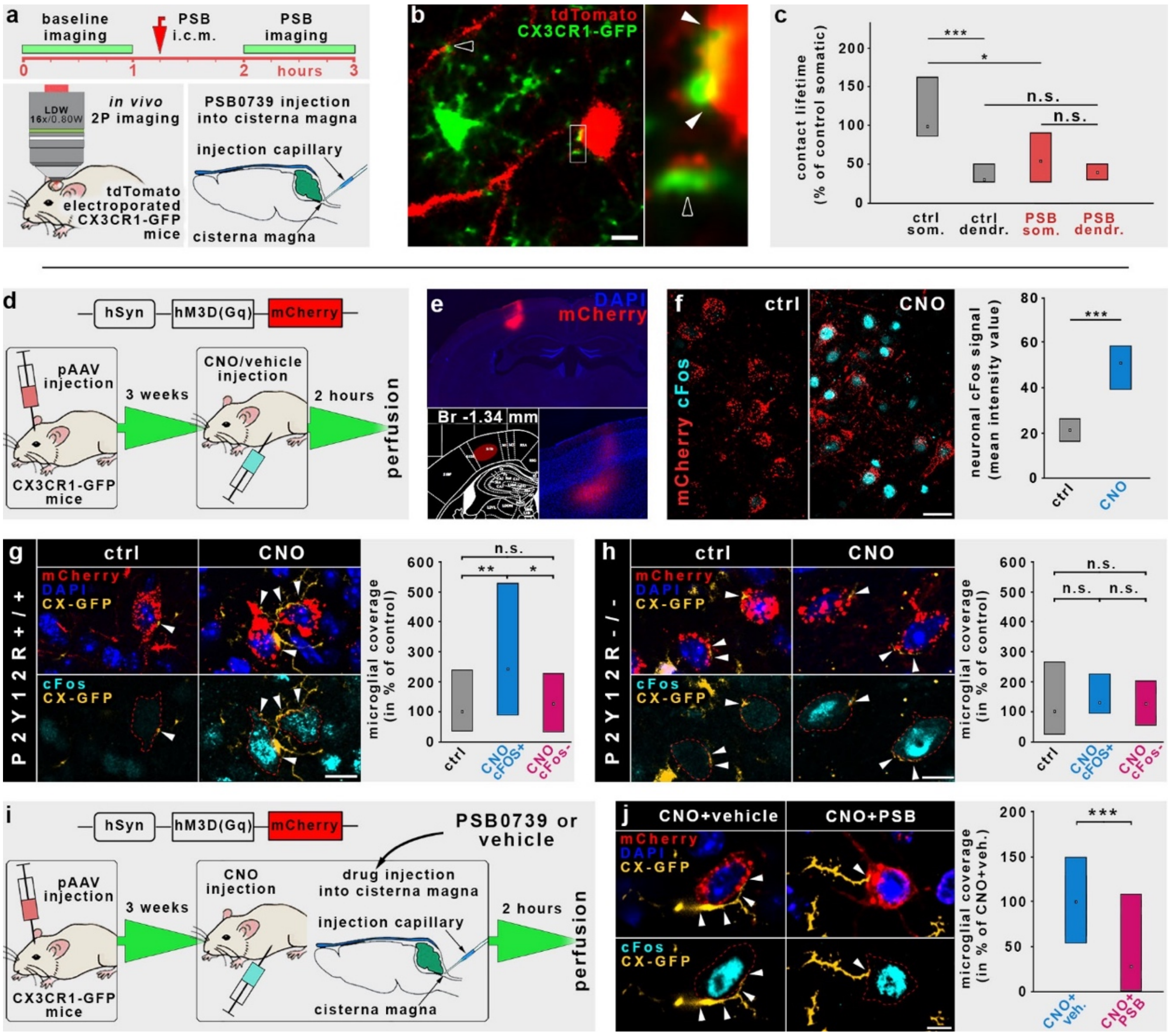
a
baseline imaging
PSB i.c.m.
PSB imaging
0
1
2
hours
3
LDW 16x/0.80W
in vivo 2P imaging
tdTomato electroporated CX3CR1-GFP mice
PSB0739 injection into cisterna magna
injection capillary
cisterna magna
b
tdTomato
CX3CR1-GFP
c
contact lifetime (% of control somatic)
200
150
100
50
0
***
*
n.s.
n.s.
ctrl som.
ctrl dendr.
PSB som.
PSB dendr.
d
hSyn
hM3D(Gq)
mCherry
pAAV injection
3 weeks
CNO/vehicle injection
2 hours
perfusion
CX3CR1-GFP mice
e
DAPI
mCherry
Br -1.34 mm
f
ctrl
CNO
mCherry cFos
neuronal cFos signal (mean intensity value)
80
60
40
20
0
***
ctrl
CNO
g
P2Y12R+/+
ctrl
CNO
mCherry
DAPI
CX-GFP
cFos
CX-GFP
microglial coverage (in % of control)
600
500
400
300
200
100
0
n.s.
**
*
ctrl
CNO cFos+
CNO cFos-
h
P2Y12R-/-
ctrl
CNO
mCherry
DAPI
CX-GFP
cFos
CX-GFP
microglial coverage (in % of control)
600
500
400
300
200
100
0
n.s.
n.s.
n.s.
ctrl
CNO cFos+
CNO cFos-
i
hSyn
hM3D(Gq)
mCherry
pAAV injection
3 weeks
CNO injection
PSB0739 or vehicle
drug injection into cisterna magna
injection capillary
cisterna magna
2 hours
perfusion
CX3CR1-GFP mice
j
CNO+vehicle
CNO+PSB
mCherry
DAPI
CX-GFP
cFos
CX-GFP
microglial coverage (in % of CNO+veh.)
200
150
100
50
0
***
CNO+ veh.
CNO+ PSB

Figure 4. Physiological microglia-neuron communication at the somatic junction site is P2Y12R-dependent

a) Outline of acute P2Y12R-blockade experiments. Baseline in vivo 2P imaging of cortical microglia-neuron contacts of tdTomato electroporated CX3CR1$^{+/GFP}$ *mice was followed by administration of the P2Y12R-inhibitor PSB0739 (PSB) into the cisterna magna (i.c.m.) and a further imaging session. b) CLSM images show examples of the recorded microglia-neuron contacts. Empty arrowheads point to dendritic contacts, full arrowheads mark somatic junctions. c) Acute i.c.m. administration of PSB significantly reduced somatic junction lifetime, but did not affect the lifetime of dendritic microglia-neuron contacts (ctrl som. vs. PSB som. p=0.0331, n=40). d) Outline of chemogenetic experiments. e) An example of an injection site. f) CNO administration* *induced a 2.3-fold increase in cFos mean fluorescent intensity value in DREADD expressing neurons ($p<0.001$, $n=100$). g) Neuronal activity induced a robust elevation of microglial process coverage of neuronal cell bodies in CNO-treated animals ($p=0.0139$, but not in DREADD+/cFos- cells, $p=1$, $n=101$ cells from 8 mice). h) CNO-triggered neuronal activity could not induce an elevation of microglial process coverage of neuronal cell bodies in P2Y12R$^{-/-}$ mice ($p=0.7497$, $n=85$ cells from 6 mice). i) Outline of combined chemogenetic - acute P2Y12R-blockade experiments. j) Acute inhibition of microglial P2Y12Rs prevented neuronal-activity induced increase of microglial process coverage ($p<0.001$, $n=124$ cells from 6 mice). Scale bars: 5 µm on b and j, 20 µm on f, 8 µm on g and h. Median values and interquartile ranges are plotted.*

We found that chemogenetic neuronal activation resulted in an increased microglial process coverage of the soma of DREADD- and cFos-coexpressing neurons in P2Y12R$^{+/+}$ mice (Fig. 4g, 243% of control, $p=0.0139$, $n=101$ neurons from 8 mice), but not in P2Y12R$^{-/-}$ mice (Fig. 4h, 133% of control, $p=0.7497$, $n=85$ neurons from 6 mice). We also tested the effect of acute central pharmacological blockade of microglial P2Y12Rs (Fig. 4i), and found that PSB injected i.c.m. completely abolished the neuronal activity-induced increase in microglial process coverage (Fig. 4j, 72.34% lower process coverage in CNO+PSB than in CNO+vehicle, $p<0.001$, $n=124$ neurons from 6 mice). Collectively, these results confirmed that microglia dynamically react to changes in neuronal activity at somatic microglia-neuron junctions in a P2Y12R-dependent manner, leading to a rapid increase of somatic coverage by microglial processes.

Microglia protect neurons after acute brain injury in a P2Y12R-dependent manner via altered somatic junctions

Since somatic microglia-neuron junctions were abundant in the healthy brain, we next examined how these morpho-functional communication sites are altered in response to brain injury. Microglia are known to rapidly respond to changes in neuronal activity in the boundary zone of the infarct after stroke (*44*). Thus, we performed experimental stroke and delineated the evolving penumbra based on the metabolic activity of the tissue as assessed by the redox indicator TTC (tetrazolium chloride) coregistered with the immunofluorescent signal for MAP2 and microglia (Fig. S6a). We observed the fragmentation of mitochondria (Fig. 5a, 74% decrease of individual mitochondrial area, 46% decrease of mitochondrial major axis, p<0.001 for both, n=189 mitochondria) and an almost complete declustering of Kv2.1 proteins (*45*, *46*) in morphologically intact penumbral neurons (Fig. 5b; Fig. S6e, from 4 to 0 median cluster/cross section and from 0.0947 to 0 cluster/µm in control and stroke, respectively, p<0.001, n=58 cells). These morphological changes were accompanied by a robust increase in the microglial process coverage of neuronal cell bodies, originating from somatic microglia-neuron junctions in both mice and human post-mortem brain tissues (Fig. 5b-e, mouse: 3.8-fold increase, p<0.001, n=30 neurons; human: 1.5-fold increase, p=0.007, n=249 neurons). Strikingly, acute i.c.m. administration of the P2Y12R-inhibitor PSB, or preventing mitochondrial injury by using the mitochondrial ATP-sensitive potassium (KATP) channel opener diazoxide (*47*, *48*), completely abolished stroke-induced increases in microglial process coverage around somatic junctions (Fig. 5d, ctrl vs. stroke: p<0.001, PSB ctrl vs. PSB stroke: p=0.792, diazo. ctrl vs. diazo. stroke: p=0.053, n=140 neurons). Viability of the examined neurons with increased microglial process coverage was confirmed by normal chromatin structure and membrane integrity (Fig. S6b, c). Transmission electron tomography also confirmed increased microglial process coverage and mitochondrial fragmentation of neurons (Fig. 5c).

To test the impact of P2Y12R-dependent microglial functions on neuronal viability *in vivo*, we investigated pharmacological inhibition of P2Y12R by injection of PSB i.c.m. prior to middle cerebral artery occlusion (MCAo). Inhibition of microglial P2Y12R not only prevented increases in microglial process coverage of neuronal cell bodies in the penumbra, but it also altered functional connectivity in the brain as assessed by a widefield imaging approach in Thy1-GCaMP6s mice (Fig. 5f, g,). In fact, an absence of P2Y12R signaling significantly increased the area of functional disconnection (global connectivity < 0.6) in the ipsilateral hemisphere during ischemia, accompanied by a trend towards elevated neuronal calcium-load (Fig. 5f; Fig. S6f, p=0.0439, n=17 mice). Seed-based connectivity analysis revealed a significant increase in the contralateral sensory hindlimb area after reperfusion in PSB treated animals. Moreover, connectivity analysis of 14 functional areas revealed a substantial and widespread increase in connectivity strength in the absence of microglial P2Y12R signaling (Fig. 5g, p=0.0077, n=7 mice).

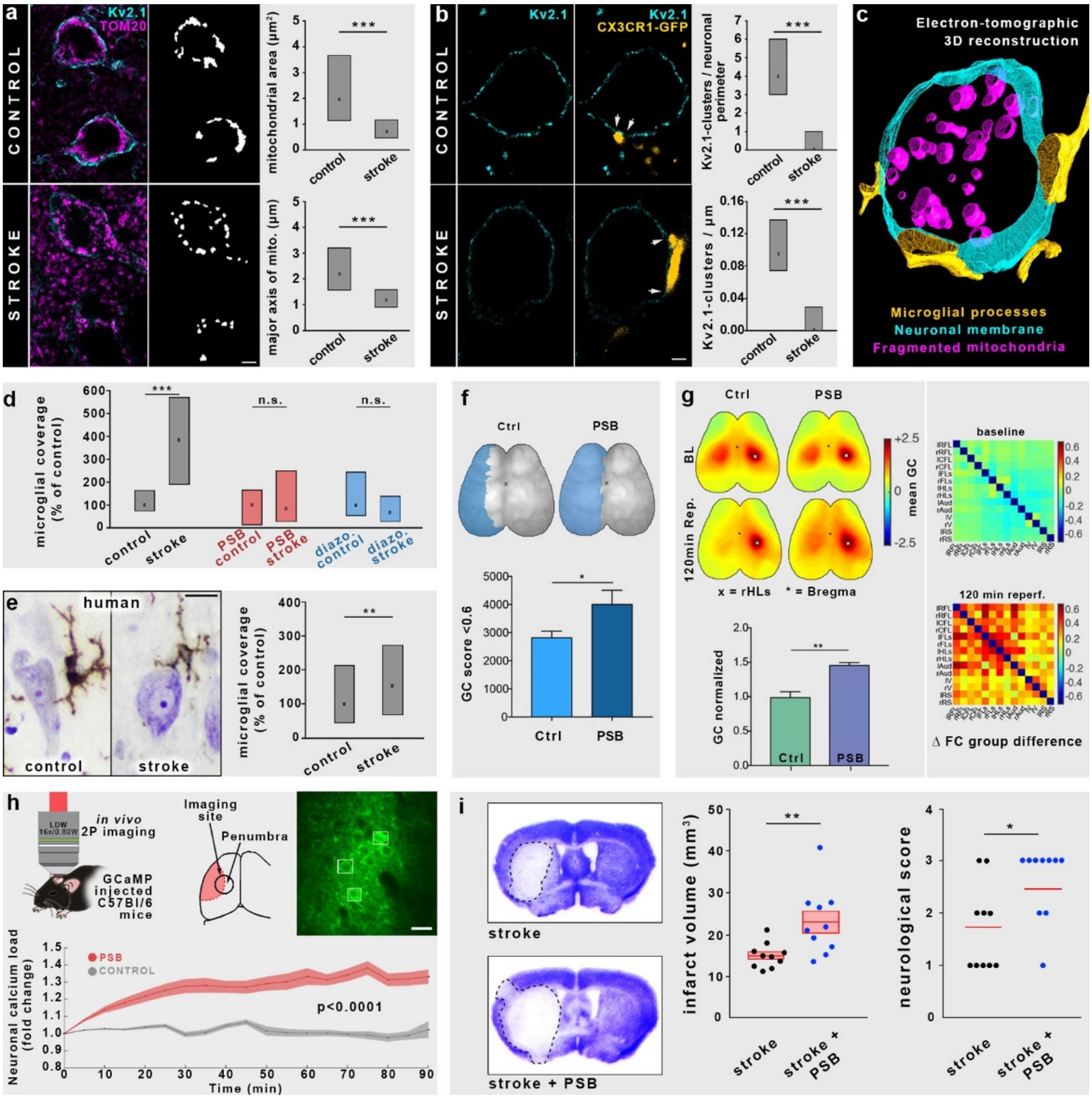

Figure 5. Microglia protect neurons after acute brain injury in a P2Y12R-dependent manner via altered somatic junctions

a) CLSM images show that stroke induces the fragmentation of mitochondria (magenta) in neuronal cell bodies (Kv2.1 labeling, cyan) in the penumbra. Mitochondrial area and mitochondrial major axis are both significantly decreased ($p<0.001$, $n=189$ mitochondria). b) CLSM images of cortical neurons show that in parallel with the declustering of Kv2.1-channels (cyan) microglial coverage (yellow) is significantly increased after stroke in the penumbra ($p<0.001$, $n=30$ neurons). c) 3D reconstruction from electron tomographic volume shows elevated microglial coverage and fragmentation of neuronal mitochondria. d) Microglial coverage of neuronal cell bodies is robustly increased after stroke, while acute central blockade of P2Y12Rs *or activation of mitochondrial ATP-sensitive potassium (KATP) channels completely abolishes the stroke-induced increase of coverage (ctrl vs. stroke: $p<0.001$, PSB ctrl vs. PSB stroke: $p=0.792$, diazo. ctrl vs. diazo. stroke: $p=0.053$, $n=140$ neurons). e) Stroke induces a 1.5-fold increase in somatic microglia coverage of human cortical neurons ($p=0.007$, $n=249$ neurons). f) Topographical maps show the area of pixels with a global connectivity (GC) score less than 0.6 after ischemia. The sum of outlined pixels revealed higher dropdown of GC in PSB treated animals after stroke ($p=0.0439$, $n=17$ mice). g) Left panel: Topographical maps show increased ROI-to-GC of the contralateral HLs in PSB-treated mice 120 min after stroke. Individual ROI-to-GC scores were normalized to baseline and quantified for group comparison ($p=0.0077$, $n=7$ mice). Right panel: Seed-to-seed connectivity is increased in PSB-treated animals after stroke. h) In vivo 2P calcium imaging reveals a significant increase of neuronal calcium load during reperfusion after acute P2Y12R inhibition with PSB ($p<0.0001$, $n=96$ neurons from 3 mice). i) Infarct volume is increased after acute central P2Y12R-inhibition (stroke: 14.96±0.95 mm^3; stroke+PSB: 23.06±2.519 mm^3, $p=0.008$, $n=20$ mice), which is accompanied by a significantly worse neurological outcome. Scale bars: 4 µm on a, 2 µm on b, 8 µm on e, 20 µm on h. Median values and interquartile ranges are plotted on a, b, d and e, mean+SEM on f, g, h and i.*

To examine the effect of P2Y12R inhibition at the single neuron level in the evolving ischemic penumbra in vivo, we investigated GCaMP6f-injected mice with 2P microscopy. In control mice, neuronal GCaMP6f signal remained unchanged for the first 90 minutes of reperfusion, while blockade of microglial P2Y12Rs with PSB resulted in a strong elevation in neuronal calcium load (Fig. 5h, $p<0.0001$, $n=96$ neurons, 3 mice), corroborating the findings obtained from the widefield imaging approach also at the cellular level. Most importantly, P2Y12R inhibition significantly increased lesion volume at 24 h reperfusion (Fig. 5i, stroke: 14.96±0.95 mm^3 /mean±SEM/; stroke+PSB: 23.06±2.519 mm^3, $p=0.008$) and resulted in worse neurological outcome (Fig. 5i, Bederson score, stroke: 1.7±0.26; stroke+PSB: 2.5±0.224, $p=0.033$, $n=20$ mice).

To investigate the duration of PSB effect *in vivo*, two-hour long imaging sessions were performed with 2P microscopy 1-3 hours and 24-26 hours after i.c.m. PSB-injection (n=173 contacts analyzed, from 3 mice). The lifetime of somatic junctions was significantly reduced up to 3 hours following PSB administration (56.3% of lifetime under baseline conditions, $p=0.0139$), while there was no effect observed one day later (93.8% of lifetime under baseline conditions, $p=1$), suggesting an acute effect of i.c.m. PSB (Fig. S6h, i). The acute effect of PSB is also confirmed by the histological measurements performed 4 hours after MCAo (Fig. 5d). To verify that i.c.m. injected PSB only inhibited microglial P2Y12Rs but not those expressed by circulating platelets, we measured ADP-induced platelet activation in plasma samples 1h after MCAo, when BBB injury is apparent (*44*, *49*, *50*). ADP-induced increases in platelet CD62P were not altered in mice treated with i.c.m. PSB compared to vehicle-treated animals (Fig. S5f). We also attempted to study whether genetic deletion of P2Y12R has similarly detrimental effect on neuronal injury after MCAo as seen after i.c.m. PSB administration. However, P2Y12R$^{-/-}$ mice displayed over 50% mortality after MCAo, therefore this study was discontinued due to ethical considerations (data not shown).

Taken together, the above data collectively show that disintegration of somatic microglia-neuron junctions after neuronal injury triggers increased microglial process coverage of the cell bodies of compromised but potentially viable neurons via P2Y12R and mitochondrial signaling, allowing the initiation of protective microglial responses that limit brain injury.

Discussion

Here we identify a novel form of interaction between microglia and neurons. We show that under physiological conditions, somatic microglia-neuron junctions are present on the majority of neurons in both mice and humans, function as major communication sites and are rapidly altered in response to brain injury. We propose that microglia constantly monitor neuronal status via these newly identified somatic junctions, allowing neuroprotective actions to take place in a targeted manner.

Our *in vivo* 2P imaging, CLSM and electron microscopic studies showed that sites of somatic junctions in neurons are preferentially and repeatedly contacted by microglia and such interactions have profoundly increased lifetime compared to the microglial contacts targeting dendrites. In previous studies, the proximity between microglial cell bodies or processes with neuronal somata has been observed in zebrafish and mice (*51*, *52*). However, the formation of direct membrane-to-membrane junctions, the molecular identity of neuronal membranes contacted, activity-dependent recruitment of microglial processes to neuronal cell bodies, the mechanisms of junction formation, and the function of somatic microglia-neuron interactions have not been experimentally addressed. Thus, we took advantage of cutting edge neuroanatomical approaches that have not been previously used to study microglia-neuron interactions, and discovered that somatic microglia-neuron junctions are characterized by unique ultrastructural and molecular composition. These morphological and molecular features are absent in perisomatic boutons contacted by microglia, suggesting that the main form of neuronal quality control by microglial processes is not mediated by interactions between microglia and perisomatic axon terminals.

Mitochondria are the primary energy generators in cells, playing fundamental roles in calcium homeostasis, intracellular signaling (*53–55*), neuronal quality control (*56*), and in determining cellular fate (*57*, *58*). While neuronal mitochondria are also considered as "immunometabolic hubs" involved in antigen presentation and the regulation of innate immune responses (*59*, *60*), changes in mitochondrial function due to metabolic imbalance, oxidative stress, inflammation, cellular injury or cell death occur in most neuropathological states (*61*). Mitochondria-associated membranes (MAM) are also considered to be key integrators of metabolic and immunological signals, playing a central role in neurodegeneration and cell-fate decisions (*33*, *62–64*). Thus, somatic mitochondria and MAMs are ideally positioned to report neuronal status to microglia and to mediate neuronal quality control. In line with this, we show that the recruitment of microglial processes to somatic junctions in the vicinity of neuronal mitochondria is linked with mitochondrial activity (NADH fluorescence). This may indicate rapid sensing of mitochondrial activity-associated changes of neurons by microglial processes via the release of ATP and other mediators, or the impact of microglia-derived substances on neuronal activity and/or mitochondrial function at somatic junctions. Since potential shifts in the fluorescence of NADH indicates both oxidative and glycolytic metabolism (*65*), the precise molecular interactions involved need to be investigated in future studies. Neurons can execute somatic ATP release via pannexin hemichannels, voltage-dependent anion channels or through activity-dependent vesicle exocytosis (*24*, *25*, *42*). Vesicular nucleotide transporter (vNUT) is known to be responsible for somatic vesicular ATP-release in neurons (*38*). In fact, we demonstrated the enrichment of vNUT between neuronal mitochondria and the somatic membranes contacted by microglia, and using time-lapse imaging and HPLC measurements, we confirmed the presence of activity-dependent somatic ATP release from neurons that was blocked by vNUT inhibition. TOM20-positive mitochondria-derived vesicles and other vesicles were also observed within the neuronal cytoplasm at somatic microglia-neuron junctions, together with the enrichment of LAMP1-positive lysosomes, which could – together with the released ATP – provide a constant readout of neuronal activity and mitochondrial function as seen in neurons and other cells (*35*, *66*, *67*). The strong enrichment of vNUT in these contacts (Fig. 2i, j), the existence of an activity- and vNUT-dependent somatic ATP-release (Fig. 3h-k), the presence of filamentous cytoplasmatic structures connecting vesicles to the core of the junction (Fig. 2a, b), the presence of TOM20 immunogold positive vesicles within the contacts attached to the neuronal plasma membrane (Fig. 2h), close association of neuronal lysosomes (Fig. S4g), and the massive accumulation and nanoscale clustering of exocytosis-promoting Kv2.1-proteins within these contact sites (Fig. 1k) collectively indicate the convergence of multiple parallel vesicular exocytotic pathways at microglia-neuron junctions.

Kv2.1 channels are major regulators of neuronal potassium levels. However, they tend to assemble into discrete clusters on the surface of neurons, where they do not function as ion channels, but provide sites for intensive membrane trafficking as exo- and endocytotic hubs (*20*, *68–70*). Furthermore, Kv2.1 clusters are known to induce stable ER-plasma membrane junctions (*69*), anchoring MAMs and mitochondria into these morpho-functional units, providing an ideal site for release of mitochondria-associated messenger molecules (*35*). The functional importance of these interactions is confirmed by our results showing that Kv2.1-clusters on transfected HEK-cells readily induced the formation of microglial process-contacts to these clusters, which could not be observed on HEK-cells transfected with the dominant-negative mutant Kv2.1. Furthermore, using STORM super-resolution imaging, we found that microglial P2Y12R clusters are precisely aligned with neuronal Kv2.1 clusters at somatic junctions (Fig. 1k).

Interestingly, the activation of P2Y12Rs was mainly associated with injury or pathological states in previous studies, and was considered negligible for physiological microglial surveillance, based on *ex vivo* studies (*71*). Compared to normal extracellular ATP levels in the brain, high levels of ATP (1 mM) were shown to induce P2Y12R-dependent microglial recruitment, similarly to that seen during microglial phagocytosis or in models of synaptic plasticity, while microglial surveillance is considered to be P2Y12R-independent (*71–74*). Our *in vivo* results refine this view and highlight the importance of compartment-dependent effects of P2Y12R on microglial process responses: PSB0739 significantly reduced somatic junction lifetime but did not affect the lifetime of dendritic microglia-neuron contacts, while abolished microglial reactions to altered neuronal activity, confirming P2Y12R-dependence of microglial actions under physiological conditions. Furthermore, neuronal mitochondrial activity was also linked with physiological microglial P2Y12R activity at these junctions. Based on our data, it is also possible that P2Y12R-mediated actions are more important for the sustainment than for the formation of somatic junctions during the communication between neuronal somata and microglial processes. The contact-dependent clustering of P2Y12 receptors further confirms their involvement in physiological microglia-neuron interactions at somatic junctions. Interestingly, blockade of microglial P2Y12R left cortical synapse numbers completely unchanged (Fig. S6g) and contact-dependent nano-clustering of microglial P2Y12Rs was not seen when microglia contacted synaptic boutons. The above structural and functional data in addition to the markedly longer lifetime of these somatic junctions *in vivo* collectively suggest that microglia-neuron interactions at these sites are not only P2Y12R-dependent, but are fundamentally different from those seen at synapses.

The failure of most neuroprotection trials in stroke and other brain diseases strongly indicates the importance of understanding the complexity of pathophysiological processes, including microglial actions. In fact, potentially salvageable neurons around the infarct core may show metabolic activity up to 6-17 hours following stroke in patients and experimental animals (*75*–*77*). Concerning the fate of these neurons, both the detrimental role of inflammatory mechanisms and the protective nature of microglial actions have been previously demonstrated (*44*, *78*, *79*). We found that Kv2.1 declustering takes place in compromised neurons of the penumbra as early as 4 hours after brain injury that paralleled mitochondrial fragmentation in neurons, and increased microglial process coverage around somatic microglia-neuron junctions. Our results reveal that P2Y12R-dependent microglial actions protect neurons, while blockade of microglial P2Y12R signaling alone impairs cortical network function, increases calcium load, and the area of ischemia-induced disconnection within two hours following stroke (a clinically relevant time window), leading to augmented brain injury, similarly to that seen after the complete and selective elimination of microglia (*44*). We also show that these protective microglia- and P2Y12R-mediated effects are linked with mitochondrial actions initiated upon neuronal injury, since the KATP channel opener diazoxide abolished the increases in microglial process coverage of neurons after stroke, similarly to the blockade of P2Y12R signaling. All these results unequivocally indicate that microglia continuously monitor neuronal status via these newly described somatic junctions, rapidly respond to neuronal changes and initiate neuroprotective actions.

Clinical significance

Genome-wide association studies, clinical data and experimental research collectively identify both microglia and neuronal mitochondria as key effectors in common neurological diseases including dementia and other psychiatric disorders, acute brain injury and different forms of neurodegeneration (*4*, *5*, *61*, *80*). The exact mechanisms underlying these conditions are currently unclear and effective therapies are lacking, despite all research efforts and numerous clinical trials performed to protect injured neurons in the brain. Based on the available data, microglia-mediated effects in health and disease cannot be explained merely by microglia-synapse interactions that often occur at a great distance from injured neuronal somata, where the majority of mitochondria critical for cell fate decisions are localized (*57*, *81*). To resolve these controversies, we describe a novel form of intercellular interaction through which microglia recognize neuron-intrinsic somatic signaling hubs, dynamically monitor neuronal state and mitochondrial function, respond to changes in neuronal activity through increased coverage of neuronal cell bodies and influence neuronal fate in a P2Y12R-dependent manner. These unique somatic microglia-neuron junctions exist in both mice and human in the majority of neurons and are altered in response to brain injury, suggesting their importance. These structures are likely to accommodate presently unexplored molecular fingerprints and signaling pathways involved in intercellular communication, in addition to recently described cell surface signals and intercellular communication pathways (*2*, *4*, *18*, *82*). We propose that healthy neurons may constitutively release ATP and other signaling molecules at these junctions, reflecting their “well-being“ towards microglia. In turn, disintegration of these specialized morpho-functional hubs due to excitotoxicity, energy depletion or other noxious stimuli may trigger rapid and inherently protective microglial responses, leading to the restoration of neuronal function or isolation and phagocytosis of dying neurons, in case terminal neuronal injury occurs (*74*). Along with P2Y12R-mediated microglial process recruitment, it is likely that a broad range of signals is integrated at somatic microglial junctions through which microglia may sense products of neuronal exocytosis, changes in the cell membrane (e.g. apoptotic signals), and alter the duration of physical contact or initiate phagocytosis. The most important open questions include the clarification of additional signaling mechanisms (vesicular and non-vesicular) involved in neuron-to-microglia communication at these junctions, and the mechanisms of microglial neuroprotection (e.g. regulation of neuronal ion-fluxes, neuronal calcium dynamics (*83*) or the metabolism of neuronal mitochondria). Since the role of microglia-neuron somatic junctions in most brain diseases is completely unknown, we assume that microglia-neuron interactions through these sites markedly differ in different forms of acute and chronic neuropathologies and have enormous therapeutic potential.

Author contributions

C.C., B.P. and A.D. conceived the project. Surgery was performed by N.L. and A.D.; two-photon imaging was performed by R.F., immunohistochemistry and light microscopy was performed by C.C., B.P., A.D., B.O., A.D.S and E.S.; STORM microscopy was performed by B.O., Electron microscopy was performed by C.C., B.P., E.S. and A.D.S., electron tomography was performed by C.C. and B.P., *in vitro* NADH imaging was performed by G.M. under the supervision of G.T., plasmid engineering and *in utero* electroporation was performed by Z. L. and Z. I. L., *in vitro* cell culture transfection and experiments were performed by Zs.K., K.T. and Z.I.L.; virus injection was performed by R. F. and B.M., widefield calcium imaging was performed by S.H. under the supervision of A.L.; HPLC measurements were performed by M.B. under the supervision of B.S.; C.C., B.P., B.O., G.M., S.H., N.L., A.D.S., K.U., A.L., A.D. analyzed data, L.C., T.H., Z.M. G.S., M.M.T. and F.E. contributed with critically important clinical and neuropathological data and materials, R.S. optimized the laser-optical setup for dual wavelength *in vitro* 2P measurements, I.K., G.T. and A.L. provided resources and essential intellectual contribution, and revised the manuscript. A.D. obtained funding and supervised the project. C.C. B.P. and A.D. wrote the paper with input from all authors.

Acknowledgements

This work was supported by „Momentum" research grant from the Hungarian Academy of Sciences (LP2016-4/2016 to A.D.) and ERC-CoG 724994 (A.D.), by the János Bolyai Research Scholarship of the Hungarian Academy of Sciences (C.C., and N.L), the UNKP-19-3-I (B.P.) and UNKP-19-4 (C.C.) New National Excellence Program of the Ministry for Innovation and Technology. Additionally, this work was funded by Hungarian Academy of Sciences (G.T.), the National Research, Development and Innovation Office of Hungary (GINOP-2.3.2-15-2016-00018, VKSZ-14-1-2015-0155, G.T.), the Ministry of Human Capacities, Hungary (grant 20391-3/2018/FEKUSTRAT, G.T.), by the Munich Cluster for Systems Neurology (EXC 2145 SyNergy) and ERC-StG 802305 to A.L.; I.K. was supported by „Momentum" research grant from the Hungarian Academy of Sciences (LP2013-54), Hungarian Scientific Research Fund (OTKA, K 116915) and National Research, Development and Innovation Fund (VKSZ_14-1-2015-0155); M.M.T. was supported by National Institutes of Health grant RO1GM109888; Zs.M. was supported by National Research, Development and Innovation Office of Hungary (grant K 125436) and by National Brain Research Program (2017-1.2.1-NKP-2017-00002); G.M. was supported by Hungarian Scientific Research Fund (OTKA, K 128863); R.S. was supported by Hungarian Scientific Research Fund (OTKA, K 129047). We thank László Barna and the Nikon Imaging Center at the Institute of Experimental Medicine for kindly providing microscopy support, David Mastronarde at MCDB for his continuous help with IMOD software, and Solt Kovács from ETH Zurich for scripting analytic tools. We are also grateful to Norbert Hájos (IEM) and Zoltán Nusser (IEM) for their useful comments. We thank the Department of Pathology, St. Borbála Hospital, Tatabánya, and the Human Brain Research Lab at the Institute of Experimental Medicine (IEM) for providing human brain tissue and Dóra Gali-Györkei for her excellent technical assistance. We also thank for Plexxikon for providing PLX5622.

Declaration of Interests

The authors declare no competing interests.

Methods

Ethical considerations

All experiments were performed in accordance with the Institutional Ethical Codex and the Hungarian Act of Animal Care and Experimentation guidelines (40/2013, II.14), which are in concert with the European Communities Council Directive of September 22, 2010 (2010/63/EU). The Animal Care and Experimentation Committee of the Institute of Experimental Medicine and the Animal Health and Food Control Station, Budapest, have also approved the experiments under the number PE/EA/1021-7/2019, PE/EA/673-7/2019. Control human brain tissue was obtained from two female (59- and 60-years-old) and one male (73-years-old) subjects who died from causes not linked to brain diseases, and did not have a history of neurological disorders (ethical approval ETT TUKEB 31443/2011/EKU [518/PI/11]). Tissues from patients who died after ischemic stroke affecting the MCA area were obtained from two female (77- and 78-years-old) and one male (66-years-old) subjects (ethical approval ETT-TUKEB 62031/2015/EKU, 34/2016 and 31443/2011/EKU (518/PI/11)) See Supplementary Table 2. Informed consent was obtained for the use of brain tissue and for access to medical records for research purposes. Tissue was obtained and used in a manner compliant with the Declaration of Helsinki.

Post-mortem human brain tissues

Brains of patients who died in non-neurological diseases were removed 3-5 h after death. The internal carotid and the vertebral arteries were cannulated, and the brains were perfused first with physiological saline (using a volume of 1.5 l in 30 min) containing heparin (5 ml), followed by a fixative solution containing 4% paraformaldehyde, 0.05% glutaraldehyde and 0.2% picric acid (vol/vol) in 0.1 M PB, pH 7.4 (4–5 l in 1.5–2 h). The cortical and hippocampal samples were removed from the brains after perfusion, and were postfixed overnight in the same fixative solution, except for glutaraldehyde, which was excluded. Blocks were dissected, and 50 µm thick sections were prepared on a vibratome (VT1200S, Leica, Germany). Brains of stroke patients were removed after 10-15 h after death and immersion fixed in 4% paraformaldehyde. Small regions from the affected cerebral cortex were dissected, embedded into paraffin both from the ipsilateral and contralateral hemisphere and 6-8 µm thick sections were cut on a sledge microtome.

Animals

Experiments were carried out on 12-18 weeks old C57BL/6 (RRID:IMSR_JAX:000664), CAMK2 GFP, PVA GFP, GAD65 GFP, CX3CR1$^{+/GFP}$ (IMSR_JAX:005582), CX3CR1$^{+/GFP}$/P2Y12$^{-/-}$ and C57BL/6J-Tg(Thy1-GCaMP6s)GP4.12Dkim/J mice (*26*, *84*–*87*). Mice were bred and genotyped at the SPF unit of the Animal Care Unit of the Institute of Experimental Medicine (IEM, Budapest, Hungary) as described earlier (*44*). Mice had free access to food and water and were housed under light-, humidity- and temperature-controlled conditions. All experimental procedures were in accordance with the guidelines set by the European Communities Council Directive (86/609 EEC) and the Hungarian Act of Animal Care and Experimentation (1998; XXVIII, section 243/1998), approved by the Animal Care and Use Committee of the IEM. All experiments were performed in accordance with ARRIVE guidelines.

In vivo pharmacological treatments and chemogenetics

To study the effect of P2Y12 receptor (P2Y12R) antagonists in healthy mice or after experimental stroke, either a single dose of PSB0739 (Tocris, R&D Systems, Minneapolis, USA, 15 µg dissolved in saline), or vehicle was administered to the cisterna magna in 5 µl final volume using a glass capillary. The diffusion of materials injected i.c.m. was controlled with i.c.m. dye injections (Fig. S5e). For experiments aiming to assess the effect of microglial P2Y12R blockade on infarct size and neurological outcome, PSB0739 was administered at reperfusion after 30 min MCAo. For technical reasons, mice subjected to *in vivo* widefield calcium imaging and two-photon imaging received i.c.m. PSB0739 60 min prior to MCAo. Brains were harvested 24 hours later for histology. Diazoxide (#D9035, Sigma, Merck KGaA, Darmstadt, Germany) dissolved in 0.4% DMSO and 0.01 M NaOH was administered in a single dose of 10 mg/kg intraperitoneally, immediately before reperfusion of the MCAo took place during the stroke surgeries. Brains were prepared 4 hours later for histological assessment. For selective microglia elimination, C57BL/6J mice were fed a chow diet containing the CSF1 receptor antagonist, PLX5622 (Plexxikon Inc., 1200 mg PLX5622 in 1 kg chow) for 3 weeks to eliminate microglia from the brain (and another group of C57BL/6J mice were fed control chow diet). For the chemogenetic activation of neurons 0.1 µl of AVV8-pAAV-hSyn-HA-hM3D(Gq)-MCherry (RRID: Addgene_50474, Addgene, USA) was injected into the neocortex of CX3CR1$^{+/GFP}$ mice. After 3 weeks of incubation, mice received saline or clozapine-N-oxide (0.1 mg/ml) intraperitoneally to induce DREADD activation. Animals were perfused 1 hour after the injections, and processed for histology. For *in vivo* calcium imaging C57BL/6 mice were used. 200 nl concentrated AAV1.Syn.GCaMP6f.WPRE.SV40 (RRID:Addgene_100837, Penn Vector Core) was injected into the cortex 200-300 µm below the surface with glass capillary. The injection coordinates were 1.5 mm lateral from midline, 1.2 mm posterior from bregma. Cranial window surgery and two-photon (2P) resonant imaging were performed 2 weeks after injection.

Experimental stroke

MCAo was performed using the intraluminal filament technique as described earlier (*88*). In brief, animals were anaesthetized with isoflurane and a silicone-coated monofilament (210-230 µm tip diameter, Doccol, Sharon, US) was introduced into the left external carotid artery and advanced along the internal carotid artery to occlude the MCA for 30 or 45 min. Occlusion was confirmed by a laser Doppler (Moor Instruments, UK). During surgery, core temperature was maintained at 37±0.5°C. The following exclusion criteria were set up: animals having less than 70% relative reduction in blood flow, either having haemorrhage or having shorter survival than 24 h were excluded from any further analysis pre hoc. In total 2 animals (one control and one PSB treated) were excluded post hoc due to intracerebral haemorrhage, 1 PSB treated animal died before 24 h. Altogether 3 out of 36 animals were excluded (28.26%) from the analysis, and total mortality was 2.77%.

Functional outcome of mice was assessed 24 h after MCAo using the corner test (*89*) and the 5-point Bederson's sensory-motor deficit scoring system (*90*). Briefly, the following scores were given: a 0, no motor deficit; 1, flexion of torso and contralateral forelimb when mouse was lifted by the tail; 2, circling to the contralateral side when mouse is held by the tail on a flat surface, but normal posture at rest; 3, leaning to the contralateral side at rest, 4, no spontaneous motor activity, 5, early death due to stroke.

Infarct size was calculated based on cresyl-violet stained coronal sections as described previously in (*44*, *91*, *92*). In brief, lesion volume at 24 h reperfusion was calculated by integration of areas of damage measured at eight neuro-anatomically defined coronal levels (between 2.9 mm rostral and 4.9 mm caudal to bregma) followed by correction for oedema.

To delineate the ischemic penumbra, unfixed 1 mm thick brain slices were incubated in 1% TTC (2,3,5-Triphenyltetrazolium chloride, Sigma) dissolved in PBS at 37°C for 20 minutes. Slices were then postfixed with 4% PFA in PB for 24 hours at 4°C, resectioned and processed for immunostaining.

Perfusion, tissue processing for histology

Adult mice were anesthetized by intraperitoneal injection of 0.15-0.25 ml of an anaesthetic mixture (containing 20 mg/ml ketamine, 4 mg/ml xylazine-hydrochloride). Animals were perfused transcardially with 0.9% NaCl solution for 1 minute, followed by 4% freshly depolymerized paraformaldehyde (PFA) in 0.1 M phosphate buffer (PB) pH 7.4 for 40 minutes, and finally with 0.1 M PB for 10 minutes to wash the fixative out. Blocks containing the primary somatosensory cortex and dorsal hippocampi were dissected and coronal sections were prepared on a vibratome (VT1200S, Leica, Germany) at 20 μm thickness for STORM experiments, 50 μm thickness for immunofluorescent experiments and electron microscopy/electron tomography.

Cloning

*CAG-IRES-tDTomato (pCAG-IRES-tDTomato)***:** The GFP-polyA part of the pCAGIG plasmid (a gift from Connie Cepko, Addgene plasmid #11159, RRID:Addgene_11159 (*93*)) was replaced with tDTomato-pA (a gift from Gyula Balla, IEM, Hungary) using blunt-end cloning (pCAGIG:PstI-BstXI, pcDNA3-tDTomato: HindIII-PvuII), fragments were blunted via Klenow chewback/fill-in respectively.

CAG-Mito-R-Geco: CMV-Mito-R-Geco1 (a gift from Robert Campbell; Addgene plasmid #46021, RRID:Addgene_46021 (*94*)) was digested PmeI and the mito-R-Geco fragment then subcloned into EcoRV-digested pBSKII SK+ (Stratagene). Orientation was checked with restriction analysis. Then pBSKII-Mito-R-Geco was cut with Acc65I-NotI and cloned into pCAG-GFP (a gift from Connie Cepko (Addgene plasmid #11150, RRID:Addgene_11150 (*93*)) digested with Acc65I-NotI.

Kv2.1-EGFP: *CMV-hKv2.1-pEGFP-C1* was a gift from Federico Sesti (Addgene plasmid #111538; http://n2t.net/addgene:111538 ; RRID:Addgene_111538)

Kv2.1-ruby: *CMV-Kv2.1-Ruby2* encoding plasmid was constructed by removing the NheI-GFP-EcoRI fragment in pEGFPC1-rKv2.1 (described earlier (*69*)) and replacing it with an in frame NheI-Ruby2-EcoRI fragment.

DNKv2.1-YFP (*CMV-DNKv2.1-YFP*): A YFP and myc epitope tagged Kv2.1 dominant negative construct was assembled using standard PCR-based cloning methods to insert the desired nucleotide sequences. Rat Kv2.1 cDNA fragment corresponding to amino acids 1-218 and encoding the N-terminus and first transmembrane domain was amplified and tagged with the myc epitope on the 3' end. This fragment was then inserted into the BamHI-XbaI sites of the pEYFP-C1 polylinker. The resulting construct expresses the Kv2.1 peptide with YFP on the N-terminus and the myc epitope on the C-terminus.

In utero **electroporation:**

Timed-pregnant C57Bl/6J (Jackson) females bred with homozygous CX3CR1$^{GFP/GFP}$ transgenic animals were anesthetized by isoflurane vaporization at embryonic day 14.5. Abdominal cavity was opened longitudinally and uterine horns were exposed. Approximately 1µl of expression vector (1 µg/µl all of the constructs) in endotoxin-free water containing Fast Green dye (Roth 1:10000 dilution) was injected into the embryonic lateral ventricles, using glass capillary and mouth pipette. Electroporation was performed with tweezer electrodes, 5x50 V pulses of 50 millisecond duration were applied with 950 millisecond intervals using the In Utero Electroporator SP-3c (Supertech). After the electroporation, uterine horns were returned into the abdominal cavity, the muscle wall and skin were sutured, and embryos were allowed to continue their normal development. All the littermates were CX3CR1$^{+/GFP}$ heterozygous and were born naturally.

Mito-R-Geco1 *in vitro* transfection into HEK-cells

HEK-293 cells were cultured in Dulbecco's Modified Eagle Medium (4.5 g/L glucose, L-glutamine & sodium pyruvate; Corning) with 10% heat-inactivated Fetal Bovine Serum (Biosera) and incubated at 37 °C in 5% CO_2 in air. On the day of transfection, cells were plated on poly-D-lysine (Sigma) coated 18 mm coverslips in 12-well cell culture plates. For transfection 2 µl Lipofectamine® 2000 Reagent (Thermo Fisher Sc.) were mixed with 2 µg Mito-R-Geco1 in Gibco® Opti-MEM™ Media (Thermo Fisher Sc.) and stored in the hood approximately half an hour. Transfection solution was mixed with the culturing media and cells were incubated overnight. Next day, cells were fixed with 4% PFA for 10 minutes, then washed with PBS. Permeabilization and blocking steps were performed by 0.1% TritonX and 5% NDS (Normal Donkey Serum; Sigma)/PBS solution for 30 mins. TOM20 antibody (1:1000) was applied in PBS for 90 mins. After several PBS washes cell were treated with secondary antibodies/PBS solution for an hour. Finally coverslips were washed in PBS and mounted with VECTASHIELD® HardSet™ mounting medium and sealed with nail polish. Confocal images were taken with 60X objective by Nikon A1R confocal system guide by NIS-Elements Microscope Imaging Software.

Isolation of microglial cells

Primary microglial cells were isolated from astroglia/microglia mixed cell cultures, as described earlier (*74*). In brief, meninges were removed and tissue pieces were subjected to enzymatic dissociation, using 0.05% w/v trypsin and 0.05% w/v DNase for 10 minutes at room temperature. The cells were plated onto poly-L-lysine coated plastic dishes and were grown in Minimal Essential Medium (MEM, ThermoFisher Sc. 21090-055) supplemented with 10% fetal bovine serum (FBS, Thermofisher 16000044), glutamine (4 mM; Sigma-Aldrich G3126), gentamycin (40 µg/ml; Gentamicin Sandoz, 80 mg/ml injection) and amphotericin B (2.5 µg/ml; Sigma-Aldrich A2411) in humidified air atmosphere containing 5% CO_2, at 37°C. The culture medium was changed on the first two days and every third day afterwards. Microglial cells were isolated from 21-28 day old mixed cultures by mild trypsinization. In some experiments, microglia were isolated from P8 mice using anti-CD11b conjugated magnetic microbeads (Miltenyi Biotec 130-093-634) and magnetic-activated cell sorting (MACS), according to the manufacturer's protocol. The P8-derived cells were maintained in the presence of 10 nM Macrophage Colony-Stimulating Factor (M-CSF; Thermofisher PMC2044) until use.

HEK-microglia co-cultures and Kv2.1 construct transfections

In co-cultures used for transfection HEK293 cells were plated at 2.5×10^4 cell/cm^2 density and microglial cells were seeded on top of HEK293 cell cultures in 2.5×10^4 cell/cm^2 density a day prior to transfection. The cells were transfected with 1 μg Kv2.1-GFP, Kv2.1-Ruby2 or DNKv2.1-YFP plasmid DNA. Transfection was carried out using Lipofectamine™ 3000 Transfection Reagent (ThermoFisher Sc. L3000001) and Opti-MEM™ Media (ThermoFisher Sc. 31985-062), according to the manufacturer's instructions. In brief, 1.5 μl Lipofectamine™ 3000 reagent was mixed with 25 μl Opti-MEM ™ and 1 μg DNA was mixed with 1 μl P-3000 reagent and 25 μl Opti-MEM™. The two solutions were combined, incubated for 20 min at room temperature and the mix was added to the cells. Gene expression was evaluated the day after transfection. To label microglia, isolectin B4–Alexa 488 or 594 (Isolectin GS-IB4 From Griffonia simplicifolia, Alexa Fluor™ 488 or 594 Conjugate, ThermoFisher Sc. I21411 and I21413) was applied in 5 μg/ml during imaging sessions. Live imaging was performed in HEPES buffered ACSF (NaCl 124.5 mM, KCl 2.5 mM, glucose 10 mM, MgCl2 2 mM, CaCl2 2 mM, NaHCO3 8 mM, HEPES 20 mM) at room temperature on a Nikon A1R confocal microscope at 60× magnification (Plan Apo VC NA=1.2 WD=0.31-0.28mm FOV=215.04um). Images were analyzed using the NIS-Elements AR software.

Neuronal cultures

Primary cultures of embryonic hippocampal cells were prepared from C57Bl/6 mice on embryonic day 18, as described earlier (*74*). Briefly, cells were seeded onto poly-L-lysine coated tissue culture plates or laminin coated glass coverslips at 1×10^5 cells/cm^2 density and grown in NeuroBasal medium (ThermoFisher Sc. 21103-049) supplemented with 5% FBS (ThermoFisher Sc. 16000044), B-27™ Supplement (50×) (ThermoFisher Sc. 17504-044), GlutaMax™ Supplement (0.5 mM; ThermoFisher Sc. 35050061), gentamicin (40 μg/ml; Gentamicin Sandoz, 80 mg/ml injection), amphotericin B (2.5 μg/ml; Sigma-Aldrich A2411). Cytosine-arabinofuranoside (CAR, 10 μM; Sigma-Aldrich C1768) was added to the cultures 24-120 h after plating to limit glia growth. 48 h after CAR treatment half of the culture medium was changed to BrainPhys-SM1 medium (BrainPhys™ Neuronal Medium and SM1 Kit, Stemcell Technologies 05792) without FBS. Medium change was repeated every 3-4 days thereafter. Media of cultures treated with CAR as early as DIV1 were supplemented with astroglial conditioned media (1:1) collected from 1-2 week old primary astrocytic cultures after 72 h incubation. Primary neuronal cultures were cultivated for 7-14 days at 37 °C in 5% CO_2, 95% air atmosphere.

***In vitro* quinacrine experiments**

To monitor vesicular ATP release, neuronal cultures were incubated with 20 µM quinacrine-dihydrochloride (Sigma-Aldrich Q3251) for 20 min at 37 ºC. Live imaging was performed in HEPES buffered ACSF (NaCl 124.5 mM, KCl 2.5 mM, glucose 10 mM, $MgCl_2$ 2 mM, $CaCl_2$ 2 mM, $NaHCO_3$ 8 mM, HEPES 20 mM) at room temperature on a Nikon A1R confocal microscope at 60× magnification (Plan Apo VC NA=1.2 WD=0.31-0.28mm FOV=215.04 µm). Images were analyzed using the NIS-Elements AR software. For neuron-microglia cocultures microglial cells were seeded on top of primary neuronal cultures in 2.5 × 104 cell/cm2 density a day prior to quinacrine-loading and imaging.

Quantification of ATP

The levels of ATP was determined in culture media by using HPLC method. The primary cultures were highly

enriched in neurons, as non-neuronal cell proliferation was blocked by CAR as early as DIV1, as described above. Cell culture supernatants were collected at DIV7, 5 min after 40 mM KCl treatment, preceded by a 20 min incubation period with combinations of the following drugs: Nimodipine (20 µM; Alomone Labs N-150), Clodronate disodium (10 µM; Sigma Aldrich D4434), Omega-Agatoxin IVA (100 nM; Alomone Labs STA-500), Omega-Conotoxin GVIA (1 µM; Alomone Labs SNX-124). Media (400 µl/well) were separated into a cold Eppendorf tube which contained 50 µl of homogenization solution (0.1 M perchloric acid containing theophylline as an internal standard at 10 μM concentration). Perchloric anion from the supernatant was precipitated by 1 M potassium hydroxide, the precipitate was then removed by centrifugation. The extracted purines were kept at -20°C until analysis. The adenine nucleotides and adenosine in culture media were determined by online column switching separation using Discovery HS C18 50 x 2 mm and 150 x 2 mm columns. The flow rate of the mobile phases [“A” 10 mM potassium phosphate, 0.25 mM EDTA “B” with 0.45 mM octane sulphonyl acid sodium salt, 8% acetonitrile (v/v), 2% methanol (v/v), pH 5.2] was 350 or 450 μl/min, respectively, in a step gradient application. The enrichment and stripping flow rate of buffer [10 mM potassium phosphate, pH 5.2] was during 4 min and the total runtime was 55 min. The HPLC system used was a Shimadzu LC-20 AD Analytical & Measuring Instruments System, with an Agilent 1100 Series Variable Wavelength Detector set at 253 nm. Concentrations were calculated by a two-point calibration curve using internal standard method.

Platelet aggregation in response to P2Y12 receptor inhibition after stroke

12-14 weeks old male C57BL/6J mice were subjected to 30 min MCA occlusion and immediately after the induction of reperfusion a specific P2Y12 receptor inhibitor (PSB0739, #3983 Tocris, 15 μg in 5μl volume) or vehicle (PBS) was administered to the cisterna magna. 1 h later mice were sacrificed and venipuncture was performed from the vena cava inferior. Platelet-rich plasma samples from anticoagulated (3.8% Sodium citrate) blood samples were isolated by centrifugation (100 x g, 10 min), were plated (30 μl/ well in a 24-well plate) and incubated at 37°C for 30 min before treatment with 0.5 mM ADP for 1 h at 37°C. ADP-induced platelet activation was measured by FACS based on CD62-P and CD42d fluorescence intensity, as described earlier in (*50*, *95*). After 10 min antibody staining (CD62-P-APC, 1:400, #17-0626-80 eBioScience, CD42d-PE, 1:400, #12-0421-80 eBioScience) samples were lysed to remove any red blood cell contamination (BD FACS Lysing Solution), acquired with a BD FACSVerse instrument, and analyzed with BD FACSSuite software (BD Biosciences). Changes in CD62P mean fluorescence intensity values were determined on CD42d-positive platelets.

In vivo two-photon imaging

Animals were anaesthetized using fentanyl (100-200 µl). Cranial window (3 mm diameter) was opened on the left hemisphere above the primary somatosensory area and supplementary somatosensory area border (centered 3 mm lateral and 2 mm posterior to bregma) without hurting the dura mater. After removal of the skull bone a 3 mm and 5 mm double glass coverslip construct was fixed with 3M™ Vetbond™ tissue glue on top of the dura mater. Then a custom made metal headpiece (Femtonics Ltd., Budapest, Hungary) was fixed with dental cement on the surface of the skull. All experiments were performed on a Femto2D-DualScanhead microscope (Femtonics Ltd., Budapest, Hungary) coupled with a Chameleon Discovery laser (Coherent, Santa Clara, USA). For tDTomato electroporated animals the wavelength of the laser was set to 920 nm to measure the tdTomato and GFP signals simultaneously. For Mito-R-Geco1 mitochondrial electroporated animals the wavelength was set to 1000 nm. Following excitation the fluorescent signal was collected using a Nikon 18X water immersion objective. Data acquisition was performed by MES software (Femtonics Ltd.). Since it has recently been shown that volatile anesthetics such as isoflurane may influence microglial process motility (*71*), we used fentanyl anaesthesia for these studies, which did not block microglial responses. (Fig. S5b; median process motility observed: isoflurane 0.6 µm/min, 0.3-0.83 interquartile; fentanyl 0.6 µm/min, 0.42-0.78; urethane 0.48 µm/min, 0.36-0.84; n=153 processes from 9 animals).

To analyze contacts established by microglial processes on neuronal cell bodies and proximal dendrites, we used *in utero* tdTomato electroporated CX3CR1$^{+/GFP}$ mice. To visualize microglial processes and neuronal mitochondria simultaneously, we used Mito-R-Geco1 electroporated CX3CR1$^{+/GFP}$ mice. Galvano Z-stacks of 7 images (820x820 pixels, 5 µm step size, range=200-225 µm from pial surface) were made at every 2 or 2.5 minutes. Two-photon image sequences were exported from MES and analyzed using FIJI. Dual colour images were analyzed with the Manual Tracking plugin of FIJI. We applied a local maximum centring correction method with a search square of 5 pixels. Pixel size was 167 nm/px. Microglial process velocity was measured on time-series images acquired with 2P microscopy. Following motion correction, monocolour images from the same region of CX3CR1$^{+/GFP}$ mice taken 135 seconds apart were analyzed with the Manual Tracking plugin of FIJI. We applied a local maximum centring correction method with a search square of 5 pixels. Pixel size was 167 nm/px. Processes were included in the measurement, when they were clearly traceable for at least 10 minutes. The GCaMPf signal was imaged with the laser wavelength set to 920 nm, using the resonant scanner at 32.75 Hz. Image size was 512x488 pixels.

Immunofluorescent labeling and confocal laser scanning microscopy (CLSM)

Before the immunofluorescent staining, the 50 µm thick sections were washed in PB and Tris-buffered saline (TBS). This was followed by blocking for 1 hour in 1% human serum albumin (HSA; Sigma-Aldrich) and 0.1% Triton X-100 dissolved in TBS. After this, sections were incubated in mixtures of primary antibodies overnight at room temperature. After incubation, sections were washed in TBS and were incubated overnight at 4°C in the mixture of, all diluted in TBS. Secondary antibody incubation was followed by washes in TBS, PB, the sections were mounted on glass slides, and coverslipped with Aqua-Poly/Mount (Polysciences). Immunofluorescence was analyzed using a Nikon Eclipse Ti-E inverted microscope (Nikon Instruments Europe B.V., Amsterdam, The Netherlands), with a CFI Plan Apochromat VC 60X oil immersion objective (numerical aperture: 1.4) and an A1R laser confocal system. We used 405, 488, 561 and 647 nm lasers (CVI Melles Griot), and scanning was done in line serial mode. Image stacks were obtained with NIS-Elements AR software and deconvolved using Huygens Professional software (www.svi.nl). For primary and secondary antibodies used in this study, please see Supplementary Table 3.

Quantitative analysis of CLSM data

Quantitative analysis of each dataset was performed by at least two observers, who were blinded to the origin of the samples, the experiments and did not know of each other's results. For the analysis of somatic junction prevalence, confocal stacks with double immunofluorescent labeling (cell type-marker and microglia) were acquired from at least three different regions of mouse cortex. All labeled and identified cells were counted, when the whole cell body was located within the Z-stack. A somata was considered to be contacted by microglia, when a microglial process clearly touched it.

For the analysis of synaptic contact prevalence, confocal stacks with triple immunofluorescent labeling (pre- and postsynaptic markers and microglia) were analyzed in an unbiased, semi-automatic method. First, the two channels representing the pre- and postsynaptic markers were exported from a single image plane. The channels were thresholded automatically in FIJI, the „fill in holes" and „erode" binary processes applied. After automatic particle tracking, synapses were identified where presynaptic puncta touched postsynaptic ones. From these identified points we selected 200/animal in a systematic random manner. After this, the corresponding synapses were found again in the original Z-stacks. A synapse was considered to be contacted by microglia, when a microglial process was closer than 200 nm (4 pixels on the images).

To measure the distribution of Kv2.1 and Kv2.1 labeling relative to microglial processes, confocal stacks were exported into single-channel TIFF-series. Identical measuring frames (1.32 μm^2) were placed randomly along the surface of pyramidal cells and integrated Kv2.1

fluorescent density was measured in each frame in FIJI. Afterwards, frames containing microglial contacts were identified (“contact” group) and compared with frames not containing microglial processes (“non-contact” group).

For the measurements of mitochondrial fragmentation, we used tissue from mice that were sacrificed 4 hours after a one hour-long unilateral MCAo. Confocal stacks with double immunofluorescent labeling (Kv2.1 and TOM20) were taken from the penumbra and the corresponding contralateral region. We used the Kv2.1 labeling to trace neuronal cell bodies as regions of interest (ROI). Every cell was counted once using the confocal plane containing its largest cross-section. Within the ROIs TOM20 labeling was investigated with FIJI: after automatic thresholding, we ran the ‘Analyze Particles’ command to obtain the area and the major axis of individual somatic mitochondria.

For the analysis of Kv2.1 clusters, individual cells were measured by using the confocal Z-plane containing the largest cross-section of the cell body. The intensity profile of Kv2.1 labeling was plotted using FIJI. A cluster was identified when at least three adjacent pixels’ intensity was more than 25 grayscale values (10% of an 8-bit image) larger than the average fluorescent intensity of that particular cells Kv2.1 labeling.

Microglial process coverage was measured on CLSM Z-stacks acquired with a step size of 300 nm. On single-channel images, Kv2.1-positive cells were selected randomly, the cell bodies of which were fully included in the captured volume. The surface of these cells was calculated by measuring the circumference of the soma on every section multiplied by section thickness. The length of microglial process contacts was measured likewise.

TOM20 and vesicular nucleotide transporter (vNUT) fluorescent intensity profiles were analyzed using a semi-automatic method. Confocal stacks with triple immunofluorescent labeling (microglia, Kv2.1 and TOM20/vNUT) were collected. The section containing the largest cross-section of a pyramidal cell was used to trace the cell membrane according to

Kv2.1-labeling. This contour was then expanded and narrowed by 0.5 µm to get an extracellular and an intracellular line, respectively. The intensity of fluorescent labeling was analyzed along these lines. After normalizing and scaling, microglial contact was identified where microglial fluorescent intensity was over 20% of total, for at least 500 nm. Then the contact area was extended 500-500 nm on both sides, and TOM20/vNUT fluorescent intensity within these areas was measured for “contact” value.

3-dimensional reconstruction of CLSM and 2P imaging stacks was performed using the IMOD software package (*96*).

STORM super-resolution imaging

Free-floating brain sections were blocked with 2% normal donkey serum followed by immunostaining with rabbit anti-P2Y12R and mouse anti-Kv2.1 antibodies, followed by anti-rabbit Alexa 647 and anti-mouse Alexa 594 secondary antibodies. Sections were mounted onto #1.5 borosilicate coverslips and covered with imaging medium containing 5% glucose, 0.1 M mercaptoethylamine, 1 mg/ml glucose oxidase, and catalase (Sigma, 1500 U/ml) in Dulbecco’s PBS (Sigma), immediately before imaging (*97*). STORM imaging was performed for P2Y12R (stimulated by a 647 nm laser) by using a Nikon N-STORM C2+ super-resolution system that combines ‘Stochastic Optical Reconstruction Microscopy’ technology and Nikon’s Eclipse Ti research inverted microscope to reach a lateral resolution of 20 nm and axial resolution of 50 nm (*29*, *98*). Imaging was performed using the NIS-Elements AR 4.3 with N-STORM 3.4 software, and we used VividSTORM open-source software (*98*). Molecule lists were exported from NIS in txt format, and the three image planes of the ics-ids file pairs from the deconvolved confocal stacks matching the STORM volume were converted to the ome-tiff format using FIJI software. Confocal and corresponding STORM images were fitted in VividSTORM. Localization points exceeding a photon count of 2000 were counted as specific superresolution localization points. Local density filter (10 neighbours within 150 nm for P2Y12R and Iba1, and 5 neighbours within 150 nm for Kv2.1) and Z-filter (±300 nm from focal plane) was applied to the localization points.

Pre-embedding immunoelectron microscopy

After extensive washes in PB and 0.05 M TBS sections were blocked in 1% HSA in TBS. Then, they were incubated in primary antibodies (Supplementary Table 3) diluted in TBS containing 0.05% sodium azide for 2-3 days. After repeated washes in TBS, the sections were incubated in blocking solution (Gel-BS) containing 0.2% cold water fish skin gelatine and 0.5% HSA in TBS for 1 h. Next, sections were incubated in gold-conjugated or biotinylated secondary antibodies (Supplementary Table 3) diluted in Gel-BS overnight. After extensive washes in TBS the sections were treated with 2% glutaraldehyde in 0.1 M PB for 15 min to fix the gold particles into the tissue. This was occasionally followed by incubation in avidin–biotinylated horseradish peroxidase complex (Elite ABC; 1:300; Vector Laboratories) diluted in TBS for 3 h at room temperature or overnight at 4°C. The immunoperoxidase reaction was developed using 3,3-diaminobenzidine (DAB; Sigma-Aldrich) as chromogen. To enlarge immunogold particles, sections were incubated in silver enhancement solution (SE-EM; Aurion) for 40-60 min at room temperature. The sections were then treated with 1% (for electron tomography) or 0.5% OsO4 in 0.1 M PB, at room temperature (for electron tomography) or on ice, dehydrated in ascending alcohol series and in acetonitrile and embedded in Durcupan (ACM; Fluka). During dehydration, the sections were treated with 1% uranyl acetate in 70% ethanol for 20 min. For electron microscopic analysis, tissue samples from the CA1 area of dorsal hippocampus/somatosensory cortex (S1) were glued onto Durcupan blocks. Consecutive 70 nm thick (for conventional electron microscopic analysis) or 150 nm thick (for electron tomography) sections were cut using an ultramicrotome (Leica EM UC6) and picked up on Formvar-coated single-slot grids. Ultrathin sections for conventional electron microscopic analysis were examined in a Hitachi 7100 electron microscope equipped with a Veleta CCD camera (Olympus Soft Imaging Solutions, Germany). 150 nm thick electron tomography sections were examined in FEI Tecnai Spirit G2 BioTwin TEM equipped with an Eagle 4k HS camera.

Electron tomography

For the electron tomographic investigation, we used 150 nm thick sections from the hippocampal CA1 region from the anti-P2Y12R immunogold stained material (see: "Pre-embedding immunoelectron-microscopy"). Before electron tomography, serial sections on single-slot copper grids were photographed with a Hitachi H-7100 electron microscope and a Veleta CCD camera. After this, grids were put on drops of 10% HSA in TBS for 10 minutes, dipped in distilled water (DW), put on drops of 10 nm gold conjugated Protein-A (Cytodiagnostics #AC-10-05) in DW (1:3), and washed in DW. Finally, we deposited 5 nm thick layers of carbon on both sides of the grids. Electron tomography was performed using a Tecnai T12 BioTwin electron microscope equipped with a computer-controlled precision stage (CompuStage, FEI). Acquisition was controlled via the Xplore3D software (FEI). Regions of interest were pre-illuminated for 4-6 minutes to prevent further shrinkage. Dual-axis tilt series were collected at 2 degree increment steps between -65 and +65 degrees at 120 kV acceleration voltage and 23000x magnification with -1.6 – -2 μm objective lens defocus. Reconstruction was performed using the IMOD software package (*96*). Isotropic voxel size was 0.49 nm in the reconstructed volumes. After combining the reconstructed tomograms from the two axes, the nonlinear anisotropic diffusion filtering algorithm was applied to the volumes. Segmentation of different profiles has been performed on the virtual sections using the 3Dmod software, and measurements were done on the scaled 3D models.

Analysis of the connection between membrane distance and P2Y12R density was carried out by investigating all points of the microglial membrane facing neuronal soma, using reconstructed 3D models. Coordinates of the points of neuronal membrane, soma-facing microglial membrane and P2Y12R labeling gold particles were exported using IMOD. For every single point of microglial membrane, the lowest distance to the neuronal membrane and the number of P2Y12R labeling gold particles within 40 nm was calculated with a unique algorithm running in program R (The R Foundation). Since neuronal junctions established by microglial processes are dynamic, a strong linear correlation can not be expected, therefore statistical analysis was carried out by dividing data into two groups. In the analyzed tomograms the average distance between neuronal somatic membranes and facing microglial membranes was 13.06 nm, which we used as demarcation point.

Analysis of P2Y12R density along different surfaces of microglial processes was done using reconstructed 3D models. We identified segments of microglial membranes facing (running parallel with) different neuronal membranes. These segments were grouped depending on opposing neuronal profiles (e.g neuronal soma or other neuronal parts). Using IMOD, the surfaces of microglial profiles were measured and gold particles were assigned to the closest membrane part. Due to different labeling density and penetration differences, we only performed pairwise comparisons between ‘somatic’ and ‘non-somatic’ microglial membranes within the same microglial processes. Only those gold particles were counted that localized within 40 nm of the microglial membrane.

In vitro nicotinamide adenine dinucleotide (NADH) imaging

Mice were anaesthetized by inhalation of halothane, and following decapitation 200 µm thick coronal slices were prepared from the somatosensory and visual cortex with a vibrating blade microtome (Microm HM 650 V) immersed in slicing solution containing (in mM): 130 NaCl, 3.5 KCl, 1 NaH2PO4, 24 NaHCO3, 1 CaCl2, 3 MgSO4, 10 D(+)-glucose, saturated with 95% O2 and 5% CO2. The solution used during experiments was identical to the slicing solution, except it contained 3 mM CaCl2 and 1.5 mM MgSO4. Experiments were carried out less than 4 hours after slicing. During image acquisition slices were kept at ~36˚C. Imaging with multiphoton excitation was performed using a Zeiss LSM 7MP scanning microscope (Carl Zeiss, Germany) through a 40X water-immersion objective (W-Plan, NA 1.0, Carl Zeiss). To acquire simultaneous excitation of GFP and NADH autofluorescence of acute brain slices we used two single wavelength mode-locked Ti:sapphire lasers the beams of which were coupled to each other by a dichroic beam splitter (t810lpxr, Chroma Technology Corp, USA). One of our lasers (MaiTai DeepSee, Spectra-Physics, Santa Clara, USA) exciting GFP operated at 885 nm, while our second laser (FemtoRose 100 TUN, R&D Ultrafast Lasers, Hungary) exciting NADH had an operation wavelength of 750 nm. Both laser systems delivered ~100 fs pulses at ~80 MHz and ~76 MHz repetition rate, respectively. A total average laser power of 16-18 mW was measured after the objective during imaging. Time-lapse images (1024x1024 pixels) were collected continuously for up to 55 minutes with 30.98 seconds frame scan time. Emission filters were chosen to separate intrinsic NADH fluorescence (ET460/50m, Chroma Technology Corp, USA) from GFP fluorescence (ET525/50m, Chroma Technology Corp, USA). Time lapse images were processed and analyzed in FIJI (ImageJ, NIH) software. As a first step images were spatial filtered (mean filter smooth with 1 pixel diameter) and corrected for contrast. To remove jitter in image series stabilization was applied with a FIJI plugin (K. Li, "The image stabilizer plugin for ImageJ," http://www.cs.cmu.edu/ ~kangli/code/Image_Stabilizer.html, February, 2008). Analysis and quantification of NADH fluorescence was carried out in manually selected areas of compartments of cell bodies at microglial contact site.

In vivo widefield calcium imaging

In vivo widefield calcium imaging was performed as previously described in detail (*99*). In brief, as an optogenetic calcium-reporter mouse strain, C57BL/6J-Tg(Thy1-GCaMP6s)GP4.12Dkim/J (*87*) heterozygous mice were bred at the Institute for Stroke and Dementia Research, Munich. The skin covering the skull and the underlying connective tissue were removed in head-fixed mice and a layer of transparent dental cement was distributed on the window area and covered with a coverslip. Afterwards, the mice were allowed to recover from the surgery for more than 48 h before the first image acquisition. For image acquisition, mice were injected with 0.05 mg/kg bodyweight of medetomidine intraperitoneally 5 minutes prior to inducing inhalation anesthesia with a mixture of 5% isoflurane in 70% nitrous oxide and 30% oxygen. After 70 seconds, the animals were fixed in a stereotactic frame, the dose of isoflurane was decreased to 1.5% for 140 seconds and finally decreased to 0.75% for 4 minutes to maintain steady-state before data-acquisition. *In vivo* widefield calcium imaging was performed on a custom-built imaging setup described in (*99*). This setup allowed widefield imaging through the chronic window on top of the skull into the cortex of both forebrain hemispheres by covering a field-of-view of 12x12 mm, corresponding to an image matrix of 330x330 pixels. Image acquisition was conducted for 29 minutes (44 x 1000 frames, immediately after MCAo induction, starting 60 min after injection of PSB) or 4 minutes (6 x 1000 frames, baseline acquisition, starting 60 min after injection of PSB and after 120 min reperfusion, respectively). After the imaging session, anesthesia was terminated by intraperitoneally injecting the mice with 0.1 mg/kg bodyweight Atipamezole. During all anesthetized procedures body temperature was maintained using a feedback-controlled heating system. After end of surgeries animals were put in a heating chamber until they had recovered from anesthesia. Post-surgery analgesia and sedation protocols were conducted in accordance with approved protocols by the governmental committee.

Images of every acquisition were masked in a two-step procedure. First, a general mask was applied to exclude lateral cortical areas, which were out of focus due to the curvature of the cortical surface as described in (*99*). Second, an individual mask was computed to exclude all pixels, in which the calcium signal was saturated due to autofluorescence, as occurring in areas affected by the infarct (*99*). Both, the general and the individual masks were combined for every acquisition.

To characterize changes in the cortical network after stroke, functional connectivity was computed between pairs of ROIs, representing functional cortical areas, previously defined (*99*). Functional connectivity was calculated as the Fisher z-transformed Pearson-moment correlation between the ROI signal time-courses. The average connectivity scores were calculated within each group (PSB-treated and control group), and the difference between groups was depicted for all ROI pairs in a heatmap.

For seed-based functional connectivity analysis, connectivity scores were calculated in the same way but between a selected ROI in the right hindlimb sensory area (rHLs) and the signal time series of all pixels on the cortical surface included in the combined general and individual masks. In order to quantify connectivity change of the rHLs after stroke, the connectivity scores were normalized by dividing through the connectivity scores resulting in the baseline condition. Results were visualized as topographical maps of all brain pixel.

Overall functional connectivity alterations due to treatment of the mice with PSB(naïve and stroke) were assessed by computing the global connectivity (GC) (*100*, *101*) for each pixel inside the combined general and individual mask. For a given pixel, GC was calculated by calculating the functional connectivity with each other pixel inside the mask, followed by averaging across the resulting connectivity scores. In order to assess treatment effects, GC scores were averaged pixel-wise within group (PSB and control group). The difference between groups was then visualized as topographical map of all brain pixels.

To compare the extent of GC dropdown between PSB and control treated animals after stroke, the sum of all pixels with a moderate GC (i.e. global connectivity less than 0.6 according to (*102*)) was calculated for every mouse. The mean area of each group was contoured within the GC map and the area was assessed quantitatively per animal and compared between the groups.

To represent the non-functionality of cortical tissue during the occlusion of the middle cerebral artery, the number of saturated pixels during the occlusion was calculated. During the occlusion, cortical spreading depressions (CSDs) appeared. Given the high degree of neuronal activation within areas covered by these waves, the high amplitude of the Ca^{2+} derived signal caused saturation in these areas. Therefore, we quantified the spatial extent of CSDs by counting the saturated pixels during these waves. The start- and end-time of every cortical wave were defined as first appearance of saturated pixels and the full disappearance of saturated pixels. The absolute maximum spatial extent of every cortical wave was identified and used to align the individual cortical waves of all animals. The area of saturated pixels was then acquired for every CSD wave for every animal atthe endpoint of the shortest wave (which ended 37 seconds after the aligned absolute maximum). The area of saturated pixels was groupwise depicted as overlay of the area of every CSD wave upon the general mask.

Statistical analysis

All quantitative assessment was performed in a blinded manner and based on power calculation wherever it was possible. Based on the type and distribution of data populations (examined with Shapiro-Wilks W test) we applied appropriate statistical tests: in case of two independent groups of data unpaired t-test or Mann Whitney U-test, for two dependent groups of data Wilcoxon signed-rank test, for multiple comparisons one-way ANOVA (with Tukey's test) or Kruskal-Wallis test was used. Statistical analysis was performed with the Statistica 13.4.0.14 package (TIBCO), differences with $p<0.05$ were considered significant throughout this study.

References

1. M. S. Thion, F. Ginhoux, S. Garel, Microglia and early brain development: An intimate journey. *Science*. **362**, 185–189 (2018).
2. K. Kierdorf, M. Prinz, Microglia in steady state. *J. Clin. Invest.* **127**, 3201–3209 (2017).
3. Y. Zhan *et al.*, Deficient neuron-microglia signaling results in impaired functional brain connectivity and social behavior. *Nat. Neurosci.* **17**, 400–6 (2014).
4. M. W. Salter, B. Stevens, Microglia emerge as central players in brain disease. *Nat. Med.* **23**, 1018–1027 (2017).
5. W. M. Song, M. Colonna, The identity and function of microglia in neurodegeneration. *Nat. Immunol.* **19**, 1048–1058 (2018).
6. D. Davalos *et al.*, ATP mediates rapid microglial response to local brain injury in vivo. *Nat. Neurosci.* **8**, 752–8 (2005).
7. A. Nimmerjahn, Resting Microglial Cells Are Highly Dynamic Surveillants of Brain Parenchyma in Vivo. *Science (80-.).* **308**, 1314–1318 (2005).
8. Y. Wu, L. Dissing-Olesen, B. A. MacVicar, B. Stevens, Microglia: Dynamic Mediators of Synapse Development and Plasticity. *Trends Immunol.* **36**, 605–613 (2015).
9. L. Weinhard *et al.*, Microglia remodel synapses by presynaptic trogocytosis and spine head filopodia induction. *Nat. Commun.* **9**, 1228 (2018).
10. J. M. Cioni, M. Koppers, C. E. Holt, Molecular control of local translation in axon development and maintenance. *Curr. Opin. Neurobiol.* (2018), , doi:10.1016/j.conb.2018.02.025.
11. T. Misgeld, T. L. Schwarz, Mitostasis in Neurons: Maintaining Mitochondria in an Extended Cellular Architecture. *Neuron*. **96** (2017), pp. 651–666.
12. M. Terenzio, G. Schiavo, M. Fainzilber, Compartmentalized Signaling in Neurons: From Cell Biology to Neuroscience. *Neuron*. **96**, 667–679 (2017).
13. A. Holtmaat, K. Svoboda, Experience-dependent structural synaptic plasticity in the mammalian brain. *Nat. Rev. Neurosci.* **10**, 759–759 (2009).
14. J. Aarum, K. Sandberg, S. L. B. Haeberlein, M. A. A. Persson, Migration and differentiation of neural precursor cells can be directed by microglia. *Proc. Natl. Acad. Sci.* **100**, 15983–15988 (2003).
15. M. Ueno *et al.*, Layer V cortical neurons require microglial support for survival during postnatal development. *Nat. Neurosci.* **16**, 543–551 (2013).
16. J. L. Marín-Teva, M. A. Cuadros, D. Martín-Oliva, J. Navascués, Microglia and neuronal cell death. *Neuron Glia Biol.* **7**, 25–40 (2011).
17. A. Sierra *et al.*, Surveillance, Phagocytosis, and Inflammation: How Never-Resting Microglia Influence Adult Hippocampal Neurogenesis. *Neural Plast.* **2014**, 1–15

(2014).
18. L. Fourgeaud *et al.*, TAM receptors regulate multiple features of microglial physiology. *Nature*. **532**, 240–244 (2016).
19. H. Wake, A. J. Moorhouse, S. Jinno, S. Kohsaka, J. Nabekura, Resting microglia directly monitor the functional state of synapses in vivo and determine the fate of ischemic terminals. *J. Neurosci.* (2009), doi:10.1523/JNEUROSCI.4363-08.2009.
20. E. Deutsch *et al.*, Kv2.1 cell surface clusters are insertion platforms for ion channel delivery to the plasma membrane. *Mol. Biol. Cell*. **23**, 2917–2929 (2012).
21. D. P. Mohapatra, K.-S. Park, J. S. Trimmer, Dynamic regulation of the voltage-gated Kv2.1 potassium channel by multisite phosphorylation. *Biochem. Soc. Trans.* **35**, 1064–1068 (2007).
22. M. Kirmiz, N. C. Vierra, S. Palacio, J. S. Trimmer, Identification of VAPA and VAPB as Kv2 Channel-Interacting Proteins Defining Endoplasmic Reticulum–Plasma Membrane Junctions in Mammalian Brain Neurons. *J. Neurosci.* **38**, 7562–7584 (2018).
23. B. Jiang, X. Sun, K. Cao, R. Wang, Endogenous Kv channels in human embryonic kidney (HEK-293) cells. *Mol. Cell. Biochem.* **238**, 69–79 (2002).
24. A. Menéndez-Méndez *et al.*, Specific Temporal Distribution and Subcellular Localization of a Functional Vesicular Nucleotide Transporter (VNUT) in Cerebellar Granule Neurons. *Front. Pharmacol.* **8**, 951 (2017).
25. R. D. Fields, Nonsynaptic and nonvesicular ATP release from neurons and relevance to neuron-glia signaling. *Semin. Cell Dev. Biol.* **22**, 214–9 (2011).
26. S. E. Haynes *et al.*, The P2Y12 receptor regulates microglial activation by extracellular nucleotides. *Nat. Neurosci.* **9**, 1512–1519 (2006).
27. Y. Zhang *et al.*, An RNA-Sequencing Transcriptome and Splicing Database of Glia, Neurons, and Vascular Cells of the Cerebral Cortex. *J. Neurosci.* **34**, 11929–11947 (2014).
28. O. Butovsky *et al.*, Identification of a unique TGF-β–dependent molecular and functional signature in microglia. *Nat. Neurosci.* **17**, 131–143 (2014).
29. B. Dudok *et al.*, Cell-specific STORM super-resolution imaging reveals nanoscale organization of cannabinoid signaling. *Nat. Neurosci.* **18**, 75–86 (2015).
30. I. D. Campbell, M. J. Humphries, Integrin Structure, Activation, and Interactions. *Cold Spring Harb. Perspect. Biol.* **3**, a004994–a004994 (2011).
31. H. Akiyama, P. L. McGeer, Brain microglia constitutively express beta-2 integrins. *J. Neuroimmunol.* **30**, 81–93 (1990).
32. F. E. McCann *et al.*, The size of the synaptic cleft and distinct distributions of filamentous actin, ezrin, CD43, and CD45 at activating and inhibitory human NK cell immune synapses. *J. Immunol.* **170**, 2862–70 (2003).
33. G. Csordás, D. Weaver, G. Hajnóczky, Endoplasmic Reticulum-Mitochondrial Contactology: Structure and Signaling Functions. *Trends Cell Biol.* **28**, 523–540 (2018).
34. U. Ahting *et al.*, The TOM core complex: the general protein import pore of the outer membrane of mitochondria. *J. Cell Biol.* **147**, 959–68 (1999).
35. A. Sugiura, G.-L. McLelland, E. A. Fon, H. M. McBride, A new pathway for mitochondrial quality control: mitochondrial-derived vesicles. *EMBO J.* **33**, 2142–56 (2014).
36. V. Soubannier *et al.*, A vesicular transport pathway shuttles cargo from mitochondria to lysosomes. *Curr. Biol.* (2012), doi:10.1016/j.cub.2011.11.057.
37. T. Ho *et al.*, Vesicular expression and release of ATP from dopaminergic neurons of

the mouse retina and midbrain. *Front. Cell. Neurosci.* **9**, 389 (2015).

38. Y. Moriyama, M. Hiasa, S. Sakamoto, H. Omote, M. Nomura, Vesicular nucleotide transporter (VNUT): appearance of an actress on the stage of purinergic signaling. *Purinergic Signal.* **13**, 387–404 (2017).
39. A. M. Brennan, J. A. Connor, C. W. Shuttleworth, NAD(P)H Fluorescence Transients after Synaptic Activity in Brain Slices: Predominant Role of Mitochondrial Function. *J. Cereb. Blood Flow Metab.* **26**, 1389–1406 (2006).
40. C. W. Shuttleworth, A. M. Brennan, J. A. Connor, NAD(P)H fluorescence imaging of postsynaptic neuronal activation in murine hippocampal slices. *J. Neurosci.* **23**, 3196–208 (2003).
41. Y. Imura *et al.*, Microglia release ATP by exocytosis. *Glia*. **61**, 1320–1330 (2013).
42. X. Zhang, Y. Chen, C. Wang, L.-Y. M. Huang, Neuronal somatic ATP release triggers neuron-satellite glial cell communication in dorsal root ganglia. *Proc. Natl. Acad. Sci.* **104**, 9864–9869 (2007).
43. C. Trueta, B. Méndez, F. F. De-Miguel, Somatic Exocytosis of Serotonin Mediated by L-Type Calcium Channels in Cultured Leech Neurones. *J. Physiol.* **547**, 405–416 (2003).
44. G. Szalay *et al.*, Microglia protect against brain injury and their selective elimination dysregulates neuronal network activity after stroke. *Nat. Commun.* **7**, 11499 (2016).
45. M. Kislin *et al.*, Reversible Disruption of Neuronal Mitochondria by Ischemic and Traumatic Injury Revealed by Quantitative Two-Photon Imaging in the Neocortex of Anesthetized Mice. *J. Neurosci.* **37**, 333–348 (2017).
46. H. Misonou, Calcium- and Metabolic State-Dependent Modulation of the Voltage-Dependent Kv2.1 Channel Regulates Neuronal Excitability in Response to Ischemia. *J. Neurosci.* **25**, 11184–11193 (2005).
47. B. O'Rourke, Mitochondrial ion channels. *Annu. Rev. Physiol.* **69**, 19–49 (2007).
48. J. O. Onukwufor, D. Stevens, C. Kamunde, Bioenergetic and volume regulatory effects of mitoKATP channel modulators protect against hypoxia-reoxygenation-induced mitochondrial dysfunction. *J. Exp. Biol.* **219**, 2743–51 (2016).
49. F. Orsini *et al.*, Mannose-Binding Lectin Drives Platelet Inflammatory Phenotype and Vascular Damage After Cerebral Ischemia in Mice via IL (Interleukin)-1α. *Arterioscler. Thromb. Vasc. Biol.* **38**, 2678–2690 (2018).
50. K. Bekő *et al.*, Contribution of platelet P2Y12 receptors to chronic Complete Freund's adjuvant-induced inflammatory pain. *J. Thromb. Haemost.* **15**, 1223–1235 (2017).
51. Y. Li, X.-F. Du, C.-S. Liu, Z.-L. Wen, J.-L. Du, Reciprocal regulation between resting microglial dynamics and neuronal activity in vivo. *Dev. Cell.* **23**, 1189–202 (2012).
52. R. D. Stowell *et al.*, Cerebellar microglia are dynamically unique and survey Purkinje neurons in vivo. *Dev. Neurobiol.* **78**, 627–644 (2018).
53. C. N. Hall, M. C. Klein-Flügge, C. Howarth, D. Attwell, Oxidative phosphorylation, not glycolysis, powers presynaptic and postsynaptic mechanisms underlying brain information processing. *J. Neurosci.* **32**, 8940–51 (2012).
54. T. E. Gunter, L. Buntinas, G. Sparagna, R. Eliseev, K. Gunter, Mitochondrial calcium transport: mechanisms and functions. *Cell Calcium*. **28**, 285–296 (2000).
55. N. S. Chandel, Mitochondria as signaling organelles. *BMC Biol.* **12**, 34 (2014).
56. E. I. Rugarli, T. Langer, Mitochondrial quality control: a matter of life and death for neurons. *EMBO J.* **31**, 1336–49 (2012).
57. P. D. Bhola, A. Letai, Mitochondria-Judges and Executioners of Cell Death Sentences. *Mol. Cell.* **61**, 695–704 (2016).
58. A. Kasahara, L. Scorrano, Mitochondria: from cell death executioners to regulators

of cell differentiation. *Trends Cell Biol.* **24**, 761–70 (2014).

59. G. R. Bantug *et al.*, Mitochondria-Endoplasmic Reticulum Contact Sites Function as Immunometabolic Hubs that Orchestrate the Rapid Recall Response of Memory CD8 + T Cells. *Immunity*. **48**, 542-555.e6 (2018).
60. D. Arnoult, F. Soares, I. Tattoli, S. E. Girardin, Mitochondria in innate immunity. *EMBO Rep.* **12**, 901–910 (2011).
61. A. U. Joshi, D. Mochly-Rosen, Mortal engines: Mitochondrial bioenergetics and dysfunction in neurodegenerative diseases. *Pharmacol. Res.* **138**, 2–15 (2018).
62. J. Rieusset, Mitochondria-associated membranes (MAMs): An emerging platform connecting energy and immune sensing to metabolic flexibility. *Biochem. Biophys. Res. Commun.* **500**, 35–44 (2018).
63. M. Krols *et al.*, Mitochondria-associated membranes as hubs for neurodegeneration. *Acta Neuropathol.* **131**, 505–23 (2016).
64. R. Bravo-Sagua *et al.*, Cell death and survival through the endoplasmic reticulum-mitochondrial axis. *Curr. Mol. Med.* **13**, 317–29 (2013).
65. K. A. Kasischke, Neural Activity Triggers Neuronal Oxidative Metabolism Followed by Astrocytic Glycolysis. *Science (80-.).* **305**, 99–103 (2004).
66. G.-L. McLelland, S. A. Lee, H. M. McBride, E. A. Fon, Syntaxin-17 delivers PINK1/parkin-dependent mitochondrial vesicles to the endolysosomal system. *J. Cell Biol.* **214**, 275–91 (2016).
67. V. J. J. Cadete *et al.*, Formation of mitochondrial-derived vesicles is an active and physiologically relevant mitochondrial quality control process in the cardiac system. *J. Physiol.* **594**, 5343–62 (2016).
68. L. Feinshreiber, D. Singer-Lahat, U. Ashery, I. Lotan, Voltage-gated Potassium Channel as a Facilitator of Exocytosis. *Ann. N. Y. Acad. Sci.* **1152**, 87–92 (2009).
69. P. D. Fox *et al.*, Induction of stable ER-plasma-membrane junctions by Kv2.1 potassium channels. *J. Cell Sci.* **128**, 2096–105 (2015).
70. K. M. S. O'Connell, R. Loftus, M. M. Tamkun, Localization-dependent activity of the Kv2.1 delayed-rectifier K + channel. *Proc. Natl. Acad. Sci. U. S. A.* (2010), doi:10.1073/pnas.1003028107.
71. C. Madry *et al.*, Microglial Ramification, Surveillance, and Interleukin-1β Release Are Regulated by the Two-Pore Domain K + Channel THIK-1. *Neuron*. **97**, 299-312.e6 (2018).
72. Y. Hayashi *et al.*, The intrinsic microglial molecular clock controls synaptic strength via the circadian expression of cathepsin S. *Sci. Rep.* **3**, 2744 (2013).
73. G. O. Sipe *et al.*, Microglial P2Y12 is necessary for synaptic plasticity in mouse visual cortex. *Nat. Commun.* **7**, 10905 (2016).
74. R. Fekete *et al.*, Microglia control the spread of neurotropic virus infection via P2Y12 signalling and recruit monocytes through P2Y12-independent mechanisms. *Acta Neuropathol.* **136**, 461–482 (2018).
75. G. Marchal *et al.*, Prolonged persistence of substantial volumes of potentially viable brain tissue after stroke: a correlative PET-CT study with voxel-based data analysis. *Stroke*. **27**, 599–606 (1996).
76. J. C. Baron, M. E. Moseley, For how long is brain tissue salvageable? Imaging-based evidence. *J. Stroke Cerebrovasc. Dis.* **9**, 15–20 (2000).
77. A. Bunevicius, H. Yuan, W. Lin, The Potential Roles of 18 F-FDG-PET in Management of Acute Stroke Patients. *Biomed Res. Int.* **2013**, 1–14 (2013).
78. C. Iadecola, J. Anrather, The immunology of stroke: from mechanisms to translation. *Nat. Med.* **17**, 796–808 (2011).

79. G. Kato *et al.*, Microglial Contact Prevents Excess Depolarization and Rescues Neurons from Excitotoxicity. *eNeuro*. **3** (2016), doi:10.1523/ENEURO.0004-16.2016.

80. L. Shao *et al.*, Mitochondrial involvement in psychiatric disorders. *Ann. Med.* **40**, 281–295 (2008).

81. M. R. Duchen, Mitochondria, calcium-dependent neuronal death and neurodegenerative disease. *Pflugers Arch.* **464**, 111–21 (2012).

82. J. J. Neher, U. Neniskyte, G. C. Brown, Primary Phagocytosis of Neurons by Inflamed Microglia: Potential Roles in Neurodegeneration. *Front. Pharmacol.* **3** (2012), doi:10.3389/fphar.2012.00027.

83. N. C. Vierra, M. Kirmiz, D. van der List, L. F. Santana, J. S. Trimmer, Kv2.1 mediates spatial and functional coupling of L-type calcium channels and ryanodine receptors in neurons. *bioRxiv*, 702514 (2019).

84. X. Wang, C. Zhang, G. Szábo, Q.-Q. Sun, Distribution of CaMKIIα expression in the brain in vivo, studied by CaMKIIα-GFP mice. *Brain Res.* **1518**, 9–25 (2013).

85. A. H. Meyer, I. Katona, M. Blatow, A. Rozov, H. Monyer, In vivo labeling of parvalbumin-positive interneurons and analysis of electrical coupling in identified neurons. *J. Neurosci.* **22**, 7055–64 (2002).

86. G. López-Bendito *et al.*, Preferential origin and layer destination of GAD65-GFP cortical interneurons. *Cereb. Cortex*. **14**, 1122–33 (2004).

87. H. Dana *et al.*, Thy1-GCaMP6 Transgenic Mice for Neuronal Population Imaging In Vivo. *PLoS One*. **9**, e108697 (2014).

88. A. Denes, N. Humphreys, T. E. Lane, R. Grencis, N. Rothwell, Chronic Systemic Infection Exacerbates Ischemic Brain Damage via a CCL5 (Regulated on Activation, Normal T-Cell Expressed and Secreted)-Mediated Proinflammatory Response in Mice. *J. Neurosci.* **30**, 10086–10095 (2010).

89. K. L. Schaar, M. M. Brenneman, S. I. Savitz, Functional assessments in the rodent stroke model. *Exp. Transl. Stroke Med.* **2**, 13 (2010).

90. J. B. Bederson *et al.*, Rat middle cerebral artery occlusion: evaluation of the model and development of a neurologic examination. *Stroke*. **17**, 472–6 (1986).

91. A. Denes *et al.*, AIM2 and NLRC4 inflammasomes contribute with ASC to acute brain injury independently of NLRP3. *Proc. Natl. Acad. Sci.* **112**, 4050–4055 (2015).

92. B. W. McColl, H. V. Carswell, J. McCulloch, K. Horsburgh, Extension of cerebral hypoperfusion and ischaemic pathology beyond MCA territory after intraluminal filament occlusion in C57Bl/6J mice. *Brain Res.* **997**, 15–23 (2004).

93. T. Matsuda, C. L. Cepko, Electroporation and RNA interference in the rodent retina in vivo and in vitro. *Proc. Natl. Acad. Sci.* **101**, 16–22 (2004).

94. J. Wu *et al.*, Improved orange and red $Ca^2\pm$ indicators and photophysical considerations for optogenetic applications. *ACS Chem. Neurosci.* **4**, 963–72 (2013).

95. K. L. Singel *et al.*, Mitochondrial DNA in the tumour microenvironment activates neutrophils and is associated with worse outcomes in patients with advanced epithelial ovarian cancer. *Br. J. Cancer* (2019), doi:10.1038/s41416-018-0339-8.

96. J. R. Kremer, D. N. Mastronarde, J. R. McIntosh, Computer visualization of three-dimensional image data using IMOD. *J. Struct. Biol.* **116**, 71–6 (1996).

97. A. Dani, B. Huang, J. Bergan, C. Dulac, X. Zhuang, Superresolution imaging of chemical synapses in the brain. *Neuron*. **68**, 843–56 (2010).

98. L. Barna *et al.*, Correlated confocal and super-resolution imaging by VividSTORM. *Nat. Protoc.* **11**, 163–183 (2016).

99. J. V. Cramer *et al.*, In vivo widefield calcium imaging of the mouse cortex for analysis

of network connectivity in health and brain disease. *Neuroimage*. **199**, 570–584 (2019).

100. M. W. Cole, S. Pathak, W. Schneider, Identifying the brain's most globally connected regions. *Neuroimage*. **49**, 3132–48 (2010).
101. M. Rubinov, O. Sporns, Weight-conserving characterization of complex functional brain networks. *Neuroimage*. **56**, 2068–79 (2011).
102. D. Hinkle, W. Wiersma, S. Jurs, *Applied Statistics for the Behavioural Sciences* (2003).

Supplementary Material

Table S1.

Localisation point density (LP/um2)						
animal	category	mean	S.E.M.	n	comparison (Tukey's multiple comparisons test)	p-value
GCamp6-injected	contact	136.8	10.02	12	contact vs. non-contact	<0,0001
	non-contact	60.42	7.719	12	contact vs. whole microglia	<0,0001
	whole microglia	76.8	5.128	12	whole microglia vs. non-contact	0.3179
camK2A/gfp/22	contact	142.6	17.17	18	contact vs. non-contact	<0,0001
	non-contact	52.2	10.08	17	contact vs. whole microglia	0.0008
	whole microglia	76.47	6.054	18	whole microglia vs. non-contact	0.3423
gad65_3e/gfp 5.5/30	contact	81.05	15.37	11	contact vs. non-contact	0.0116
	non-contact	38.62	4.892	13	contact vs. whole microglia	0.0197
	whole microglia	41.58	7.661	13	whole microglia vs. non-contact	0.973
BAC_pva/gfp/2	contact	93.75	21.59	10	contact vs. non-contact	0.0009
	non-contact	20.03	2.746	10	contact vs. whole microglia	0.003
	whole microglia	31.17	5.736	12	whole microglia vs. non-contact	0.7957
Cluster density (cluster/um2)						
animal	category	mean	S.E.M.	n	comparison (Tukey's multiple comparisons test)	p-value
GCamp6-injected	contact	0.9705	0.084	12	contact vs. non-contact	<0,0001
	non-contact	0.4451	0.071	12	contact vs. whole microglia	0.0004
	whole microglia	0.5401	0.055	12	whole microglia vs. non-contact	0.6164
camK2A/gfp/22	contact	0.6089	0.069	18	contact vs. non-contact	0.0002
	non-contact	0.3111	0.046	18	contact vs. whole microglia	0.0031
	whole microglia	0.3673	0.02	18	whole microglia vs. non-contact	0.7007
gad65_3e/gfp 5.5/30	contact	0.368	0.072	9	contact vs. non-contact	0.4608
	non-contact	0.2659	0.052	13	contact vs. whole microglia	0.4681
	whole microglia	0.2684	0.051	14	whole microglia vs. non-contact	0.9994
BAC_pva/gfp/2	contact	0.3726	0.062	10	contact vs. non-contact	0.0107
	non-contact	0.1839	0.024	11	contact vs. whole microglia	0.0553
	whole microglia	0.2293	0.036	12	whole microglia vs. non-contact	0.7145

Table S2.

Subject	**Code**	**Gender**	**Age (years)**	**Health status**	**Survival after**	**Comorbidities**	**Cause of death**	**Tissue sample type**
Stroke patient	2011/0092	female	77	normal	2	arterial hypertension, type II diabetes, hyperthyreosis	stroke	paraffin embedded sections
Stroke patient	2003/0029	male	66	preceeding systemic inflammatory burden	1	arterial hypertension	stroke	paraffin embedded sections
Stroke patient	2014/0050	female	78	normal	1	unknown	stroke	paraffin embedded sections

Control subject	SKO3	female	59	normal	n.a.	ischemic cardiomyopathy	cardiogenic shock	free floating and paraffin sections
Control subject	SKO13	female	60	normal	n.a.	chronic bronchitis	respiratory arrest	free floating and paraffin sections
Control subject	SKO16	male	73	normal	n.a.	atherosclerosis, pneumonia	respiratory arrest	free floating and paraffin sections

Table S3.

Primary an-	host	source	catalog nr.	RRID
CB1	goat	MyBioSource	MBS422809	n.a.
CytC	mouse	BioLegend	612302	RRID:AB_315774
c-fos	guinea-pig	Synaptic Sys-	226 004	RRID:AB_2619946
CD206	rat	BioRad	MCA2235	RRID:AB_324622
CD42d	armenian	eBioScience	12-0421-80	RRID:AB_10804037
CD62-P-	mouse	eBioScience	17-0626-80	RRID:AB_11218294
Gephyrin	mouse	Synaptic Sys-	147 021	RRID:AB_2232546
GFAP	chicken	Synaptic Sys-	173 006	RRID:AB_2619873
GFP	chicken	Invitrogen	A10262	RRID:AB_2534023
Homer1	chicken	Synaptic Sys-	160 006	RRID:AB_2631222
Iba1	goat	Novusbio	NB100-1028	RRID:AB_521594
Iba1	rabbit	Wako Chemi-	019-19741	RRID:AB_839504
Kv2.1	mouse	NeuroMab	75-014	RRID:AB_10673392
Kv2.1	rabbit	Synaptic Sys-	231 002	RRID:AB_2131650
Kv2.2	rabbit	Synaptic Sys-	231 103	RRID:AB_10805652
Lamp1	rabbit	Abcam	ab24170	RRID:AB_775978
MAP2	guniea-pig	Synaptic Sys-	188 004	RRID:AB_2138181
NTPDase1	rabbit	Labome	rN1-6L	n.a.
P2Y12R	rabbit	Anaspec	AS-55042A	RRID:AB_2267540
P2Y12R	rabbit	Anaspec	AS-55043A	RRID:AB_2298886
Parvalbumin	goat	Swant	PVG 213	RRID:AB_2721207
PDGFRB	goat	R and D Sys-	AF1042	RRID:AB_2162633
Pecam1	rat	BioLegend	102501	RRID:AB_312908
RFP	rat	ChromoTek	5f8-100	RRID:AB_2336064
SMA	mouse	Abcam	ab7817	RRID:AB_262054
SMI32	mouse	Covance	SMI-32P	RRID:AB_10719742
TOM20	rabbit	Santa Cruz	sc-11415	RRID:AB_2207533

vGAT	guinea pig	Synaptic Sys-	131 004	RRID:AB_887873
vGluT1	guinea pig	Millipore	AB5905	RRID:AB_2301751
vGLuT3	guinea pig	Synaptic Sys-	135 204	RRID:AB_2619825
vNUT	guinea pig	Millipore	ABN83	n.a.
Secondary				
biotinylated	donkey	BioRad	644008	RRID:AB_619842
DyLight 405	donkey	Jackson	715-475-150	RRID:AB_2340839
Alexa 405	donkey	Jackson	711-475-152	RRID:AB_2340616
Alexa 488	donkey	Jackson	703-546-155	RRID:AB_2340376
Alexa 488	donkey	Jackson	705-546-147	RRID:AB_2340430
Alexa 488	donkey	Jackson	711-546-152	RRID:AB_2340619
CF568 anti-	donkey	Biotium	20802	RRID:AB_10853136
Alexa 594	donkey	LifeTech	A11058	RRID:AB_2534105
Alexa 594	goat	LifeTech	A11076	RRID:AB_141930
Alexa 594	donkey	LifeTech	A21203	RRID:AB_141633
Alexa 594	donkey	LifeTech	A21207	RRID:AB_141637
Alexa 594	donkey	Jackson	712-585-150	RRID:AB_2340688
Alexa 647	donkey	Jackson	705-606-147	RRID:AB_2340438
Alexa 647	donkey	Jackson	706-606-148	RRID:AB_2340477
Alexa 647	donkey	Jackson	715-605-150	RRID:AB_2340866
Alexa 647	donkey	Jackson	711-605-152	RRID:AB_2492288

Supplementary Figures

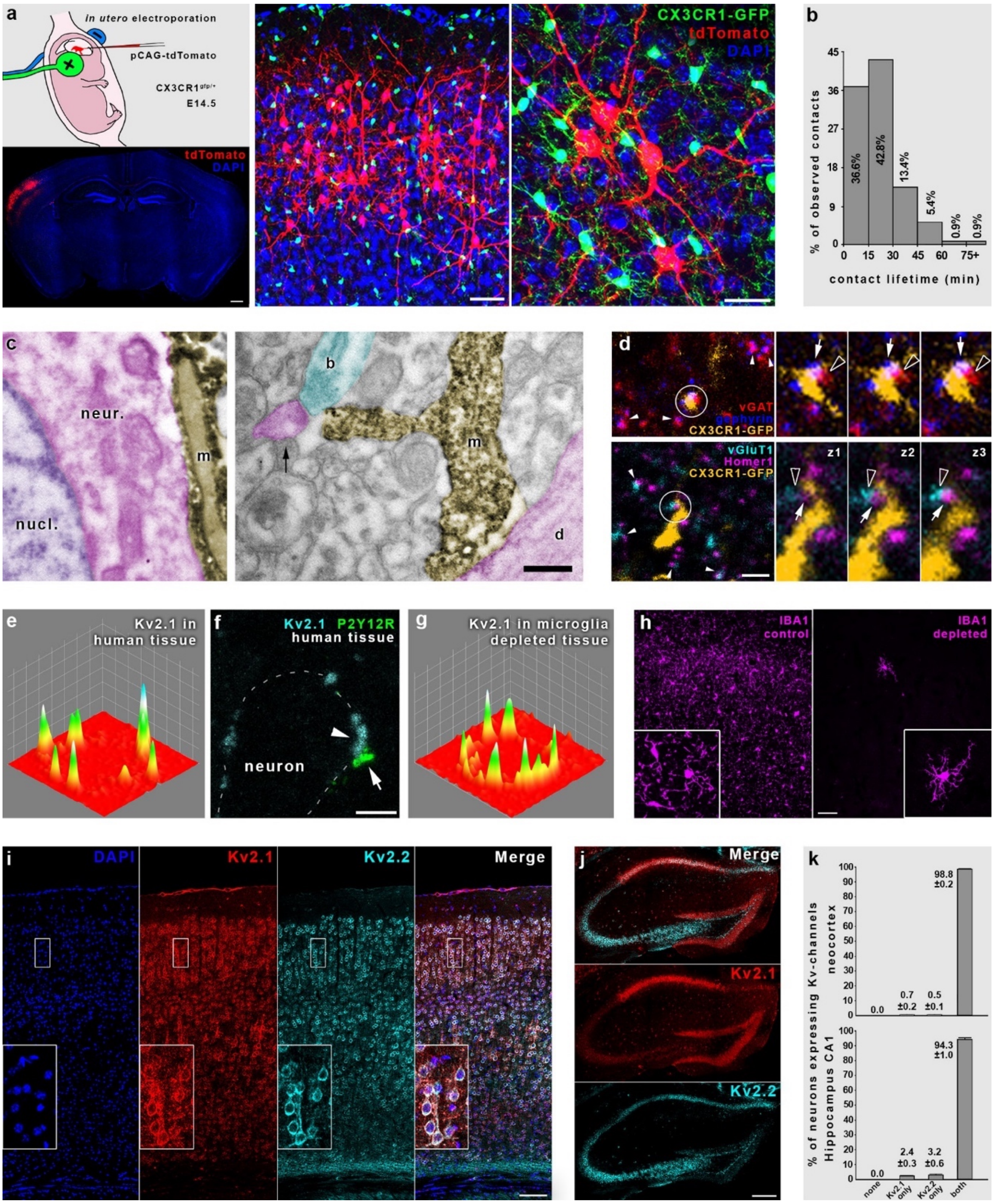
a
in utero electroporation
pCAG-tdTomato
CX3CR1gfp/+
E14.5
tdTomato
DAPI
CX3CR1-GFP
tdTomato
DAPI
b
% of observed contacts
0
9
18
27
36
45
36.6%
42.8%
13.4%
5.4%
0.9%
0.9%
0
15
30
45
60
75+
contact lifetime (min)
c
neur.
m
nucl.
b
m
d
d
vGAT
gephyrin
CX3CR1-GFP
vGluT1
Homer1
CX3CR1-GFP
z1
z2
z3
e
Kv2.1 in human tissue
f
Kv2.1 P2Y12R
human tissue
neuron
g
Kv2.1 in microglia depleted tissue
h
IBA1 control
IBA1 depleted
i
DAPI
Kv2.1
Kv2.2
Merge
j
Merge
Kv2.1
Kv2.2
k
% of neurons expressing Kv-channels
neocortex
Hippocampus CA1
0
10
20
30
40
50
60
70
80
90
100
0.0
0.7 ±0.2
0.5 ±0.1
98.8 ±0.2
0.0
2.4 ±0.3
3.2 ±0.6
94.3 ±1.0
none
Kv2.1 only
Kv2.2 only
both

Figure S1. *a) Result of CX3CR1*$^{+/GFP}$ *mouse in utero electroporation with pCAG-IRES-tdTomato. Lower left panel shows the outspread of tdTomato-positive neurons in red. Middle and right panels show the non-overlapping staining of electroporated neurons (red) and microglia (green). Cell nuclei are visible in blue. b) Distribution of microglial contact lifetimes. c) Electron microscopic images showing microglial processes (m) establishing direct contact with neuronal cell body (left, neur.), dendritic shaft (right, d) and presynaptic* *bouton (b) in mice. Microglia are visualized by immunoperoxidase reaction against Iba1. Pseudocoloring shows microglia in yellow, neuronal cell body and dendritic processes in magenta, presynaptic bouton in cyan and nucleus (nucl.) in purple. Arrow points at a dendritic spine receiving asymmetric synaptic contact. d) Microglial processes contacting cortical inhibitory and excitatory synapses. Presynaptic terminals are visible by stainings against vesicular GABA transporter (vGAT, red) and type 1 vesicular glutamate transporter (vGlut1, cyan), while postsynaptic side is characterized by stainings against gephyrin (blue) and Homer1 (magenta). White arrowheads point at colocalization of pre- and postsynaptic markers. Microglial contacts in white circles are enlarged in the panels right, with the previous and following Z-planes from the stack (Z-step = 250 nm). Empty arrowheads point at the presynaptic marker, white arrows point at the postsynaptic side. e) Heatmap shows Kv2.1 clusters of a human cortical neuron. f) CLSM image shows that a P2Y12R-labeled microglial process contacts a human cortical neuron exactly at the spot where a Kv2.1 cluster is located. g) Heatmap shows that Kv2.1-clustering of mouse cortical neurons is not affected by microglia depletion. h) CLSM images show that 3 week PLX5622-diet almost completely depleted microglia from the brain. i) CLSM images show labeling patterns of Kv2.1 and Kv2.2 in the neocortex. j) CLSM images show labeling patterns of Kv2.1 and Kv2.2 in the hippocampus. k) Percentages of neurons expressing Kv-channels in the neocortex and hippocampus. Scale bars: 500 µm on a, 50 µm on left panel of b and on h, 25 µm on right panel of b, 1 µm on c, 2 µm on d and f, 100 µm on i and j.*

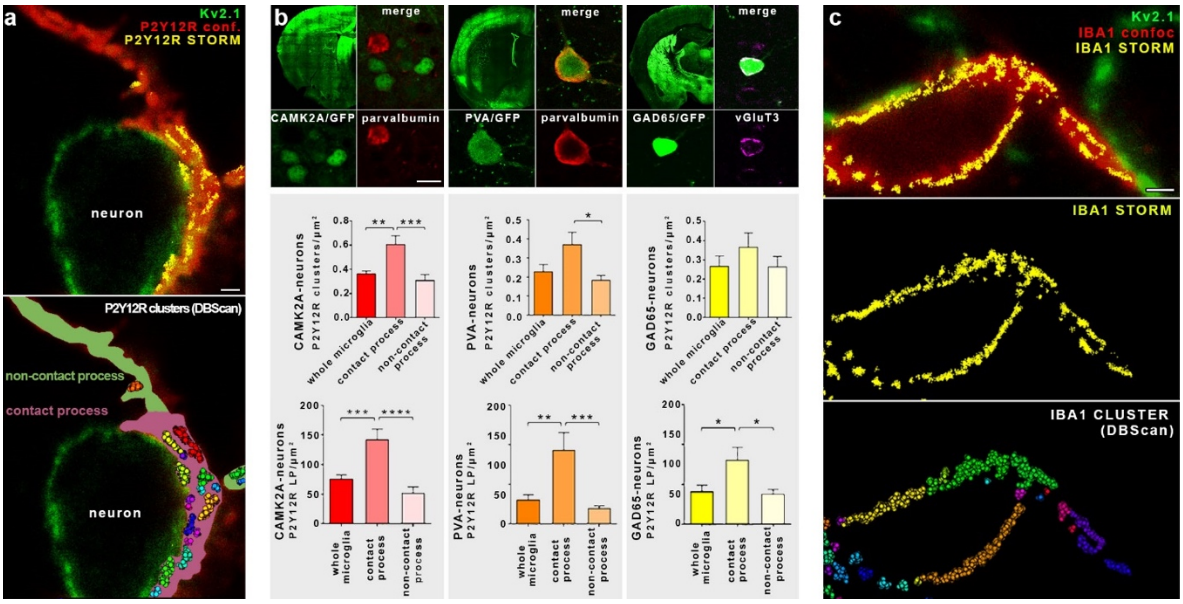
a
Kv2.1
P2Y12R conf.
P2Y12R STORM
neuron
P2Y12R clusters (DBScan)
non-contact process
contact process
neuron
b
merge
merge
merge
CAMK2A/GFP
parvalbumin
PVA/GFP
parvalbumin
GAD65/GFP
vGluT3
CAMK2A-neurons P2Y12R clusters/µm²
PVA-neurons P2Y12R clusters/µm²
GAD65-neurons P2Y12R clusters/µm²
0.8
0.6
0.4
0.2
0.0
0.5
0.4
0.3
0.2
0.1
0.0
**
***
*
whole microglia
contact process
non-contact process
CAMK2A-neurons P2Y12R LP/µm²
PVA-neurons P2Y12R LP/µm²
GAD65-neurons P2Y12R LP/µm²
200
150
100
50
0
****
c
Kv2.1
IBA1 confoc
IBA1 STORM
IBA1 STORM
IBA1 CLUSTER (DBScan)

Figure S2. *a) P2Y12R clustering differs depending on location. Microglial processes were classified depending on neuronal contacts established: contact processes are pale magenta, non-contact processes are pale green on bottom panel. b) Analysis of P2Y12R cluster and LP density on different microglial processes* *contacting distinct cell populations. Microglial contact processes on CamK2a (red) and PVA-positive cells (orange) possess significantly higher cluster density, than non-contact segments, while there is a similar trend observable in the case of GAD65-positive cells (yellow, for detailed results see Supplementary Table 1.). Contact processes had significantly higher number of P2Y12R LPs in all populations. Anti-PV and vGluT3 labelings were used to confirm cell specificity. c) Superresolution imaging of microglial Iba1 shows no clustering at somatic junctions. CLSM images show neuronal Kv2.1 (green) and a contacting microglial process made visible by Iba1-labeling (red). Iba1 (yellow) STORM-signal is overlaid and shown individually in the middle panel. Lower panel shows a homogenous distribution of Iba1 LPs using DBScan analysis. Scale bars: 1 µm on a and c, 10 µm on b. Mean+SEM is plotted.*

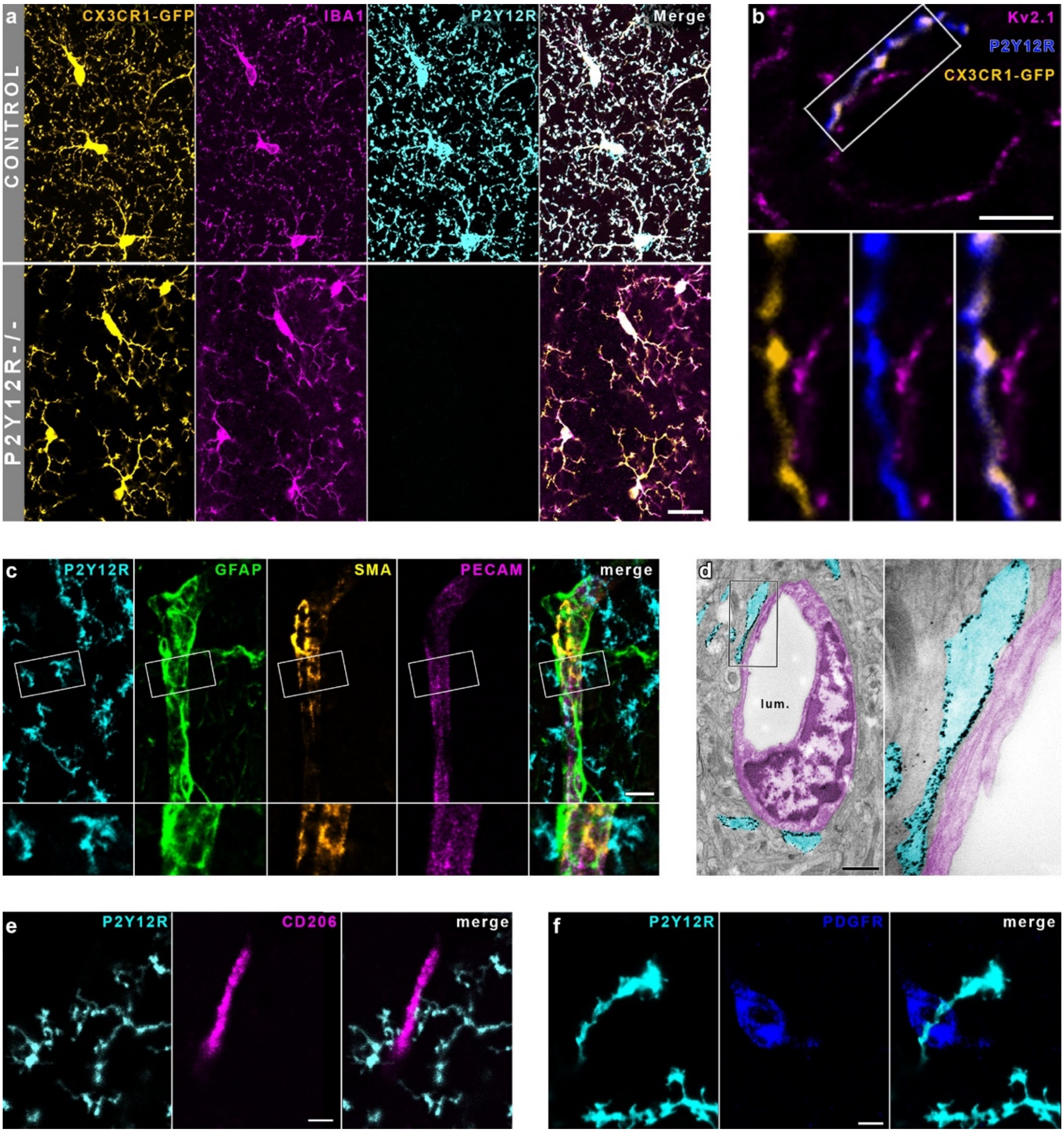
a
CX3CR1-GFP
IBA1
P2Y12R
Merge
CONTROL
P2Y12R-/-
b
Kv2.1
P2Y12R
CX3CR1-GFP
c
P2Y12R
GFAP
SMA
PECAM
merge
d
lum.
e
P2Y12R
CD206
merge
f
P2Y12R
PDGFR
merge

Figure S3. *a) CLSM images show triple immunolabeling for GFP, Iba1 and P2Y12R in CX3CR1*$^{+/GFP}$ *and CX3CR1*$^{+/GFP}$ *–P2Y12R*$^{-/-}$ *animals. b) CX3CR1-GFP and P2Y12R double positive microglial processes touch Kv2.1 clusters on neuronal somatic membrane. c) P2Y12R-positive microglial processes contact cells of the neurovascular unit. d) Transmission electron micrographs show P2Y12R-immunogold labeled microglial processes touching vascular endothelial cell. P2Y12R expression is clearly restricted to microglia. e) P2Y12R-labeled microglial processes are contacting CD206-positive perivascular macrophages (PVM). PVMs do not express P2Y12Rs. f) P2Y12R-labeled microglial processes are contacting PDGFRβ-positive pericytes. Pericytes are not expressing P2Y12Rs. Scale bars: 20 µm on a, 4 µm on b, 10 µm on c, 1 µm on d, 5 µm on e, 3 µm on f.*

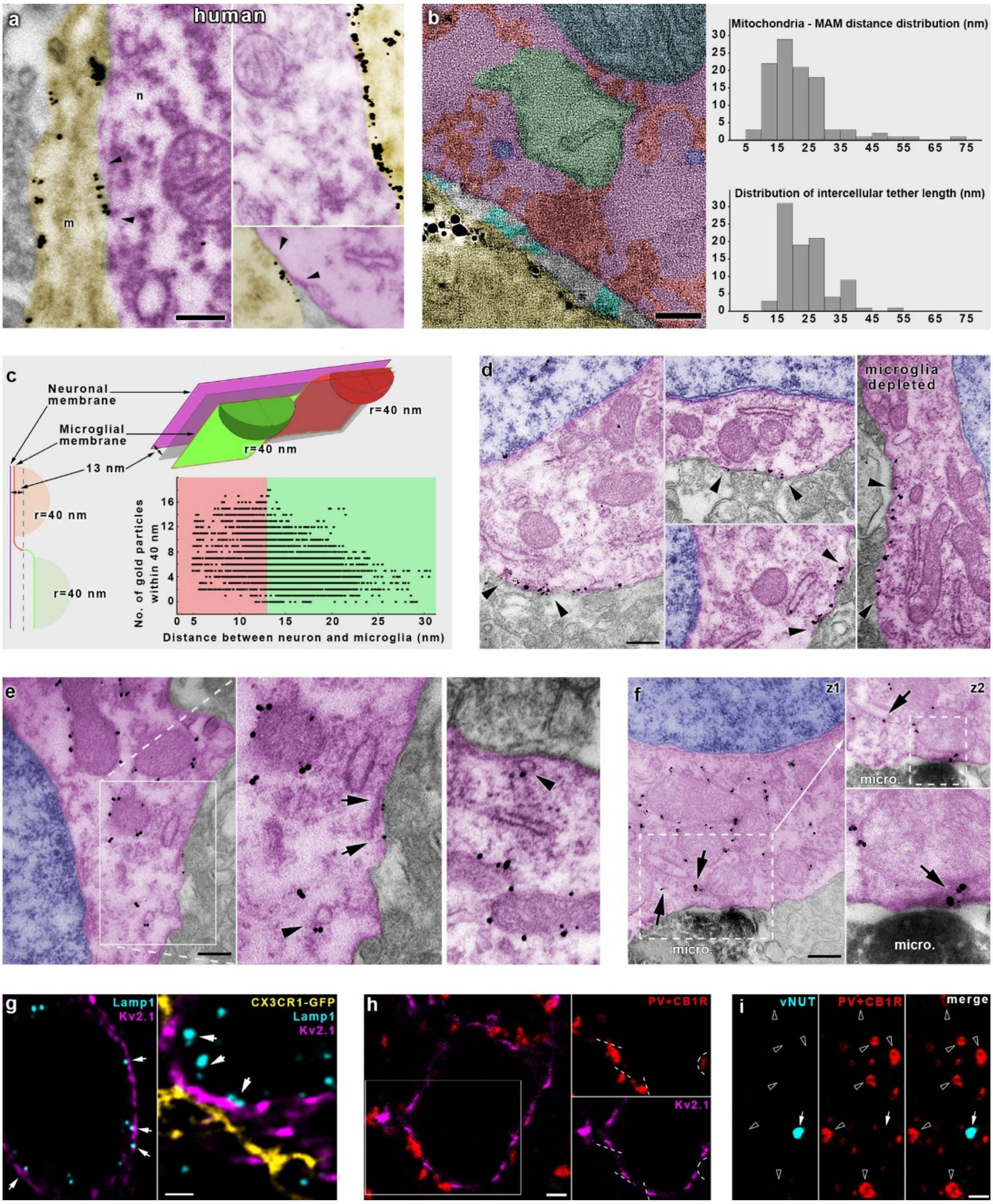
a
human
n
m
b
Mitochondria - MAM distance distribution (nm)
30
25
20
15
10
5
0
5 15 25 35 45 55 65 75
Distribution of intercellular tether length (nm)
c
Neuronal membrane
Microglial membrane
13 nm
r=40 nm
r=40 nm
r=40 nm
r=40 nm
No. of gold particles within 40 nm
16
12
8
4
0
0 5 10 15 20 25 30
Distance between neuron and microglia (nm)
d
microglia depleted
e
f
z1
z2
micro.
micro.
micro.
g
Lamp1
Kv2.1
CX3CR1-GFP
Lamp1
Kv2.1
h
PV+CB1R
Kv2.1
i
vNUT
PV+CB1R
merge

Figure S4. *a) Electron microscopic image shows a microglial process (m) establishing direct contact with neuronal cell body (n) in human tissue. Microglia is visualized by immunogold-labeling against P2Y12R. Arrowheads point at accumulation of gold particles at contact sites. b) Single virtual plane of an electron tomographic volume (thickness: 0.49 nm) showing a P2Y12R-positive (black immunogold particles) microglial process (yellow) contacting a neuronal cell body (magenta). Mitochondria (blue), mitochondria-associated* *membranes (MAM, green), vesicles (purple) and intracellular densities (red) are commonly visible in the vicinity of these junctions. In some cases, intercellular linking structures (cyan) can be seen within the cleft. Right: distribution of measured distances between mitochondria and MAM (upper chart, n=105) and measured length of intercellular tethers (lower chart, n=89). c) Schematic illustration showing the principles of P2Y12R density and membrane distance measurements using electron tomography (Fig. 2c, d). Single points of the microglial membrane were divided into two groups based on their closest distance from the neuronal membrane: closer than the average distance of 13 nm (red) or farther (green). For every observed point, P2Y12R labeling gold particles were counted within a radius of 40 nm. In the bottom right corner, the distribution of measured points is shown in the case of a representative junction. d) Transmission electron micrographs show Kv2.1 clusters on cortical neuronal cell bodies (arrowheads). Kv2.1-clustering and the association of the cluster with neuronal organelles is not affected by microglia depletion. e) Transmission electron micrographs show TOM20-immunogold labeling in neocortical neurons. Immunogold labeling (black grains) is specifically associated with outer mitochondrial membranes, while TOM20-positive vesicles can also be observed (arrowheads). Some immunogold particles can be found on the plasma membrane of the neurons (arrows), suggesting the exocytosis of mitochondria-derived vesicles. Nucleus is blue, neuronal cytoplasm is magenta. Left and middle panel is the same as on Fig. 2h, f) Electron micrographs from TOM20-Iba1 combined immunogold-immunoperoxidase reaction. Right upper panel is taken from a consecutive serial section and corresponds to the dashed area on the left panel. Right lower panel is enlarged from the right upper. Iba1-positive (dark DAB precipitate) microglial process contacts the cell body of a cortical pyramidal cell. TOM20-immunogold signal decorates the outer mitochondrial membrane, while arrows point to smaller membrane structures (putative MDVs), also positive for TOM20. Note the presence of a TOM20 positive vesicle attached to the neuronal plasmamembrane within the somatic junction on the right lower panel. g) CLSM images show Lamp1-positive neuronal lysosomes closely apposed to neuronal Kv2.1-clusters. Right panel shows a microglial process touching a neuronal Kv2.1-cluster with closely located/attached Lamp1-positive lysosomes. h) Kv2.1 accumulation does not overlap with somatic inhibitory terminals. CLSM images show perisomatic terminals stained with antibodies against PV and CB1 (red) and neuronal Kv2.1 (magenta). Panels on the right show the area in white rectangle on the first image. Dashed lines mark clear separation between perisomatic boutons and Kv2.1-signal, n=220 perisomatic boutons tested for Kv2.1 from two mice. i) Neuronal vNUT signal (cyan) is not present in perisomatic inhibitory terminals (red), n=194 perisomatic boutons tested for vNUT from two* *mice. Scale bars: 300 nm on a (400 for right bottom panel), 50 nm on b, 300 nm on d and e, 300 nm on f, 1 µm on g (2 µm for left panel), 2 µm on h and i.*

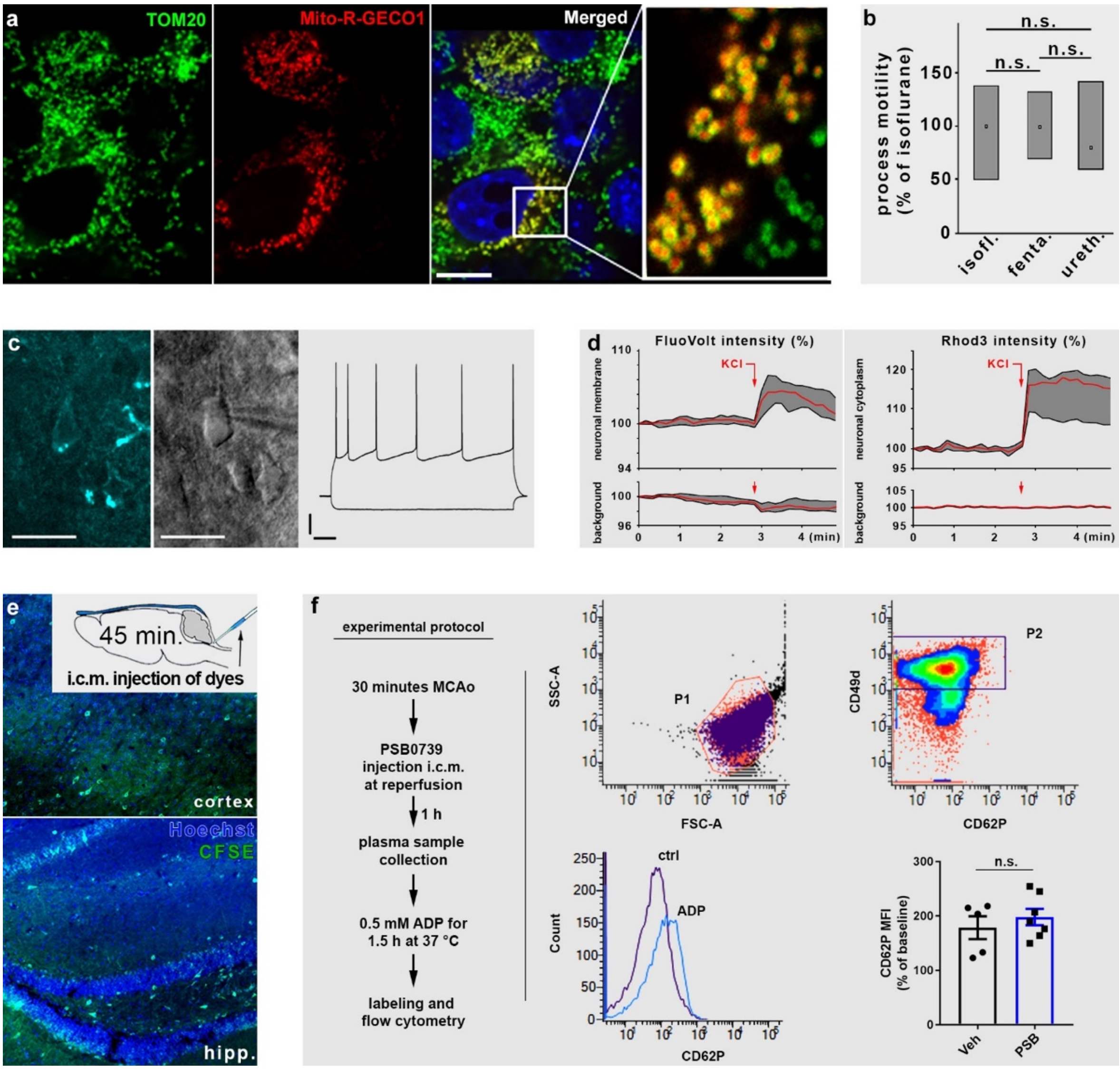
a
TOM20
Mito-R-GECO1
Merged
b
n.s.
n.s.
n.s.
process motility (% of isoflurane)
150
100
50
0
isofl.
fenta.
ureth.
c
d
FluoVolt intensity (%)
Rhod3 intensity (%)
KCl
neuronal membrane
neuronal cytoplasm
background
110
100
94
96
120
105
95
0
1
2
3
4 (min)
e
45 min.
i.c.m. injection of dyes
cortex
Hoechst
CFSE
hipp.
f
experimental protocol
30 minutes MCAo
PSB0739 injection i.c.m. at reperfusion
1 h
plasma sample collection
0.5 mM ADP for 1.5 h at 37 °C
labeling and flow cytometry
SSC-A
FSC-A
P1
CD49d
CD62P
P2
Count
ctrl
ADP
250
200
150
100
50
0
CD62P MFI (% of baseline)
300
n.s.
Veh
PSB

Figure S5. *a) Neuronal cell culture transfected with CMV-Mito-R-Geco1 and counterstained with TOM20 and DAPI. Scale bar is 10 µm. b) Effects of different anaesthetics on microglial process motility. Median process motility observed: isoflurane 0.6 µm/min, 0.3-0.83 interquartile; fentanyl 0.6 µm/min, 0.42-0.78; urethane 0.48 µm/min, 0.36-0.84; n=153 processes from 9 animals). c) Representative NADH intrinsic fluorescence image of a pyramidal cell. Left: Sample image of NADH fluorescence of neuronal somata. Middle: DIC image of the same region with whole cell patch clamp electrode. Right: Electrophysiological recordings of membrane potential response to -100 and +160 pA current injections. Scales: 20 mV and 100 ms. d) 40 mM KCl induces rapid membrane depolarization and calcium influx in cultured neurons in vitro. e) Mixture of carboxyfluorescein succinimidyl ester (CFSE) and Hoechst injected into the cisterna magna (i.c.m.) rapidly diffuses to all* *layers of neocortex and hippocampus. f) Central blockade of microglial P2Y12R with PSB does not alter ADP-induced platelet activation. Platelet rich plasma samples were collected from mice 1h after 30min MCAo and stimulated ex vivo with 0.5mM ADP for 1.5h at 37 °C. Platelets shown on SSC x FSC dot blots were labeled with CD49d and CD62P. ADP-induced increases in platelet CD62P were not altered in mice treated with i.c.m. PSB compared to vehicle-treated animals. Unpaired t-test, n.s. – not significant. Median and interquartile ranges are plotted on c, mean+SEM is plotted on e.*

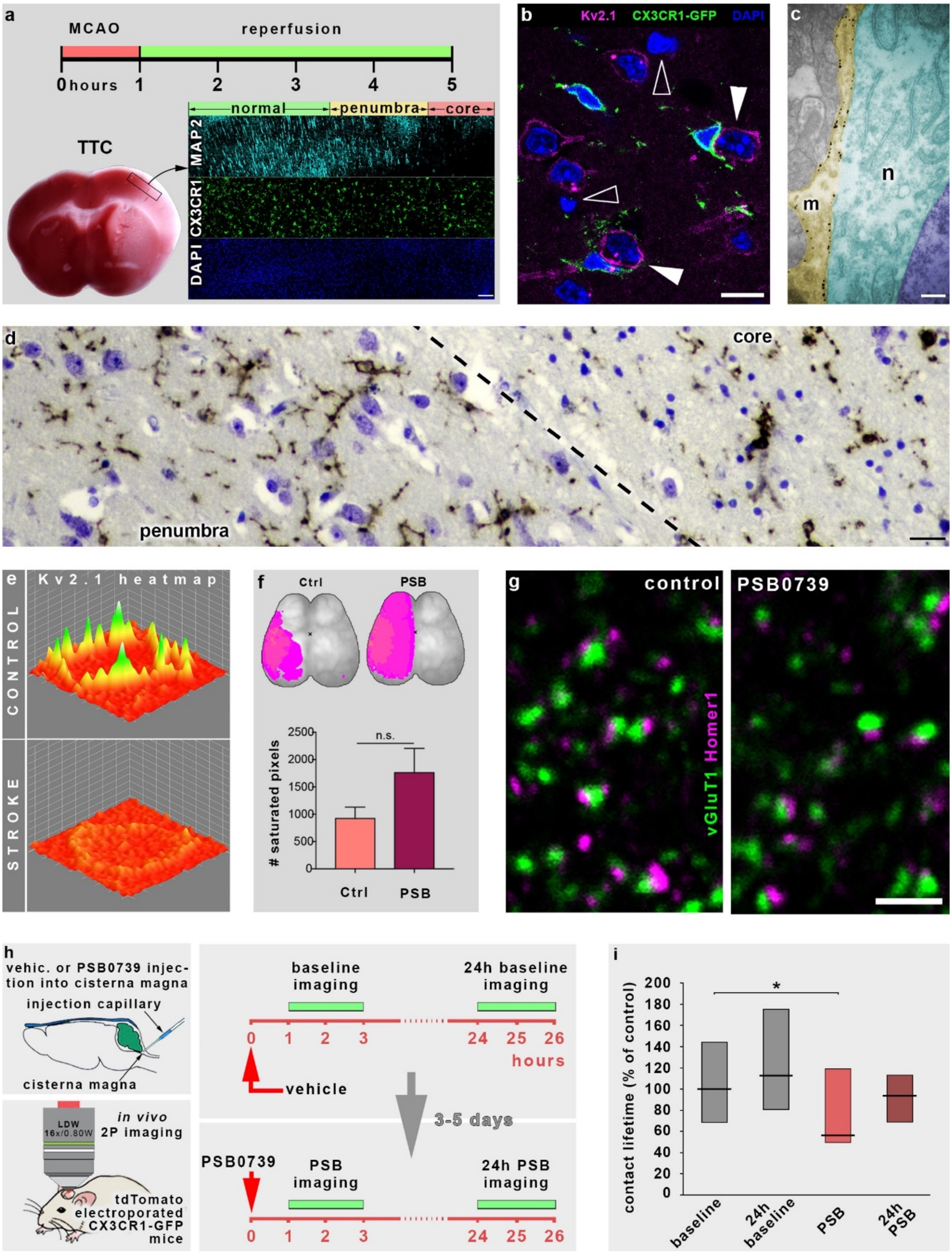
a
MCAO
reperfusion
0 hours 1 2 3 4 5
normal
penumbra
core
TTC
MAP2
CX3CR1
DAPI
b
Kv2.1 CX3CR1-GFP DAPI
c
m
n
d
core
penumbra
e
Kv2.1 heatmap
CONTROL
STROKE
f
Ctrl
PSB
n.s.
# saturated pixels
2500
2000
1500
1000
500
0
Ctrl
PSB
g
control
PSB0739
vGluT1 Homer1
h
vehic. or PSB0739 injection into cisterna magna
injection capillary
cisterna magna
LDW 16x/0.80W
in vivo 2P imaging
tdTomato electroporated CX3CR1-GFP mice
baseline imaging
24h baseline imaging
0 1 2 3
24 25 26
hours
vehicle
3-5 days
PSB0739
PSB imaging
24h PSB imaging
0 1 2 3
24 25 26
i
contact lifetime (% of control)
200
180
160
140
120
100
80
60
40
20
0
*
baseline
24h baseline
PSB
24h PSB

Figure S6. *a) Outline of middle cerebral artery occlusion (MCAo) experiment and delineation of core/penumbra regions of stroke affected brain. 1 hour MCAo was followed by 4 hours of reperfusion. Delineation was performed with the use of TTC staining and immunofluorescent labeling of MAP2 and microglia. b) DAPI staining pattern reveals that neurons with increased microglial coverage (white* *arrowheads) in the penumbra region possess normal chromatin structure, confirming their viability. Empty arrowheads point to pycnotic nuclei. c) Transmission electron micrograph shows a P2Y12R-immunogold particle labeled microglial process covering a neuron in the penumbra region. Note the increased coverage, the disappearance of cytoplasmatic structures like closely apposed mitochondria and MAM. Neuronal membrane integrity and chromatin structure are sustained. d) Delineation of core/penumbra border in postmortem human cortical tissue. Neurons and nuclei are visualized by Nissl-staining (blue), microglia is labeled by anti-P2Y12R DAB-Ni immunoperoxidase reaction (dark brown precipitate). e) Heatmaps of Kv2.1 immunostaining reveal that Kv2.1 clusters disappear after stroke in the penumbra. f) The saturated calcium signal after experimental stroke (left MCAo in every experiment) corresponds to the dysfunctional tissue during the occlusion. The maps show an overlay of the area of saturated pixels (pink) of every animal in the two groups. g) CLSM images show type 1 vesicular glutamate transporter (vGlut1) and Homer1 immunolabeling after acute i.c.m. administration of vehicle (control) or PSB. The closely apposed vGluT1 and Homer1 puncta represent glutamatergic synaptic contacts. PSB-treatment did not alter neocortical synapse numbers (0.353 synapse/µm^2 in control, and 0.352 synapse/µm^2 in PSB-injected, n=423 appositions from 4 animals). h) Schematic outline of repeated 2P imaging of PSB effects. Vehicle was administered i.c.m., and baseline imaging performed between the 1st and 3rd hours after injection. The imaging session was repeated after 24h (24h baseline). After 3-5 days, PSB was injected i.c.m., and imaging performed between the 1st and 3rd hours after injection (PSB). The imaging session was repeated after 24h (24h PSB). i) Acute central PSB administration decreased the contact lifetime to 56% of control, but this effect could not be observed after 24 hours (68.8-143.8% baseline interquartile range, 112.5% (81.3-175) 24h baseline, 56.3% (50-118.8) after PSB, 93.8 (68.8-112.5) 24h after PSB; p=0.0139, n=173 contacts from 3 mice). Scale bars: 100 µm on a, 10 µm on b, 300 nm on c, 12 µm on d, 2 µm on g. Mean+SEM is plotted.*

Supplementary Movie legends

Movie S1. *In vivo 2P time-lapse imaging shows temporal dynamics of microglia-neuron contacts. A tdTomato expressing neocortical neuron (red) is being contacted by processes of a microglial cell (green) in CX3CR1$^{+/GFP}$ mouse electroporated in utero with pCAG-IRES-tdTomato. The analyzed trajectories of microglial processes contacting the neuron are shown on the right panel, warm colors label trajectories of somatic* *contacts, while cold colors label trajectories of microglial processes contacting neuronal dendrites. The middle panel shows the trajectories overlaid on the recording.*

Movie S2. *In vitro CLSM time-lapse imaging of cocultured HEK293 and microglial cells. HEK cells were transfected with GFP-coupled control Kv2.1 construct on the left panel, and with YFP-coupled dominant-negative (DN) Kv2.1 construct on the right panel. Microglia is visualised by Alexa594-conjugated Lectin (red). Microglial processes contact Kv2.1-transfected HEK-cells at the clusters, but not those transfected with a dominant-negative mutant.*

Movie S3. *Left: stack of electron tomographic 0.5 nm thick virtual sections shows the special nano-architecture of a somatic microglia-neuron junction with closely apposed mitochondria, mitochondria-associated membranes (MAMs) and cytoplasmatic structures. The silver-intensified P2Y12R-immunogold grains are clearly visible at the cytoplasmatic surface of microglial membrane. Note that large number of gold particles are clustered exactly where the neuronal cytoplasmatic structure is anchored. Right: 3D model of the same tomographic volume, neuronal membrane is magenta, microglial membrane is green, immunogold particles white, mitochondria light blue, MAM light green, cytoplasmatic densities red, vesicle-like structures blue and microglial reticular membrane structures darker green. Note the specific enrichment of P2Y12R labeling at the core of the junction.*

Movie S4. *Stack of electron tomographic virtual sections shows the special nano-architecture of the core of a somatic microglia-neuron junction. The silver-intensified P2Y12R-immunogold grains are clearly visible at the cytoplasmatic surface of microglial membrane. The tethers between the anchored mitochondria and MAM are clearly visible. The neuronal cytoplasmatic structure (mitochondria, MAM) is anchored to a membrane segment that is precisely facing the high density of P2Y12Rs on the microglial membrane. Note that distance between the neuronal and microglial membrane is the smallest exactly here, and intercellular tethers are also clearly visible.*

Movie S5. *Left: stack of electron tomographic virtual sections shows the special nano-architecture of a somatic microglia-neuron junction with closely apposed mitochondria, MAMs and cytoplasmatic structures. The silver-intensified P2Y12R-immunogold grains are clearly visible at the cytoplasmatic surface of microglial membrane that touches the neuronal cell body, but are present only at a lower density at membrane segments, where the microglia touches a perisomatic bouton. Right: 3D model of the same tomographic volume, neuronal membrane is magenta, microglial membrane is ocker, immunogold particles white, mitochondria light blue, MAM light green, bouton membrane vivid green.*

Movie S6. *In vivo 2P imaging of CX3CR1*$^{+/GFP}$ *mice in utero electroporated with CAG-Mito-R-Geco1 construct. Dashed lines show the outline of a neuron, green microglial processes touch neuronal cell body where somatic mitochondria are present. White arrow indicates the contact site of microglia.*

Movie S7. *In vitro CLSM time-lapse imaging of KCl-stimulation of quinacrine-loaded cultured neuron. Left panel shows transmitted channel and superimposed green channel (quinacrine-labeled ATP-containing vesicles), right panel shows the green channel and the outline of the neuron (white dashed line). White arrows point to vesicles that are released spontaneously, red arrows point to vesicles that are released after 40 mM KCl stimulation. MIP of z-stack (z-range: 2.5 µm), frame dimension: 12.3 x 22.2 µm.*

6. Publication III - Short-Chain Fatty Acids Improve Poststroke Recovery via Immunological Mechanisms.

Sadler R, Cramer JV, **Heindl S**, Kostidis S, Betz D, Zuurbier KR, Northoff BH, Heijink M, Goldberg MP, Plautz EJ, Roth S, Malik R, Dichgans M, Holdt LM, Benakis C, Giera M, Stowe AM, Liesz A. (2020). Short-Chain Fatty Acids Improve Poststroke Recovery via Immunological Mechanisms. ***J Neurosci.*** Jan 29;40(5):1162-1173. doi: 10.1523/JNEUROSCI.1359-19.2019.

Journal: **Journal of Neuroscience**

Impact Factor: 6.074 Ranking: 29/267 in Neurosciences

Source: https://www.jneurosci.org/content/40/5/1162/tab-article-info

Copyright 2020 Society for Neuroscience

1162 • The Journal of Neuroscience, January 29, 2020 • 40(5):1162–1173

Neurobiology of Disease

Short-Chain Fatty Acids Improve Poststroke Recovery via Immunological Mechanisms

Rebecca Sadler,[1,2] **Julia V. Cramer,**[1] **Steffanie Heindl,**[1] **Sarantos Kostidis,**[3] **Dene Betz,**[4] **Kielen R. Zuurbier,**[4] **Bernd H. Northoff,**[5] **Marieke Heijink,**[3] **Mark P. Goldberg,**[4] **Erik J. Plautz,**[4] **Stefan Roth,**[1] **Rainer Malik,**[1] **Martin Dichgans,**[1,2] **Lesca M. Holdt,**[5] **Corinne Benakis,**[1] **Martin Giera,**[3] **Ann M. Stowe,**[4,6] **and Arthur Liesz**[1,2]

[1]Institute for Stroke and Dementia Research, University Hospital, Ludwig-Maximilians-University LMU, 81377, Munich, Germany, [2]Munich Cluster for Systems Neurology (SyNergy), 81377, Munich, Germany, [3]Leiden University Medical Center, Center for Proteomics & Metabolomics, 2300 RC Leiden, The Netherlands, [4]Department of Neurology and Neurotherapeutics, Peter O'Donnell Jr. Brain Institute, University of Texas Southwestern Medical Center, Dallas, Texas 75390, [5]Institute of Laboratory Medicine, University Hospital, Ludwig-Maximilians-University LMU, 81377, Munich, Germany, and [6]Department of Neurology, University of Kentucky, Lexington, Kentucky 40508

Recovery after stroke is a multicellular process encompassing neurons, resident immune cells, and brain-invading cells. Stroke alters the gut microbiome, which in turn has considerable impact on stroke outcome. However, the mechanisms underlying gut–brain interaction and implications for long-term recovery are largely elusive. Here, we tested the hypothesis that short-chain fatty acids (SCFAs), key bioactive microbial metabolites, are the missing link along the gut–brain axis and might be able to modulate recovery after experimental stroke. SCFA supplementation in the drinking water of male mice significantly improved recovery of affected limb motor function. Using *in vivo* wide-field calcium imaging, we observed that SCFAs induced altered contralesional cortex connectivity. This was associated with SCFA-dependent changes in spine and synapse densities. RNA sequencing of the forebrain cortex indicated a potential involvement of microglial cells in contributing to the structural and functional remodeling. Further analyses confirmed a substantial impact of SCFAs on microglial activation, which depended on the recruitment of T cells to the infarcted brain. Our findings identified that microbiota-derived SCFAs modulate poststroke recovery via effects on systemic and brain resident immune cells.

Key words: microbiome; neuroinflammation; plasticity; stroke models

Significance Statement

Previous studies have shown a bidirectional communication along the gut–brain axis after stroke. Stroke alters the gut microbiota composition, and in turn, microbiota dysbiosis has a substantial impact on stroke outcome by modulating the immune response. However, until now, the mediators derived from the gut microbiome affecting the gut-immune-brain axis and the molecular mechanisms involved in this process were unknown. Here, we demonstrate that short-chain fatty acids, fermentation products of the gut microbiome, are potent and proregenerative modulators of poststroke neuronal plasticity at various structural levels. We identified that this effect was mediated via circulating lymphocytes on microglial activation. These results identify short-chain fatty acids as a missing link along the gut–brain axis and as a potential therapeutic to improve recovery after stroke.

Introduction

Stroke induces a multiphasic pathophysiological cascade, which consists of an initial excitotoxicity followed by a longer neuroinflammatory phase within the brain (Dirnagl et al., 1999; Iadecola and Anrather, 2011). Moreover, stroke can be regarded as a systemic disease affecting also remote organ function, including the lung (Austin et al., 2019), heart (Bieber et al., 2017), and immune system and intestinal function (Singh et al., 2016). Recently, it has been shown that a dysbiotic gut microbiota is correlated with a

---

Received June 12, 2019; revised Nov. 25, 2019; accepted Dec. 3, 2019.

Author contributions: R.S., J.V.C., S.K., D.B., K.R.Z., B.H.N., M.H., E.J.P., and S.R. performed research; R.S., J.V.C., S.H., S.K., K.R.Z., B.H.N., M.P.G., E.J.P., R.M., M.D., L.M.H., C.B., M.G., A.M.S., and A.L. analyzed data; R.S. wrote the first draft of the paper; S.H., S.K., B.H.N., M.P.G., E.J.P., M.D., L.M.H., C.B., M.G., and A.M.S. edited the paper; S.R., A.M.S., and A.L. designed research; A.L. wrote the paper.

This work was supported by the German Research Foundation (Deutsche Forschungsgemeinschaft, LI2534/2-1), the European Research Council (ERC-StG 802305), the Vascular Dementia Research Foundation, and the Munich Cluster for Systems Neurology (EXC 2145 SyNergy) ID 390857198 to A.L., the Texas Institute for Brain Injury and Repair to M.P.G. and A.M.S., and National Institutes of Health/National Institute of Neurological Disorders and Stroke (NS088555) to A.M.S. We thank Kerstin Thuβ-Silczak for excellent technical assistance.

The authors declare no competing financial interests.

Correspondence should be addressed to Arthur Liesz at Arthur.Liesz@med.uni-muenchen.de.

https://doi.org/10.1523/JNEUROSCI.1359-19.2019

Copyright © 2020 the authors

worsened outcome in patients (Xia et al., 2019), and that these changes are evident up until 3 weeks after hospitalization (Swidsinski et al., 2012). We have previously demonstrated an important role of the gut microbiome on stroke outcome in proof-of-principle experiments using germ-free and recolonized mice (Singh et al., 2018). Further experimental studies in rodent stroke models have identified a key role for the immune system, particularly brain-invading lymphocytes originating from the intestinal immune compartment, in mediating along the gut–brain axis (Benakis et al., 2016; Singh et al., 2016).

The gut microbiome produces a large number of bioactive metabolites which may affect brain function via modulating the immune system or afferent neuronal pathways (Kau et al., 2011; Cryan and Dinan, 2012). In particular, the metabolite group of short-chain fatty acids (SCFAs) acetate, butyrate, and propionate have been shown to readily cross the blood–brain barrier (Frost et al., 2014; Morrison and Preston, 2016) and affect brain function in development, health, and disease. For example, SCFA treatment improved the disease course in experimental autoimmune encephalitis by promoting anti-inflammatory mechanisms and reducing axonal damage (Haghikia et al., 2015). In mouse models of chronic stress, mice that received SCFA treatment exhibited significant improvements in antidepressant and anxiolytic behaviors, which was accompanied by reduced plasma corticosterone levels and differential gene regulation (van de Wouw et al., 2018).

More recently, the role of SCFAs in modulating the immune system has been studied in great detail. Through these investigations, they have been shown to play a role in the polarization of T cells in the intestinal immune compartment and inducing anti-inflammatory T-cell subset (Smith et al., 2013; Tan et al., 2016). Other studies have shown a critical role for microbiota-derived SCFAs in the maturation of microglial cells, the brain's resident immune cells (Erny et al., 2015). However, SCFAs can have far-reaching pleiotropic effects also beyond the immune system, including a direct effect on neuronal function through their potent function as histone deacetylase inhibitors (Bourassa et al., 2016). Accordingly, the importance of SCFA function has been implicated in neurodegenerative diseases and even in postischemic neurogenesis (Chuang et al., 2009; Kim et al., 2009).

Despite the key contribution of the gut microbiome to stroke outcome and the identification of SCFA as one of the microbiome's primary bioactive mediators, the role of SCFAs and their potential therapeutic use for poststroke recovery in the chronic phase after brain ischemia have not yet been investigated. In this study, we comprehensively investigated the effect of SCFA administration on poststroke recovery using advanced behavior analyses, *in vivo* wide-field calcium imaging, transcriptomic studies, and histological analyses to study and link SCFA-mediated recovery mechanisms from the molecular level up to behavior.

Materials and Methods

Animals and treatment. All experimental protocols were approved by the responsible governmental committees (Regierung von Oberbayern, Munich, Germany and Institutional Animal Care and Use Committee, University of Texas Southwestern, Dallas). Specific pathogen-free C57BL/6J female and male mice were purchased from Charles River Laboratories or The Jackson Laboratory. On the day of arrival, mice were 6–8 weeks of age. Male mice were used for all experiments, except for analysis of dendritic spine densities (see Fig. 2*A–F*), in which female mice were used. Mice were given SCFAs (25.9 mM sodium propionate, 40 mM sodium butyrate, and 67.5 mM sodium acetate) or salt-matched control (133.4 mM sodium chloride) (9265.1, ROTH) in drinking water *ad libitum* for 4 weeks as previously reported (Smith et al., 2013; Erny et al., 2015). Mice were continuously given supplemented water until the end of the experiment. For antibiotic treatment, mice received metronidazol 0.5 mg/ml (Millipore Sigma, #46461), neomycin 0.5 mg/ml (Millipore Sigma, # N1142), ampicillin 0.5 mg/ml (Millipore Sigma, #31591), and vancomycin 0.5 mg/ml (Millipore Sigma, #V8138) and with 5% sucrose in drinking water. All drinking water solutions were prepared and changed twice a week and blinded for experimenters.

Experimental stroke model. For the photothrombotic stroke model (PT), mice were anesthetized with isoflurane, delivered in a mixture of 30% O_2 and 70% N_2O. Mice were placed into a stereotactic frame; and throughout the surgical procedure, body temperature was maintained at 37°C with a mouse warming pad. Dexpanthenol eye ointment was applied to both eyes. A skin incision was used to expose the skull. Bregma was located and using the laser the lesion location was marked in the left hemisphere (1.5 mm lateral and 1.0 mm rostral to bregma). Mice were then injected intraperitoneally with Rosa Bengal (Millipore Sigma, #198250). Shielding was placed on the skull, allowing a 2-mm-diameter circular exposure over the lesion area. After 10 min, the laser (Cobolt Jive, 561 nm, 25 mV output power with fiber collimation at $f = 7.66$ mm) was applied to the lesion area for 17 min.

For the distal, permanent occlusion of the middle cerebral artery (dMCAo), the distal middle cerebral artery (MCA) was permanently electrocoagulated as previously described (Llovera et al., 2014). In brief, under isoflurane anesthesia, mice were placed in the lateral position. A skin incision was made to expose the skull. Using a drill, a burr hole into the skull revealed the bifurcated MCA. Using electric forceps, the artery was occluded and checked for no blood flow. Mice were then sutured across the skull incision.

For the filament, transient occlusion of the MCA (fMCAo), the internal carotid artery was transiently occluded for 60 min as previously described (Singh et al., 2016). In brief, mice were anesthetized with isoflurane, and an incision was made to expose the temporal bone. A laser doppler probe was affixed to the MCA territory to determine blood flow. Mice were included when a >80% cerebral blood flow drop was induced. At the neck, an incision to the skin exposed the common carotid and external carotid artery, which were ligated. The filament was inserted into the internal carotid artery for 60 min, and the MCA was occluded. Mice were sutured across the neckline. In total, 13 mice per group were used. In the control group, 8 mice died. In the SCFA-supplemented group, 3 mice died and 3 mice had no quantifiable infarct.

After all surgeries, mice were recovered in a nursing box at 37°C for 15 min and then returned to home cages.

Wide-field calcium imaging. In vivo wide-field calcium imaging was performed as previously published (Cramer et al., 2019). Briefly, we used Thy1GCaMP6s heterozygous reporter mice. Mice were scalped, and transparent dental cement was placed upon the intact skull at least 3 d before the start of the experiment. Resting-state *in vivo* imaging was performed under mild anesthesia (0.5 mg/kg body weight of medetomidin with 0.75% isoflurane inhalation). Mice were placed in a stereotactic frame below a customized macroscopic imaging setup, and the mouse cortex was illuminated with 450 nm blue LED light. We recorded for 4 min in resting state with a CCD camera at 25 Hz frame rate. Functional connectivity was computed for seed-based analysis with a seed pixel time series centered in the right caudal forelimb cortex, contralesional to the infarcted cortex. Pearson's correlation between the time course of this seed, and any other signal time course within the masked area was computed; then Fisher's z-transformed and topographically displayed. Analogous functional connectivity between seed pairs was calculated as correlation between signal time courses of two seeds within the sensorimotor cortex. Seeds were defined as previously described (Cramer et al., 2019). Mean correlation per group was calculated for each time point. We used two-sample t test and Bonferroni correction for statistical testing.

Automated skilled reaching. Behavioral training and assessments were measured using an automated reach task previously described (Becker et al., 2016). Mice are trained to pull an isometric lever using the contralesional forelimb, with each successful application of force criteria rewarded by a drop of peanut oil. For the first week, mice were trained in groups of 23 littermates for 6 h. During this time, spontaneous peanut oil deliveries occurred at randomly spaced time intervals ranging from 30 s to 5 min. Additionally, the isometric handle was positioned ~0.5 cm from the inner edge of the chamber during these 6 h sessions. The force criterion necessary to trigger a 4 μl peanut oil droplet was set just above electrical noise so that any slight touch could trigger peanut oil dispersion. For the next 3 weeks, mice were trained individually for 2 h sessions. The handle was positioned further back at 1 cm from the inner edge of the chamber. The criterion for success during training sessions was changed based on a customized, adaptive MATLAB program. The adaptive program initially set the criterion for success at a specified value of at least 1 g. After the first 15 pulls, the criterion was adjusted to the median force value. The adjustments continued for the duration of the session unless the median reached the maximum force requirement of 20 g. Finally, we fixed the criterion at 20 g to measure baseline motor function for three consecutive sessions. After stroke, assessments of reaching behaviors were measured weekly for 6 weeks.

SCFA quantification. Mice were saline perfused, and organs extracted. For feces, colon content was collected; and for plasma, cardiac puncture blood was centrifuged at 4°C at 3000 rpm and the plasma removed. All samples were frozen immediately on dry ice. SCFAs (acetic, propionic, and butyric acid) were determined according to published protocols, using gas chromatography-mass spectrometry (Hoving et al., 2018). Briefly, for plasma, 10 μl was used and feces were homogenized with LC-MS grade water in a bead beater. Samples were spiked with deuterated internal standards for each SCFA. Subsequently, SCFAs were derivatized using pentafluorobenzyl bromide and analyzed using gas chromatography-electron capture negative ionization in single ion monitoring mode. Quantification was performed against external calibration lines.

Infarct volumetry. After saline perfusion, the brain was removed from the skull and placed immediately on dry ice. Microscopy slides were mounted with 20-μm-thick coronal cryosections cut at 400 μm intervals for dMCAo and fMCAo lesions, and at 120 μm intervals for PT lesions. Sections were then stained with cresyl violet solution. For the infarct volume, all slides were scanned using 600 dpi. The area of infarct tissue was measured using the ImageJ software (National Institutes of Health) and integrated for calculation of infarct volume.

Spine density analysis. Following saline perfusion, mice were perfused with aldehyde fixative solution (Bioenno, #003780). Brains were then carefully removed and placed in fixative solution at 4°C overnight. Brains were then sliced at 100-μm-thick vibratome sections and immersed in impregnation solution (Bioenno, sliceGolgi Kit, #003760) for 5 d. Further staining was performed as described by the manufacturer (Bioenno). Images of dendrites were obtained at the same anatomical level for all brains, 400 μm from the lesion perimeter in cortical layer 2/3. In total, 5 dendrites from 5 neurons each in both hemispheres were imaged (100× brightfield). Dendrites from the images were then reconstructed using Imaris ×64 (version 8.4.0, Bitplane).

Immunohistochemistry. Mice were perfused with saline and then 4% PFA. Brains were removed and postfixed in 4% PFA at 4°C overnight. Brains were then dehydrated in 30% sucrose in 1× PBS. Microglia staining was performed on 100-μm-thick sections using rabbit anti-iba1 (1:200, Wako, #019-19741), and then goat anti-rabbit 594 (1:200, Thermo Fisher Scientific, #A-11012). Automated analysis of microglial cell counts and morphology was performed using a MATLAB-automated morphology protocol as previously described (Heindl et al., 2018). For microglial costaining, we used anti-CD68 (1:300, Bio-Rad, #MCA1957GA), anti-inducible nitric oxide synthases (iNOS) (1:300, Thermo Fisher Scientific, #MA5-17139), and anti-Arginase1 (1:300, Novus Biologicals, #NB100-59740SS), and the corresponding secondary antibodies. Coverage analysis was performed using ImageJ software. Quantification was done for overlapping activation markers with Iba-1 from the maximum intensity projections generated from *z* stacks of the ipsilateral cortex. For synaptic staining, sections were incubated with guinea pig anti-VGlut1 (1:1000, Millipore, #AB5905) and chicken anti-Homer1 (1:2000, Synaptic Systems, #160006) for 3 d at 4°C, and then counterstained with goat anti-guinea pig 488 (1:500, Invitrogen, #A11073) and goat anti-chicken 647 (1:500, Invitrogen, #A21449) for 18 h at room temperature. For synaptic puncta analysis, a *z* stack of 3 slices at 0.33 μm was used as previously described (Ippolito and Eroglu, 2010) using FIJI with the SynapseCounter plugin (Schindelin et al., 2012).

Flow cytometric analysis. Following saline perfusion in deep anesthesia, the entire spleen and both brain hemispheres were dissected. Spleens were immediately placed on ice-cold 1× PBS, passed through a 40 μm cell strainer, and treated with red blood cell lysis buffer. Cell surface markers were stained using the following antibodies: anti-CD3 FITC (clone 17A2) and anti-CD45 eFluor450 (clone 30-F11). Stained cells were analyzed on a BD FACSVerse flow cytometer (BD Biosciences) and analysis performed by FlowJo software (version 10.0). For brain, hemispheres were isolated and cells isolated by mechanical dissociation. Mononuclear cells were enriched using discontinuous Percoll gradient centrifugation by standard protocols and then with 30 μm cell strainer, as described previously (Benakis et al., 2016). Cell staining for flow cytometry was performed by first preincubation of cells with Fc receptor blocker (1:100, Invitrogen, 14–91-61–73) for 10 min and then staining with the following monoclonal antibodies: anti-CD3 FITC (clone 17A2), anti-CD45 eFluor450 (clone 30-F11), and anti-CD11b Pe-Cy7 (clone M1/70). Stained cells were analyzed on a BD FACSVerse flow cytometer (BD Biosciences) and analysis performed by FlowJo software (version 10.0).

RNA sequencing and data analysis. Fourteen days after stroke, brains were extracted from the skulls and placed into a stainless-steel brain matrix. Brains were sliced coronally at 2 mm distance caudally and rostrally away from the lesion. The cortex was removed, frozen on dry ice, and the mRNA isolated using the RNeasy Mini Kit (QIAGEN, #74109). For library preparation, 100 ng of total RNA was fragmented and processed using the Ovation Human FFPE RNA-Seq Library Systems (Nugen) according to the instructions of the manufacturer.

Barcoded libraries were quantified using the Library Quantification Kit-Illumina/Universal (KAPA Biosystems). Cluster generation was performed with a concentration of 10 nM using a cBot (Illumina). Sequencing of 2× 100 bp paired-end reads was performed with a HiScanSQ sequencing platform (Illumina) using version 3 chemistry at the sequencing core facility of the IZKF Leipzig (Faculty of Medicine, University Leipzig, Leipzig, Germany). Raw reads were mapped to the reference genome mm10 using split-read mapping algorithm implemented in segemehl (Hoffmann et al., 2009). Mapped reads were counted using feature Counts (Liao et al., 2014) according to RefSeq annotation. Differential expression was computed using DESeq2 algorithm (Love et al., 2014). Raw data have been deposited at Gene Expression Omnibus database (Accession number GSE131788).

RT-PCR. mRNA from brain tissue around the lesion was isolated as described above and transcribed using the High Capacity cDNA Reverse Transcription Kit (Applied Biosystems, #4368814) with Rnasin Plus RNase Inhibitor (Promega, #N2611). The following primers were used: BDNF (forward: CGGCGCCCATGAAAGAAGTA; reverse: AGACCT CTCGAACCTGCCCT), TrkB (forward: ACTTCGCCAGCAGTAGCAG; reverse: ACCTCAGGGCTGGGGAG), synaptophysin (forward: AGTACCCATTCAGGCTGCAC; reverse: CCGAGGAGGAGTAGTCA CCA), EphrinA5 (forward: CTGGTGCTCTGGATGTGTGT; reverse: CCCTCTGGAATCTGGGGTTG), PPIA (forward: ACACGCCATAATG GCACTGG; reverse: ATTTGCCATGGACAAGATGCC), Claudin-5 (forward: GTTAAGGCACGGGTAGCACT; reverse: TACTTCTGTG ACACCGGCAC), ICAM-1 (forward: CAATTTCTCATGCCGCACAG; reverse: AGCTGGAAGATCGAAAGTCCG), and VCAM-1 (forward: TGAACCCAAACAGAGGCAGAG; reverse: GGTATCCCATCACTTG AGCAGG). The QuantiNova SYBR Green PCR Kit (QIAGEN, #208052) was used with a LightCycler 480 II (Roche Diagnostics). All gene expression was expressed relative to the PPIA housekeeping gene and calculated using the relative standard curve method.

Experimental design and statistical analysis. All statistical analyses were performed using Prism software (GraphPad, version 6.0). Sample size was chosen based on comparable experiments from previous experiments (Singh et al., 2016). For experimental design details on sample size, see Results and figure legends. A p value of <0.05 was regarded as statistically significant.

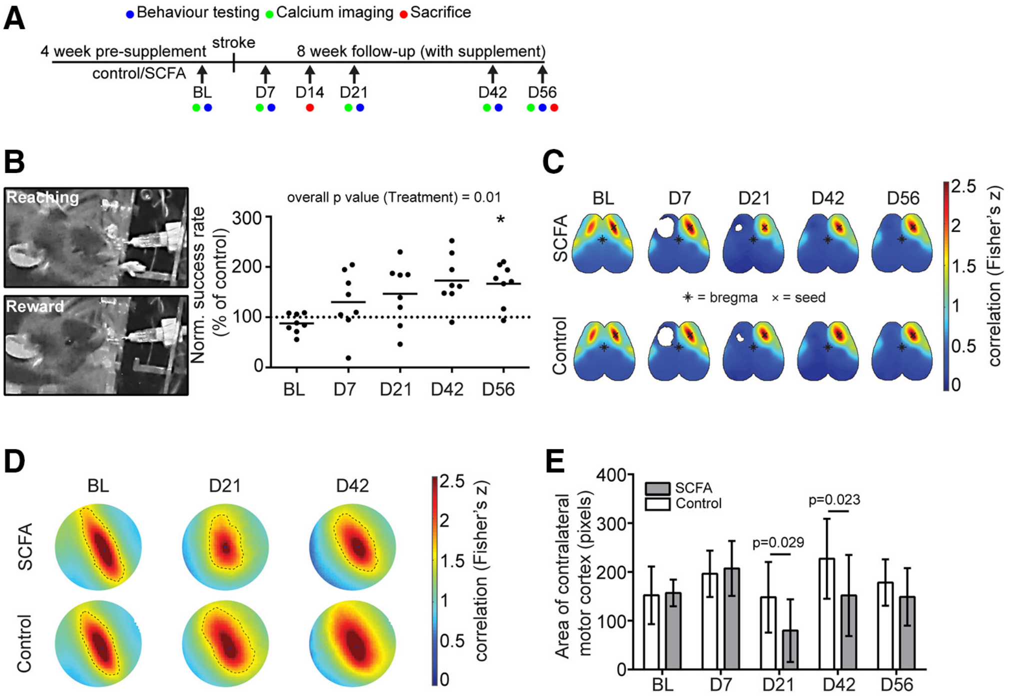

Figure 1. SCFA supplementation improves recovery after stroke. ***A***, Schematic diagram illustrating the timeline of SCFA supplementation and analysis time points. BL, Baseline; D, day (after stroke). See Figure 1-1 (available at https://doi.org/10.1523/JNEUROSCI.1359-19.2019.f1-1). ***B***, Representative images obtained during the lever pull test of trained mouse successfully reaching for the lever (left, above) and obtaining the peanut oil reward (left, below). Right, Normalized success rate for lever pulls by the affected (contralesional) forelimb. Relative values are shown per time point normalized to the mean of the control group. $N = 8$ per group. Horizontal line indicates mean. Two-way repeated measure ANOVA with Holm–Sidak's *post hoc* test. ***C***, Topographic depiction of seed-based functional connectivity of both hemispheres at indicated time points of SCFAs and control-treated mice. Seed is placed in the homotopic contralesional region to the ipsilesional lesion area (i.e., the contralesional motor cortex). Color code represents Fisher's *z* correlation between the seed and every other pixel in the cortex. ***D***, Enlarged images of the contralesional motor cortex (region homotypic to the infarct lesion). Area highlighted with dotted line represents the highly connected functional motor cortex area (pixels with Fisher's *z* values > 2.25). ***E***, Quantification of highly correlated (Fisher's $z > 2.25$) area of the contralesional motor cortex in control (open bars) and SCFA-treated mice (gray bars). $N = 15$ per group. Multiple *t* tests per time point with Holm–Sidak's correction for multiple testing.

Results

SCFA supplementation improves recovery and cortical reorganization after stroke

We previously showed that stroke induces dysbiosis of the gut microbiome with the hallmark of reduced bacterial diversity (Singh et al., 2016). To test the impact of poststroke gut dysbiosis on the metabolic function of the microbiome, we performed targeted analysis of plasma samples for SCFA concentrations after fMCAo stroke and sham surgery in mice by mass spectrometry. This analysis revealed significantly reduced plasma SCFA concentrations 3 d after fMCAo stroke surgery compared with sham-operated mice (Fig. 1-1*A*, available at https://doi.org/10.1523/JNEUROSCI.1359-19.2019.f1-1). Therefore, we hypothesized that supplementation of SCFA would increase circulating SCFA concentrations and potentially induce therapeutic effects within the chronic poststroke recovery period. To test this hypothesis, we supplemented mice for 4 weeks with drinking water containing either a mix of acetate, butyrate, and propionate (for details, see Materials and Methods) or control drinking water with matched sodium chloride concentration. SCFA supplementation did not affect body weight (Fig. 1-1*B*, available at https://doi.org/10.1523/JNEUROSCI.1359-19.2019.f1-1) or overt behavior of the animals. We performed PT stroke surgery after 4 weeks of SCFA supplementation and assessed poststroke motor deficits of the affected forelimb with an automated lever pull test while animals received further SCFA supplementation during the complete survival period (Fig. 1*A*,*B*). Mice receiving SCFA supplementation performed significantly better compared with control-treated animals (Fig. 1*B*). A two-way ANOVA for repeated measurements revealed an overall *p* value of 0.01 for the treatment effect, and a significant difference (after correction for multiple comparisons) between treatment groups at 56 d after stroke (Fig. 1*B*). To analyze cortical network plasticity as the morphological surrogate of behavioral recovery, we used Thy1-GCaMP6s mice and performed resting-state *in vivo* calcium to record cortical wide-field fluorescence from a neuronal based calcium reporter. Using the homotypical contralesional region of the cortex, we performed seed-based correlation analysis, indicating the connectivity strength (*z* score) of this area to every other pixel in the cortex (Fig. 1*C*). Previous research using fMRI in stroke patients has indicated that the homotypical contralesional region receives less neuronal inhibition from the stroked hemisphere, leading to disinhibition of the contralesional hemisphere (Rehme and Grefkes, 2013). To analyze the size of highly connected homotypical contralesional regions (i.e., the contralesional motor cortex), we measured the area of pixels with a *z* score > 2.25 (Fig. 1*D*). We observed a significantly reduced area of the contralesional motor cortex in SCFA- compared with control-treated mice at D21 and D42 (Fig. 1*E*). In contrast, SCFA treatment did not significantly affect the primary infarct area by *in vivo* imaging (Fig. 1-1*C*, available at https://doi.org/10.1523/JNEUROSCI.1359-19.2019.f1-1) and histological analyses with infarct volumetry in three different focal stroke models after stroke (Fig. 2-1*A*-*E*, available at https://doi.org/10.1523/JNEUROSCI.1359-19.2019.f2-1). These results indicated that, while SCFA supplementation did not affect the initial lesion development, SCFAs improved behavioral stroke outcome and modulated cortical network plasticity at later stages after stroke.

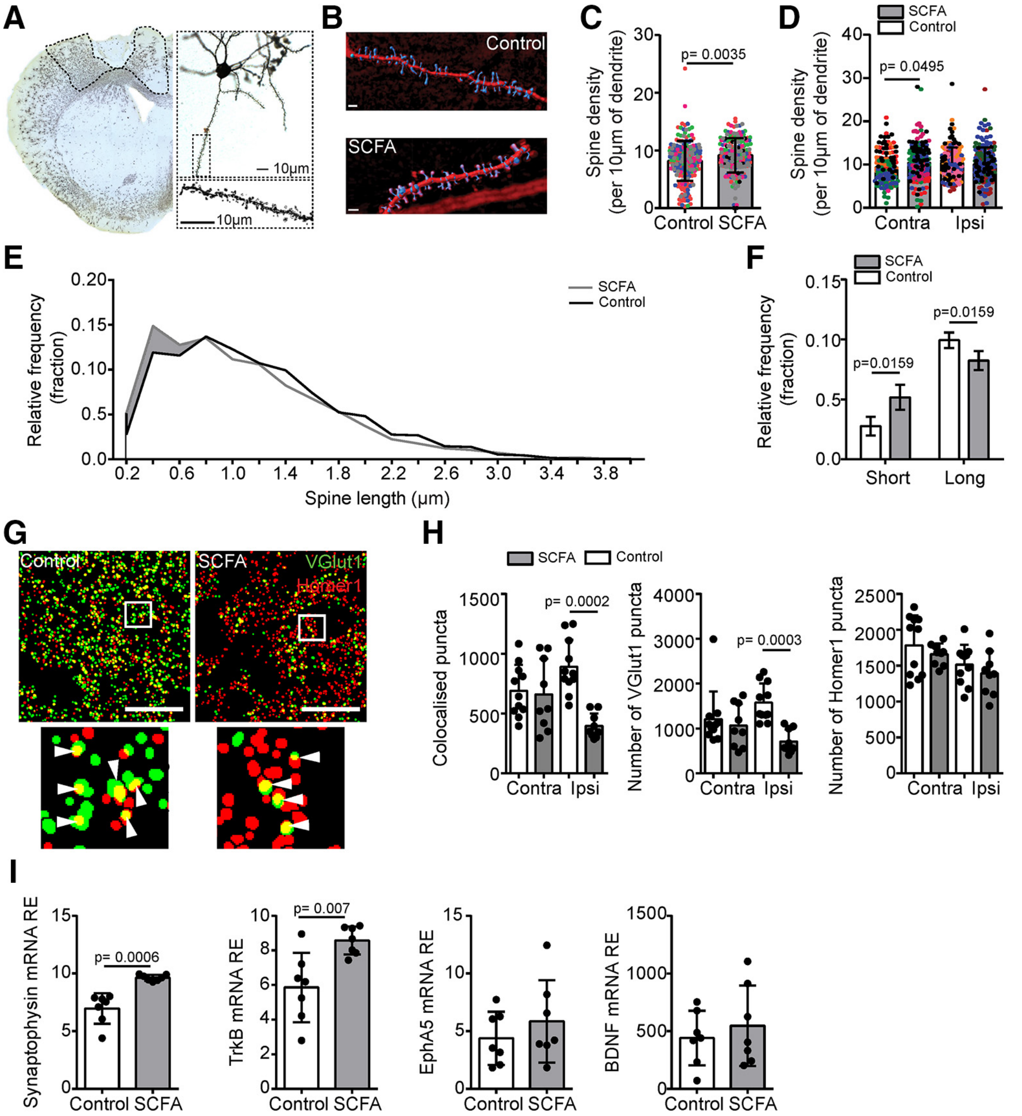

Figure 2. Poststroke neuronal plasticity is altered by SCFA treatment. ***A***, Representative images of Golgi-Cox stained brain sections 14 d after PT stroke (Figure 2-1 *A*–*E*, available at https://doi.org/10.1523/JNEUROSCI.1359-19.2019.f2-1). Dotted area in overview image represents perilesional cortical area used for spine analysis. Magnifications show representative pyramidal neuron and high-magnification image as used for spine analysis. Top right, Cortical pyramidal neuron. Bottom right, Example of spines identified on dendrite. Scale bar, 10 μm. ***B***, 3D reconstruction for a dendrite section with spines as used for further quantification of spine densities and lengths. Scale bar, 2 μm. ***C***, Quantification of pyramidal spine density per 10 μm of dendrite in the cortex of control and SCFA-treated naive mice (no stroke induction). Each color represents a different mouse, and each dot indicates a different dendrite. Five neurons per hemisphere analyzed in total for 4 or 5 mice per group (Mann–Whitney *U* test). ***D***, Quantification of spine density per 10 μm of dendrite in the perilesional and contralesional cortex at 14 d after stroke (Kruskal–Wallis test with Dunn's correction for multiple comparisons). ***E***, Histogram of the relative frequency (fraction) of spines found at different lengths 14 d after PT lesion in the perilesional cortex. Bin width is 0.2 μm (Figure 2-1 *F*, *G*, available at https://doi.org/10.1523/JNEUROSCI.1359-19.2019.f2-1). ***F***, Quantification of short (0.2 μm) and long (1.4 μm) spines in control (open bars) and SCFA (gray bars) treated mice. $N = 4$ or 5 per group. Mann–Whitney *U* test. ***G***, Representative particle images of presynaptic terminals by VGlut1 (green), postsynaptic densities by Homer1 (red), and nuclei with DAPI (blue) of the cortex from control and SCFA-treated mice, as used for quantification of colocalized presynaptic and postsynaptic particles (puncta). Scale bar, 20 μm. Arrowheads indicate colocalized (yellow) puncta. ***H***, Synapse counts were quantified as colocalized VGlut1 and Homer1 puncta (Figure 2-1 *H*, available at https://doi.org/10.1523/JNEUROSCI.1359-19.2019.f2-1). Quantification for colocalization (left) and for single markers (middle and right) revealed significantly changed synapse counts as a result of the reduced number of VGlut1$^+$ terminals in the perilesional cortex. contra, Contralesional hemisphere; ipsi, ipsilesional hemisphere. $N = 3$ or 4 mice (3 sections per mouse). Statistical analysis was performed with Kruskal–Wallis test with Dunn's multiple comparison correction. ***I***, Relative expression (RE) of mRNA for key molecules involved in synaptic plasticity (left), synaptophysin (left middle), TrkB (right middle), and EphA5 (right) BDNF from the perilesional cortex in control (open bars) and SCFA (gray bars) treated mice. $N = 7$ per group. Mann–Whitney *U* test.

SCFA supplementation modulates poststroke synaptic plasticity

After an ischemic brain injury, the entire cortex undergoes rapid functional and morphological reorganization, including neuronal dendritic plasticity, which allows adult neurons to form new connections. This process is correlated with improved functional connectivity after a cortical lesion (Jones and Schallert, 1994; Biernaskie et al., 2004). To analyze underlying morphological plasticity of the observed functional recovery in behavior and cortical connectivity, we performed Golgi-Cox staining of brain sections to investigate the effects of SCFA supplementation on dendritic spine density of pyramidal cells (Fig. 2*A*,*B*). We initially performed this analysis in the brains of naive animals that received either SCFA or control treatment, which revealed a higher pyramidal cortical spine density in the SCFA-treated mice (Fig. 2*C*). Next, we quantified brains at 14 d after PT stroke to capture a time period before the behavioral and cortical connectivity improvements were evident. Correspondingly, we observed

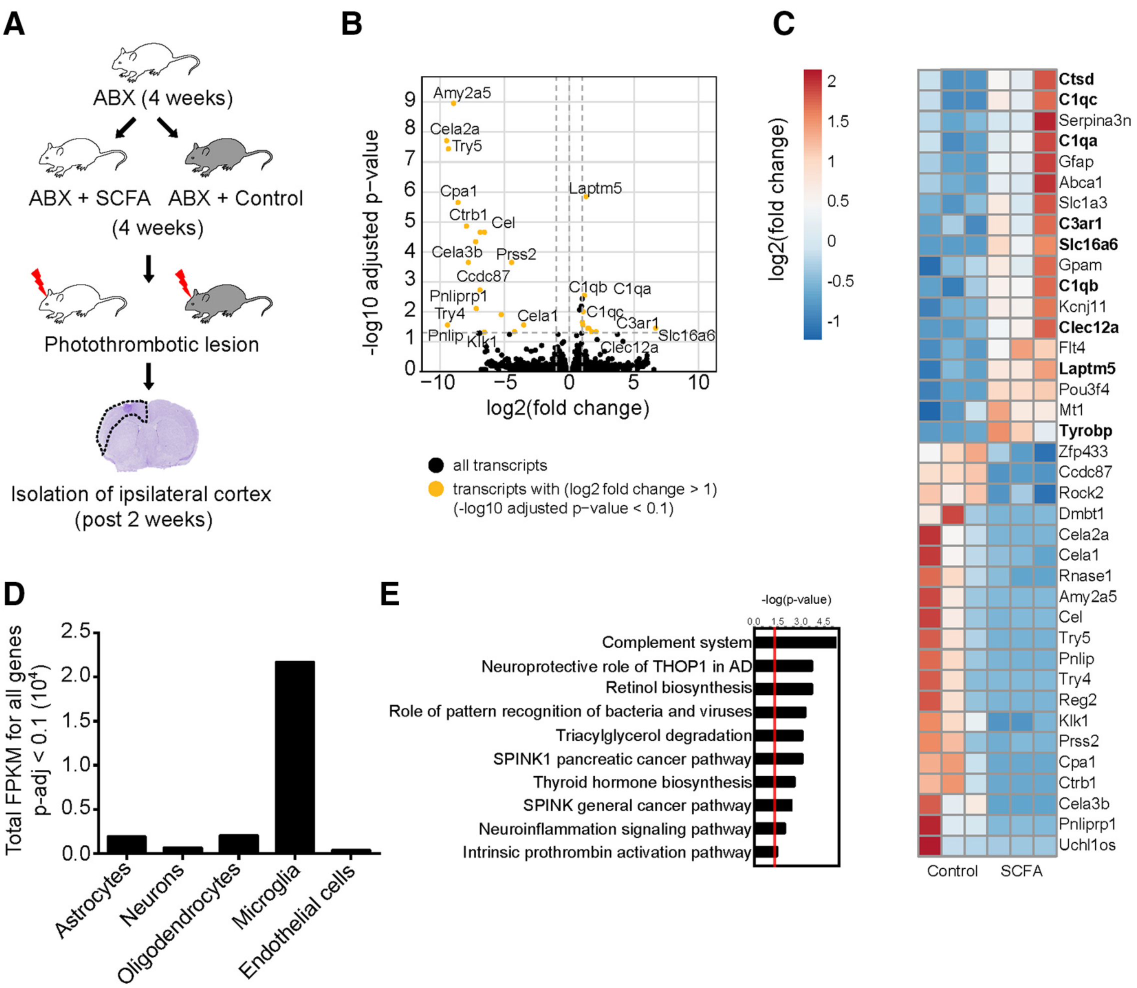

Figure 3. SCFA supplementation affects microglial gene signature after stroke. ***A***, Schematic diagram illustrating antibiotic (ABX) treatment regimen and followed by supplementation with SCFAs or control saline in drinking water (Figure 3-1, available at https://doi.org/10.1523/JNEUROSCI.1359-19.2019.f3-1). Delineated area on histological image represents perilesional cortex isolated for mRNA sequencing. ***B***, Volcano plot of regulated transcripts (SCFAs/control) in the perilesional cortex 14 d after PT stroke; $n = 3$ per group. Black represents gene transcripts. Orange represents gene transcripts with fold change (log2) > 1 and $-$log10-adjusted $p < 0.1$. ***C***, Heatmap of fold change (log2) for significantly regulated genes with an adjusted $p < 0.1$. Each column represents 1 individual mouse. ***D***, FPKN abundance and association per cerebral cell type of all significantly regulated genes (***C***) were performed as detailed in Materials and Methods, revealing the strongest association of the significantly regulated genes with microglial cells. ***E***, Ingenuity pathway analysis showing the top networks regulated by SCFA supplementation compared with control treatment.

that, after stroke, SCFA supplementation was associated with a significantly higher spine density in the homotypic contralesional region; however, these differences were not observed in the ipsilesional hemisphere (Fig. 2*D*) and were independent of infarct volume (Fig. 2-1, available at https://doi.org/10.1523/JNEUROSCI.1359-19.2019.f2-1). Moreover, the analysis of spine length distribution revealed that SCFA treatment induced a shift toward shorter spine lengths, specifically in the ipsilateral, but not contralesional, hemisphere (Fig. 2*E*,*F*; Fig. 2-1*F*,*G*, available at https://doi.org/10.1523/JNEUROSCI.1359-19.2019.f2-1). To further investigate synaptic plasticity under control of SCFA supplementation, we assessed synaptic density using costaining for VGlut1 (presynaptic) and Homer1 (postsynaptic) (Fig. 2*G*). We detected a significant reduction of the number of synapses (i.e., colocalized VGlut1 and Homer1 puncta) in the perilesional cortex of SCFA-supplemented mice (Fig. 2*H*). Interestingly, the difference in synapse counts was exclusively driven by the number of presynaptic VGlut1 puncta while Homer1-positive puncta remained unaffected.

Additionally, this pattern was also mirrored in the mean size of VGlut1 and Homer1 puncta (Fig. 2-1*H*, available at https://doi.org/10.1523/JNEUROSCI.1359-19.2019.f2-1). Finally, we analyzed the transcriptional regulation of key factors involved in synaptic plasticity (Fig. 2*I*). We observed that SCFAs significantly increased the expression of the presynaptic vesicle molecule synaptophysin and the BDNF receptor TrkB. BDNF itself, or the receptor tyrosine kinase EphA2, was not affected by SCFA supplementation. These results indicate effects of SCFA on morphological, synaptic plasticity, which could potentially precede the effects observed on functional recovery at later time points after stroke.

Brain transcriptomic analysis indicates microglia as the main cellular target of SCFA

To determine whether the observed effects of SCFA were either directly mediated on neuronal function or affecting other cerebral cell populations, we took an unbiased approach to investigate the effects of SCFA on gene expression in the peri-infarct cortex. For this, we first depleted the gut microbiome of mice as the main SCFA source by administration of antibiotics, followed by supplementation of SCFA (Fig. 3*A*). Plasma gas chromatography-mass spectrometry quantification confirmed an increase of SCFA after supplementation in drinking water (Fig. 3-1, available at https://doi.org/10.1523/JNEUROSCI.1359-19.2019.f3-1). Fourteen days after surgery, the infarct and peri-infarct regions were isolated for RNA sequencing, identifying 18 upregulated and 20 downregulated genes in SCFA supplemented mice (Fig. 3*B*,*C*).

The list of the top upregulated genes (Fig. 3*C*) hinted at a role for microglia as we found numerous genes that have previously been reported to be involved in microglial function and/or activation, such as Ctsd, various complement molecules, Tyrobp and Laptm5 (Zhong et al., 2018; Q. Li et al., 2019). To ascertain which cell type SCFA supplementation was mainly regulating in the brain, we took the 38 differentially regulated genes and compared them with an existing RNA-Seq database, which lists the fragments per kilobase of exon model per million reads found in astrocytes, neurons, oligodendrocytes, microglia, and endothelial cells (www.brainrnaseq.org) (Zhang et al., 2014). From the total number of fragments per kilobase of exon model per million read values of the 38 differentially regulated genes (Table 1-1, available at https://doi.org/10.1523/JNEUROSCI.1359-19.2019.t1-1), we discovered that the vast majority of gene reads from the significantly regulated genes were associated with microglial cells (Fig. 3*D*). Additionally, we performed an ingenuity pathway analysis on the 38 differentially regulated genes and found that the complement system was the top pathway and highly upregulated in mice supplemented with SCFA (Fig. 3*E*). Within the brain, the complement pathway is critical for microglia activation and has been associated with synaptic pruning by microglia (Schafer et al., 2012; Stephan et al., 2012; Wu et al., 2015).

SCFAs modulate microglial activation and immune cell composition

Based on the transcriptomic data's indication that microglia are the effector of SCFA-mediated poststroke recovery, we performed more in-depth analyses of microglial activation and the inflammatory response to stroke. As a surrogate of microglia activation, we performed Iba-1 immunohistochemistry of the cortex (Fig. 4*A*) and assessed microglia morphology using automated analysis (Heindl et al., 2018). Fourteen days after stroke, cortical microglia from SCFA-supplemented mice displayed a significantly more ramified and less spherical (i.e., less activated) morphology compared with controls (Fig. 4*B*). Additionally, the total number of microglia were significantly reduced in SCFA- compared with control-treated mice (Fig. 4*C*). These results indicate a modulation of the microglial response to stroke by SCFAs. Therefore, we further explored microglial function by assessing classical histological markers for microglial activation and polarization. We observed a significant reduction of CD68 expression in Iba-1$^+$ microglia (Fig. 4*D*), whereas Arginase-1 and iNOS were not significantly regulated by SCFA supplementation (Fig. 4*E*). Aside from evoking a microglial response, stroke induces invasion of peripheral immune cells into the brain parenchyma, which can deteriorate stroke outcome (Iadecola and Anrather, 2011; Liesz et al., 2015; Neumann et al., 2015; Selvaraj and Stowe, 2017). In particular, lymphocyte counts in brains after photothrombosis are still elevated 14 d after surgery (Feng et al., 2017). Additionally, cytokines secreted by brain-invading lymphocytes can modulate microglial activation (Liesz et al., 2009; Meng et al., 2019). Therefore, we performed flow cytometry of brain homogenates (Fig. 4*F*) and observed a significant reduction in cerebral lymphocyte invasion in SCFA-treated animals compared with controls (Fig. 4*G*).

The invasion of peripheral lymphocytes to the ischemic brain depends on the number of circulating lymphocytes, the expression of cerebral endothelial adhesion molecules, and the chemokine gradient derived from the injured brain tissue (Ransohoff and Engelhardt, 2012). In accordance with our nontargeted transcriptomic analysis (for results, see Fig. 3), which did not reveal significant regulation of chemokines or adhesion molecules by SCFAs, also a targeted PCR analysis of key adhesion molecules and tight junction proteins involved in poststroke lymphocyte recruitment at the blood–brain barrier did not show a significant regulation by SCFA (Fig. 4-1, available at https://doi.org/10.1523/JNEUROSCI.1359-19.2019.f4-1). In contrast, we detected a significant reduction of systemic T-cell counts by SCFA supplementation in the spleen (Fig. 4*H*), a secondary lymphatic organ that well characterizes the systemic immune response after stroke (Offner et al., 2006; Liesz et al., 2013; Roth et al., 2018).

These findings suggest that SCFAs may primarily affect lymphocytes already in the peripheral immune compartments, which then might secondarily mediate changes in the cerebral immune milieu after brain invasion. Therefore, we next aimed to test this hypothesis by investigating the effects of SCFA on microglia in the absence of lymphocytes. For this, we used lymphocyte-deficient *Rag1*$^{-/-}$ mice, which were given SCFA supplementation or control drinking water. In contrast to lymphocyte-competent WT mice, SCFA supplementation in *Rag1*$^{-/-}$ did neither affect microglia morphology, nor did it reduce microglial cell counts (Fig. 4*I*,*J*), indicating a key role of lymphocytes for mediating the SCFA effects on microglia.

Discussion

This study demonstrates that SCFAs, critical metabolites derived from the gut microbiome, are capable of improving poststroke recovery via the modulating effects of brain-invading lymphocytes on microglial function. Results from our study support this conclusion through several key findings. First, stroke lowers blood SCFA concentrations. Second, SCFA supplementation combats the deleterious effects of this poststroke response, which we demonstrated by associated SCFA supplementation with improved behavioral recovery, changes in cortical network connectivity, which are generally associated with improved stroke outcomes, and changes in histological markers of synaptic plasticity. Third, we indicated a potential mechanism for the observed improvements in the recovery of SCFA-treated animals by finding changes in microglial function, which were dependent on circulating lymphocytes. Consequently, these findings indicate that SCFAs affect peripheral lymphocytes, maturation, or egress from primary lymphatic tissue, and lymphocytes then indirectly mediate the SCFA effects on the brain micromilieu either by their overall reduction in cerebral invasion or polarization of the secreted cytokine profile.

These novel findings introduce SCFA as the most likely missing link in the pathophysiological function of the gut–brain axis in stroke and poststroke recovery, for which the microbiota-derived effector molecules were so far unknown (Benakis et al., 2016; Houlden et al., 2016; Singh et al., 2016). Our use of a novel imaging modality, *in vivo* wide-field calcium imaging, provided a highly sensitive tool for assessing cortical network plasticity after stroke (Cramer et al., 2019). This tool allowed us to perform analyses of network plasticity by comparable analytical approaches to fMRI in patients, with the exception of using a genetically encoded reporter for direct neuronal activation instead of the blood flow surrogate marker (BOLD) used in MRI (Cramer et al., 2019). The analysis of connectivity within the cortical network provides information about the dynamic changes in defined cortical areas under resting-state conditions, which gave us

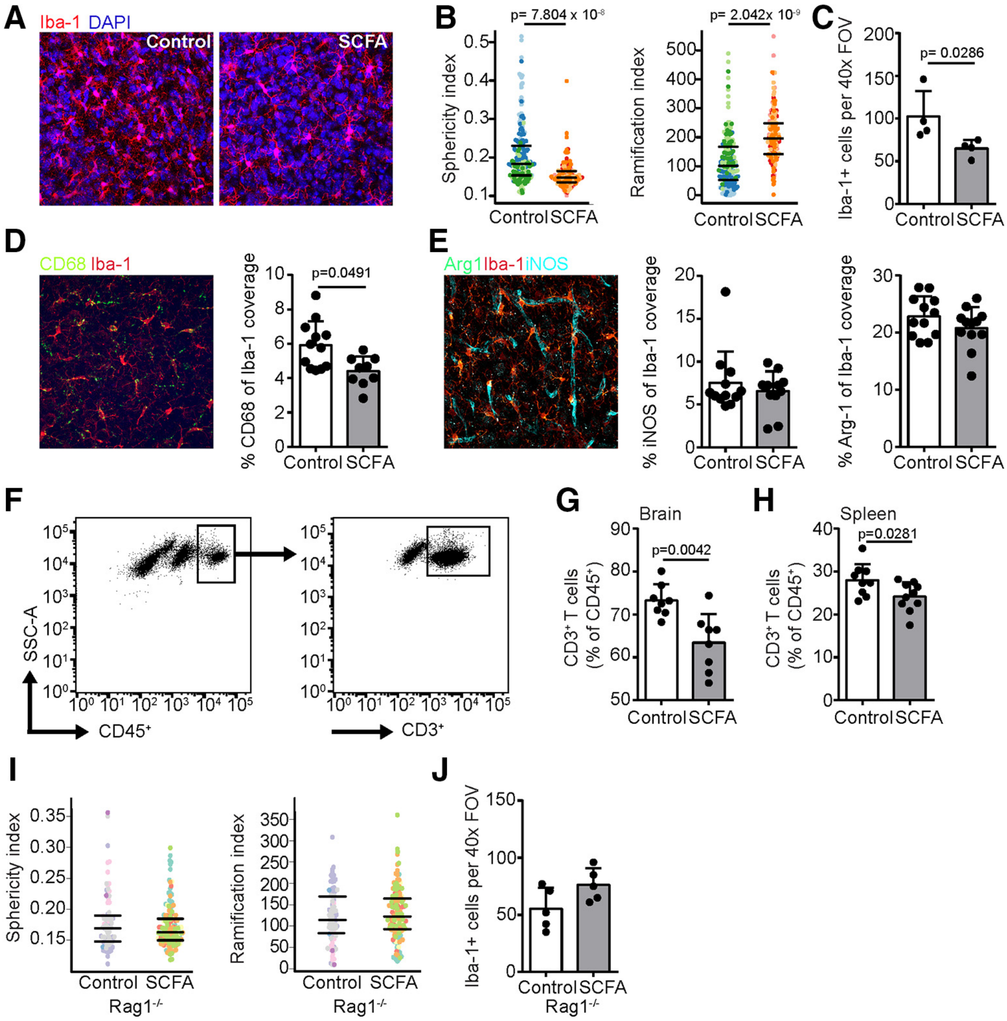

Figure 4. Modulation of poststroke neuroinflammation by SCFA depends on peripheral lymphocytes. ***A***, Representative maximum intensity projections of microglial staining using Iba-1 (red) and DAPI (blue) in the ipsilesional hemisphere 14 d after PT stroke with either control (left) or SCFA (right) supplementation. ***B***, Microglial morphology was analyzed in 3D using an automated analysis algorithm in the ipsilesional cortex of mice 14 d after stroke, which revealed significantly reduced sphericity (left) and increased number of branch nodes (right) as markers of reduced microglial activation by SCFA compared with control treatment. Each symbol represents one microglia. Different colors group together microglia from the same mouse. ***C***, Number of microglia found per 1 high-power (40×) FOV in the perilesional cortex. ***D***, Coexpression coverage analysis in the ipsilateral hemispheric cortex for CD68 and Iba-1 expressed as percentage of Iba-1 from a maximum intensity projection. Representative immunofluorescence image (red represents microglia; green represents CD68) (left) and quantification (right). ***E***, Coexpression coverage analysis in the ipsilateral hemispheric cortex for iNOS and Arginase1 (Arg1) with Iba-1 expressed as percentage of Iba-1 coverage area from a maximum intensity projection. Representative immunofluorescence image (red represents microglia; green represents Arg1; cyan represents iNOS) (left) and quantification (right). $N = 3$ mice per group and 3 images per hemisphere. In contrast to the effects of SCFA on microglia function, endothelial cells were unaffected by the SCFA treatment (Figure 4-1, available at https://doi.org/10.1523/JNEUROSCI.1359-19.2019.f4-1). ***F***, Representative gating strategy for flow cytometric analysis of T cells (CD45$^+$CD3$^+$). SCFA supplementation significantly decreased the frequency of T cells in (***G***) brains and (***H***) spleens 14 d after stroke. $N = 9$ per group. Quantification of (***I***) sphericity (left) and ramification index (right) and (***J***) absolute cell counts of microglia 14 d after stroke in the perilesional cortex of *Rag1*$^{-/-}$ mice. In contrast to WT mice (compare with ***B***,***C***), SCFA treatment did not affect microglia activation in lymphocyte-deficient *Rag1*$^{-/-}$ mice. All statistical analyses in this figure were performed using the Mann–Whitney *U* test.

a unique ability to measure even the more subtle effects of SCFA supplementation on poststroke plasticity.

In human stroke patients, interhemispheric resting-state connectivity is significantly weakened following stroke. Specifically, it is thought that inhibitory projections from the lesioned hemisphere to the homotypic contralesional hemisphere are attenuated, leading to a disinhibition of the homotypic area in the contralesional hemisphere (Rehme and Grefkes, 2013). We confirmed this effect with our optogenetic imaging approach, by observing an increase in the contralesional motor cortex area as an indicator of reduced transhemispheric inhibition. This "blooming" effect of the contralesional motor cortex was significantly ameliorated by the SCFA treatment at chronic time points after stroke, which could indicate an improvement of interhemispheric connectivity and thereby reestablish inhibition of the contralesional hemisphere. However, the further in-depth exploration of such interhemispheric inhibition is impeded by several technical limitations of our imaging tool, such as autofluorescent artifacts in the perilesional territory and the lack of directional information of the interhemispheric connections. This would require *in vivo* electrophysiological studies on connectivity between the recovering perilesional tissue and the homotypic contralesional brain area, which are currently not yet established in stroke research. The functional relevance for the changes within connectivity was ultimately confirmed by the corresponding beneficial effects of SCFAs on recovery of motor functions. Behavioral recovery was assessed in a highly sensitive, rater-blinded, and high-throughput automated test, specifically analyzing motor deficits of the affected forelimb, hence providing a reliable readout for poststroke recovery, even in the chronic phase, something that most conventional behavior tests lose their test sensitivity toward (Zausinger et al., 2000; X. Li et al., 2004; Manwani et al., 2011; Rosell et al., 2013).

As an independent line of evidence for the effects of SCFA on poststroke recovery, we detected significant changes in dendritic spine densities and synaptic counts based on histological analysis. Previous studies have demonstrated changes in dendritic spine density of the perilesional cortex as well as contralateral hemisphere and have been identified as a hallmark of poststroke tissue remodeling and marker of synaptic plasticity (Brown et al., 2008; Huang et al., 2018). After stroke, it has been shown that there is a gradual increase of spine density in the contralateral cortex (Huang et al., 2018), whereas spine density in the peri-infarct region is reduced by ~38% within the acute phase (Brown et al., 2008). Accordingly, we observed significantly increased spine densities in the contralateral motor cortex of SCFA-supplemented mice, suggesting that these microbial metabolites could aid recovery by promoting dendritic spine plasticity.

A key limitation of the various analysis readouts used in this study (calcium imaging, spine density, synapse count) is their exclusive reflection of processes in excitatory neurons. The expression of GCamp in Thy1-positive neurons, analysis of dendritic spines on pyramidal neurons, and the synapse count of VGlut1-positive (glutamatergic) synapses all limit the analysis to the excitatory system of the forebrain cortex and do not account for potential alterations in subcortical structures or the complex integration of information by (inhibitory) interneurons within the cortex (Markram et al., 2004). However, the focus on the excitatory cortical system across the different methodological approaches allowed us to thoroughly investigate the impact of SCFAs from a global network perspective (wide-field imaging) to synaptic (sub)structures within the same system. This approach revealed a striking alignment of results across different functional levels from synapse to network plasticity and behavior that strongly support the impact of SCFAs on poststroke recovery. Despite this, future studies need to address the intricate regulation of cortical microcircuits underlying this effect and particularly the role of the various interneuron types. Another relevant limitation is the use only of male mice for most of the experiments (except dendritic spine analysis). Considering recent evidence for sex-specific effects along the gut–brain axis and particularly on microglial activation (Thion et al., 2018; Villa et al., 2018), we cannot exclude a differential effect of the observed pathway in the female sex.

The transcriptomic analysis performed in this study indicated several genes which have previously been associated with microglial activity and phagocytic function to be regulated by SCFAs in the poststroke recovery phase. In contrast, only a very low amount of significantly regulated genes by the SCFA supplementation were enriched for other cell population marker genes, such as neurons or endothelial cells. Therefore, we hypothesized that the SCFA effect on poststroke recovery and neuronal plasticity might be indirectly mediated via microglial activity. Indeed, microglia are key players involved in synaptic pruning and dendritic remodeling (Salter and Stevens, 2017). Upon proinflammatory stimuli, microglial activation is associated with a change in cell morphology. While homeostatic microglia are highly ramified, activated cells acquire a more ameboid shape. We observed after stroke an increase in cell ramification by the SCFA supplementation, indicating a reduced microglial activation state. Interestingly, microglial activation after stroke has previously been associated with reduced phagocytic capacities (Faustino et al., 2011). Hence, modification of microglial activation by SCFA could have an impact on synapse elimination and thereby microglia-dependent synaptic plasticity (Salter and Stevens, 2017). However, microglial elimination ("pruning") of dendritic synapses is vice versa associated with synaptic activity (i.e., less active presynaptic inputs are more likely to be phagocytosed). Reduced synaptic activity in the perilesional cortex due to the tissue injury or in the contralesional cortex due to loss of transcallosal innervation from the injured cortex could both induce excessive (pathological) dendrite pruning (Brown et al., 2008; Riccomagno and Kolodkin, 2015; Salter and Stevens, 2017). This would suggest that dendritic spine remodeling and microglial activation are a reciprocal, bidirectional interaction of neurons and microglia in the recovering cortex after stroke. While the results of RNASeq analysis indicate that SCFAs modulate primarily microglial activation in this process, the detailed interaction of neurons and microglia as well as the directionality of their association will require further experimental studies. Finally, microglia activation has been associated with neuronal plasticity and function beyond morphological reorganization and spine remodeling. We have recently demonstrated that microglia monitor neuronal function at the cell soma and this somatic interaction are altered during pathology after stroke (Cserép et al., 2019), a process that could likely contribute to the functional changes observed in cortical calcium imaging and behavioral outcomes. However, the contribution of SCFAs to this somatic cell–cell interaction is so far unknown.

A large part of previous experimental studies with SCFA have focused on their effect on circulating immune cells. SCFAs modulate the polarization of lymphocyte subsets, such as the ratio of anti-inflammatory regulatory T cells (Treg) to proinflammatory T_H17 cells (Arpaia et al., 2013; Haghikia et al., 2015; Park et al., 2015; Asarat et al., 2016), as well as their migratory behavior between organs (Nakamura et al., 2017). Importantly, lymphocyte invasion to the ischemic brain is a hallmark of poststroke neuroinflammation (Iadecola and Anrather, 2011). It is therefore likely that SCFAs may not exclusively act directly on resident microglia per se, but also via the peripheral effects of SCFAs, which change lymphocyte function. The altered peripheral lymphocytes later invade the injured brain and indirectly influence the cerebral inflammatory milieu. Indeed, T cells have been consistently identified in several reports as the invading leukocyte subpopulation with the largest impact on stroke outcome with partially divergent functions of T-cell subsets (Kleinschnitz et al., 2010). On one hand, immunosuppressive Treg cells provide a neuroprotective function by suppressing an overshooting inflammatory reaction to the brain infarct (Liesz et al., 2015); on the other hand, the proinflammatory T_H1 and T_H17 cells induce secondary neurotoxicity and lead to infarct expansion with worsened functional outcome (Shichita et al., 2009; Gelderblom et al., 2012). In addition to the impact of SCFAs on T-cell polarization, alternative mechanisms of immunoactive SCFA effects might be mediated via regulation of micro-RNA expression (so far mainly studied in cancer) or by modulating the production of reactive oxygen species; however, these pathways are still under investigation and require further exploration in stroke.

Several experimental stroke models have been established for modeling focal ischemic brain injury in rodents. While some stroke models use occlusion of a large cerebral artery, such as intraluminal occlusion of the MCA by a suture or the direct, distal MCA occlusion model, other stroke models induce artery occlusion using other strategies, such as end arterial occlusion by photosensitive dyes or vasoconstriction using endothelin-1 (Fluri et al., 2015; Kumar et al., 2016). All of these experimental stroke methods only model certain elements of the highly complex pathophysiological events of stroke in human patients. Yet, each model provides the advantage to be particularly useful in analyzing specific targets of stroke interventions, acute neuroprotection, reperfusion, delayed apoptosis, inflammation, or chronic repair mechanisms (Carmichael, 2005). The PT stroke model, which was the main animal model used for most experiments in this study, was previously suggested as particularly suitable for analyzing recovery mechanisms after stroke, and is still widely used in this research domain (Carmichael, 2005; Murphy and Corbett, 2009). Disadvantages of this model are that it does not allow local collateral reflow and shows a profound local edema during the acute phase. Therefore, this model is not useful for studies to investigate acute neuroprotective agents or reperfusion therapies. On the other hand, PT stroke allows precise positioning of the lesion in functionally defined brain areas (i.e., the motor cortex in our study). Moreover, the highly reproducible and confined cortical lesion allows for a more detailed analysis of pathophysiological processes in the perilesional cortex compared with other stroke models; which are less consistent in the lesion localization.

Surprisingly, despite this obviously pronounced effect of lymphocytes in poststroke pathology, their role in activating or inhibiting microglial activation has so far barely been investigated. We have observed indirect evidence for T-cell effects on microglial activity in previous experiments, in which depletion of circulating Treg cells affected microglial activation and cytokine release (Liesz et al., 2009). Additional indirect evidence comes from studies demonstrating T-cell interaction and particularly the influence of T cell-secreted cytokines on multiple other cell types in the healthy and injured brain, such as T cell-derived interferon-gamma on animal behavior (Walsh et al., 2015; Filiano et al., 2016). Yet, to our knowledge, the role of T cells as indirect cellular mediators of microbiota-derived SCFAs on the brain has so far not been studied. In this study, we unequivocally demonstrate, for the first time, that T cells are crucial to mediate the immunomodulatory effects of SCFA on brain resident microglia because, in lymphocyte-deficient mice, this effect became abolished. This finding is also in accordance with our previous proof-of-concept experiments showing that circulating T cells were key in facilitating the impact of the gut microbiome on stroke outcome in germ-free versus recolonized animals as well as in mice with a healthy versus a dysbiotic microbiome (Singh et al., 2016, 2018). These previous reports by us and independent reports by others have also consistently identified a translocation of lymphocytes from the intestinal immune compartment to the poststroke brain, providing a cellular link by these circulating and highly motile cells across the gut–brain axis (Benakis et al., 2016; Singh et al., 2016).

Together, this study identified SCFAs as critical metabolites derived from the gut microbiome affecting T-cell function and thereby indirectly modulating the neuro-regenerative milieu. This expands our current understanding of the mechanisms along the gut–brain axis in acute brain injury and recovery where poststroke dysbiosis affects the production of key microbiota-derived metabolites, their impact on immunological homeostasis, and finally the capability for efficient functional recovery. The efficacy of SCFAs for promoting recovery in an experimental stroke model on a functional as well as morphological level opens up novel therapeutic possibilities for improving recovery of human stroke patients. Future studies should validate the proregenerative effect of SCFAs on poststroke recovery before further translational development. Based on the findings from this study and indications for efficacy and similar modes of actions in primary autoimmune brain disorders (Melbye et al., 2019), it is well conceivable that SCFA supplementation could be used as a safe and practical add-on therapy to stroke rehabilitation. However, further studies will be required to test the efficacy of this approach in a post-treatment paradigm, in combination with common comorbidities and comedications, and finally validate in a confirmatory, multicenter preclinical study design before further translation to human stroke patients can be considered (Llovera et al., 2015; Llovera and Liesz, 2016).

References

Arpaia N, Campbell C, Fan X, Dikiy S, van der Veeken J, deRoos P, Liu H, Cross JR, Pfeffer K, Coffer PJ, Rudensky AY (2013) Metabolites produced by commensal bacteria promote peripheral regulatory T-cell generation. Nature 504:451–455.

Asarat M, Apostolopoulos V, Vasiljevic T, Donkor O (2016) Short-chain fatty acids regulate cytokines and Th17/Treg cells in human peripheral blood mononuclear cells in vitro. Immunol Invest 45:205–222.

Austin V, Ku JM, Miller AA, Vlahos R (2019) Ischaemic stroke in mice induces lung inflammation but not acute lung injury. Sci Rep 9:3622.

Becker AM, Meyers E, Sloan A, Rennaker R, Kilgard M, Goldberg MP (2016) An automated task for the training and assessment of distal forelimb function in a mouse model of ischemic stroke. J Neurosci Methods 258:16–23.

Benakis C, Brea D, Caballero S, Faraco G, Moore J, Murphy M, Sita G, Racchumi G, Ling L, Pamer EG, Iadecola C, Anrather J (2016) Commensal microbiota affects ischemic stroke outcome by regulating intestinal gamma delta T cells. Nat Med 22:516–523.

Bieber M, Werner RA, Tanai E, Hofmann U, Higuchi T, Schuh K, Heuschmann PU, Frantz S, Ritter O, Kraft P, Kleinschnitz C (2017) Stroke-induced chronic systolic dysfunction driven by sympathetic overactivity. Ann Neurol 82:729–743.

Biernaskie J, Chernenko G, Corbett D (2004) Efficacy of rehabilitative experience declines with time after focal ischemic brain injury. J Neurosci 24:1245–1254.

Bourassa MW, Alim I, Bultman SJ, Ratan RR (2016) Butyrate, neuroepigenetics and the gut microbiome: can a high fiber diet improve brain health? Neurosci Lett 625:56–63.

Brown CE, Wong C, Murphy TH (2008) Rapid morphologic plasticity of peri-infarct dendritic spines after focal ischemic stroke. Stroke 39:1286–1291.

Carmichael ST (2005) Rodent models of focal stroke: size, mechanism, and purpose. NeuroRx 2:396–409.

Chuang DM, Leng Y, Marinova Z, Kim HJ, Chiu CT (2009) Multiple roles of HDAC inhibition in neurodegenerative conditions. Trends Neurosci 32:591–601.

Cramer JV, Gesierich B, Roth S, Dichgans M, Düring M, Liesz A (2019) In vivo wide-field calcium imaging of the mouse cortex for analysis of network connectivity in health and brain disease. Neuroimage 199:570–584.

Cryan JF, Dinan TG (2012) Mind-altering microorganisms: the impact of the gut microbiota on brain and behaviour. Nat Rev Neurosci 13:701–712.

Cserép C, Pósfai B, Lénárt N, Fekete R, László ZI, Lele Z, Orsolits B, Molnár G, Heindl S, Schwarcz AD, Ujvári K, Környei Z, Tóth K, Szabadits E, Sperlágh B, Baranyi M, Csiba L, Hortobágyi T, Maglóczky Z, Martinecz B, et al. (2019) Microglia monitor and protect neuronal function via specialized somatic purinergic junctions. Science. Advance online publication. Retrieved December 12, 2019. doi: 10.1126/science.aax6752.

Dirnagl U, Iadecola C, Moskowitz MA (1999) Pathobiology of ischaemic stroke: an integrated view. Trends Neurosci 22:391–397.

Erny D, Hrabe de Angelis AL, Jaitin D, Wieghofer P, Staszewski O, David E, Keren-Shaul H, Mahlakoiv T, Jakobshagen K, Buch T, Schwierzeck V, Utermöhlen O, Chun E, Garrett WS, McCoy KD, Diefenbach A, Staeheli P, Stecher B, Amit I, Prinz M (2015) Host microbiota constantly control maturation and function of microglia in the CNS. Nat Neurosci 18:965–977.

Faustino JV, Wang X, Johnson CE, Klibanov A, Derugin N, Wendland MF, Vexler ZS (2011) Microglial cells contribute to endogenous brain defenses after acute neonatal focal stroke. J Neurosci 31:12992–13001.

Feng Y, Liao S, Wei C, Jia D, Wood K, Liu Q, Wang X, Shi FD, Jin WN (2017) Infiltration and persistence of lymphocytes during late-stage cerebral ischemia in middle cerebral artery occlusion and photothrombotic stroke models. J Neuroinflammation 14:248.

Filiano AJ, Xu Y, Tustison NJ, Marsh RL, Baker W, Smirnov I, Overall CC, Gadani SP, Turner SD, Weng Z, Peerzade SN, Chen H, Lee KS, Scott MM, Beenhakker MP, Litvak V, Kipnis J (2016) Unexpected role of interferon-gamma in regulating neuronal connectivity and social behaviour. Nature 535:425–429.

Fluri F, Schuhmann MK, Kleinschnitz C (2015) Animal models of ischemic stroke and their application in clinical research. Drug Des Dev Ther 9:3445–3454.

Frost G, Sleeth ML, Sahuri-Arisoylu M, Lizarbe B, Cerdan S, Brody L, Anastasovska J, Ghourab S, Hankir M, Zhang S, Carling D, Swann JR, Gibson G, Viardot A, Morrison D, Thomas EL, Bell JD (2014) The short-chain fatty acid acetate reduces appetite via a central homeostatic mechanism. Nat Commun 5:3611.

Gelderblom M, Weymar A, Bernreuther C, Velden J, Arunachalam P, Steinbach K, Orthey E, Arumugam TV, Leypoldt F, Simova O, Thom V, Friese MA, Prinz I, Hölscher C, Glatzel M, Korn T, Gerloff C, Tolosa E, Magnus T (2012) Neutralization of the IL-17 axis diminishes neutrophil invasion and protects from ischemic stroke. Blood 120:3793–3802.

Haghikia A, Jörg S, Duscha A, Berg J, Manzel A, Waschbisch A, Hammer A, Lee DH, May C, Wilck N, Balogh A, Ostermann AI, Schebb NH, Akkad DA, Grohme DA, Kleinewietfeld M, Kempa S, Thöne J, Demir S, Müller DN, et al. (2015) Dietary fatty acids directly impact central nervous system autoimmunity via the small intestine. Immunity 43:817–829.

Heindl S, Gesierich B, Benakis C, Llovera G, Duering M, Liesz A (2018) Automated morphological analysis of microglia after stroke. Front Cell Neurosci 12:106.

Hoffmann S, Otto C, Kurtz S, Sharma CM, Khaitovich P, Vogel J, Stadler PF, Hackermüller J (2009) Fast mapping of short sequences with mismatches, insertions and deletions using index structures. PLoS Comput Biol 5:e1000502.

Houlden A, Goldrick M, Brough D, Vizi ES, Lénárt N, Martinecz B, Roberts IS, Denes A (2016) Brain injury induces specific changes in the caecal microbiota of mice via altered autonomic activity and mucoprotein production. Brain Behav Immun 57:10–20.

Hoving LR, Heijink M, van Harmelen V, van Dijk KW, Giera M (2018) GC-MS analysis of short-chain fatty acids in feces, cecum content, and blood samples. Methods Mol Biol 1730:247–256.

Huang SY, Chang CH, Hung HY, Lin YW, Lee EJ (2018) Neuroanatomical and electrophysiological recovery in the contralateral intact cortex following transient focal cerebral ischemia in rats. Neurol Res 40:130–138.

Iadecola C, Anrather J (2011) The immunology of stroke: from mechanisms to translation. Nat Med 17:796–808.

Ippolito DM, Eroglu C (2010) Quantifying synapses: an immunocytochemistry-based assay to quantify synapse number. J Vis Exp 45:2270.

Jones TA, Schallert T (1994) Use-dependent growth of pyramidal neurons after neocortical damage. J Neurosci 14:2140–2152.

Kau AL, Ahern PP, Griffin NW, Goodman AL, Gordon JI (2011) Human nutrition, the gut microbiome and the immune system. Nature 474:327–336.

Kim HJ, Leeds P, Chuang DM (2009) The HDAC inhibitor, sodium butyrate, stimulates neurogenesis in the ischemic brain. J Neurochem 110:1226–1240.

Kleinschnitz C, Schwab N, Kraft P, Hagedorn I, Dreykluft A, Schwarz T, Austinat M, Nieswandt B, Wiendl H, Stoll G (2010) Early detrimental T-cell effects in experimental cerebral ischemia are neither related to adaptive immunity nor thrombus formation. Blood 115:3835–3842.

Kumar A, Aakriti, Gupta V (2016) A review on animal models of stroke: an update. Brain Res Bull 122:35–44.

Liao Y, Smyth GK, Shi W (2014) featureCounts: an efficient general purpose program for assigning sequence reads to genomic features. Bioinformatics 30:923–930.

Li Q, Cheng Z, Zhou L, Darmanis S, Neff NF, Okamoto J, Gulati G, Bennett ML, Sun LO, Clarke LE, Marschallinger J, Yu G, Quake SR, Wyss-Coray T, Barres BA (2019) Developmental heterogeneity of microglia and brain myeloid cells revealed by deep single-cell RNA sequencing. Neuron 101:207–223.e10.

Li X, Blizzard KK, Zeng Z, DeVries AC, Hurn PD, McCullough LD (2004) Chronic behavioral testing after focal ischemia in the mouse: functional recovery and the effects of gender. Exp Neurol 187:94–104.

Liesz A, Suri-Payer E, Veltkamp C, Doerr H, Sommer C, Rivest S, Giese T, Veltkamp R (2009) Regulatory T cells are key cerebroprotective immunomodulators in acute experimental stroke. Nat Med 15:192–199.

Liesz A, Zhou W, Na SY, Hämmerling GJ, Garbi N, Karcher S, Mracsko E, Backs J, Rivest S, Veltkamp R (2013) Boosting regulatory T cells limits neuroinflammation in permanent cortical stroke. J Neurosci 33:17350–17362.

Liesz A, Hu X, Kleinschnitz C, Offner H (2015) Functional role of regulatory lymphocytes in stroke facts and controversies. Stroke 46:1422–1430.

Llovera G, Hofmann K, Roth S, Salas-Pérdomo A, Ferrer-Ferrer M, Perego C, Zanier ER, Mamrak U, Rex A, Party H, Agin V, Fauchon C, Orset C, Haelewyn B, De Simoni MG, Dirnagl U, Grittner U, Planas AM, Plesnila N, Vivien D, et al. (2015) Results of a preclinical randomized controlled multicenter trial (pRCT): anti-CD49d treatment for acute brain ischemia. Sci Transl Med 7:299ra121.

Llovera G, Liesz A (2016) The next step in translational research: lessons learned from the first preclinical randomized controlled trial. J Neurochem 139 [Suppl 2]:271–279.

Llovera G, Roth S, Plesnila N, Veltkamp R, Liesz A (2014) Modeling stroke in mice: permanent coagulation of the distal middle cerebral artery. J Vis Exp 89:e51729.

Love MI, Huber W, Anders S (2014) Moderated estimation of fold change and dispersion for RNA-seq data with DESeq2. Genome Biol 15:550.

Manwani B, Liu F, Xu Y, Persky R, Li J, McCullough LD (2011) Functional recovery in aging mice after experimental stroke. Brain Behav Immun 25:1689–1700.

Markram H, Toledo-Rodriguez M, Wang Y, Gupta A, Silberberg G, Wu C (2004) Interneurons of the neocortical inhibitory system. Nat Rev Neurosci 5:793–807.

Melbye P, Olsson A, Hansen TH, Søndergaard HB, Bang Oturai A (2019) Short-chain fatty acids and gut microbiota in multiple sclerosis. Acta Neurol Scand 139:208–219.

Meng H, Zhao H, Cao X, Hao J, Zhang H, Liu Y, Zhu MS, Fan L, Weng L, Qian L, Wang X, Xu Y (2019) Double-negative T cells remarkably promote neuroinflammation after ischemic stroke. Proc Natl Acad Sci U S A 116:5558–5563.

Morrison DJ, Preston T (2016) Formation of short chain fatty acids by the gut microbiota and their impact on human metabolism. Gut Microbes 7:189–200.

Murphy TH, Corbett D (2009) Plasticity during stroke recovery: from synapse to behaviour. Nat Rev Neurosci 10:861–872.

Nakamura YK, Janowitz C, Metea C, Asquith M, Karstens L, Rosenbaum JT, Lin P (2017) Short chain fatty acids ameliorate immune-mediated uveitis partially by altering migration of lymphocytes from the intestine. Sci Rep 7:11745.

Neumann J, Riek-Burchardt M, Herz J, Doeppner TR, König R, Hütten H, Etemire E, Männ L, Klingberg A, Fischer T, Görtler MW, Heinze HJ, Reichardt P, Schraven B, Hermann DM, Reymann KG, Gunzer M (2015) Very-late-antigen-4 (VLA-4)-mediated brain invasion by neutrophils leads to interactions with microglia, increased ischemic injury and impaired behavior in experimental stroke. Acta Neuropathol 129:259–277.

Offner H, Subramanian S, Parker SM, Afentoulis ME, Vandenbark AA, Hurn PD (2006) Experimental stroke induces massive, rapid activation of the peripheral immune system. J Cereb Blood Flow Metab 26:654–665.

Park J, Kim M, Kang SG, Jannasch AH, Cooper B, Patterson J, Kim CH (2015) Short-chain fatty acids induce both effector and regulatory T cells by suppression of histone deacetylases and regulation of the mTOR-S6K pathway. Mucosal Immunol 8:80–93.

Ransohoff RM, Engelhardt B (2012) The anatomical and cellular basis of immune surveillance in the central nervous system. Nat Rev Immunol 12:623–635.

Rehme AK, Grefkes C (2013) Cerebral network disorders after stroke: evidence from imaging-based connectivity analyses of active and resting brain states in humans. J Physiol 591:17–31.

Riccomagno MM, Kolodkin AL (2015) Sculpting neural circuits by axon and dendrite pruning. Annu Rev Cell Dev Biol 31:779–805.

Rosell A, Agin V, Rahman M, Morancho A, Ali C, Koistinaho J, Wang X, Vivien D, Schwaninger M, Montaner J (2013) Distal occlusion of the middle cerebral artery in mice: are we ready to assess long-term functional outcome? Transl Stroke Res 4:297–307.

Roth S, Singh V, Tiedt S, Schindler L, Huber G, Geerlof A, Antoine DJ, Anfray A, Orset C, Gauberti M, Fournier A, Holdt LM, Harris HE, Engelhardt B, Bianchi ME, Vivien D, Haffner C, Bernhagen J, Dichgans M, Liesz A (2018) Brain-released alarmins and stress response synergize in accelerating atherosclerosis progression after stroke. Science Transl Med 10:11.

Salter MW, Stevens B (2017) Microglia emerge as central players in brain disease. Nat Med 3:1018–1027.

Schafer DP, Lehrman EK, Kautzman AG, Koyama R, Mardinly AR, Yamasaki R, Ransohoff RM, Greenberg ME, Barres BA, Stevens B (2012) Microglia sculpt postnatal neural circuits in an activity and complement-dependent manner. Neuron 74:691–705.

Schindelin J, Arganda-Carreras I, Frise E, Kaynig V, Longair M, Pietzsch T, Preibisch S, Rueden C, Saalfeld S, Schmid B, Tinevez JY, White DJ, Hartenstein V, Eliceiri K, Tomancak P, Cardona A (2012) Fiji: an open-source platform for biological-image analysis. Nat Methods 9:676682.

Selvaraj UM, Stowe AM (2017) Long-term T cell responses in the brain after an ischemic stroke. Discov Med 24:323–333.

Shichita T, Sugiyama Y, Ooboshi H, Sugimori H, Nakagawa R, Takada I, Iwaki T, Okada Y, Iida M, Cua DJ, Iwakura Y, Yoshimura A (2009) Pivotal role of cerebral interleukin-17-producing gamma delta T cells in the delayed phase of ischemic brain injury. Nat Med 15:946–950.

Singh V, Roth S, Llovera G, Sadler R, Garzetti D, Stecher B, Dichgans M, Liesz A (2016) Microbiota dysbiosis controls the neuroinflammatory response after stroke. J Neurosci 36:7428–7440.

Singh V, Sadler R, Heindl S, Llovera G, Roth S, Benakis C, Liesz A (2018) The gut microbiome primes a cerebroprotective immune response after stroke. J Cereb Blood Flow Metab 38:1293–1298.

Smith PM, Howitt MR, Panikov N, Michaud M, Gallini CA, Bohlooly-Y M, Glickman JN, Garrett WS (2013) The microbial metabolites, short-chain fatty acids, regulate colonic T-reg cell homeostasis. Science 341:569–573.

Stephan AH, Barres BA, Stevens B (2012) The complement system: an unexpected role in synaptic pruning during development and disease. Annu Rev Neurosci 35:369–389.

Swidsinski A, Loening-Baucke V, Krüger M, Kirsch S (2012) Central nervous system and the colonic bioreactor: analysis of colonic microbiota in patients with stroke unravels unknown mechanisms of the host defense after brain injury. Intestinal Research 10:332.

Tan J, McKenzie C, Vuillermin PJ, Goverse G, Vinuesa CG, Mebius RE, Macia L, Mackay CR (2016) Dietary fiber and bacterial SCFA enhance oral tolerance and protect against food allergy through diverse cellular pathways. Cell Rep 15:2809–2824.

Thion MS, Low D, Silvin A, Chen J, Grisel P, Schulte-Schrepping J, Blecher R, Ulas T, Squarzoni P, Hoeffel G, Coulpier F, Siopi E, David FS, Scholz C, Shihui F, Lum J, Amoyo AA, Larbi A, Poidinger M, Buttgereit A, et al. (2018) Microbiome influences prenatal and adult microglia in a sex-specific manner. Cell 172:500–516.e516.

van de Wouw M, Boehme M, Lyte JM, Wiley N, Strain C, O'Sullivan O, Clarke G, Stanton C, Dinan TG, Cryan JF (2018) Short-chain fatty acids: microbial metabolites that alleviate stress-induced brain-gut axis alterations. J Physiol 596:4923–4944.

Villa A, Gelosa P, Castiglioni L, Cimino M, Rizzi N, Pepe G, Lolli F, Marcello E, Sironi L, Vegeto E, Maggi A (2018) Sex-specific features of microglia from adult mice. Cell Rep 23:3501–3511.

Walsh JT, Hendrix S, Boato F, Smirnov I, Zheng J, Lukens JR, Gadani S, Hechler D, Gölz G, Rosenberger K, Kammertöns T, Vogt J, Vogelaar C, Siffrin V, Radjavi A, Fernandez-Castaneda A, Gaultier A, Gold R, Kanneganti TD, Nitsch R, et al. (2015) MHCII-independent CD4(+) T cells protect injured CNS neurons via IL-4. J Clin Invest 125:699–714.

Wu Y, Dissing-Olesen L, MacVicar BA, Stevens B (2015) Microglia: dynamic mediators of synapse development and plasticity. Trends Immunol 36:605–613.

Xia GH, You C, Gao XX, Zeng XL, Zhu JJ, Xu KY, Tan CH, Xu RT, Wu QH, Zhou HW, He Y, Yin J (2019) Stroke Dysbiosis Index (SDI) in gut microbiome are associated with brain injury and prognosis of stroke. Front Neurol 10:397.

Zausinger S, Hungerhuber E, Baethmann A, Reulen H, Schmid-Elsaesser R (2000) Neurological impairment in rats after transient middle cerebral artery occlusion: a comparative study under various treatment paradigms. Brain Res 863:94–105.

Zhang Y, Chen K, Sloan SA, Bennett ML, Scholze AR, O'Keeffe S, Phatnani HP, Guarnieri P, Caneda C, Ruderisch N, Deng S, Liddelow SA, Zhang C, Daneman R, Maniatis T, Barres BA, Wu JQ (2014) An RNA sequencing transcriptome and splicing database of glia, neurons, and vascular cells of the cerebral cortex. J Neurosci 34:11929–11947.

Zhong S, Zhang S, Fan X, Wu Q, Yan L, Dong J, Zhang H, Li L, Sun L, Pan N, Xu X, Tang F, Zhang J, Qiao J, Wang X (2018) A single-cell RNA-seq survey of the developmental landscape of 720 the human prefrontal cortex. Nature 555:524–528.

Figure 1-1

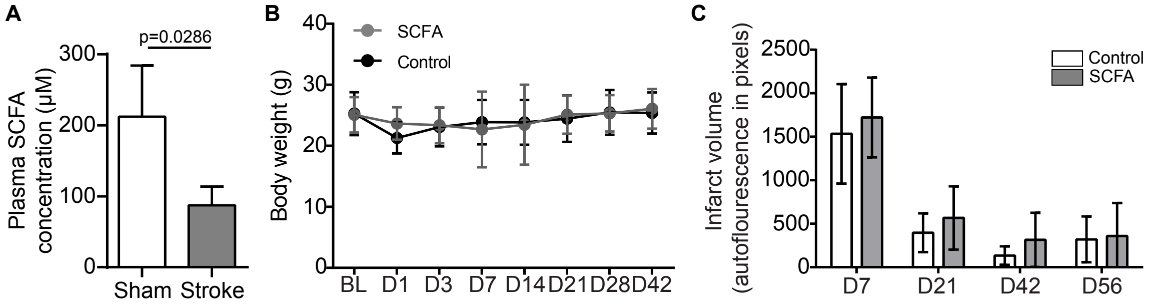

SCFA concentrations are reduced after stroke. (**A**) Plasma concentration (µM) showing a decrease of total SCFA (sum of acetate, propionate and butyrate) in mice 3 days after fMCAo stroke surgery (grey bars) compared to sham (open bars). N=4 per group (Mann-Whitney U test). (**B**) No difference of body weight in grams at baseline (BL) until D42 post PT in mice supplemented with SCFA (grey line) or control (black line). N=14/15 per group (2-way ANOVA with Holm-Sidak correction for multiple testing). (**C**) Lesion size as measured in pixels did not differ between SCFA (grey bar) and control mice (open bar) at any time points. N=11/10 and statistical test with multiple T tests per time point and Holm-Sidak method correction for multiple testing. Download

Figure 2-1

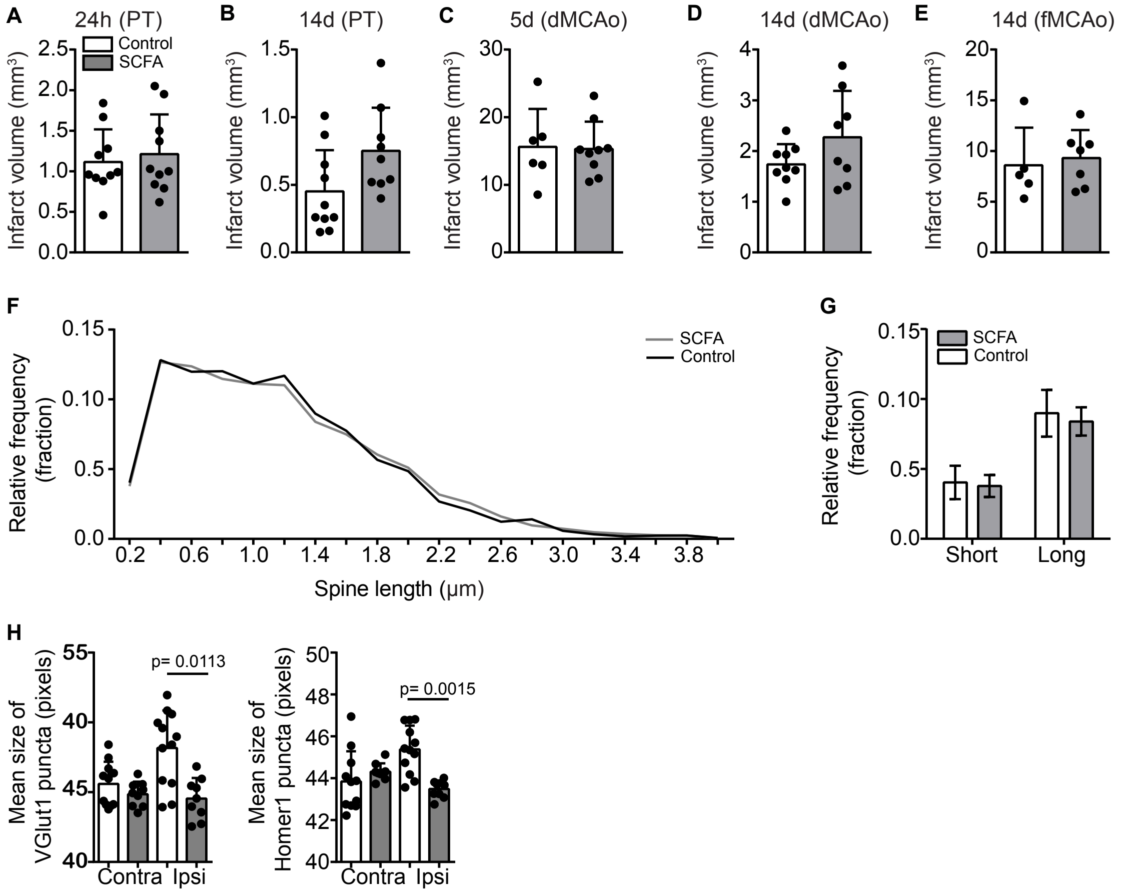

SCFA supplementation does not alter tissue injury in 3 focal stroke models. Infarct volume from Nissl staining in mice supplemented with control mix (open bar) or SCFA (grey bar). (**A**) 24 h after PT, N=10 per group; (**B**) 14 d after PT, N=10/9 per group; (**C**) 5 d after dMCAo, N=6/9 per group; (**D**) 14 d after dMCAo, N=9/8 per group; and (**E**) 14 d after fMCAo, N=5/7 per group. Statistical analyses were performed using the Mann-Whitney U test. (**F**) As in Figure 2E, histogram of the relative frequency (fraction) of spines found at different lengths 14 d after PT in the contralateral cortex (bin width = 0.2 µm). (**G**) Quantification of short (0.2 µm) and long (1.4 µm) spines in control (open bars) and SCFA (grey bars) treated mice. N=4/5 per group, Mann-Whitney U test. (**H**) The size in pixels of synapses stained with VGlut1 (left) and Homer1 (right). Quantification revealed larger synapse areas in the peri-lesional cortex which was significantly ameliorated with SCFA supplementation. Contra: contralateral hemisphere; ipsi: ipsilateral hemisphere, N=3/4 mice (3 sections per mouse), statistical analysis performed with Kruskal-Wallis test with Dunn's multiple comparison correction.

Figure 3-1

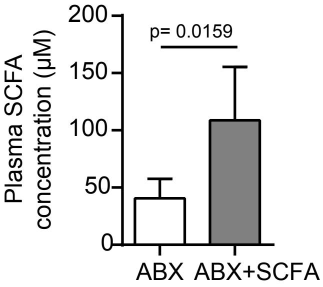

SCFA supplementation increases plasma concentrations. Mice were pre-treated with antibiotic mix for 4 weeks, and then additionally given control (ABX, open bars) or SCFA supplementation (ABX+SCFA, grey bars). Total plasma concentration (µM) of total SCFA (acetate, propionate and butyrate) showing significant increase after SCFA supplementation compared to control treated mice, N=4/5 per group (Mann-Whitney U test).

Figure 4-1

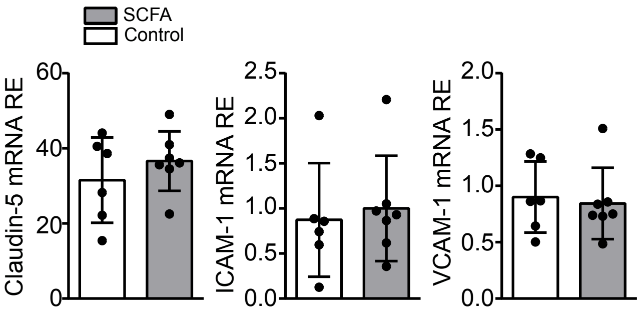

SCFA supplementation does not affect cerebral endothelial expression. Relative mRNA expression (RE) for the tight-junction and adhesion molecules Claudin-5 (left), ICAM-1 (middle) and VCAM-1 (right) from the peri-lesional cortex in control (open bars) and SCFA (grey bars) treated mice (Mann-Whitney U test).

7. Acknowledgements

First and foremost, I would like to thank my supervisor, Prof. Dr. med. Arthur Liesz, for giving me the opportunity to work in his research group and for being a truly inspiring mentor and role model since 2016, when I joined his lab for an internship. His enthusiasm for research has always been contagious for me. Moreover, I want to thank him for all the constant support and advice he gave me through all these years, helping me to believe in myself and to grow skills I never thought I would be capable of.

I would like to thank Prof. Dr. med. Marco Düring and PD Dr. Florence Bareyre, who both were members of my Ph. D. Thesis Advisory Committee, for giving me valuable advice and ideas for my research project. Moreover, I want to express my gratitude to Prof. Ann Stowe, who welcomed me so warm and friendly in her lab and home during my lab visit in Dallas – discussions with her always inspired me. Additionally, I would like to thank all collaborators I worked with over the past years for giving me the chance to contribute to their fascinating research, which was really an exciting experience for me.

Furthermore, I would like to thank the whole LieszLab for always making working in our lab a truly pleasurable experience, for all fruitful scientific and non-scientific discussions, for sharing valuable expertise, for spending time outside of the lab, and helping me believe that everything is possible as long as we work together as a team. I would also like to express my gratitude especially to Alessio Ricci and Olga Carofiglio for all their help with the revision experiments for my first author paper – I was very happy to have support from someone I could fully rely on. Additionally, I want to thank my office colleagues, Dr. Alba Simats, Dr. Daniel Varga and Dr. Stefan Roth, who always had a cup of coffee, an open ear and helpful advice. And I would like to thank the colleagues from the institute, Joshua J Shrouder and Bernhard Groschup for becoming true friends over the past years.

Finally, I would like to thank my friends and family for all the support and motivating words - especially my boyfriend, who was always supporting, encouraging and understanding me.

8. Scientific publications

Heindl S, Ricci A, Carofiglio O, Zhou Q, Arzberger T, Lenart N, Franzmeier N, Hortobagyi T, Nelson PT, Stowe AM, Denes A, Edbauer D, Liesz A. (2021). Chronic T cell proliferation in brains after stroke could interfere with the efficacy of immunotherapies. ***J Exp Med.*** doi: 10.1084/jem.20202411.

Aswendt M Green C, Sadler R, Llovera G, Dzikowski L, **Heindl S**, Gomez de Agüero M, Diedenhofen M, Vogel S, Wieters F, Wiedermann D, Liesz A, Hoehn M. (2021). The gut microbiota modulates brain network connectivity under physiological conditions and after acute brain ischemia. iScience. doi: 10.1016/j.isci.2021.103095

Colombo AV, Sadler RK, Llovera G, Singh V, Roth S, **Heindl** S, Sebastian Monasor L, Verhoeven A, Peters F, Parhizkar S, Kamp F, Gomez de Aguero M, MacPherson AJ, Winkler E, Herms J, Benakis C, Dichgans M, Steiner H, Giera M, Haass C, Tahirovic S, Liesz A. (2021). Microbiota-derived short chain fatty acids modulate microglia and promote Aβ plaque deposition. **Elife**. 2021 Apr 13;10:e59826. doi: 10.7554/eLife.59826

Zhou Q, Mareljic N, Michaelsen M, Parhizkar S, **Heindl S**, Nuscher B, Farny D, Czuppa M, Schludi C, Graf A, Krebs S, Blum H, Feederle R, Roth S, Haass C, Arzberger T, Liesz A, Edbauer D. (2020). Active poly-GA vaccination prevents microglia activation and motor deficits in a C9orf72 mouse model. ***EMBO Mol Med.*** Feb 7;12(2):e10919. doi: 10.15252/emmm.201910919.

Cserép C, Pósfai B, Lénárt N, Fekete R, László ZI, Lele Z, Orsolits B, Molnár G, **Heindl S**, Schwarcz AD, Ujvári K, Környei Z, Tóth K, Szabadits E, Sperlágh B, Baranyi M, Csiba L, Hortobágyi T, Maglóczky Z, Martinecz B, Szabó G, Erdélyi F, Szipőcs R, Tamkun MM, Gesierich B, Duering M, Katona I, Liesz A, Tamás G, Dénes Á. (2020). Microglia monitor and protect neuronal function through specialized somatic purinergic junctions. ***Science.*** Jan 31;367(6477):528-537. doi: 10.1126/science.aax6752.

Sadler R, Cramer JV, **Heindl S**, Kostidis S, Betz D, Zuurbier KR, Northoff BH, Heijink M, Goldberg MP, Plautz EJ, Roth S, Malik R, Dichgans M, Holdt LM, Benakis C, Giera M, Stowe AM, Liesz A. (2020). Short-Chain Fatty Acids Improve Poststroke Recovery via Immunological Mechanisms. ***J Neurosci.*** Jan 29;40(5):1162-1173. doi: 10.1523/JNEUROSCI.1359-19.2019.

Heindl S, Gesierich B, Benakis C, Llovera G, Duering M, Liesz A. (2018). Automated Morphological Analysis of Microglia After Stroke. ***Front Cell Neurosci.*** Apr 19;12:106. doi: 10.3389/fncel.2018.00106

Singh V, Sadler R, **Heindl S**, Llovera G, Roth S, Benakis C, Liesz A. (2018). The gut microbiome primes a cerebroprotective immune response after stroke. ***J Cereb Blood Flow Metab.*** Aug;38(8):1293-1298. doi: 10.1177/0271678X18780130.

Preprints:

Benakis C, Simats A, Tritschler S, **Heindl S**, Besson-Girard S, Llovera G, Pinkham K, Kolz A, Theis F, Gökce O, Peters A, Liesz. (2021). T cells modulate the microglial response to brain ischemia. Available from: bioRxiv, doi: https://doi.org/10.1101/2021.09.23.461546

Reifschneider A, Robinson S, van Lengerich B, Gnörich J, Logan T, **Heindl S**, Vogt MA, Weidinger E, Riedl L, Wind K, Zatcepin A, Haberl S, Nuscher B, Kleinberger G, Klimmt J, Götzl JK, Liesz A, Bürger K, Brendel M, Levin J, Diehl-Schmid J, Suh J, Di Paolo G, Lewcock JW, Monroe KM, Paquet D, Capell A, Haass C. (2021). Reduction of TREM2 signaling reduces hyperactivation of PGRN loss-of-function microglia but fails to ameliorate lysosomal dysfunction and brain pathology. Available from: bioRxiv, doi: https://doi.org/10.1101/2021.07.08.451574